Thermodynamic description of bacterial metal-sensing: A cellular logic for metals

MARIA ALESSANDRA MARTINI

Thermodynamic description of bacterial metal-sensing: A cellular logic for metals

Maria Alessandra Martini

A thesis presented for the degree
of Doctor of Philosophy

Durham University
Department of Biosciences

November 2019

Thermodynamic description of bacterial metal-sensing: A cellular logic for metals

Maria Alessandra Martini

Almost half of all enzymes require a metal ion to function; yet most proteins will bind the 'wrong' metal more tightly than the 'right' one. Cells can achieve correct metalation provided the tight binding, competitive metals are kept less available than the weak binding ones. However, 'metal availability' has been challenging to define and measure. The purpose of this thesis was to address these challenges.

Bacterial metal-sensing DNA-binding transcriptional regulators are tuned to respond within a narrow range of intracellular availabilities of the metals they sense. Therefore, sensors can be used as a window through which to observe intracellular metal availability in a bacterial cell.

Two sensors from the set of metalloregulators in *Salmonella*, MntR and Fur, have been characterised *in vitro* to determine their affinities for their cognate metals and for DNA. In order to calculate sensor responses to metals, a thermodynamics-based mathematical model was developed and applied to MntR and Fur, as well as to the other sensors within the set. From the sensitivities of the metal sensors, the standard free energies for metal complex formation in *Salmonella* cells were determined. Notably, these free energies follow the inverse of the Irving-Williams series: The more competitive the metal, the more favourable the free energy for metal complex formation and hence the lesser availability to which the cognate sensor is attuned.

These results not only illustrate a cellular logic for metalation, but also enable predictions of what metal a molecule of interest will bind *in vivo* and the fractional metalation state of that molecule. Here, this has been exemplified by examining how cobalt partitions into the vitamin B_{12} biosynthetic pathway in *Salmonella*. As metal availability can change in response to growth conditions, a methodology to refine and adapt the model to bespoke culture conditions has also been tested.

Table of Content

List of Figures

List of Tables

Memorandum

Parts of this work have been published as:

Osman, D., Martini, M. A., Foster, A. W., Chen, J., Scott, A. J. P., Morton, R. J., Steed, J. W., Lurie-Luke, E., Huggins, T. G., Lawrence, A. D., Deery, E., Warren, M. J., Chivers, P. T. & Robinson, N. J. 2019. Bacterial sensors define intracellular free energies for correct enzyme metalation. *Nat Chem Biol,* 15**,** 241-249.

Declaration

No portion of this work has been submitted in support of an application for another degree or qualification from this or any other University or institute of learning.

Statement of copyright

Acknowledgements

Above all, I would like to express my most heartfelt gratitude to Prof. Nigel Robinson, for his patient and continuous guidance over these years and for his invaluable advice on science. His enthusiasm encouraged this work from beginning to end.

I would like to extend my sincere thanks to Dr. Peter Chivers, Dr. Karrera Djoko and my thesis committee: Prof. Marc Knight and Dr. Tony Fawcett. I am grateful for your suggestions, constructive comments and encouragement.

I am indebted to everyone who produced the additional data that I used in this work. In particular: The past and present members of the Robinson and Chivers groups for the characterisation of the other *Salmonella* sensors; Dr. Thomas Huggins, Dr. Junjun Chen (Procter and Gamble) and Dr. Deenah Osman for the protein abundance measurements; Dr. Andrew Foster for the CbiK metal-affinities (in collaboration with Prof. Martin Warren, University of Kent) and Zur data; Dr. Richard Morton for the MATLAB scripts. I gratefully acknowledge financial support from Procter and Gamble, which made this work and my permanence in Durham possible.

I cannot fail to mention those who have come through Lab 209 in my time here. Thank you for sharing the joys and sorrows of research in the lab: You have all been a pleasure to work with! I am grateful for the guidance and expertise you provided, as well as the stimulating discussions (not exclusively about science!). I owe a special acknowledgment to Dr. Deenah Osman for her endless patience while training and supervising me in the lab. She always took time to answer my many "quick" questions and, together with Dr. Andrew Foster, taught me to have confidence in my skills.

Completing this work would have been all the more difficult without all of the amazing friends who have made me feel at home in Durham. It is impossible for me to explicitly mention you all. Still, I would like each and every one of you to know how grateful I am for the time we spent together.

I am deeply grateful to my parents and my sister for their unwavering love and support. Un ringraziamento particolare va anche alle mie nonne, agli zii a tutto alla famiglia tutta. Grazie di non avermi mai fatto mancare il vostro affetto e sostegno, anche se lontana. Un pensiero speciale va ai miei nonni. So che sareste stati orgogliosi di vedermi raggiungere questo traguardo.

My final thank you is to my partner Elia Fioravanti. First of all, for his help in solving the equations in Chapter 5. But most of all, thank you, Elia, for having shared this amazing

adventure with me. Thank you for always being there and for believing in me even when I do not. I am profoundly grateful for your love, your understanding and your faith in me.

Chapter 1.

Introduction

1.1 Metal ions in biological systems

Metals are essential nutrients to all living organisms. Together with the abundant s-block metals like sodium, potassium, calcium and magnesium, trace metals from the d-block (zinc, iron, manganese, cobalt, nickel, molybdenum, tungsten and vanadium) play critical roles in biological systems. A bioinformatic survey estimated that about half of all the enzymes (and approximately from one-quarter to one-third of all proteins) need a metal ion in order to function (Andreini et al, 2008; Waldron et al, 2009). Metals across the periodic table each display a unique collection of properties. Metal ions can, for example, differ in charge, d-shell electronic configuration, preferences for particular ligands and particular coordination structures, Lewis acid character and redox activity (Haas & Franz, 2009). Nature took advantage of these diverse chemical properties to perform several different functional roles, more challenging (or perhaps impossible) to achieve with the sole organic chemistry characterising the building block elements of biomolecules (carbon, hydrogen, oxygen, nitrogen, phosphorus and sulphur). Some of the functions metal ions have in biological systems include the maintenance of charge balance (for example, through potassium channels), maintenance of biomolecule structure (e.g. Zinc finger proteins, Mg(II) stabilization of tRNA), signalling (e.g. Ca(II) release in biochemical signalling pathways), electron transfer (e.g. iron-sulphur proteins, cytochromes), acid-base catalysis (e.g. Zn(II) in carbonic anhydrases), atom or group transfer (e.g. dioxygen transport via haemoglobin), redox catalysis (e.g. nitrogen fixation) (Bertini et al, 1994; Williams & Da Silva, 2001).

Organisms have adapted to use the metal elements that were available in their environment. Metal utilisation was altered during evolution in response to environmental changes (Dupont et al, 2010). For example, the great oxidation event due to the accumulation of dioxygen from the photosynthetic processes in the Paleoproterozoic era, greatly affected the solubility of metal ions in ocean waters. While in the anoxic and reducing Archean ocean, iron, manganese and cobalt would have been soluble and readily available, the increasing concentration of oxygen led to a gradual decrease if bioavailability of these metals in sea water, for instance due to the formation of insoluble oxides. Conversely, while scarcely bioavailable before, zinc and copper availability greatly increased after the great oxidation event (Dupont et al, 2010). Such change in bioavailability is reflected in metal utilisation by the different domains of life. For example, eukaryotes have a greater utilisation of zinc and copper compared to archaea and prokaryotes (Dupont et al, 2006). Nevertheless, crucial enzymes that could not be adapted to

the change in metal bioavailability have created dependence of organisms on some elements that were readily available pre-great oxidation event and then became scarce. One example is iron, which under anoxic reducing conditions is soluble as Fe(II) but, in the presence of oxygen, becomes oxidised to Fe(III) and forms insoluble oxides at neutral and alkaline pH. Therefore, both bacteria and plants have evolved strategies for scavenging and storing the scarce iron from the environment (Crowley et al, 1991).

1.2 The challenge for correct metal-protein speciation

As most nutrients, there is an optimal range of metal content for an organism to sustain vital function. If the organism experiences metal starvation, it might not be able to fully metalate the metal-utilising biomolecules, with the possible consequence of accumulation of inactive apo-proteins. Conversely, excess of metals can have toxic effects. An excess of some redox-active metals, such as iron and copper, can lead to the generation of toxic reactive oxygen species (ROS) by Fenton chemistry, causing oxidative damage to biomolecules. In addition, a metal in excess can replace a native metal ion within protein structural sites or enzyme active sites. The replacement of a cognate metal with the 'wrong' one within a metal-binding site is termed mis-metalation and often results in enzyme inactivation. For example, one effect of copper-mediated toxicity in *Escherichia coli* is the mis-metalation of iron-sulphur clusters (Macomber & Imlay, 2009). Mis-metalation is challenging as, inherently, proteins will form more stable complexes with some metals than with others. In the absence of steric selection in flexible nascent proteins, the order of stability of the divalent metal-protein complexes follows the Irving-Williams series (Irving & Williams, 1948):

$$Mg(II) < Mn(II) < Fe(II) < Co(II) < Ni(II) < Cu(II) > Zn(II)$$

Metal ions to the right of series (e.g. Cu(II)) form more stable complexes than those to the left (e.g. Mg(II)). Cu(I) also tends to form tight complexes with proteins and is often considered together with Cu(II) at the right of the Irving-Williams series. The series is usually explained by the regular decrease in ionic radius from Mn(II) to Zn(II), along with the increase in ligand field stabilization energy (LFSE) along the series. The great stability of the d^9 Cu(II) complexes can be attributed to the LFSE obtained through Jahn-Teller distortion, while the d^{10} Zn(II) exhibits a diminished complex stability due to the lack of LFSE (Haas & Franz, 2009).

In a series of reviews from Dudev and Lim, the physical and chemical properties of metal and ligands that could determine metal ion selectivity in proteins were evaluated from computational studies (Dudev & Lim, 2008; 2014). Properties of the metal ion include the valence state, the ionic radius and the charge-accepting ability. Regarding the protein, possible selectivity-determining factors are the properties of the ligand groups (for example charge,

dipole moment and polarizability, charge-donating/accepting ability and denticity), effects of the second-shell ligands (for example first-second shell hydrogen bonds or salt bridges might stabilise a particular conformation of the first shell) and effects of the protein matrix (for example solvent accessibility and rigidity of the binding site). Nevertheless, although these properties can, at least to some extent, tune the preference of the binding site for a particular metal, protein metal preferences *in vitro* follow the trend given by the Irving-Williams series. Proteins are not rigid and therefore selection of the metal ion based on steric properties (e.g. coordination number or geometry) is inherently imperfect. For example, a mis-metalating ion could bind to the same metal-binding locus of the native one, but employing only a subset of the ligands, recruiting an adventitious ligand, or adopting a distorted geometry.

1.3 How do cells achieve correct metalation?

If proteins bind metal ions following the Irving-Williams series, how can cells use at the same time weakly and tightly binding metals to metalate proteins and achieve correct metal speciation? Approximately one third of metalloenzymes acquire their cognate metal ions or a pre-formed metal cofactor (for example, haem or iron-sulphur clusters for iron, or cobalamin for cobalt) from dedicated delivery proteins (Foster et al, 2014a). These proteins are called metallochaperones, by extension of the traditional concept of molecular chaperones assisting folding of nascent proteins (Capdevila et al, 2017). This confers a kinetic bias to metal selectivity, as the correct metal-recipient protein can be recognised by specific protein-protein interactions and the metal-binding ligands in the two proteins can even be oriented to facilitate the metal exchange (Banci et al, 2006; Robinson & Winge, 2010). Several metallochaperones delivering different metals have been characterised, with different biochemical mechanisms of action. For example, some metallochaperones require hydrolysis of GTP or ATP for metal delivery (e.g. UreG for urease maturation) while others do not require nucleotides cofactors (e.g. the copper metallochaperone CopZ) (Capdevila et al, 2017; Robinson & Winge, 2010). Nevertheless, the mechanisms of action (and delivered metal) of other metallochaperones is still unclear (Haas et al, 2009). How metals partition into the various metal-delivery pathways is currently uncertain. One hypothesis is that metallochaperones acquire their metal from direct interactions with the membrane-associated metal import systems. However, this is not yet supported by strong experimental evidences (Foster et al, 2014a). Alternatively, metal-loading of metallochaperones might occur within the cytosol and be under thermodynamic control (*vide infra*).

The remaining 70% of metalloenzymes are presumed to acquire their cognate metal ions from the cytosolic metal pools (Foster et al, 2014a). Correct metalation can be achieved if metalation occurs in a metal controlled environment: That is the availability of the metals is the opposite of their competitiveness in binding to proteins (Tottey et al, 2008). Studies on

two periplasmic cupins (MncA and CucA) revealed that these two proteins bind metal ions via identical ligands. However, the former acquires Mn(II) *in vivo*, while the latter Cu(II) (Tottey et al, 2008). *In vitro*, both proteins exhibited metal-preference as predicted by the Irving-Williams series, with 10,000-fold excess Mn(II) being required to outcompete Cu(II) for MncA-binding. Cu(I) also outcompetes Mn(II) and cuprous ions are thought to predominate in the reducing cytosol. However, once Mn(II) is bound to MncA, the metal is kinetically trapped and cannot be exchanged for Cu(II). The correct metal can be acquired *in vivo* because folding of these two proteins occurs in different cellular locations: CucA is a Sec substrate and folds in the periplasm while MncA folds in the cytosol and it is then translocated to the periplasm by the Tat system. In this way, MncA can acquire manganese because it folds in a location where copper is maintained at least 10,000-fold less available than its cognate metal (Changela et al, 2003). After translocation in the periplasm, MncA can coexist with high Cu(II), as the Mn(II) ion is kinetically trapped in the binding site (Tottey et al, 2008).

As mentioned earlier, it is possible that also metallochaperones acquire their metal (which is then delivered to the recipient protein(s)) from the cytosolic metal pools. Therefore, the proportion of metalloproteins relying on cellular metal availability being strictly controlled to achieve correct metalation, can be considered greater than 70%. This highlights the importance of maintaining a controlled and low availability of tightly binding metals *in vivo*, so that cells can overcome the inherent metal-binding preferences of biomolecules and achieve correct metalation. Organisms have therefore evolved efficient regulatory systems to control the intracellular availability of the essential metals. An example of the metallostasis system in a bacterial cell is reported in **Figure 1.1**. This systems includes transmembrane metal transporters to import deficient metals and export the ones in excess, systems to store or sequester excess metals and regulatory mechanisms that detect changes in metal levels and consequently adapt the cellular environment (for example by affecting gene expression, protein stability etc.) (Waldron & Robinson, 2009; Waldron et al, 2009). In bacterial cells, a set of DNA-binding, metal-binding transcriptional regulators known as metal sensors or metalloregulators control the expression of the genes involved in metal homeostasis (section 1.5).

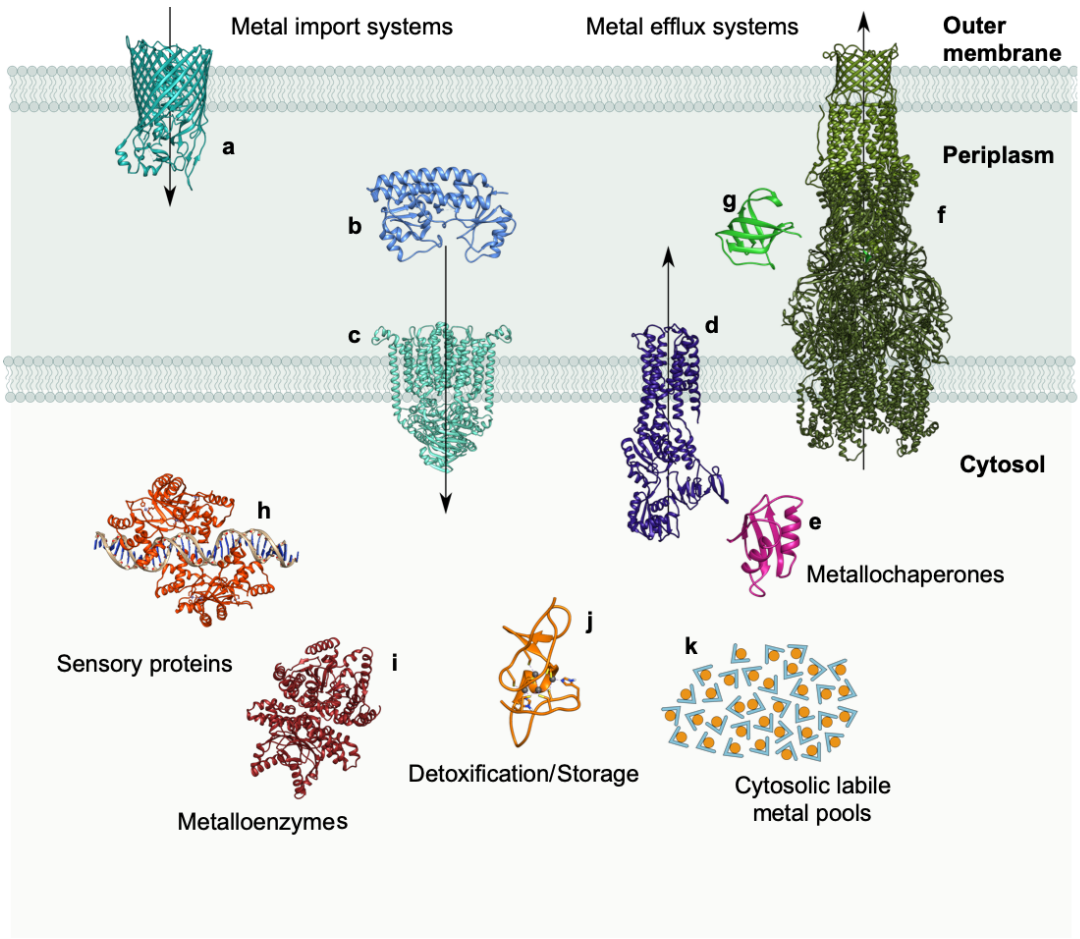

Figure 1.1. The components of metal homeostasis in bacteria
Schematic (not to scale) metal homeostasis model of proteins involved in metal homeostasis in Gram-negative bacteria. Representative structures of proteins involved in zinc import, copper export and intracellular homeostasis are reported as an example. This model is not intended as a complete representation of all the proteins involved in metal homeostasis and it does not represent any specific organism or metal-trafficking system. Instead, it was designed to illustrate some of the components of the system and possible fates of metal ions in the cytosol. The arrows illustrate metal fluxes across the outer and cytosolic membrane. In Gram-negative bacteria, metals can diffuse across the outer membrane through porins, for example the outer-membrane Zn(II)-uptake component D (ZnuD) from *Neisseria meningitidis* (**a**). Some metals ions can be acquired in complex with other molecules (for example, iron bound to the Fe(III)-scavenging siderophores) and utilise different energy-coupled transporters to cross the outer membrane (for example, ferric hydroxamate uptake via FhuA is coupled with TonB, not shown). Metals can be transported through the cytosolic membrane via several different transport systems. Some transporters can drive metal transport by coupling it with hydrolysis of ATP on the cytoplasmic side of the membrane (for example, ABC (ATP-binding cassette) transporters or P1-type ATPases). Other transporters couple metal transfer with transfer of protons (or other ions) across the membrane (examples are the cation diffusion facilitator (CDF) proteins and the natural resistance associated with macrophage proteins (NRAMP)). ZnuABC is an ABC high-affinity transporter for Zn(II)-import in the cytosol. The transporter is composed by three proteins: ZnuA (a periplasmic Zn(II)-binding protein), ZnuB (an integral membrane protein transporting Zn(II) across the lipid bilayer) and ZnuC (an ATPase responsible for coupling ion transport to ATP hydrolysis). The whole structure of ZnuABC is not available. The model depicted in the figure shows *E. coli* ZnuA (**b**) and the

BtuC and BtuD components (corresponding to ZnuB and ZnuC, respectively) from the *E. coli* vitamin B_{12} import system BtuCD–F (**c**). P_1-type ATPases act mostly as metal exporters. One example is CopA from *Legionella pneumophila* (**d**), a Cu(I)-export system. P_1-type ATPases usually possess one (or more) cytosolic metal-binding domain (CopA has two). Interestingly, the metallochaperone CopZ (**e**) has been shown to bypass the cytosolic metal-binding domain, donating copper directly to the transmembrane metal-binding site. Metals can also be exported through resistance-nodulation-cell division (RND) transporters, tripartite efflux pumps that span both the cytosolic and outer membranes. An example is the *E. coli* CusCBA complex (**f**), which couples Cu(I) and Ag(I) export with proton import. CusA is a proton-dependent efflux pump on the cytosolic membrane, CusC is an outer membrane channel and CusB is a periplasmic membrane fusion protein bridging CusA and CusC. A small periplasmic protein, CusF (**g**) can interact and deliver metal to CusCBA for metal export from the periplasm. In the cytosol, metal-sensing DNA-binding transcriptional regulators control the expression of genes encoding metal homeostasis proteins (for example, the aforementioned transporters, see section 1.5). One example is the Zn(II)-sensing metalloregulator Zur (**h**, see section 1.5.3.2). Metallochaperones can facilitate metal-trafficking inside cells, imposing a kinetic bias to metal-delivery. For example, other than interacting with CopA, CopZ from *Enterococcus hirae* (**e**) has been shown to deliver Cu(I) to a Cu(I)-dependent regulator. Other metallochaperones couple nucleotide hydrolysis with metal transfer and might have essential functional roles in the biosynthetic pathways of several metal cofactors (for example, the GTPases UreG and HypB are involved in urease and hydrogenase maturation, respectively). Metalloenzymes need to acquire their (correct) metal(s) in order to function (either from a metallochaperone or from the cytosolic pool). For example, *E. coli* β-carbonic anhydrase (**i**) contains essential Zn(II) required for the catalytic mechanism. Surplus metal can be stored in storage proteins, for example ferritin for iron. Some organisms can express some cysteine-rich small proteins called metallothioneins to tightly bind and sequester metals such as zinc. An example is SmtA (**j**) from *Synechococcus elongatus* PCC 7942. The crowded cytosol can provide a polydisperse buffer system to form accessible labile metal pools (**k**) where metals are in complex with a variety of ligands including small molecules and adventitious binding sites on macromolecules (section 1.5).

Bibliographic references on the bacterial metal homeostasis components can be found in the review papers: (Ma et al, 2009; Waldron & Robinson, 2009) plus (Long et al, 2012) for CusCBA-F. Structures generated from PDB entries: 4RDR for ZnuD; 2PRD for ZnuA; 4FI3 (BtuCDF) to model ZnuBC; 3RFU for CopA; 1CPZ for CopZ; 3NE5 for CusAB plus 3PIK for CusC; 2Vb2 for CusF; 4MTD for Zur; 1I6O for β-carbonic anhydrase; 1JJD for SmtA.

1.4 Intracellular metal availability

Although metal availability can differ per cell type, cellular compartment and even due to growth conditions or lifetime phase, several reports over the last two decades highlighted how the availability of the least competitive metals can be several orders of magnitude greater than the tightly binding ones (Foster et al, 2014a). For example, the availabilities of metals such as magnesium, iron and manganese, at the low end of the Irving-Williams series, have been estimated to be ~10^{-3} M for Mg(II) (Grubbs, 2002), and between 10^{-7}–10^{-6} M for Mn(II) and Fe(II) (Williams, 1982). Conversely, based on the use of metal-responsive fluorescent probes *in vivo*, the availability of tight binding Zn(II) in prokaryotic and eukaryotic cells has been estimated to be between 10^{-12}–10^{-10} M (Carter et al, 2014; Krezel & Maret, 2006; Wang et al, 2011). Typically, the affinities of Zn(II)-binding proteins fall within this range, or below (Kochanczyk et al, 2015). Another study, based on the concentrations that trigger the response of the *E. coli* Zn(II)-responsive sensors, suggested the availability of Zn(II) to be as low as ~10^{-15} M (Outten & O'Halloran, 2001). Similarly, estimates of the intracellular availability of copper obtained from intracellular copper-responsive fluorescent probes have been reported from 10^{-15} down to 10^{-21} M (Carter et al, 2014; Dodani et al, 2011; Huang et al, 2014; Wegner et al, 2011). Studies on the Cu(I)-responding metalloregulator from *E. coli* estimated that this sensors can sense ~10^{-21} M 'free' copper in the cytosol (Changela et al, 2003). The copper zinc superoxide dismutase (SOD1) from *Saccharomyces cerevisiae* is not able to acquire Cu(I) *in vivo* in the absence of the copper chaperone for superoxide dismutase (CCS). Using a thermodynamic model (based on the affinity of SOD for Cu(II) being estimated ~10^{-15} M), the copper availability in *S. cerevisiae* cells has been proposed to be lower than 10^{-18} M (Rae et al, 1999). However, it should be noted that CCS also assists the formation of an essential disulphide bond in SOD1 (Furukawa et al, 2004) and, therefore, this could provide an alternative explanation for why SOD1 cannot mature in the absence of CCS (Foster et al, 2014a). Similar considerations can be made based on the affinities of the bacterial metal sensors for their cognate metals. For example, the determined affinities of the Mn(II)-sensing or Fe(II)-sensing metalloregulators for their cognate metals range from 10^{-5} to 10^{-6} M. Zn(II)-sensing regulators, for instance, bind zinc with affinities of 10^{-12}–10^{-13} M (Foster et al, 2014a; Reyes-Caballero et al, 2011).

What does the term 'available metal' precisely refer to? Several contextual definitions of metal availabilities have been reported in the literature (Finney & O'Halloran, 2003). For example, 'available metal' is often used as a synonym of 'free or unbound metal'. Notably, estimates of the availability of the most competitive metals fall below the theoretical threshold of one atom per cell (for *E. coli*, this was estimated to be equivalent to 10^{-9} M (Changela et al, 2003; Outten & O'Halloran, 2001)). However, despite the concentration of free metal being negligible, it

remains probable that metalloenzymes, chaperones and sensors acquire their metal ions from labile, exchangeable pools where the metal is coordinated by a polydisperse buffer (see section 1.5) (Cobine et al, 2004; Foster et al, 2017; Osman et al, 2017). There is a need to identify a general way to define (and measure) intracellular metal availability.

1.5 Metal sensors

To tightly control metal availability, bacteria have evolved networks of metal-sensing DNA-binding transcriptional regulators, known as metal sensors or metalloregulators (Giedroc & Arunkumar, 2007; Reyes-Caballero et al, 2011; Waldron et al, 2009). Typically, the same organism will have several different metalloregulators, each selectively sensing one (or a small group of) cognate metal(s). Binding (or release) of metal to the sensor drives a change in the conformation or dynamics of the protein, allosterically affecting the interaction with DNA. By interacting with the DNA, the sensors can regulate the expression of genes encoding proteins involved in metal homeostasis, for example the aforementioned metal-import and export systems, metallochaperones and storage systems (such as ferritin and metallothioneins). Depending on the mode of action, sensors can be classified as co-repressors, de-repressors and activators (Giedroc & Arunkumar, 2007; Waldron et al, 2009). The canonical model describes co-repressors and de-repressors binding to the promoter region of the gene they regulate, competing with binding of the RNA-polymerase to the same site. Metal-binding enhances DNA-binding of the co-repressors, so that target gene expression is downregulated when metal availability increases from the optimal set-point. Conversely, metal-binding decreases the affinity of the de-repressors for DNA, allowing gene expression to be up-regulated in metal-replete conditions. However, new studies are reporting that the same sensor might be able to repress the expression of some genes in response to metals while activating others via different mechanisms of action. Some of these mechanisms of actions will be discussed further in the next sections. A third class of metal sensors is represented by the MerR activators. Regulation of these proteins occurs with the sensor binding to the same DNA target in both the apo- and metalated forms. Metal-binding drives a conformational change that distorts the local structure of DNA, converting a sub-optimal promoter to an optimal one (Brown et al, 2003) (section 1.5.4.3).

It was originally hypothesised that the sensitivity of the metal sensors (i.e. the metal availability which triggers their allosteric response) largely governed the intracellular availability of their cognate metals. Foster, Pernil, Robinson and co-workers studied the relationship between intracellular metal availability and sensor response by generating *Synechocystis* PCC 6803 variants where the sensitivity of the Ni(II)-sensing InrS was altered (for example, in a variant the sensitivity was 20-fold weaker) (Foster et al, 2017). They discovered that instead of modulating the intracellular Ni(II) availability in the cell (there were

only modest changes in total Ni(II) atoms cell^{-1}), the InrS mutation weakening the sensitivity caused the sensor to cease responding to Ni(II) *in vivo*. This, therefore, suggested that sensor sensitivity is not the sole point of reference governing intracellular metal availability. Instead, the sensitivity of the sensors must be tuned to the availability of their cognate metal in order to respond *in vivo* (Foster et al, 2017). The cellular metal availability is defined by the intracellular buffer system. The crowded cytosol, in fact, provides a unique polydisperse buffer rich in a multitude of donor ligands associated with inorganic anions, small metabolites and biomolecules which can easily be arranged in different coordination geometries without steric hindrance. This provides the perfect medium for the Irving Williams series where the most competitive metals are tightly bound to the buffer system and therefore buffered at lower availability (Foster et al, 2017). Certain species might dominate the buffer system for various metals. For example, histidine, glutathione and bacillithiol, are known to be a significant constituent of the buffer systems for certain metals (Foster et al, 2017; Hider & Kong, 2011; Ma et al, 2014). However, it is probable that many more components of metal buffer systems are yet to be identified. For example, it is possible that proteins with weak, exposed metal-binding ligands will contribute to buffering intracellular metals.

Metal sensors have evolved to respond at the intracellular availability of their cognate metals and by controlling the expression of metal homeostasis genes they can prevent the buffer from being depleted or saturated with metals. Therefore, they can be used as reporters to define the intracellular metal availability. That is, their sensitivity can be determined and used as an alternative approach to define the buffered metal concentration of their cognate metals (Osman et al, 2017). In this work, the sensitivities of metal sensors from *Salmonella enterica* serovar Typhimurium (hereafter *Salmonella* or *S*. Typhimurium) will be characterised to define the intracellular metal availabilities in this organism.

1.5.1 Metal-sensing proteins in *Salmonella*

Salmonella species are Gram-negative, facultative aerobic enterobacteria. They are facultative intracellular pathogens causing disease in both humans and several animal species. The infection can manifest in different forms, depending on the serovar of the invading *Salmonella* and the susceptibility of the host (Coburn et al, 2007). In humans, the most common manifestations are typhoid fever (caused for example by the *Salmonella Typhi* and *Salmonella Paratyphi* type A, B, or C) and gastrointestinal disease (caused by the non-typhoid *Salmonella* serovars). Non-typhoidal *Salmonella* infections are a primary cause of foodborne diseases, causing hundreds of millions of cases of gastroenteritis worldwide, both in developing and industrialised countries, with over 100,000 fatalities every year (Majowicz et al, 2010). Additionally, multi-drug resistance in *Salmonella* isolates has increasingly been reported in the last decades (Meakins et al, 2008; Molbak et al, 1999; Rowe et al, 1997; Threlfall, 2000).

S. Typhimurium is one of the most commonly isolated serovars in the cases of invasive non-typhoidal salmonellosis (Crump et al, 2015; Sanchez-Vargas et al, 2011). The ability of *S.* Typhimurium to acquire essential metals and export excess of toxic ones has been related to the virulence of this pathogen (Achard et al, 2010; Ammendola et al, 2007; Boyer et al, 2002; Campoy et al, 2002; Kehres et al, 2000; Osman et al, 2010). During invasion of the host, in fact, *S.* Typhimurium encounters diverse microenvironments imposing dramatic changes in metal availability (Osman & Cavet, 2011). For example, the host will release antimicrobial agents to sequester essential metal from the pathogen (Becker & Skaar, 2014). The ability of surviving within macrophages is a critical factor for *S.* Typhimurium virulence (Fields et al, 1986). *S.* Typhimurium can survive despite the antimicrobial strategies employed by the host in these compartments, including subjecting the invading pathogen to drastic metal fluxes (Botella et al, 2012; Osman et al, 2010; White et al, 2009). Therefore, in order to survive metal-starvation and metal-mediated toxicity challenges during host infection, *S.* Typhimurium has evolved efficient mechanisms of regulation of metal-homeostasis, including a set of metal-sensing DNA-binding transcriptional regulators (**Figure 1.2**) (Osman & Cavet, 2010; 2011).

The sensors **Figure 1.2** include four metal-dependent co-repressors (the manganese transport regulator MntR, the ferric uptake regulator Fur, the zinc uptake regulator Zur and the nickel responsive regulator NikR), two metal-dependent transcriptional activators (the copper efflux regulator CueR and the zinc transcriptional regulator ZntR) and one a metal-dependent de-repressor (the resistance to cobalt and nickel regulator RcnR). These proteins belong to five distinct structural families of metalloregulators: DtxR/MntR, Fur, NikR, CsoR/RcnR and MerR. Each sensor was demonstrated to selectively respond *in vivo* to its cognate metal(s) (Osman et al, 2019). Some of the sensors have been characterised *in vitro* and *in vivo* (Osman et al, 2017; Osman et al, 2015; Osman et al, 2016).

In addition to the ones depicted in **Figure 1.2**, other metal sensors are present in the *Salmonella* genome. These include a second Cu(I)-sensing MerR-like regulator GolS (absent in *E. coli* and initially identified as a Au(I)-sensor), which contributes to copper resistance (Checa et al, 2007; Osman & Cavet, 2010; 2011). Other examples are a fourth MerR-like activator (SoxR) which senses redox stress through an iron-sulphur cluster (Pomposiello & Demple, 2000), the two-component sensor-regulator plasmid-mediated silver resistance system SilS–SilR (Gupta et al., 1999) and another two-component system PmrA–PmrB which can sense extracellular iron (Wösten et al, 2000). Other putative sensors were identified based on similarities with *E. coli* homologues (Osman & Cavet, 2011), for example the molybdate-sensing ModE (Grunden et al, 1996; Hall et al, 1999) and the arsenic-sensing ArsR (Xu et al, 1996). Nevertheless, additional uncharacterised metal sensors might also exist.

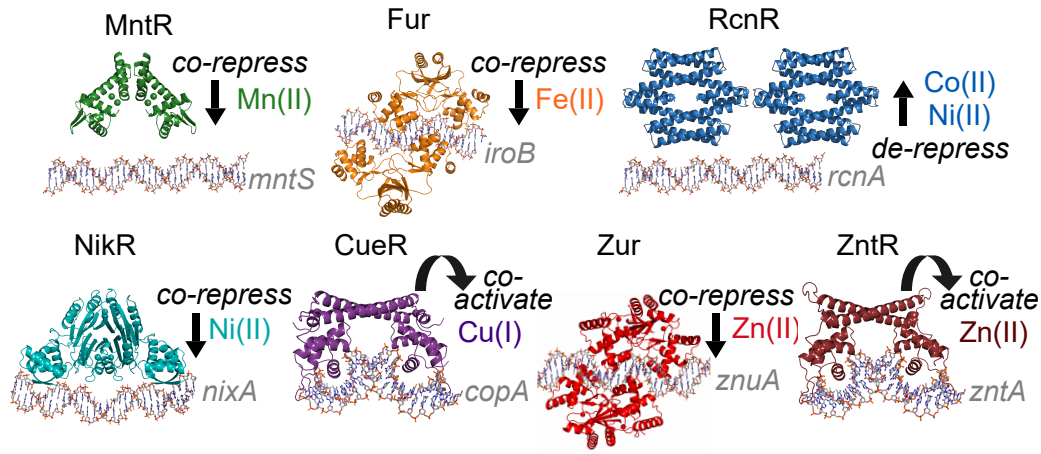

Figure 1.2 The set of metal sensors from *Salmonella*.
Structural models of the *Salmonella* sensors illustrating the modes of action on target genes. There are representatives from five structural families of metal sensors: DtxR/MntR (MntR), Fur (Fur, Zur), CsoR-RcnR (RcnR), NikR (NikR) and MerR (ZntR, CueR). Structures from PDB entries: 2F5D (MntR), 4RB1 (Fur), 5LCY (RcnR), 2HZV (NikR), 4WLW (CueR and ZntR), 4MTD (Zur). Figure and caption adapted from (Osman et al, 2019).

The properties of some of the structural families of metal sensors will be discussed in the following sections.

1.5.2 DtxR family

The founding member of this structural family is the Fe(II)-responsive sensor DtxR (diphtheria toxin repressor) from *Corynebacterium diphtheriae*, where it controls the expression of the diphtheria toxin and of proteins with functions in iron homeostasis (Boyd et al, 1990; Schmitt & Holmes, 1991; 1994). Members of the DtxR structural family predominantly sense iron (e.g. DtxR, IdeR) and manganese (e.g. MntR). However, *in vivo* responses also to other metals (for example cadmium, see 1.5.2.1) have been reported, even though it is not clear whether these responses are physiologically relevant. These sensors are commonly considered to be co-repressors binding to DNA when activated by metal-binding (Tao et al, 1994). For example, members of the MntR sub-family down-regulate the expression of Mn(II)-import systems in metal-replete conditions by binding to the promoter of the target genes (Guedon et al, 2003; Ikeda et al, 2005; Kehres et al, 2002a; Patzer & Hantke, 2001). Nevertheless, some sensors (for example, MntR from *Bacillus subtilis* and *E. coli*, and SloR from *Streptococcus mutans*) have been reported to up-regulate the expression of some genes in their metalated state (see section 3.4.1).

Several DtxR-like sensors have been characterised *in vitro*. Some of the proteins that have been structurally characterised are DtxR from *C. diphtheriae*, IdeR from *Mycobacterium tuberculosis*, MntR from *E. coli*, *B. subtilis* and *M. tuberculosis*, MtsR from *Streptococcus pyogenes*, SloR from *S. mutans* and ScaR from *Streptococcus gordonii* (Cong et al, 2018; Do et al, 2019; Glasfeld et al, 2003; Pohl et al, 1999; Spatafora et al, 2015; Stoll et al, 2009; Tanaka et al, 2009; White et al, 1998). DtxR has been reported to form monomers and dimers in equilibrium in the apo-form and that the dimerization is activated by metal-binding (Spiering et al, 2003; Tao et al, 1995). In the metalated form, most DtxR proteins form dimers folding in three domains: a DNA-binding N-terminal domain, a dimerization domain containing the metal-binding site, and a C- terminal domain containing other residues involved in metal-binding and adopting a conformation similar to the SRC Homology 3 (SH3) domain (Pohl et al, 1999; Schiering et al, 1995; White et al, 1998). This last domain is also known as the FeoA domain for its structural similarity with the ferrous iron transport protein FeoA from *E. coli* (Lau et al, 2013). *B. subtilis* and *E. coli* MntR (section 1.5.2.1) both lack this third domain (Glasfeld et al, 2003; Tanaka et al, 2009). The N-terminal domain (~ 70 amino acids) comprises a winged helix-turn-helix (wHTH) domain which interacts with the DNA major groove (White et al, 1998). Most DtxR-like proteins have been reported to bind two metal ions per monomer (D'Aquino et al, 2005; Spiering et al, 2003), either in separate sites or in a dinuclear site. However, the structure of *S. mutans* Zn(II)-SloR and *M. tuberculosis* Mn(II)-

MntR revealed the presence of three metal ions per monomer (Cong et al, 2018; Spatafora et al, 2015). PsaR from *Streptococcus pneumoniae* seems to be another special case, as one of the two sites within the monomer is predicted to acquire Zn(II) *in vivo*, while the other is the regulatory Mn(II) site (Lisher et al, 2013). Despite several DtxR-like sensors having been characterised, the functional relationship between metal-binding sites occupancy and transcriptional regulation remains (with a few exceptions) largely unknown (D'Aquino et al, 2005). The next section will discuss more in detail the properties of the Mn(II)-sensing MntR.

1.5.2.1 Mn(II)-sensing MntR

B. subtilis MntR is the prototype of the Mn(II)-sensing MntR subfamily. It was identified for the first time by Que and Helmann in 2000 as the central regulator of Mn(II)-import (Que & Helmann, 2000) and since then it has probably become one of the best biochemically characterised sensors. The *E. coli* homologue was identified shortly thereafter (Patzer & Hantke, 2001); however, even though its structure has been solved (Tanaka et al, 2009), a thorough biochemical characterisation of this regulator is still lacking. *B. subtilis* MntR represses the transcription of the manganese uptake genes *mntH* and *mntABCD* when activated by Mn(II) (Guedon et al, 2003; Que & Helmann, 2000). It has been reported to respond *in vivo* and *in vitro* also to the toxic metal cadmium (Golynskiy et al, 2005; Golynskiy et al, 2006; Que & Helmann, 2000). *B. subtilis* has in fact been reported to accumulate Cd(II) through the Mn(II)-import systems (Burke & Pfister, 1986), and the response of MntR to this metal might be part of a detoxification mechanism in the presence of toxic/non-essential metals. A recent study reported that MntR can also activate in a Mn(II)-dependent way the expression of the Mn(II)-efflux pump (MneP) and of another protein involved in Mn(II)-export (MneS) (Huang et al, 2017).

As opposed to DtxR, MntR forms stable dimers even in the absence of bound metals (Lieser et al, 2003). Structural studies have been performed on both apo-MntR (DeWitt et al, 2007) and MntR in complex with several metal ions (Glasfeld et al, 2003; Kliegman et al, 2006; McGuire et al, 2013) (**Figure 1.3**). The structure of *B. subtilis* MntR revealed an unusual Mn(II)-binding site, differing from both the Fe(II)-binding sites of DtxR and IdeR and the Mn(II)-binding sites of the other sensors. In fact, while the other DtxR sensors bind metals in spatially distinct sites, *B. subtilis* MntR binds two Mn(II) ions per monomer (four per dimer) in a dinuclear metal-binding site (**Figure 1.3b**). The binding site is located at the interface of the N-terminal DNA-binding domain and the C-terminal dimerization domain, recruiting ligand groups from six amino acid residues: Asp8, Glu11, His77, Glu99, Glu102, His103 and two solvent molecules to bind the two Mn(II) ions (Kliegman et al, 2006; McGuire et al, 2013).

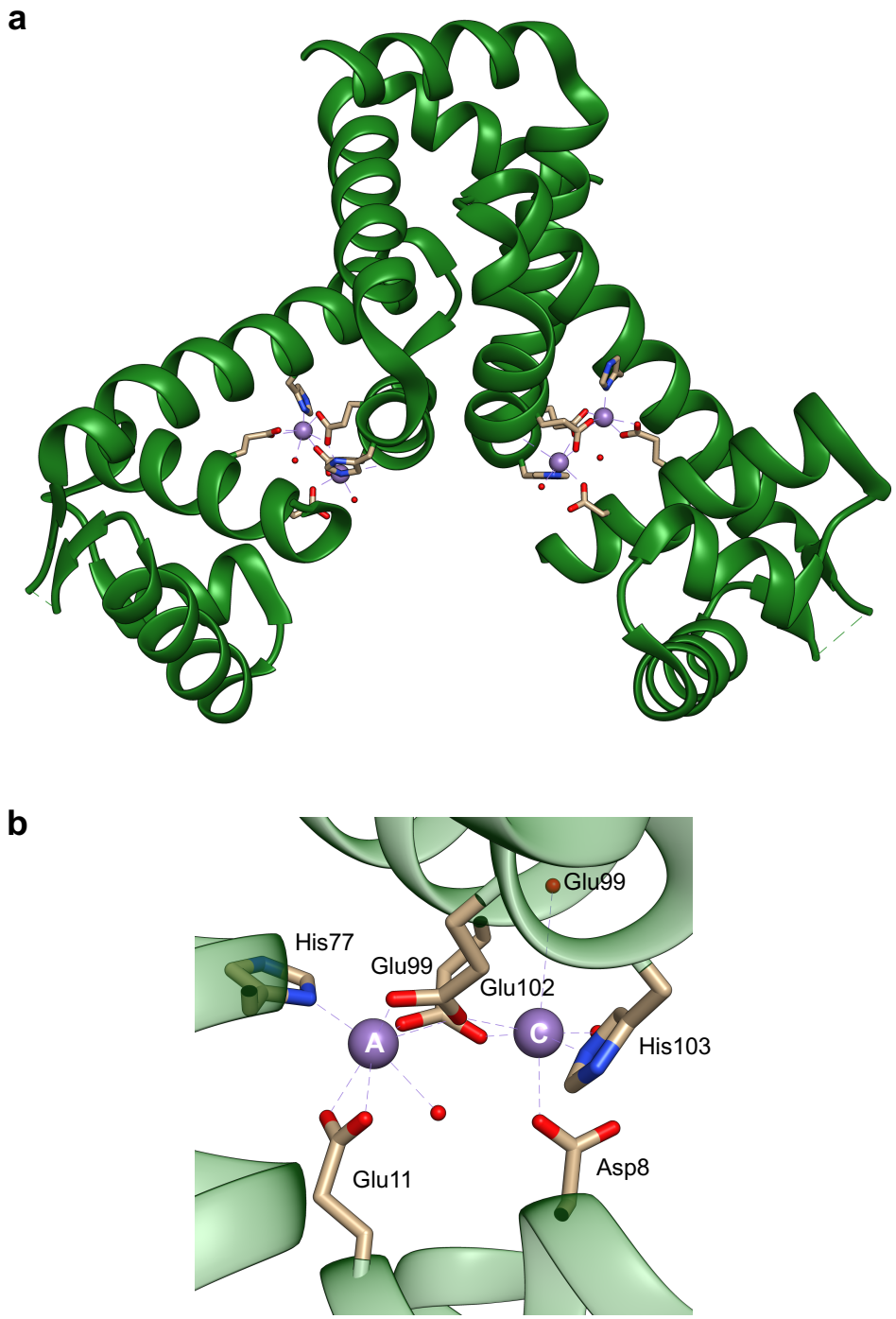

Figure 1.3. Structure of Mn(II)-sensing MntR.
a, structure of MntR from *B. subtilis* in the presence of Mn(II) (Kliegman et al, 2006). The protein forms a dimer, folding in two domains: the N-terminal domain involved in DNA-binding and the C-terminal involved in the formation of the dimer. Each subunit has a binuclear metal-binding site at the interface between the two domains (Mn(II) in purple). **b**, structure of the binuclear metal-binding site filled with Mn(II). The two sites (A and C) are linked by bridging carboxylates from the Glu99 and Glu102 residues (both from the C-terminal domain). At site A, Mn(II) coordination is completed by Glu11 (from the N-terminal domain), His77 (from the helix linking the two domains), and one water molecule. In addition to the bridging ligands, the metal at site C is also coordinated by Asp8 (N-terminal domain), a water molecule, His103 (C-terminal domain) and the backbone carbonyl of Glu99. Structure from PDB entry 2F5D.

Binuclear sites are unusual in metal sensors, while they have been reported in enzymes (Glasfeld et al, 2003); examples are the enzymes arginase (Kanyo et al, 1996), amino peptidase (Wilce et al, 1998) and the *Lactobacillus plantarum* manganese catalase (Barynin et al, 2001).

MntR has been reported to bind several metal ions *in vitro*, with affinities following the Irving-Williams series (Golynskiy et al, 2006). However, metals other than Mn(II) and Cd(II) have been reported to poorly activate MntR DNA-binding. The unusual coordination of Mn(II) in the binding site has been proposed to contribute to MntR metal selectivity (Guedon & Helmann, 2003; Kliegman et al, 2006; McGuire et al, 2013). Metals such as Zn(II), Fe(II), Co(II)) have been reported to occupy only the first site (site A) within the binuclear binding site. By contrast, Mn(II) and Cd(II) can form the binuclear site occupying both the positions A and C (the first structure identified the two sites as A and B, but the conformation of the latter was later discovered to be an artefact of the data collection conditions (Glasfeld et al, 2003; Kliegman et al, 2006)). This was attributed to the larger ionic radii of Mn(II) and Cd(II), which can adopt an heptacoordinate coordination geometry in site A. This can arrange the correct conformation of site C for metal-binding. However, it has been hypothesised that a significant contribution towards the selectivity of Mn(II) sensing might arise also from the cellular milieu (Golynskiy et al, 2006).

Recently, the structural analysis of MntR from *M. tuberculosis* has been reported (Cong et al, 2018). The structure of Mn(II)-MntR revealed the presence of three Mn(II)-ions bound per subunit (a similar stoichiometry for a DtxR protein had previously been reported only for SloR (Spatafora et al, 2015)). Two Mn(II) ions bind in a binuclear site which is equivalent to the binuclear site in *B. subtilis* MntR. The third ion binds in a mononuclear site located by the crevice formed by the DNA-binding, the dimerization and the FeoA domains. This site comprises coordinating residues mainly from the dimerization domain, FeoA domain and the loop region between these two domains. These residues appear to be conserved (or at least similar) in other DtxR sensors, while the other MntR sensors do not possess these conserved amino acids (moreover, they also lack the FeoA domain, see section 3.1).

MntR was identified in *Salmonella* as the Mn(II)-dependent regulator of *mntH* and *sitABCD* (Ikeda et al, 2005; Kehres et al, 2002a). It possesses the same residues involved in the binuclear binding site in *B. subtilis* MntR (section 3.1). Interestingly, MntR in *Salmonella* can respond to Fe(II) *in vivo* in a mutant with a disrupted iron regulatory circuit (Ikeda et al, 2005; Kehres et al, 2002a). The regulatory networks of the Mn(II) and Fe(II) sensors in *Salmonella* greatly overlap (see section 3.4.1). However, it is not clear if the MntR response to Fe(II) might be physiologically relevant or if it might be a mal-response due to an altered Fe(II)-availability in the *Salmonella* mutants.

1.5.3 Fur Family

The family of structurally related Fur proteins is widespread in prokaryotes and is one of the most studied families of metalloregulators. In 2007, Lee and Helmann estimated about 800 Fur homologues present across prokaryotes (Lee & Helmann, 2007). Currently, the Pfam protein family database (El-Gebali et al, 2019) reports over 17,000 sequences for Fur proteins in more than 7,000 bacterial and archaeal species. The founding member of this family is the iron-dependent repressor Fur from *E. coli*. However, not all the members of this family sense ferrous iron, or even metals. Examples of other metal-sensing regulator belonging to the Fur family are the Zn(II)-sensing Zur, the Ni(II)-sensing Nur (nickel uptake regulator) and the Mn(II)-sensing Mur (manganese uptake regulator). Fur proteins have been characterised to sense also other types of signal: PerR (peroxide-sensing regulator) regulates gene expression in response to peroxides, while regulation by Irr (iron response regulator) depends on haem. More than one Fur protein with different functions can be present in the genome of the same organism (Hantke, 2001). For example, *Salmonella* has both the Fe(II)-sensing Fur and the Zn(II)-sensing Zur (**Figure 1.2**), and Fur, Zur and PerR are all present in *Bacillus subtilis* (Fuangthong & Helmann, 2003). Cross-talk and overlapping of the various regulatory networks can be present (Ma et al, 2012).

Biochemical properties of members of all the Fur subfamilies have been characterised, including crystallographic structures. Collectively, Fur family members are ~150 amino acid proteins forming dimers. They predominantly fold in two domains: An N-terminal DNA-binding domain and a C-terminal dimerization domain (**Figure 1.4**). Recently, some Fe(II)-sensing Fur proteins have been proposed to form tetramers under physiological conditions (Nader et al, 2019; Perard et al, 2016; Perard et al, 2018). Fur proteins bind to A/T-rich DNA recognition sequences through the helix-turn-helix (HTH) motif found in the N-terminal domain (Sarvan et al, 2018). A common feature among Fur proteins is a metal-binding site within the dimerization domain that coordinates Zn(II) in a tetracoordinate fashion. The Zn(II) ion is typically coordinated by one or two C-XX-C motifs (Lee & Helmann, 2007) (**Figure 1.4c**). Different stoichiometries of metal-binding have been reported for Fur proteins, up to three metal-binding sites per protein monomer. The properties of Fe(II)-sensing Fur, as well as of the other Fur proteins, will be discussed more in detail in the following sections.

1.5.3.1 Fe(II)-sensing Fur proteins

A *fur* mutant strain with constitutive expression of several high-affinity iron import systems was initially isolated in *S.* Typhimurium (Ernst et al, 1978). Shortly thereafter, the same mutant was isolated in *E. coli* (Hantke, 1981) and in the following years the *fur* gene was isolated and sequenced (Schaffer et al, 1985). Fur was overexpressed and purified from *E. coli* (Wee et al, 1988) and Bagg and Neilands demonstrated *in vitro* the role of this protein in

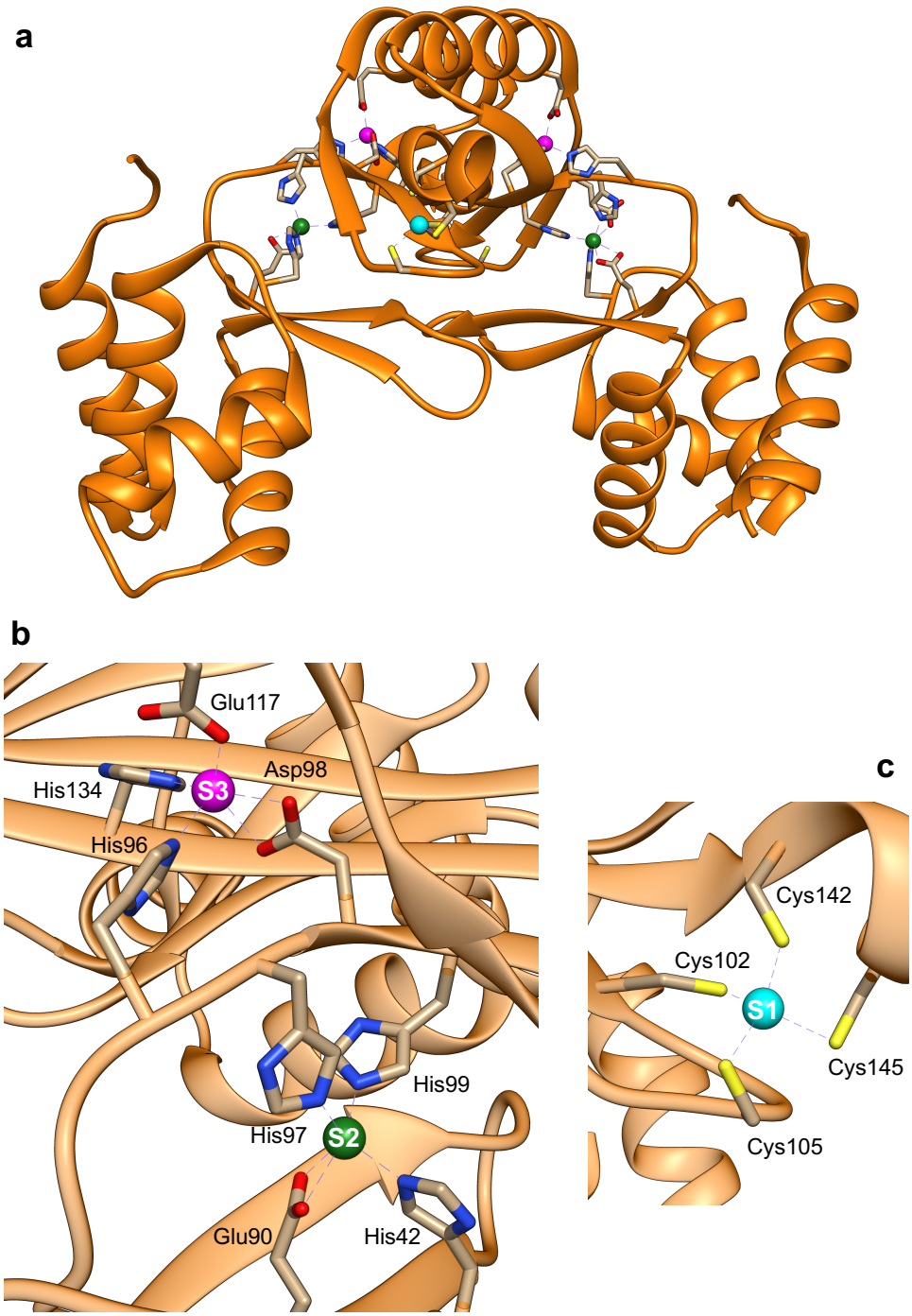

Figure 1.4. Structure of Fe(II)-sensing Fur.
a, structure of Fur from *H. pylori* Fur in the presence of Zn(II) (Dian et al, 2011). The protein forms a dimer, folding in two domains: the N-terminal domain involved in DNA-binding and the C-terminal involved in the formation of the dimer. The structure of *H. pylori* Fur contains three Zn(II)-binding sites per subunit, named site 1 (S1, in cyan), site 2 (S2, in green) and site 3 (S3 in magenta). S1 and S3 are located within the dimerization domain, while S2 is at the interface of between the two domains. **b**, structure of the S2 and S3 sites. In *H. pylori* Fur, the Zn(II) ion in S2 exhibits a different coordination sphere in the two subunits. In chain A, Zn(II) in S2 adopts a distorted octahedral geometry, with its coordination sphere comprising His42, Glu90, His97, His99 and Glu110. In S1 of chain B (shown), Zn(II) has a tetrahedral geometry and is coordinated by His42 and Glu90 (from the N-terminal domain), His97 (from the loop)

and His99 (from the C-terminal domain). The different coordination spheres observed for S2 in the two subunits suggests that the geometry at this site is flexible. In S3, Zn(II) has a tetrahedral geometry, coordinated by His96 (from the loop) and Asp98, Glu117 and His134 (from the C-terminal domain). **c**, structure of the S1 site. In this site, Zn(II) is coordinated in a tetracoordinate fashion. In *H. pylori* Fur, the ion is coordinated by four Cys residues from two C-XX-C motifs: Cys102, Cys105 and Cys142, Cys145. In *E. coli* Fur, the Zn(II) ion is proposed to be coordinated by only two Cys residues (Cys92 and Cys95, corresponding to Cys102, Cys105 in *H. pylori* Fur) and by two N/O donor ligands. Structure from PDB entry 2XIG.

repressing the expression of iron-uptake systems in response to Fe(II) (Bagg & Neilands, 1987a). Since then, Fur homologues have been identified in a wide range of organisms and, over the course of almost three decades, the metal-binding, DNA-binding and structural properties of several Fur proteins have been characterised *in vitro*. Other than the aforementioned *E. coli* Fur, examples of biochemically or structurally characterised proteins are Fur from *B. subtilis*, *Campylobacter jejuni*, *Helicobacter pylori*, *Magnetospirillum gryphiswaldens*, *Francisella tularensis*, *Vibrio cholerae*, *Yersinia pestis*, *Pseudomonas aeruginosa* and *L. pneumophila* (Butcher et al, 2012; Deng et al, 2015; Dian et al, 2011; Gao et al, 2008; Ma et al, 2012; Perard et al, 2016; Perard et al, 2018; Pohl et al, 2003; Sheikh & Taylor, 2009).

1.5.3.1.1 Structural properties and metal-binding

P. aeruginosa Fur was the first member of the Fur family to be structurally characterised, revealing the two-domains folding as described above and providing for the first time a detailed view on the metal-binding sites in Fur proteins (Pohl et al, 2003). *P. aeruginosa* Fur was crystalized with two Zn(II) equivalents per monomer. The first metal-binding site was located in the dimerization domain, while the second site was found at the interface between the DNA-binding and the dimerization domains. The first site (later renamed site 3, consistent with the nomenclature adopted to describe the binding sites of other Fur proteins) was reported to be readily exchangeable with Fe(II), while, in contrast, the other site (later renamed site 2) was not. For this reason, the first site (site 3) was assigned as the regulatory site, while the second (site 2) as a Zn(II) structural site (Pohl et al, 2003). *P. aeruginosa* Fur lacks what was later defined site 1, the Cys-coordinated Zn(II)-structural site commonly found in Fur proteins. This protein, in fact, misses the conserved cysteine residues of the C-XX-C motif involved in Zn(II)-binding in site 1 (for the amino acid sequence alignment of Fur proteins see section 4.1). However, later studies suggested that site 2 was the regulatory site while site 3 might be a weak-affinity site which is not essential for protein function (Lee & Helmann, 2007; Lewin et al, 2002). This is consistent with studies on other Fur proteins (*vide infra*).

In the following years, more homologous proteins were characterised. *H. pylori* Fur (**Figure 1.4**) was the first Fur protein reported to crystalize with three Zn(II) ions per subunit (Dian et al, 2011). A stoichiometry of two to three metal-binding sites per protein monomer was reported for the other characterised proteins. Despite the variety of reported stoichiometries, the residues involved in metal-binding in all of the three sites are well conserved across the Fur proteins (section 4.1). Most of the characterised Fur proteins were reported to have the structural Zn(II) site (site 1, **Figure 1.4c**), with the exception of *M. gryphiswaldens* and *V. cholerae* Fur. *M. gryphiswaldens* Fur, as the *P. aeruginosa* homologue, lacks the Cys residues required to bind Zn(II) in site 1 (Deng et al, 2015). By contrast, *V. cholerae* Fur has the

conserved residues for a putative Zn(II) site, however in the crystallographic structure the thiols were not available to coordinate the metal ion, as they were forming a disulphide bond (nevertheless, this could potentially reflect a crystallisation artefact) (Sheikh & Taylor, 2009). Metals at site 2 and 3 are coordinated by N- and O-donor ligands (**Figure 1.4b**). Studies performed on Fur mutants with altered site 2 or site 3 suggested that the former is essential for metal-depended DNA-binding, while the latter can modulate the response by increasing the affinity for DNA when metalated (Deng et al, 2015; Dian et al, 2011).

1.5.3.1.2 Regulatory mechanisms

The canonical model for the mode of action of Fur describes this sensor acting as a co-repressor, binding to the promoter of its target gene in the metal-bound form to repress gene expression. Fur recognises a 19-base pairs (bp) A/T-rich DNA sequence known as the 'Fur box', first identified in *E. coli* as 5′-GATAATnATTATCATTATC-3′ (De Lorenzo et al, 1987). Compared to other sensors, the Fur box appears to be more tolerant towards nucleotide substitutions without overall loss of functionality (Deng et al, 2015). Sequence identity of experimentally determined iron boxes and the canonical Fur Box were found to range from 50% to 80% (Fillat, 2014). All the Fur-binding DNA sequences contain A/T-rich regions, and this had been related to the mode of recognition of the DNA by this protein (*vide infra*). Often, multiple partially overlapping Fur box sequences are found in the promoter region of the genes regulated by Fur (Griggs & Konisky, 1989; Hunt et al, 1994), and the sensor tends to multimerize on these long recognition sequences (De Lorenzo et al, 1988). Initially, the Fur box was considered as a 9 bp inverted repeat binding one Fur dimer. Subsequent studies suggested that the Fur box comprised tandem repeats of three forward-reverse hexamers (5′-GATAAT-3′) (Escolar et al, 1998). Based on this proposed model, Fur recognises a 5′-NAT(A/T)AT-3′ unit, with three adjacent hexamers (in any order and orientation) being the shorter sequence required for sensor binding. This model could explain the multimerization on promoters containing several adjacent Fur boxes (Escolar et al, 1999), however it failed to clearly define the stoichiometry of Fur-binding to the Fur box sequence. Later, Baichoo and Helmann revisited the model based on their studies in *B. subtilis*, proposing that Fur recognises a 15 bp 7-1-7 motif (Baichoo & Helmann, 2002). The canonical Fur box, therefore, comprises two of these sequences and can bind two Fur dimers (this was confirmed experimentally both in *E. coli* and *B. subtilis* (Baichoo & Helmann, 2002; Lavrrar et al, 2002). Moreover, the 7-1-7 motif was used to identify new Fur-regulated genes in *B. subtilis* that lack the full Fur box (Baichoo et al, 2002). Recent structural studies on *M. gryphiswaldens* Fur showed one Fur dimer binding to a native promoter from the same organism, while two dimers were shown to bind to the Fur box from *P. aeruginosa* (Deng et al, 2015). In the same study it has been proposed that Fur recognises its DNA targets based on DNA shape readout rather than on the

specific nucleotide sequence. In fact, A/T-rich Fur boxes tend to form narrow minor grooves due to electrostatic interactions (Rohs et al, 2009); Fur binds to DNA inserting a conserved lysine residue (Lys15) in the minor groove, so that it interacts with the negative electrostatic potential.

Fur has been reported to be involved in Fe(II)-dependent positive gene regulation (Lee & Helmann, 2007). In 1994 proteomic analysis of *V. cholerae* mutans revealed for the first time that Fur and iron were required for the expression of some genes (Litwin & Calderwood, 1994). Since then, positive gene regulation has been reported also in other organisms (Fillat, 2014; Sarvan et al, 2018). Several different mechanisms seem to be involved in Fe(II)-Fur gene activation, in some cases still not well understood. In a sub-set of cases, positive regulation by Fur is indirect and it is mediated by the action of antisense regulatory small RNA (sRNA). The best characterised sRNA is RyhB from *E. coli* (Masse & Gottesman, 2002). RyhB acts as a post-transcriptional regulator, binding to and decreasing the stability of its mRNA targets, repressing translation (Massé et al, 2003). In the presence of Fe(II), Fur can repress the expression of RyhB, therefore determining an increase in mRNA and in consequence an increase in translation of RyhB target genes (Masse & Gottesman, 2002). Conversely, in Fe(II)-deplete conditions, Fur de-represses the expression of RyhB, indirectly causing a down-regulation of the RyhB targets. RyhB regulates the expression of non-essential Fe(II)-containing enzymes and iron storage proteins. Therefore, this regulatory mechanism allows *E. coli* to remodel its proteome to use iron more efficiently in response to iron depletion (Masse & Arguin, 2005). This mechanism is also known as the "iron-sparing response" (the zinc-sparing response will be briefly discussed in section 5.3.3) and has been reported in other prokaryotes and eukaryotes (Lee & Helmann, 2007; Masse & Arguin, 2005).

In other cases, Fe(II)-Fur interacts with the promoter of the up-regulated genes. For example, binding of Fe(II)-Fur to DNA can hinder binding of another regulator. This is the case of the iron storage protein FtnA from *E. coli*, which is upregulated by Fur in Fe(II)-replete conditions (Nandal et al, 2010). Fur binds to a long binding site upstream of the *ftnA* promoter, competing with the histone-like protein H-NS for the same site. H-NS acts as a repressor on *ftnA*, therefore its displacement by Fe(II)-Fur causes de-repression of this gene (Nandal et al, 2010). Finally, Fur has been reported to act as a direct transcriptional activator in several organisms (Fillat, 2014; Sarvan et al, 2018), even though the mechanism it is not fully understood. Fur from *Neisseria meningitidis* was proposed to activate the expression of the *norB* gene by somehow recruiting the RNA polymerase (Delany et al, 2004). In addition to regulation by Fe(II)-Fur, there is also evidence that this regulator can bind to DNA in the apo-form, either acting as a repressor or an activator (Butcher et al, 2012; Carpenter et al, 2013; Carpenter et al, 2009). In *E. coli*, a recent genome-wide study reported the presence of three groups of Fur-

regulated genes: genes repressed by Fe(II)-Fur, activated by Fe(II)-Fur activated or repressed by apo-Fur (Seo et al, 2014).

A genomic profiling study of iron-regulated genes in *Salmonella*, suggested that 7% of the genome may be regulated directly or indirectly by iron (Bjarnason et al, 2003). Genes regulated by iron include iron import systems, iron storage and mobility proteins, iron-containing enzymes, transcriptional regulators, the energy transducer TonB, as well as virulence-associated genes (Bjarnason et al, 2003). Further characterisation identified three classes of genes: two regulated directly by Fur (either positively or negatively) and others regulated in a Fur-independent manner (Bjarnason et al, 2003). The mechanism of Fur-mediated positive regulation in this organism is not fully understood. Interestingly, *Salmonella* has two small regulatory RNAs, RfrA and RfrB, homologues of the *E. coli* RyhB (Ellermeier & Slauch, 2008). However, why two isoforms are present is still unclear.

Fur has been reported to regulate not only genes involved in iron metabolism. Examples of Fur-regulated genes have roles in many fundamental cellular processes, such as in nitrate/nitrite respiration, acid and oxidative stress tolerance, virulence, DNA synthesis, energy and nutrients metabolism and biofilm production (Bjarnason et al, 2003; Ellermeier & Slauch, 2008; Fillat, 2014; Hall & Foster, 1996; Sarvan et al, 2018; Seo et al, 2014; Teixido et al, 2010). Therefore, Fur has been considered to be a global regulator, coordinating the overall shift in gene expression in response to changes in metal availability.

1.5.3.2 Zn(II)-sensing Fur proteins

Zur proteins represent one of the major and best characterised sub-families within the Fur-like sensors. This Zn(II)-dependent sensor was concurrently discovered in *B. subtilis* and *E. coli* (Gaballa & Helmann, 1998; Patzer & Hantke, 1998). As Fur, Zur was initially identified as a Zn(II)-dependent co-repressor, downregulating the expression of the high-affinity zinc uptake system ZnuABC (Patzer & Hantke, 1998) in Zn(II)-replete conditions. Nevertheless recent data suggest that Zur-dependent positive gene regulation could occur (Mikhaylina et al, 2018). Structural characterisation of Zur proteins revealed that they predominantly form dimers folding in two domains: A N-terminal DNA-binding domain and a C-terminal dimerization domain (Gilston et al, 2014). Zur homologues from several different organisms have been characterised, including the highly similar *E. coli* and *Salmonella* Zur proteins. In *E. coli* Zur, two metal-binding sites per monomer were identified. One is the thiol-containing high affinity structural Zn site commonly found in Fur proteins (section 1.5.3), while the other is the regulatory site (Outten et al, 2001). *Salmonella* Zur can bind three Zn(II) ions per monomer (six per dimer) (Osman et al, 2015). One is the Zn(II) structural site, where the metal ion cannot be exchanged even in the presence of chelators. The two regulatory sites within the same subunit exhibited negative cooperativity in metal-binding assays (Osman et al, 2015).

Binding of two Zn(II) ions per dimer (in addition to the structural site) is sufficient to elicit the allosteric response and binding of other two per dimer further increases the affinity of Zur for DNA (Osman et al, 2017).

1.5.4 Other families of metal sensors

1.5.4.1 CsoR/RcnR

Ni(II)/Co(II)-sensing RcnR from *E. coli* and Cu(I)-sensing CsoR from *M. tuberculosis* are the founding members of the CsoR/RcnR structural family (Iwig et al, 2006; Liu et al, 2007). In addition to metals, other members of this family have been characterised to respond to other signals, for example sulphides (CstR) and formaldehyde (FrmR). RcnR and CsoR both regulate the expression of genes encoding metal efflux proteins. They act as de-repressors, binding to DNA in their apo-form, dissociating when the DNA-affinity is weakened by metal-binding. Structural analysis revealed that proteins from the CsoR/RcnR family fold in an all α-helical fold forming tetramers (Dwarakanath et al, 2012; Liu et al, 2007; Osman et al, 2016). CsoR binds Cu(I) with a distinctive x-Cys-His-Cys motif, which is altered to His-Cys-His-His in RcnR (Ma et al, 2009). One Ni(II) or Co(II) ion per monomer (four ions per tetramer) have been reported to bind to *E. coli* RcnR (Iwig et al, 2008). Similarly, *Salmonella* RcnR has been characterised to bind four Co(II) ions per tetramer. Metal-binding experiments revealed negative cooperativity in binding of Co(II) to the various sites (Osman et al, 2015). *Salmonella* FrmR has a similar metal-binding motif to RcnR, with an Asp residue instead of the final His. A single amino acid mutation A54H was sufficient to generate a metal-sensing protein from FrmR (Osman et al, 2015).

1.5.4.2 NikR

NikR was the first Ni(II)-responsive metal sensor to be identified. It was characterised for the first time in *E. coli* as a Ni(II)-sensing repressor of the anaerobically induced NikABCDE nickel transporter (Chivers & Sauer, 1999; 2000; De Pina et al, 1999). NikR folds in a N-terminal DNA-binding domain with homology to ribbon-helix-helix transcriptional regulators, and a C-terminal domain involved in protein multimerization (Schreiter et al, 2003). This sensor forms homotetramers with a modular design, with two dimeric N-terminal DNA-binding binding domains attached at either end of the core of the structure formed by the tetrameric C-terminal domain (Schreiter et al, 2003). NikR contains two sets of Ni(II)-binding sites. Four tight Ni(II)-binding sites are located at the tetramer interface and are thought to drive the conformational change required to activate DNA-binding. The second set of sites has a weaker affinity for Ni(II) and it is proposed to enhance DNA-binding (Bloom & Zamble, 2004; Chivers & Sauer, 2002; Schreiter et al, 2003; Schreiter et al, 2006).

1.5.4.3 MerR

The founding member of this family of metalloregulators is the mercuric ion resistance regulator MerR, considered the prototype of metalloregulatory proteins (Ma et al, 2009; O'Halloran & Walsh, 1987). The MerR family has been reported to comprise sensors for a variety of metals, for example zinc (e.g. the aforementioned ZntR), cadmium, copper (e.g. CueR), silver, gold (e.g. GolS), mercury and lead, and even non- metal responsive sensors such as SoxR (mentioned in 1.5.1) (Osman & Cavet, 2011). As already introduced in section 1.5, MerR-like sensors act as activators by allosterically underwinding the target DNA sequence (Ansari et al, 1995; Ansari et al, 1992; O'Halloran et al, 1989). These sensor bind to DNA both in the apo- and metalated form, with a slightly weaker affinity in the presence of the metal (O'Halloran et al, 1989). In the promoters of the genes regulated by MerR proteins, the spacing between the −35 and −10 elements is greater than the one found in most bacterial promoters. This causes the two regulatory elements to be mis-aligned and suboptimal for recognition by RNA polymerase. Metal-activation of the sensors drives a conformational change that distorts the DNA, aligning the −35 and −10 sequences for optimal recognition by RNA polymerase (Ansari et al, 1995; Ansari et al, 1992; Brown et al, 2003; Philips et al, 2015). Structural studies on *E. coli* CueR and ZntR revealed that these proteins form dimers folding in three domains: An N-terminal DNA-binding domain, a dimerization helix and a C-terminal domain responsible for metal binding, containing one metal-binding site per subunit (Changela et al, 2003).

1.6 Understanding intracellular metal availabilities for vitamin B_{12} production

As introduced in section 1.3, how metals correctly partition into the various metal-delivery pathways and how metallochaperones acquire the correct metals to be delivered to their target proteins is unclear. In this study, using the information of metal availability obtained from the metal sensors, the insertion of cobalt into the pathway for the synthesis of vitamin B_{12} in *Salmonella* will be examined. Vitamin B_{12}, or cobalamin, is an essential vitamin to humans. Clinical features of vitamin B_{12} deficiency can go from mild fatigue and anaemia to severe neurological damage (Stabler, 2013). However, despite the essential role of this vitamin, only a subset of prokaryotes are able to perform the synthesis *de novo* of cobalamin (Martens et al, 2002). Moreover, the human microbiome might be able to produce cobalamin, but it is not localised in the intestinal regions where B_{12} is absorbed. Humans, therefore, need to rely on the assimilation of vitamin B_{12} from the diet. Cobalamin can be found in animal source foods, while is practically absent in plant-based food. Therefore, the dietary vitamin B_{12} deficiency is a severe problem in those areas where access to animal-based food is limited, and will gradually become a major global health issue as a more sustainable plant-based diet is adopted

worldwide (Stabler & Allen, 2004). Possible strategies to prevent cobalamin deficiency are prescribing supplements to those at risk and fortifying plant-based food to increase the dietary intake of vitamin B_{12} (Stabler & Allen, 2004).

Cobalamin is one of the more complex molecules in nature. It consists of a Co(III) ion coordinated by a corrin ring (a tetradentate ligand), an axial dimethylbenzimidazole group and variable ligand in the remaining axial position (depending on the vitamer, it can be a 5′-deoxyadenosyl group, a methyl group, a cyano group or a hydroxyl group) (Martens et al, 2002). Due to the complexity of structure, although the total chemical synthesis was achieved in 1972 (Eschenmoser & Wintner, 1977), the industrial production of vitamin B_{12} by chemical methods is not economically feasible. Currently, large-scale production of this vitamin relies exclusively on biosynthetic fermentation processes, using selected microorganisms (Martens et al, 2002). Nevertheless, the organisms commonly used for cobalamin production can be slow growers and difficult to engineer. An attractive alternative would be to engineer for the production of vitamin B_{12} an heterologous organism such as *E. coli* (Li, 2014), a bacterium much easier to grow but not able to synthesise *de novo* cobalamin. *S.* Typhimurium can synthesise cobalamin under anaerobic conditions (Jeter et al, 1984) and an *E. coli* strain engineered with 20 cobalamin genes from the *S.* Typhimurium *cob* operon was able to produce vitamin B_{12} (Raux et al, 1996). However, the optimisation of the production of metalloproteins or metal-containing molecules in heterologous hosts, requires the knowledge of the mechanisms controlling correct partitioning of metals in the biosynthetic pathways. In the anaerobic biosynthetic pathways, as in *S.* Typhimurium, cobalt insertion into the tetrapyrrole ring occurs at an early stage and it is performed by the chelatase CbiK (Raux et al, 1997; Warren et al, 2002). Although CbiK has been characterised *in vitro* (including the determination protein structure with metal, (Romao et al, 2011; Schubert et al, 1999)), how this protein can selectively insert cobalt into sirohydrochlorin is currently unknown. This work will allow the prediction of the metalation state of CbiK in *S.* Typhimurium cells.

1.7 Aims

This work was part of a collaborative project (work done by others is identified as such herein) aimed at characterising the complete set of metal sensors from *Salmonella*, in order to thoroughly understand metal sensing and selectivity across the complement. Moreover, as the sensors are tuned to the intracellular availability of the metals they sense, metal availability in *Salmonella* cells can be defined from the sensitivity of the various sensors. Therefore, the aims of this project were three-fold:

1) The first aim of this project was to study two of the remaining uncharacterised sensors within the set in *Salmonella* (**Figure 1.2**): Mn(II)-sensing MntR and Fe(II)-sensing Fur. The

two proteins were recombinantly expressed and purified to homogeneity to allow the determination of thermodynamic parameters. Specifically, the affinity for the cognate metals and the affinity for DNA (of both the apo- and metal-activated forms of the sensor) were determined *in vitro* (Chapter 3 and Chapter 4). These values completed a set of experimentally determined thermodynamic parameters already available from previous studies on the other *Salmonella* sensors.

2) Several models to describe sensor responses and hence determine their sensitivity have been proposed. However, to date, none of them have considered the coupled equilibria of metal-binding and DNA-binding reactions together with sensor autoregulation. Therefore, the second aim of this work was to develop a thermodynamics-based mathematical model to calculate sensor response to metal availability (Chapter 5). The model not only allowed the calculation of sensor responses to metal considering their autoregulation, but also allowed simulations to further understand quantitatively how the various parameters dictate sensor sensitivity or how a modification of the model (for example by introducing binding to non-specific DNA) affect the sensitivities.

3) Intracellular metal availabilities can be inferred from the sensitivities of the metal sensors. However, there are several definitions for what 'available metal' refers to. In order to find a clear and direct definition for metal availability, sensor sensitivities were converted to standard free energies for metalation of a hypothetical molecule in the *Salmonella* cytosol (Chapter 6). The determined intracellular availabilities provide a thermodynamic framework and cellular logic for correct metalation. Moreover, these results allow the prediction (both qualitative and quantitative) of the metalation state of a molecule of interest. In this work, this will be exemplified with the cobalt chelatase CbiK, using experimental values collected by other members of the Robinson's group. With the knowledge that metal availability can be modulated in response to the microorganism environment and growth conditions, a strategy to refine metal availabilities was proposed and applied to the two *Salmonella* Zn(II) sensors (Chapter 6).

Chapter 2.

Materials and Methods

2.1 Reagents and chemicals

Unless otherwise stated, chemicals and reagents were sourced from standard suppliers (Sigma-Aldrich, Melford, Thermo Fisher Scientific, Merck, Bio-Rad Laboratories). Fluorescent affinity probes were sourced from Invitrogen (Thermo Fisher Scientific). Primers and fluorescently labelled oligonucleotides were obtained from Sigma-Aldrich (**Table 2.1**). Molecular biology kits and enzymes were sourced from Promega, Qiagen and Thermo Fisher Scientific. All growth media, buffers and reagent solutions were prepared using ultrapure water from a Milli-Q system (Millipore). Where necessary, glassware was acid-washed in 4% v/v HNO_3 for at least 12 h and then rinsed thoroughly in ultrapure H_2O to remove trace metal contamination.

2.2 Bacterial strains and growth conditions

E. coli strain DH5α (genotype: F^- φ80*lacZ*ΔM15 Δ(*lacZYA-argF*)U169 *recA*1 *endA*1 *hsdR*17(r_K^-, m_K^+) *phoA supE*44 λ^- *thi*-1 *gyrA*96 *relA*1) was used for molecular biology applications. For recombinant protein overexpression, *E. coli* strain BL21(DE3) (genotype: F^- *ompT hsdS*$_B$ (r_B^-, m_B^-) *gal dcm* (DE3)) was employed. *Salmonella enterica* serovar Typhimurium strain SL1344 (genotype: *hisG*46), originally from the *Salmonella* Genetic Stock Centre, was provided by Dr. Jen Cavet (University of Manchester) and used throughout as a wild-type in gene expression experiments. Liquid *E. coli* cultures were grown in Luria-Bertani (LB) medium (Sambrook & Russell, 2001). Unless otherwise stated, *E. coli* cells were cultured at 37 °C with shaking (180 rpm). Liquid *Salmonella* cultures were cultured in LB at 37 °C with shaking (200 rpm) in plastic tubes to minimise trace metal contamination. Cultures grown on solid LB agar plates were incubated statically at 37 °C overnight for colony formation. Bacterial strains were stored at 4 °C on LB agar plates for short periods and at −80 °C as glycerol stocks for long-term storage.

LB medium (10 g l^{-1} tryptone, 5 g l^{-1} yeast extract, 10 g l^{-1} NaCl) was sterilised prior to use by autoclave treatment. LB medium used to grow *Salmonella* cultures was prepared in acid-washed glassware to minimise differences in metal content between different batches. Solid medium was prepared by adding 15 g l^{-1} agar. Where required, cultures were supplemented with metals or chelants. Metal stocks were prepared in ultrapure H_2O and quantified by inductively coupled plasma mass spectrometry (ICP-MS) (section 2.7.2).

Table 2.1. List of oligonucleotides used in this thesis.

#	Name	Sequence	Source
1	mntSPro_F*	HEX-5′-CTATAAAACATAGCCTGTGCTATATCTGTATG-3′	(Osman et al, 2019)
2	mntSPro_R	5′-CATACAGATATAGCACAGGCTATGTTTTATAG-3′	(Osman et al, 2019)
3	mntSPro-short_F	HEX-5′-ACATAGCCTGTGCTATAT-3′	This study
4	mntSPro-short_R	5′-ATATAGCACAGGCTATGT-3′	This study
5	iroBPro_F*	HEX-5′-AATGATATTGGTAATTATTATCATTCTCATTAACGAC-3′	This study
6	iroBPro_R	5′-GTCGTTAATGAGAATGATAATAATTACCAATATCATT-3′	This study
7	furbox_F	HEX-5′-GGGGATAATGATAATCATTATCGGG-3′	(Osman et al, 2019)
8	furbox_R	5′-CCCGATAATGATTATCATTATCCCC-3′	(Osman et al, 2019)
9	mntSPro-swap_F	HEX-5′-CTATAAAACAATGCCTGTCATGTATCTGTATG-3′	(Osman et al, 2019)
10	mntSPro-swap_R	5′-CATACAGATACATGACAGGCATTGTTTTATAG-3′	(Osman et al, 2019)
11	mntS_RTPCR_F	5′-ACGCGTGTTCAGTCACTCTC-3′	(Osman et al, 2019)
12	mntS_RTPCR_R	5′-TTCGTGGAAGGGTTATCCTG-3′	(Osman et al, 2019)
13	iroB_RTPCR_F	5′-ATCAAAGGCGTGACGAAATC-3′	(Osman et al, 2019)
14	iroB_RTPCR_R	5′-ATACGGGACGTATTGCATGG-3′	(Osman et al, 2019)
15	rcnA_RTPCR_F	5′-TCCCAGCGCCATTTTATTAG-3′	(Osman et al, 2017)
16	rcnA_RTPCR_R	5′-ACGATCGCGGTATGAGAAAG-3′	(Osman et al, 2017)
17	copA_RTPCR_F	5′-TAAAATCTCCGCGGTATTCG-3′	(Osman et al, 2019)
18	copA_RTPCR_R	5′-CCGGAAATAATCGACATTGG-3′	(Osman et al, 2019)
19	zntA_RTPCR_F	5′-TAAACTGGTTTCCGGTTTCG-3′	(Osman et al, 2017)
20	zntA_RTPCR_R	5′-TCAATCAGCGTCAGGATACG-3′	(Osman et al, 2017)
21	znuA_RTPCR_F	5′-ACATGCATCTTTGGCTCTCC-3′	(Osman et al, 2017)
22	znuA_RTPCR_R	5′-ACCGACCTGTTTATCGGTTG-3′	(Osman et al, 2017)
23	rpoD_RTPCR_F	5′-CAACCGTATTTCTCGCCAGATG-3′	(Osman et al, 2017)
24	rpoD_RTPCR_R	5′-CACCCAGATGCGAATCTTCATC-3′	(Osman et al, 2017)

The forward strand of the oligonucleotides used in fluorescence anisotropy experiments had the 5′ end labelled with the fluorophore hexachlorofluorescein (HEX) *Unlabelled versions of these oligonucleotides were used for size-exclusion experiments.

N,N,N′,N′-tetrakis(2-pyridinylmethyl)-1,2-ethanediamine (TPEN) was dissolved in ethanol and stored at −20 °C; TPEN dilutions were prepared daily in sterile ultrapure water. Kanamicin (50 μg ml^{-1}) was used to select *E. coli* cells grown after transformation to antibiotic resistance with pET29a recombinant plasmids. Additives (e.g. metals, antibiotics) were sterilised by filtration through 0.2 μm membranes (Sartorius).

2.3 Competent bacterial cell preparation and transformation

2.3.1 Preparation of chemically competent *E. coli*

Competent *E. coli* cells were prepared using a variation of the $CaCl_2/MgCl_2$ method (Sambrook & Russell, 2001). Previously prepared competent cells were streaked on a LB plate and incubated overnight at 37 °C for single colony formation. The following day, a colony was inoculated in ~5 ml LB. The overnight culture was diluted 1:100 in 100 ml of fresh LB media and cells were incubated at 37 °C degrees with shaking (200 rpm) until an optical density ($OD_{600\ nm}$) of 0.5 was reached. Cells were transferred to two 50 ml centrifuge tubes and centrifuged at 3,082 × g for 40 min at 4 °C in a Beckman Coulter Allegra X-22R benchtop centrifuge. The supernatant was discarded and the cell pellets were re-suspended in 25 ml ice-cold sterile 100 mM $MgCl_2$. After incubation on ice for 1 h, cells were centrifuged at 3,082 × g, 15 min, 4 °C using the above centrifuge. The supernatant was discarded and the cells were re-suspended in 1 ml ice-cold sterile solution of 15% w/v glycerol, 85 mM $CaCl_2$. Re-suspended cells were divided into 50 μl aliquots, snap-frozen in liquid nitrogen and stored at -80 °C.

2.3.2 Transformation of chemically competent *E. coli*

To transform cells to antibiotic resistance, a 50 μl aliquot of competent cells was thawed on ice (5-10 min) before addition of 100−400 ng purified plasmid. Cells were incubated on ice for 10 min, heat shocked at 42 °C for 90 s and returned to ice for 2 min. Following addition of 500 μl of LB, cells were incubated at 37 °C, 200 rpm for 1 h. Cultures were centrifuged at 18,176 × g for 3 min using a Beckman Coulter Microfuge 18 benchtop centrifuge. 350 μl of supernatant was removed and the cells were re-suspended in the remaining media. Cells were plated on LB agar plates containing kanamycin (50 μg ml^{-1}) and incubated overnight at 37 °C.

2.4 DNA manipulation

2.4.1 Extraction of plasmid DNA from *E. coli*

Plasmids pET29aMntR and pET29aMntR Fur were cloned by Dr. Deenah Osman (Durham University) prior to the beginning of this study. To propagate the plasmid, *E. coli* DH5α cells were transformed to kanamycin resistance with the appropriate plasmid. Cells from an overnight culture (10 ml) were pelleted by centrifugation at 3,082 × g, 10 min, 4 °C (Beckman Coulter Allegra X-22R centrifuge). Plasmid DNA was extracted using the Wizard *Plus* SV

Minipreps DNA Purification System (Promega) according to manufacturer's instruction. The concentration of recovered plasmid DNA was measured using a microvolume spectrophotometer (NanoDrop 1,000, Thermo Fisher Scientific) reading the absorbance 260 nm. DNA samples were stored at −20 °C.

2.4.2 DNA sequencing

Plasmid DNA sequencing was conducted by DBS genomics, Durham University to verify no mutations/errors.

2.5 Protein manipulation

2.5.1 Overexpression of recombinant MntR and Fur

E. coli BL21(DE3) cells were transformed to kanamycin resistance with pET29aMntR or pET29aFur. A single colony was used to inoculate a 12 ml overnight starter culture in LB supplemented with kanamycin (50 μg ml^{-1}). The following day, the overnight culture was diluted 1:100 in fresh LB medium (1 l) and grown at 37 °C, 200 rpm. Cells transformed with pET29aMntR were grown to an OD_{600} = 0.5–0.6 (3–4 h) before induction. BL21(DE3) cells expressing Fur were grown to an OD_{600} = 0.7–0.8 (~6 h) before induction. Cells transformed with pET29aFur grew more slowly, probably due to leaky expression of Fur and consequent disruption of iron homeostasis. Recombinant protein expression was induced by addition of IPTG to a final concentration of 1 mM. For Fur expression 50 μM of $ZnSO_4$ was added at induction to encourage filling of the Zn(II)-structural site found in the iron-sensor (see 4.2.1). After induction, cells were grown for 2 to 3 h and harvested by centrifugation at 3,993 × g, 20 min, 4 °C using a Beckman Coulter Avanti J-20XP centrifuge using a JLA 8.100 rotor. Each pellet was re-suspended in 10 ml LB medium, transferred to 50 ml centrifuge tubes and centrifuged at 3,082 × g for 10 min in a Beckman Coulter Allegra X-22R benchtop centrifuge. Cell pellets were stored at –20 °C.

2.5.2 SDS-PAGE analysis

SDS-PAGE (sodium dodecyl sulfate–polyacrylamide gel electrophoresis analysis) was performed during and after the purification protocol to assess protein purity and concentration (Sambrook & Russell, 2001). 17.5% w/v acrylamide gels were routinely hand-casted with the Mini-PROTEAN 3 system (Bio-Rad Laboratories) for MntR and Fur purification. 4–20% w/v Mini-PROTEAN® TGX™ Precast Protein Gels (Bio-Rad Laboratories) were used to produce publication-quality images of the purified proteins (**Figure 3.3** and **Figure 4.7**). SDS-PAGE gels were routinely run at 150−200 V for ~1 h at room temperature using a Tris-Glycine running buffer (Sambrook & Russell, 2001). Gels were stained overnight in InstantBlue Protein Stain (Expedeon) and destained in water.

2.5.3 Protein purification

2.5.3.1 Purification of recombinant MntR

The composition of the buffers used for MntR purification is reported in **Table 2.2**. Pellets from 1 l culture were thawed at room temperature and re-suspended in 10 ml of buffer A10 with addition of 1 mM phenylmethane sulfonyl fluoride (PMSF) to inhibit protease activity. Cells were transferred to 1.5 ml microcentrifuge tubes in 750 µl aliquots and lysed by sonication on ice (30 s at 35% power). The lysate was clarified by centrifugation in a benchtop microcentrifuge (17,000 × g, 10 min, 4 °C, Heraeus Fresco 17, Fisher Scientific). The supernatant was collected and further clarified by centrifugation at 48,384 × g, 25 min, 4 °C in a Beckman Coulter Avanti J-20XP centrifuge using a JA25.50 rotor. The soluble lysate was loaded onto a 5 ml HisTrap HP column (GE Healthcare), equilibrated in buffer A10, at a flowrate of 2.5 ml min^{-1}. Bound protein was washed with 40 ml buffer A10 and eluted in buffer B100 over one 5 ml fraction followed by a wash with buffer B300. Fractions containing MntR were initially identified by reaction with Coomassie Brilliant Blue (Thermo Fisher Scientific) and by SDS-PAGE. Due to the high reproducibility of the HisTrap step, SDS-PAGE was skipped during the purification of the later protein batches. The fraction containing the highest concentration of MntR was loaded onto a HiLoad 16/600 Superdex 75 size-exclusion column (GE Healthcare) equilibrated in buffer C300 and eluted with the same buffer collecting 5 ml fractions. The fractions containing MntR (usually fractions 32−35), identified by SDS-PAGE, were pooled and applied to a 1 ml HiTrap Heparin column (GE Healthcare) equilibrated in buffer C300, at 1 ml min^{-1}. Bound protein was washed with 10 ml of buffer C300 and MntR was eluted in a single step using buffer C1000. The purity of the protein confirmed to be >95% by SDS-PAGE. To prepare protein samples for *in vitro* experiments involving metals, MntR was buffer exchanged to remove EDTA from the buffer. Pure MntR was diluted to 300 mM NaCl using buffer C0 and re-applied to a 1 ml HiTrap Heparin column equilibrated in buffer C300. Bound protein was washed with 10 ml buffer C300. To remove EDTA, MntR was washed with at least 10 ml of Chelex-treated 60 mM NaCl, 240 mM KCl, 10 mM HEPES pH 7.0 and eluted with Chelex-treated buffer D (Chelex-treated 200 mM NaCl, 800 mM KCl, 10 mM HEPES pH 7.0, for Chelex-treatment see section 2.6.1). The protein was stored at 4 °C for up to a month.

2.5.3.2 Purification of recombinant Fur

The composition of the buffers used for Fur purification is reported in **Table 2.2**. Pellets from 1 l culture were thawed at room temperature and re-suspended in 10 ml buffer A5 with addition of protease inhibitor cocktail. Cells were transferred to 1.5 ml microcentrifuge tubes in 750 µl aliquots, and lysed by sonication on ice (30 s at 35% power). The lysate was clarified by centrifugation in a Heraeus Fresco 17 benchtop microcentrifuge (17,000 × g, 10 min, 4 °C).

Table 2.2. Composition of buffers used in this work.

Buffer	Composition
Buffer A5	300 mM NaCl, 5 mM imidazole, 1 mM TCEP, 20 mM sodium phosphate pH 7.4
Buffer A10	300 mM NaCl, 10 mM imidazole, 20 mM sodium phosphate pH 7.4
Buffer B100	300 mM NaCl, 100 mM imidazole, 20 mM sodium phosphate pH 7.4
Buffer B300	300 mM NaCl, 300 mM imidazole, 20 mM sodium phosphate pH 7.4
Buffer D	200 mM NaCl, 800 mM KCl, 10 mM HEPES pH 7.0, Chelex-treated
Buffer E	100 mM NaCl, 400 mM KCl, 10 mM HEPES pH 7.0, Chelex-treated
Buffer F	60 mM NaCl, 240 mM KCl, 10 mM HEPES pH 7.0, Chelex-treated
For MntR purification only	
Buffer C0	10 mM EDTA, 10 mM HEPES pH 7.0
Buffer C300	300 mM NaCl, 10 mM EDTA, 10 mM HEPES pH 7.0
Buffer C1000	1000 mM NaCl, 10 mM EDTA, 10 mM HEPES pH 7.0
For Fur purification only	
Buffer C100	100 mM NaCl, 1 mM TCEP, 10 mM HEPES pH 7.0
Buffer C1000	1000 mM NaCl, 1 mM TCEP, 10 mM HEPES pH 7.0

The supernatant was collected and further clarified by centrifugation at 48,384 × g, 25 min, 4 °C in a Beckman Coulter Avanti J-20XP centrifuge using a JA25.50 rotor. The soluble lysate was loaded onto a 5 ml HisTrap FF column (GE Healthcare) equilibrated in buffer A5, at a flowrate of 2.5 ml min^{-1}. Bound protein was washed with 40 ml buffer A5 and 10 ml buffer A10. Fur was eluted in buffer B100, collecting one 4.5 ml fraction, and then in buffer B300, collecting seven 5 ml fractions. A large proportion of Fur eluted in buffer B100, with contaminating proteins that could not be separated during subsequent purification steps. Fur eluted at a relatively high concentration also in buffer B300. Fractions eluted with buffer B300 with the highest Fur concentration were therefore pooled and diluted to 100 mM NaCl using 1 mM TCEP, 10 mM HEPES pH 7.0. The protein sample was loaded onto a 5 ml HiTrap Q column (GE Healthcare) equilibrated in buffer C100, at 2.5 ml min^{-1}. Bound protein was washed with 25 ml of buffer C100 and Fur was eluted using buffer C1000 collecting 1 ml fractions. The protein concentration was estimated from the absorbance at 280 nm (see section 2.5.4 for extinction coefficient) and 2 equivalents of $ZnSO_4$ were gradually added. After 1 h at room temperature, EDTA was added to a final concentration of 7.5 mM and the mixture was incubated overnight at 4 °C. The Fur sample was loaded onto a HiLoad 16/600 Superdex 75 size-exclusion column equilibrated in Chelex-treated buffer C100 and eluted in the same buffer collecting 5 ml fractions. Fractions containing Fur were identified by SDS-PAGE and analysed by ICP-MS to ensure the full metalation of the structural site and the absence of any contaminating metal. SDS-PAGE routinely showed that after the size-exclusion step Fur was >95% pure. The fractions from the size exclusion column having an elution volume indicative of a dimeric species (usually fractions 31−33) and containing Fur with a fully metalated Zn(II) structural site were pooled and moved into an anaerobic glovebox (Belle Technology) (section 2.6.2).

2.5.3.3 Calibration of HiLoad 16/600 Superdex 75 size-exclusion column

To better characterise Fur oligomeric state in the fractions collected after the size-exclusion step, the HiLoad 16/600 Superdex 7 column was calibrated with molecular weight standards. Alcohol dehydrogenase (MW ≈ 150 kDa), bovine serum albumin (MW ≈ 66 kDa), albumin from chicken egg white (MW ≈ 44 kDa), carbonic anhydrase (MW ≈ 29 kDa), myoglobin (MW ≈ 17 kDa) and cytochrome c (MW ≈ 12.4 kDa) were mixed to a final concentration of ~1 mg ml^{-1} of each protein in 100 mM NaCl, 0.5 mM TCEP, 10 mM HEPES pH 7.0. 2 ml of the mixture (2 mg of each protein) was loaded on the column equilibrated in the same buffer. Protein elution with the equivalent buffer was monitored via absorbance at 280 nm and the proteins were identified by SDS-PAGE. The void volume was determined from the elution volume of Blue Dextran (2 ml, 1 mg ml^{-1}) in a separate analysis.

2.5.4 Quantification of protein stocks

Proteins were quantified by absorbance at 280 nm using the Beer-Lambert law. Experimental extinction coefficients were determined by quantitative amino acid analysis performed by Alta Bioscience. The determined extinction coefficients are: 7,940 M^{-1} cm^{-1} for MntR and 6,672 M^{-1} cm^{-1} for Fur (Osman et al, 2019).

2.6 Anaerobic manipulation of proteins

2.6.1 Preparation of oxygen-free Chelex-treated buffers

In order to remove trace metal contaminants, buffers were treated with Chelex-100. Chelex is a styrene-divinylbenzene copolymer containing the chelating group iminodiacetate, with a tight affinity for divalent cations. The Chelex resin was packed into an acid-washed glass column and prepared to its sodium form following manufacturer's instructions. To achieve metal removal, buffers were applied to the column, collecting the eluate in clean plastic 50 ml centrifuge tubes. Chelex-treated buffers to be used for experiments under anaerobic conditions were treated to remove dissolved oxygen prior to use. Buffers were bubbled with oxygen-free N_2 for at least 2 h before being moved into an anaerobic glovebox.

2.6.2 Preparation of anaerobic protein samples

In order to study the metal properties of Fur in the absence of reductant and, in particular, in order to employ Fe(II) in assays, the *in vitro* analyses of the proteins were performed in an anaerobic glovebox using oxygen-free protein samples and reagents. A purified Fur sample (section 2.5.3.2) was applied to a 1 ml HiTrap Q column (GE Healthcare) equilibrated in Chelex-treated buffer C100. Bound protein was washed with 10 ml of Chelex-treated buffer C100 and the column was transferred to an anaerobic glovebox. Fur was buffer-exchanged on the column by washing with at least 10 ml of degassed Chelex-treated 20 mM NaCl, 80 mM KCl, 10 mM HEPES pH 7.0, and eluted with degassed buffer D, collecting four 1 ml fractions. Fur routinely eluted in high concentration in the second fraction. The protein was stored at 4 °C under anaerobic conditions for up to a month. MntR lacks cysteine residues and Fe(II) was not employed with this protein; therefore, anaerobic conditions were not required.

2.6.3 Determination of reduced thiol content in protein samples

The reduced cysteine content in the anaerobic Fur samples was determined via reaction of the reduced thiols with 5,5-dithio-bis-(2-nitrobenzoic acid) (Ellman's reagent or DTNB). In water at neutral or alkaline pH, Ellmann's reagent reacts with sulfhydryl groups in a 1:1 stoichiometry to yield a coloured dianionic product 2-nitro-5-thiobenzoate (TNB^{2-}). TNB^{2-} has a strong absorption peak at 412 nm (Ellman, 1959). Ellmann's reagent was dissolved to a final concentration of 4 mg ml^{-1} in 1 mM EDTA, 100 mM sodium phosphate pH 8.0. A solution of Ellmann's reagent (~222 μg ml^{-1}) and protein (routinely 10−20 μM) was prepared under

anaerobic conditions in buffer D in a 1 ml gas-tight quartz cuvette (Hellma) and incubated in the dark at room temperature for at least 24 h, periodically monitoring the absorbance at 412 nm. For some protein preparations (e.g. **Figure 4.8**), the reaction of the reduced thiols with Ellmann's reagent was monitored with automated measurements over at least 24 h. A sample containing only Ellmann's reagent was monitored in parallel to take into account any increase in absorbance due to degradation of the reagent. The concentration of reduced thiols in the protein sample was determined from the absorbance at 412 nm using the Beer-Lambert law and an extinction coefficient of $\varepsilon_{412\ nm}$ = 14,150 M cm^{-1} (Riddles et al, 1983). Only protein preparations with a reduced cysteine content of at least 90% were used for *in vitro* assays.

2.6.4 Measurement of residual metal content of purified protein samples

Contamination of purified protein samples (sections 2.5.3.1 and 2.5.3.2) with residual metal ions was determined by ICP-MS. Protein samples were prepared (under anaerobic conditions for Fur) in buffer D to a final concentration of ~20 μM. An aliquot of each sample was diluted 1:10 in 2% v/v nitric acid and analysed for metal content. Only protein preparations with a contaminating metal content below 5% were used for *in vitro* analyses. Fur routinely contained ~1 equivalent of Zn(II).

2.7 Experimental procedures

2.7.1 UV-visible spectroscopy

Spectra were recorded on a λ35 UV–visible spectrophotometer (PerkinElmer). Protein samples for determination of protein concentration were diluted in buffer D (under anaerobic conditions for Fur) in 1 ml gas-tight quartz cuvettes. Protein samples for all the other experiments were prepared in Chelex-treated buffer E (Chelex-treated 100 mM NaCl, 400 mM KCl, 10 mM HEPES pH 7.0). All quartz cuvettes were acid-washed, rinsed with ultrapure H_2O and dried prior to use.

2.7.2 Preparation of metal stocks

All metal stocks (except for ferrous iron) were prepared by dissolving metal salts in ultrapure water. The concentration of each metal was assayed by ICP-MS after serial dilutions of the stocks. Ferrous iron was prepared by dissolving $(NH_4)_2Fe(SO_4)_2{\cdot}6H_2O$ (Mohr's salt) in oxygen-free 0.1% v/v HCl and stored at 4 °C, under strict anaerobic conditions and protected from light. Total iron concentration in the stock was determined by ICP-MS. The concentration of Fe(II) was determined by serial dilution in oxygen-free ultrapure water and titration into a solution of ferrozine (approximately tenfold in excess) in buffer E. The titration was performed under anaerobic conditions in a 1 ml gas-tight quartz cuvettes. Ferrozine forms a coloured complex with Fe(II) (but not Fe(III)), with a stoichiometry of three ferrozine molecules per Fe(II) ion (Stookey, 2002). The concentration of Fe(II) was determined from

the absorbance at 562 nm using the Beer-Lambert law with an extinction coefficient of $\varepsilon_{562\ nm}$ = 27,900 M cm (Stookey, 2002). The metal stock was used only if confirmed to be >90% Fe(II). For *in vitro* experiments, serial dilutions of the ferrous iron acidic stock were prepared daily in ultrapure water and the reduced state of the stock was confirmed by ferrozine assay.

2.7.3 Fractionation of protein-metal complexes by size-exclusion chromatography

All experiments were performed in buffer E using Sephadex G25 columns (PD10 column, GE Healthcare). Columns were prepared by washing with two column volumes of ultrapure water, addition of 0.5 ml of 0.5 M EDTA, a further wash with two column volumes of water and final equilibration with two column volumes of experimental buffer. MntR and Fur samples (20 μM monomer, 0.5 ml) were applied to the column after incubation for 30 min at room temperature with 100 μM $MnCl_2$ (MntR) and either 50 μM $(NH_4)_2Fe(SO_4)_2$ or 1 mM EDTA (Fur). Where the protein was pre-incubated with metals, the buffer was supplemented with the same concentration of metal (100 μ M $MnCl_2$ for MntR and 50 μM $(NH_4)_2Fe(SO_4)_2$ for Fur). Fractions (0.5 ml) were collected and analysed for metal content by ICP-MS and for protein content by Bradford assay (calibrated against a protein stock of known concentration) or from the absorbance at 280 nm.

2.7.4 Intrinsic protein fluorescence upon metal titration

Protein samples (10–20 μM) were prepared in buffer E with the inclusion of 5% v/v glycerol for MntR in 1 ml gas-tight quartz fluorescence cuvettes. Experiments with Fur were performed under anaerobic conditions. MntR and Fur were titrated with $MnCl_2$ and $(NH_4)_2Fe(SO_4)_2$ respectively. Protein saturation with metal during the titration was monitored with a Cary Eclipse fluorescence spectrophotometer (Agilent Technologies). Spectra were recorded at equilibrium (typically 3 min after metal addition). MntR: Excitation wavelength = 280 nm, T = 20 °C. Fur: Excitation wavelength = 276 nm, T = 25 °C.

2.7.5 Determination of metal-binding affinities

All the metal-binding experiments were performed in buffer E, with the inclusion of 5% v/v glycerol for the competition between MntR and mag-fura-2. All experiments with Fur were performed under anaerobic conditions. Data were fit using Dynafit (Kuzmic, 1996). The scripts used to fit the experimental data are reported in **Appendix B**.

2.7.5.1 Determination of mag-fura-2 affinity for Mn(II)

A solution (~2.0 μM) of the fluorescence probe mag-fura-2 (Invitrogen) was titrated with $MnCl_2$. Metal-binding to the probe was monitored from the quenching in the fluorescence excitation peak at equilibrium. Spectra were recorded (Cary Eclipse fluorescence spectrophotometer, emission wavelength = 505 nm, T = 20 °C) after incubation of the sample

in the spectrophotometer for 5 min, to reach equilibrium. Data with excitation wavelength = 380 nm were fit to a model describing Mn(II)-binding to mag-fura-2 with a 1:1 stoichiometry using Dynafit. Mag-fura-2 was quantified from the absorbance at 369 nm ($\varepsilon_{369\,nm}$ = 22,000 M^{-1} cm^{-1} (Golynskiy et al, 2006)).

2.7.5.2 Determination of MntR affinity for Mn(II)

A solution of mag-fura-2 (~2.0 μM) and MntR (7.1–18.7 μM monomer) was titrated with $MnCl_2$, monitoring the fluorescence excitation of the probe at equilibrium (fluorescence parameters as in 2.7.5.1). Data were fit to a model describing Mn(II)-binding to mag-fura-2 with a 1:1 stoichiometry and Mn(II)-binding to MntR with a stoichiometry of two Mn(II) per protein monomer, using the affinity of mag-fura-2 for Mn(II) determined in 2.7.5.1.

2.7.5.3 Determination of Fur affinity for Fe(II)

Fur (10 – 11 μM monomer) was titrated with $(NH_4)_2Fe(SO_4)_2$ in the presence of nitrilotriacetic acid (NTA, 100 μM), monitoring the quenching of Fur intrinsic fluorescence (fluorescence parameters as in 2.7.4). Data with emission wavelength = 303 nm were fit to a model describing NTA binding Fe(II) with a 1:1 stoichiometry and competition from Fur for two equivalents of metal per monomer (four sites per dimer). Positive cooperativity between two pairs of sites per dimer was included in the model. In the model, the two sites within the same pair had the same individual (or microscopic) affinity. This was equal to the (macroscopic) thermodynamic constant for the first binding event to any of the two sites within the pair. Consequently, the (macroscopic) constant for metal-binding to the second site within the pair was set four fold weaker than the first one for effect of the statistical factors (Wyman & Gill, 1990). NTA Fe(II) affinity at pH 7.0, was determined using the Schwarzenbach's α coefficient (Schwarzenbach & Flaschka, 1969):

$$K'_A = \frac{[ML]\alpha_{H-L}}{[M][L]} = K_A \alpha_{H-L}$$

$$\alpha_{H-L} = (1 + \beta_{H,1}[H] + \beta_{H,2}[H]^2 + ... + \beta_{H,n}[H]^n)^{-1}$$

where K_A' is the affinity constant at specified pH, K_A is the absolute affinity constant and α_{H-L} is Schwarzenbach's α-coefficient. The α-coefficient can be calculated at any given pH if the pKa (acid dissociation constant) values for the chelant are known ($\beta_{H,1} = 10^{pKa1}$, $\beta_{H,2} = 10^{pKa1+pKa2}$ etc., with $[H] = 10^{-pH}$). Values for NTA are: $\log K_{Fe(II)} = 8.90$ (as association constant), $pK_{a1} = 9.73$, $pK_{a2} = 2.49$, $pK_{a3} = 1.89$ (Xiao & Wedd, 2010).

2.7.6 Analysis of protein-DNA stoichiometry by size-exclusion chromatography

2.7.6.1 Production of annealed double stranded DNA probes

Single stranded complementary oligonucleotides containing the identified MntR and Fur binding sequences in the *mntS* and *iroB* promoters (plus flanking nucleotides) were designed (1 and 2 to give *mntS*Pro-un, plus 5 and 6 to give *iroB*Pro-un respectively, **Table 2.1**,). The oligonucleotides were dissolved in water to a final concentration of 100 μM and their concentration was confirmed from the absorbance at 260 nm using the theoretical extinction coefficient based on the nucleotide sequence provided by the supplier. Oligonucleotides were mixed in 150 mM NaCl, 10 mM HEPES pH 7.0 to a final concentration of 40 μM for each strand. To anneal the two strands, the mixture was heated to 95 °C for 10 min, then allowed to slowly cool to room temperature. Successful annealing of *mntS*Pro-un and *iroB*Pro-un was confirmed by native PAGE (12% w/v gel, Tris-borate-EDTA buffer system), staining the DNA with ethidium bromide.

2.7.6.2 Analysis of protein-DNA stoichiometry by size-exclusion chromatography

Annealed oligonucleotides (10 μM) were incubated with various concentrations of sensor (0–40 μM monomer for MntR, 0−140 μM monomer for Fur) in buffer F (Chelex-treated 60 mM NaCl, 240 mM KCl, 10 mM HEPES pH 7.0) supplemented with 200 μM $MnCl_2$ for MntR and 500 μM $MnCl_2$ and 0.5 mM TCEP for Fur. An aliquot of *mntS*Pro-un with MntR was resolved on a Superdex 75 10/300 GL column, while *iroB*Pro-un with Fur was resolved on a Superdex 200 10/300 GL column (both GE Healthcare). Columns were equilibrated in the above buffers. A sample of each sensor (200 μM, and after incubation in the metal-containing buffers described above) was resolved on the respective columns as a comparison. DNA elution was monitored by absorbance at 260 nm. Fractions (0.5 ml) were collected and analysed for protein content by Bradford assay calibrated with known concentrations of MntR and Fur.

2.7.7 Analysis of protein-DNA interaction by fluorescence anisotropy

2.7.7.1 Production of fluorescently labelled annealed double stranded DNA probes

The single stranded oligonucleotides described in section 2.7.6.1 plus *mntS*Pro-short, *furbox* and *mntS*Pro-swap (3 and 4, 7 and 8, 9 and 10 in **Table 2.1**, respectively) were purchased from Sigma Aldrich with the 5′ end of the forward strand labelled with the fluorophore hexachlorofluorescein (HEX). The oligonucleotides were annealed as described in section 2.7.6.1 (the concentration of each strand in the annealing reaction was lowered to 10 μM).

2.7.7.2 *Fluorescence anisotropy experiments*

Experiments were performed in gas-tight quartz cuvettes in buffer F with the inclusion of 200 µM $MnCl_2$ for Mn(II)-MntR, 500 µM $MnCl_2$ for Mn(II)-Fur, 5–50 µM $(NH_4)_2Fe(SO_4)_2$ for Fe(II)-Fur and 5 mM EDTA for apo-MntR and apo-Fur. Protein samples were prepared in buffer D, with 2.2 molar equivalents $MnCl_2$ for Mn(II)-MntR and Mn(II)-Fur, 2.2 molar equivalents of $(NH_4)_2Fe(SO_4)_2$ for Fe(II)-Fur and 5 mM EDTA for apo-MntR and apo-Fur. Protein samples were incubated at room temperature in the metal- or chelant-containing buffer for at least 15 min prior to the start of the experiment. Labelled DNA was titrated with protein measuring the change in anisotropy using a modified Cary Eclipse Fluorescence Spectrophotometer (Agilent Technologies) fitted with polarising filters. Fluorescence settings: excitation wavelength = 530 nm; emission wavelength = 570 nm; T = 25 °C (Osman et al, 2015). After each protein addition the samples were incubated at 25 °C for at least 5 min before measurement. 10 nM (plus 2 nM for MntR) DNA was used in experiments to determine the DNA-affinity. 1 µM DNA was used in experiments to determine protein-DNA stoichiometry. Change in fluorescence anisotropy (Δr_{obs}) was calculated by subtracting the fluorescence anisotropy value measured for the DNA alone at the beginning of the experiment from the r_{obs} values determined during the titration. Data for Fur binding to *furbox* were fit using Dynafit. The script used to fit the experimental data is reported in **Appendix B**. Data for MntR binding to *mntS*Pro and *mntS*Pro-swap were fit to a second-degree polynomial regression using Microsoft Excel 2016. DNA affinities were calculated from the intersection of the regression line with half the change in anisotropy associated with one MntR dimer binding to *mntS*Pro ($\Delta r_{obs} \approx 1.3 \times 10^{-2}$). Mean coupling free energies values (ΔG_c) and standard deviations were calculated with the equation described in section 5.1.1.1 by pair-wise permutations of the DNA-affinity constants (Osman et al, 2015).

2.8 Bioinformatics

Multiple sequence alignments were generated using the web-based tool Clustal Omega (https://www.ebi.ac.uk/Tools/msa/clustalo/). Protein similarity and identity percentages were calculated using EMBOSS Needle (https://www.ebi.ac.uk/Tools/psa/emboss_needle/). The ProtParam tool (https://web.expasy.org/protparam/) was used to predict protein properties based on amino acid sequence. Bioinformatic searches of sensor DNA binding sites were performed using the manually curated RegPrecise database (https://regprecise.lbl.gov/RegPrecise/) (note: as of October 2019 the RegPrecise website is unavailable). Sensor-recognition DNA sequences were aligned using Clustal Omega, and the consensus sequence logos were generated using WebLogo (https://weblogo.berkeley.edu/logo.cgi).

2.9 Mathematical calculations

Sensor responses were calculated using the equations derived in 5.2, using Microsoft Excel 2016. The buffered metal concentrations corresponding to a particular fractional DNA occupancy were calculated using MATLAB 2018. The electronic spreadsheet and the scripts are available in (Osman et al, 2019).

2.10 Analysis of gene expression in *Salmonella* cells

Overnight cultures of *Salmonella* in LB medium were diluted in fresh medium (initial $OD_{600\ nm}$ = 0.025). Cells were cultured to mid-log phase ($OD_{600\ nm} \approx 0.3$, 2−3 h) before addition of either 400 μM $MnCl_2$, 2 μM $FeSO_4$, 1 μM $CoCl_2$, 100 μM $NiSO_4$, 50 μM $CuSO_4$ or 100 μM $ZnSO_4$. Cells were exposed in the same growth conditions for 10 min before harvesting samples for RNA extraction. For calibration of Zur and ZntR responses, cells in mid-log phase were exposed to either 1 mM $ZnSO_4$ or 50 μM TPEN and cultured for a further 1 h before collection of samples for RNA extraction and enumeration on LB agar following dilution in phosphate-buffered saline. For control experiments, sterile ultrapure water was added instead of metal or chelant.

Salmonella samples (1.2 ml) for RNA extraction were treated with RNAprotect Cell Reagent (Qiagen) for immediate stabilisation of RNA and stored at −80 °C. RNA was extracted using the RNeasy Protect Bacteria Mini Kit (Qiagen) as per manufacturer's instructions. Recovered RNA was quantified by absorbance at 260 nm using a Nanodrop, and 5.5 μg was treated with DNase I (Fermentas; 1 U per 44 ng RNA). Complementary DNA was generated using 1 μg of RNA per reverse transcription reaction (50 μl; ImProm-II™ Reverse Transcription System, Promega). Negative controls without reverse transcriptase were generated in parallel. Transcript abundance was assessed with primers 11 and 12 (*mntS*), 13 and 14 (*iroB*), 15 and 16 (*rcnA*), 17 and 18 (*copA*), 19 and 20 (*zntA*), 21 and 22 (*znuA*), and 23 and 24 (*rpoD*) (**Table 2.1**); each pair designed to amplify a 100−200 bp fragment (Osman et al, 2019). qPCR analyses were conducted using 5 ng of cDNA (assuming 100% reverse transcription efficiency) as template, the appropriate primer pair (0.4 μM each primer) and PowerUp SYBR Green Master Mix (ThermoFisher Scientific) according to manufacturer's instructions. Measurements were collected using a Rotor-Gene Q 2plex (Qiagen) analysing three technical replicates per reaction. PCR conditions: 50 °C for 2 min; 95 °C for 2 min; 45 cycles of 95 °C for 20 sec, 55 °C for 20 sec, 72 °C for 60 sec. Melting curve analysis was performed at the end of the reaction to ensure the specificity of each primer pair. The threshold cycle (C_T) for each sample was calculated with LinReg after correcting for amplification efficiency (Ruijter et al, 2009). The fold change in transcript abundance was calculated relative to control conditions using the $2^{-\Delta\Delta CT}$ method (Livak & Schmittgen, 2001), with *rpoD* as reference gene.

Chapter 3.

Characterisation of the manganese sensor MntR from *Salmonella*

3.1 Bioinformatic analysis of MntR

Salmonella MntR belongs to the DtxR family of metalloregulators. Members of this family predominantly sense Mn(II) or Fe(II) (or both metals) *in vivo* (section 1.5.2). Many DtxR-like regulators have been biochemically characterised *in vitro* (Bates et al, 2005; Chou et al, 2004; Glasfeld et al, 2003; Hill et al, 1998; Lieser et al, 2003; Lisher et al, 2013; Pandey et al, 2015; Posey et al, 1999; Que & Helmann, 2000; Rolerson et al, 2006; Stoll et al, 2009; Tanaka et al, 2009; White et al, 1998). The amino acid sequence of MntR from *Salmonella* was compared with the sequence of other characterised sensors from the DtxR family, as shown in **Figure 3.1**. *Salmonella* MntR has 93.0% similarity and 89.8% identity with *E. coli* MntR and 37.0% similarity and 22.7% identity with *B. subtilis* MntR (**Table 8.1**). The structure of many DtxR-family members has been solved, including *B. subtilis* and *E. coli* MntR (see asterisk in **Figure 3.1**). DtxR-like proteins are dimers with two to three metal-binding sites per subunit. Most proteins fold in three domains: a DNA-binding N-terminal domain, a dimerization domain and a C-terminal FeoA-like domain (section 1.5.2). This third domain is absent in *E. coli* and *B. subtilis* MntR (Glasfeld et al, 2003; Tanaka et al, 2009) and, based on the sequence alignment, also in *Salmonella* MntR and *T. pallidum* TroR. Another striking difference between *B. subtilis* MntR and most of the other DtxR-family members is in the metal coordination environment (section 1.5.2.1). *B. subtilis* MntR binds two Mn(II) per subunit in a binuclear site with Glu99 and Glu102 acting as bridging ligands (McGuire et al, 2013) (section 1.5.2). In contrast, *C. diphtheria* DtxR, *M. tuberculosis* IdeR, *S. mutans* SloR and *S. gordonii* ScaR bind metals in distinct sites. The residues involved in metal-binding in *B. subtilis* MntR are conserved in both *E. coli* and *Salmonella* MntR, suggesting that these proteins might bind Mn(II) in a similar fashion (the structure of *E. coli* MntR was solved only for the apo-form). Compared to the structure of *B. subtilis* MntR, *E. coli* MntR lacks a C-terminal helix and possibly forms a longer helix at the N-terminus. Based on the similarity with its *E. coli* homologue, this feature is also likely be present in *Salmonella* MntR.

Figure 8.1 in **Appendix A** reports the amino acid composition of MntR and the calculation of some theoretical properties of the protein based on its primary sequence. MntR does not contain any Cys residues, meaning that the purification can be performed in the absence of reducing agents and that the *in vitro* characterisation (when not involving oxygen-sensitive metal ions) can be performed without the use of anaerobic conditions.

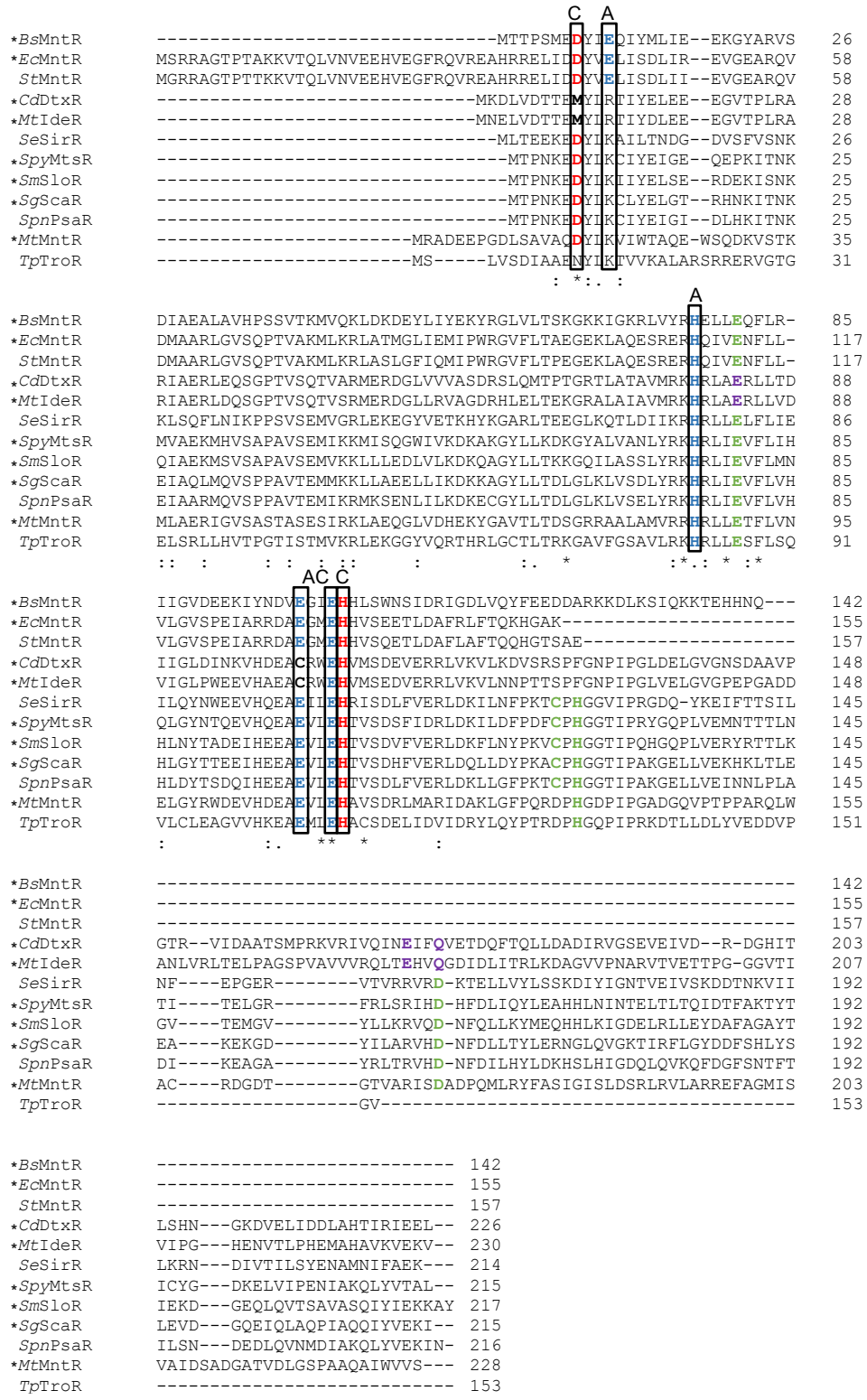

Figure 3.1. Multiple sequence alignment of characterised DtxR/MntR proteins.
Alignment of multiple protein sequences of characterised DtxR-family regulator: DtxR from *C. diphtheria* (*Cd*); MntR from *S.* Typhimurium (*St*), *B. subtilis* (*Bs*), *E. coli* (*Ec*) and *M. tuberculosis* (*Mt*); IdeR from *M. tuberculosis* (*Mt*); SirR from *S. epidermidis* (*Se*); MtsR from *S. pyogenes* (*Spy*); SloR from *S. mutans* (*Sm*); ScaR from *S. gordonii* (*Sg*); PsaR from *S. pneumoniae* (*Spn*); TroR from *T. pallidum* (*Tp*). The sensors marked with an asterisk have been structurally characterised. The residues involved in Mn(II)-binding in the binuclear site in *B. subtilis* are highlighted in blue (A site, plus the bridging ligands E99, E102) and red (C site) and

are all conserved in *S.* Typhimurium and *E. coli*. The other sensors bind metals in distinct sites. Some metal-binding residues corresponds to the ones in the A and C site of *B. subtilis* MntR, while others are highlighted in purple (*Cd*DtxR 'ancillary site') and green (*Sg*Scar, *Spn*PsaR, *Sm*SloR 'secondary site'). The Fe(II)-sensing *Cd*DtxR and *Mt*IdeR have S-donor ligands substituting two carboxylate ligands from Glu residues in site A and C. Similarity and identity scores of the amino acid sequence of *S.* Typhimurium MntR compared with the ones of the other DtxR-MntR sensors are reported in **Table 8.1**.

3.2 Expression and purification of recombinant MntR

Salmonella MntR was expressed in *E. coli* as recombinant protein without the use of any affinity tag. The purification protocol, therefore, relied on the intrinsic properties of the protein (metal-binding, DNA-binding and size). Exploiting the presence of a putative metal-binding site (**Figure 3.1**), the first step of the purification protocol involved a nickel affinity column which was loaded with the crude cell lysate. MntR bound to the column and was eluted in a single step using a high concentration of imidazole (**Figure 3.2a**). After confirming the presence of a high concentration of protein with a molecular weight consistent with MntR (theoretical molecular weight ≈ 17.7 kDa as monomer) in the fraction collected, this was further purified by size-exclusion chromatography on a HiLoad 26/600 Superdex 75 pg (**Figure 3.2b**). MntR eluted over a broad range of fractions, which appeared to comprise two distinct peaks. The first peak was found in the void volume of the size-exclusion column (fraction 23 in **Figure 3.2b**), suggesting the formation of higher order oligomers. The second peak corresponded to fractions consistent with the presence of a dimeric protein. The formation of the higher order oligomeric species is reversible and presumably concentration-dependent, as when fraction 23 was re-injected into the column, fractions containing dimeric MntR were collected (**Figure 8.2** in the **Appendix**). In the final step of the purification protocol, fractions containing dimeric MntR from **Figure 3.2b** were further purified and concentrated on a small heparin affinity column (**Figure 3.2c**). MntR was eluted with a high concentration of NaCl and SDS-PAGE confirmed >95% purity.

In order to use the protein for *in vitro* metal-binding studies, the EDTA present in the purification buffers needs to be removed. Purified MntR was therefore re-loaded on the heparin affinity column and buffer exchanged to a Chelex-treated buffer with a high concentration of KCl plus NaCl (1 M combined concentration). An equivalent procedure is usually performed on the Cys-containing sensors to remove EDTA, reducing agents and oxygen and to move the purified protein into the anaerobic glovebox (for example Fur, section 4.2.2). The concentration of residual contaminating metals was determined by ICP-MS. The protein was used for the *in vitro* characterisation only if >95% metal-free. **Figure 3.3a** shows the SDS-PAGE separation of purified apo-MntR. The protein concentration was determined from the absorbance at 280 nm using the experimentally determined extinction coefficient $\varepsilon_{280\ nm} = 7{,}940\ M^{-1}\ cm^{-1}$ (**Figure 3.3b**). The extinction coefficient was obtained from quantitative amino acid analysis (Alta Bioscience) performed on purified apo-MntR.

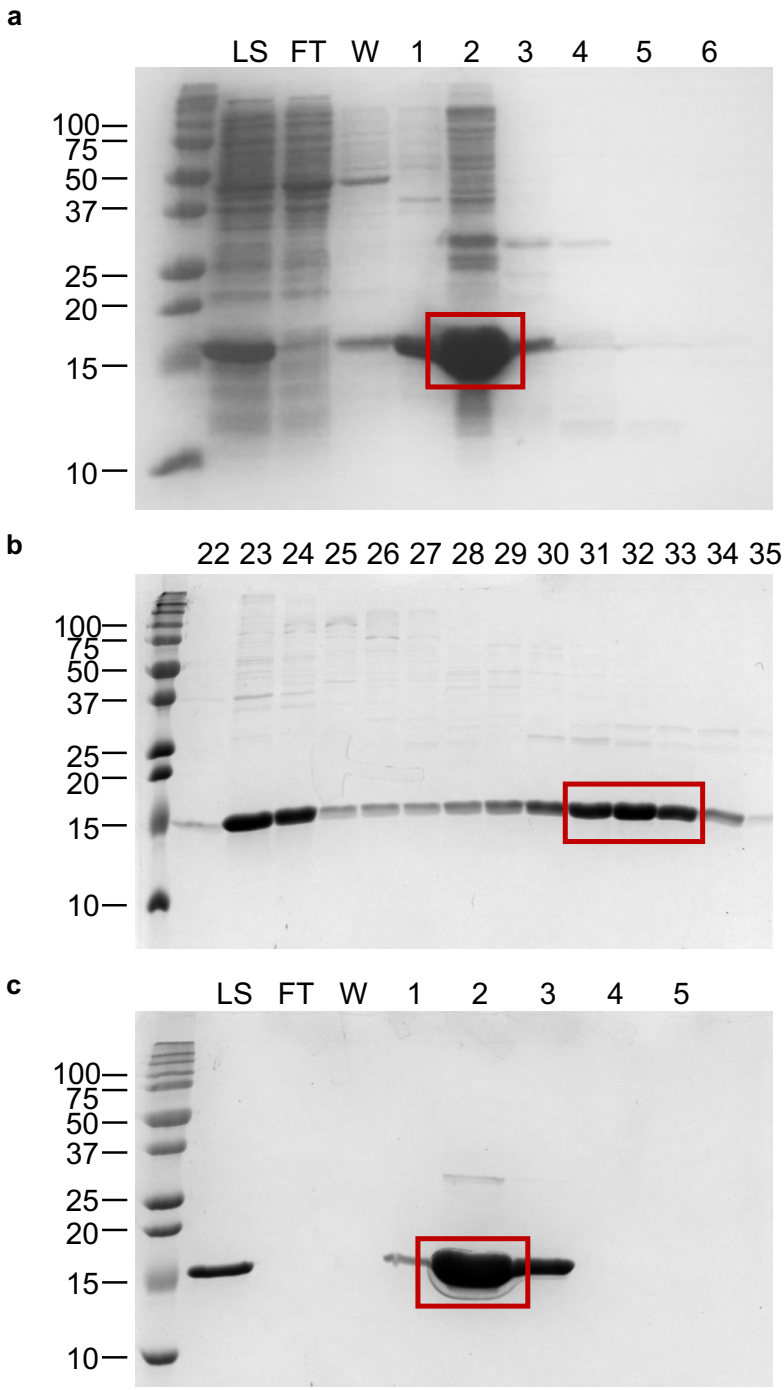

Figure 3.2. Purification of recombinant MntR.
a, SDS-PAGE of fractions eluted from a nickel affinity column. LS: loaded lysate of *E. coli* cells overexpressing MntR (1:5 dilution); FT: flowthrough with unbound species (1:5 dilution); W: wash (5 column volumes) with buffer A; 1–6: collected fractions eluted in buffer A with 10 mM (fraction 1, lag fraction 4.5 ml), 100 mM (fraction 2, 5.5 ml) and 300 mM (fractions 3–6, 5ml) imidazole. Fraction 2 (highlighted) routinely contained the highest concentration of MntR and was used for subsequent purification. **b**, SDS-PAGE of fractions (5 ml) 22–35 eluted from a HiLoad 26/600 Superdex 75 pg column loaded with 5 ml of fraction 2 from **a**. **c**, SDS-PAGE of fractions eluted from a Heparin affinity column loaded with pooled Fraction 31–33 from **b**. LS: loaded sample; FT: flowthrough W: wash (10 column volumes) with buffer C; 1–5: collected fractions eluted in buffer C with 300 mM (fraction 1, lag fraction 0.9 ml), 1000 mM NaCl (fraction 2, 1.5 ml, and fractions 3–5, 1 ml).

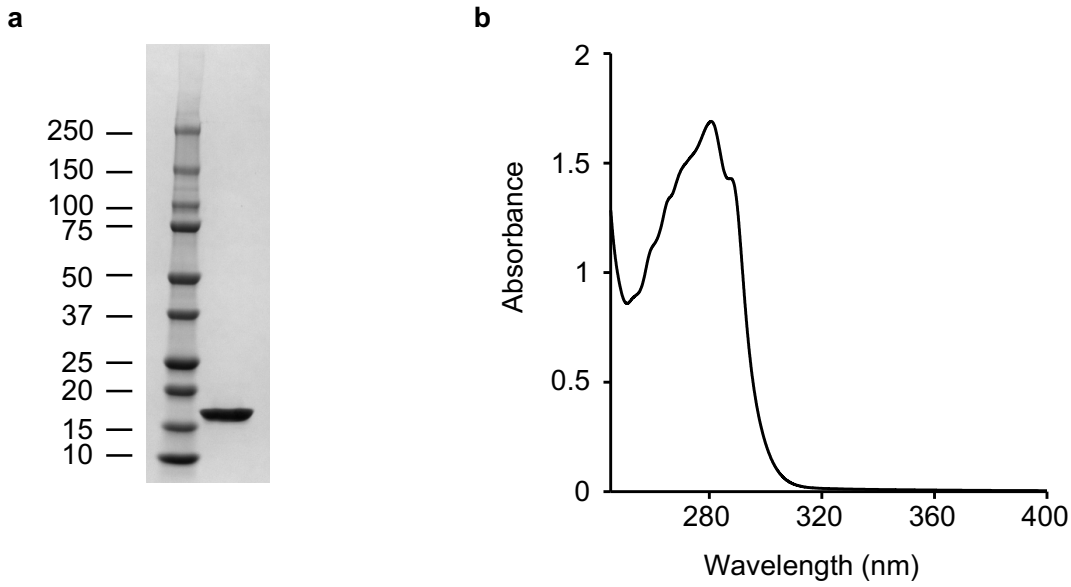

Figure 3.3. Analysis of purified MntR.
a, SDS-page of purified MntR using a 4−20% w/v gradient gel with size marker indications. **b**, UV-visible spectrum of purified MntR; the protein was quantified using the experimental extinction coefficient ε_{280nm} = 7,940 M^{-1} cm^{-1}.

3.3 Analysis of the metal-binding properties of MntR

3.3.1 Characterisation of homologous proteins

Although its structure has been characterised, the highly similar *E. coli* MntR (*Ec*MntR) has not been biochemically characterised with respect to metal- and DNA-binding properties. In contrast, *B. subtilis* MntR (*Bs*MntR) is one of the most extensively studied metal sensors. *Bs*MntR binds a total two Mn(II) ions per monomer (four per dimer) (Glasfeld et al, 2003) and, as anticipated from the sequence alignment in **Figure 3.1**, it is hypothesised that *Salmonella* MntR will bind Mn(II) with similar stoichiometry and affinity. Several different measures for *Bs*MntR $K_{Mn(II)}$ are reported in the literature, obtained using different experimental techniques and conditions (**Table 3.1**). In particular, different buffer systems and pH levels have been used and these parameters can greatly affect the determined metal-affinity (Xiao & Wedd, 2010). The metal- and DNA-binding experiments in this thesis will all be performed in HEPES at pH 7.0 to be consistent with a set of values determined for the *Salmonella* sensors (see **Table 5.2**). Even though they span two orders of magnitude, the Mn(II)-affinities determined for *Bs*MntR (**Table 3.1**) suggest a fairly weak metal-affinity, at least compared to the affinities determined for metalloregulators sensing metals such as Zn(II), Cu(I), Ni(II) and Co(II) (Osman et al, 2017; Osman et al, 2015; Osman et al, 2016).

3.3.2 Determination of Mn(II)-binding stoichiometry

A strategy commonly used to determine the metal-binding stoichiometry is to look at the co-migration of the protein with metal on a size-exclusion column. MntR was incubated with Mn(II) and the mixture was resolved on a Sephadex G25 matrix column (**Figure 3.4**). The weak affinities determined for *Bs*MntR (**Table 3.1**) suggest that MntR will lose any bound metal during the elution if the experimental buffer is not supplemented with Mn(II). Therefore, the buffer used to equilibrate the column and elute the protein contained 100 μM Mn(II) to retain metal co-migration with MntR. The fractions collected were analysed for Mn(II) content by ICP-MS and for protein content by absorbance at 280 nm (the presence of bound Mn(II) is likely to have a negligible effect of the UV-visible spectra of the protein, *vide infra*). MntR co-migrated with approximately two equivalents of Mn(II), suggesting a stoichiometry of four Mn(II) ions per dimer as observed for *Bs*MntR.

Table 3.1. Mn(II)-affinities determined for *Bs*MntR.

$K_{Mn(II)}$ ($\times 10^{-6}$ M)	Technique	Conditions	Reference
≥ 50 (too weak)	Competition with mag-fura-2	10 mM HEPES pH 7.2, 100 mM KCl	(Golynskiy et al, 2006)
92 ±14	ANS fluorescence	20 mM HEPES pH 7.2, 200 mM NaCl, 5% glycerol	
~160	EPR	20 mM HEPES pH 7.2, 300 mM NaCl, 5% glycerol	
0.2-2 (first)	ITC	25 mM Tris-HCl pH 8.0, 500 mM NaCl, 10% glycerol.	(Kliegman et al, 2006)
5-13 (second)			
6.3	Competition with mag-fura-2	20 mM Tris pH 8.0, 100 mM NaCl, 0.1 mM TCEP	(Ma et al, 2012)

Mn(II)-affinities (expressed as dissociation constants) measured for *Bs*MntR. The metal-binding experiments were performed under different conditions and using different experimental approaches. This explains the values spanning two orders of magnitude.

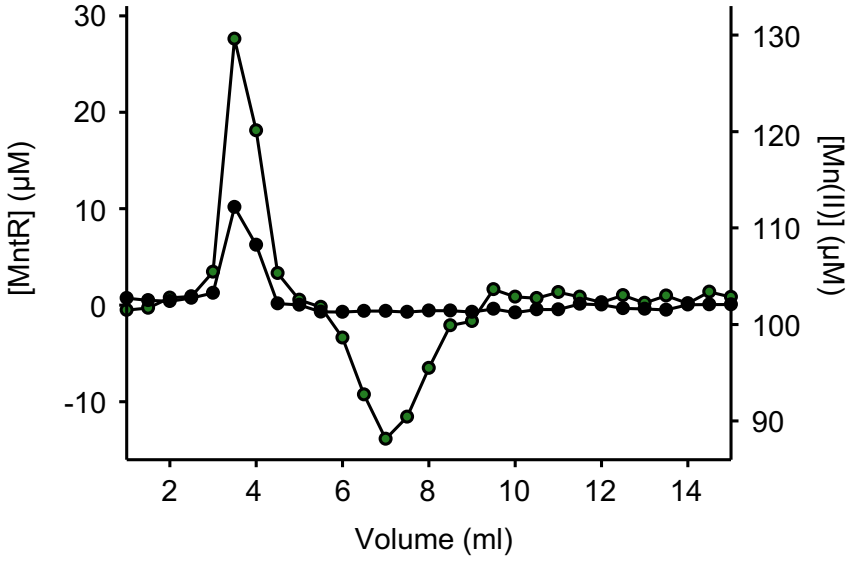

Figure 3.4. MntR co-migrates with two equivalents of Mn(II) on a size-exclusion column. Gel-filtration chromatography on Sephadex G25 of MntR (20 μM) after incubation with 100 μM Mn(II). The elution buffer contained Mn(II) to retain the co-migration of Mn(II) with MntR if the binding constant is sufficiently tight. Fractions (0.5 ml) were analysed for protein content (black symbols) by absorbance at 280 nm and for Mn(II) content (green symbols) by ICP-MS. Figure and caption are adapted from (Osman et al, 2019).

3.3.3 Determination of Mn(II)-binding affinity

3.3.3.1 Direct titration of the protein with metal

The $K_{Mn(II)}$ values determined for *Bs*MntR suggest that, in principle, the Mn(II)-affinity of *Salmonella* MntR could be determined by direct titration of the protein with metal. The absence of any Cys-thiols in MntR and the spin forbidden d-d transitions of Mn(II) (d^5) complexes predicts weak or non-existent absorption features upon Mn(II)-binding in the UV-visible range. However, MntR possesses fluorescent tyrosine and tryptophan residues which may be exploited to monitor metal binding via fluorescence spectroscopy, provided their environment is altered upon metal-binding. MntR was therefore titrated with Mn(II) monitoring the fluorescence emission (**Figure 3.5**). However, MntR spectra did not show any metal-depending feature which could reliably be employed to monitor protein saturation with metal, suggesting that the local environment of the fluorescent groups did not change upon binding of Mn(II).

3.3.3.2 Determination of mag-fura-2 Mn(II)-affinity

In the absence of protein-specific UV-visible and fluorescence spectral features changing upon metal-binding, the determination of metal-binding affinities needs to rely on spectrally active probes competing with the protein for binding the metal. Numerous probes have been developed and are available as commercial products to detect metal ions *in vitro* and *in vivo*. Often, a probe designed to detect a particular ion has been characterised and adapted to be used also for other metals. The fluorescent probe mag-fura-2 (also known as Furaptra) was originally designed as an *in vivo* probe to detect Mg(II) (Raju et al, 1989). However, mag-fura-2 has been used *in vitro* in metal-binding experiments involving Ca(II), Mn(II), Fe(II), Co(II), Ni(II), Zn(II), Cd(II) (Golynskiy et al, 2006; Raju et al, 1989; Rodrigues et al, 2015).

To determine the affinity of mag-fura-2 for Mn(II) under the conditions used in the competition assay with the protein, the probe was titrated with increasing amounts of Mn(II). Fluorescence excitation spectra were recorded after each addition to monitor probe saturation with metal (**Figure 3.6a**). Upon metal-binding, the excitation band at ~368 nm decreased in intensity, as anticipated from previous studies (Golynskiy et al, 2006). Metal-dependent fluorescence quenching at 380 nm was fit to a model describing binding of one metal ion per molecule of mag-fura-2 (**Figure 3.6b**) using Dynafit, a software package for advanced statistical analysis of biochemical, biophysical, and biological data (Kuzmic, 1996). The Dynafit script used to fit the data is reported in **Appendix B**. The fitted curve departs from the simulated curves that describe $K_{Mn(II)}$ 10-times weaker and 10-times tighter than the value obtained from the fit (**Figure 3.6b**), confirming that the experiment was performed within the limits of the assay. Mag-fura-2 $K_{Mn(II)}$, expressed as dissociation constant and as mean (±s.d.), was determined to be 6.1 (±0.4) × 10^{-6} M (n = 4 independent experiments). This value is in accordance with previous determinations from

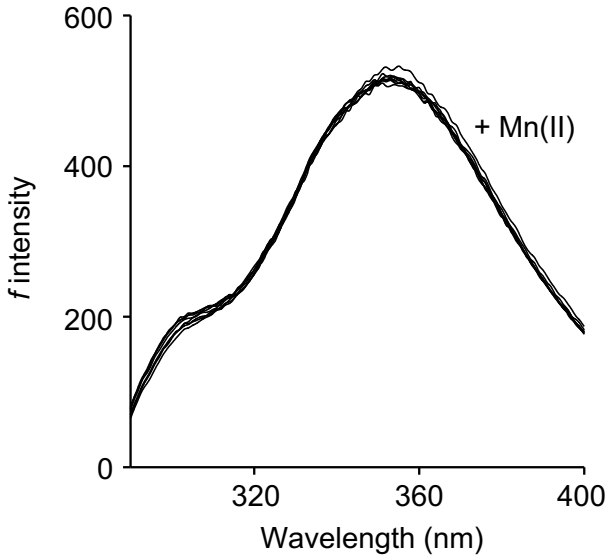

Figure 3.5. Direct titration of MntR with Mn(II) does not show significant changes in the fluorescence spectra.
Fluorescence emission spectra of MntR (17.4 μM) upon titration with Mn(II). Excitation wavelength = 280 nm, T = 20 °C.

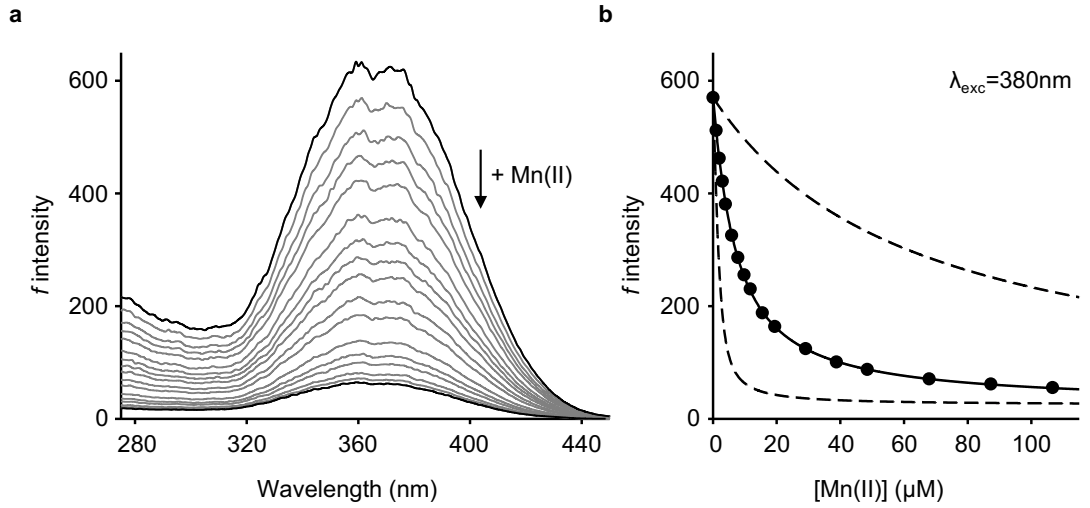

Figure 3.6. The fluorescent probe mag-fura-2 binds Mn(II) with micromolar affinity.
a, Representative (n = 4) fluorescence excitation spectra of mag-fura-2 (2.05 μM) when the probe is titrated with Mn(II). Fluorescence emission was monitored at 505 nm, T = 20 °C. **b**, Binding isotherm depicting the feature at 380 nm in **a**. The solid line represents the fit to a model describing Mn(II) binding to mag-fura-2 with 1:1 stoichiometry. The fit departs from the simulated curves with a $K_{Mn(II)}$ ten times tighter or weaker (dashed lines). Figure and caption are adapted from (Osman et al, 2019).

the literature: $K_{Mn(II)} = 0.97 \times 10^{-6}$ M (from (Golynskiy et al, 2006), determined by competition of Ca(II) and Mn(II) for the probe in 10 mM HEPES, pH 7.2) and $K_{Mn(II)} = 3.3 \times 10^{-6}$ M (from (Ma et al, 2012), determined by direct metal titration in 20 mM Tris pH 8.0).

3.3.3.3 Determination of MntR Mn(II)-affinity

Mag-fura-2 titration with Mn(II) was repeated in the presence of MntR (**Figure 3.7**). Preliminary competition experiments showed protein precipitation occurring at high concentration of metal, therefore 5% v/v glycerol was included in the experimental buffer to facilitate the retention of soluble MntR. By comparing mag-fura-2 quenching in **Figure 3.6** and **Figure 3.7** (in both experiments the concentration of mag-fura-2 was the same, ~2 μM), it is evident how in the latter a higher concentration of Mn(II) is needed to fully saturate the probe. This suggests that MntR is competing for the metal and, during the titration, Mn(II) is partitioning between mag-fura-2 and the spectrally silent protein. The fluorescence feature at 380 nm was fit to a model describing mag-fura-2 binding one Mn(II) ion (with the affinity determined in 3.3.3.2) and MntR binding four Mn(II) ions per dimer (two per monomer) as a single binding event. The Dynafit script used to fit the data is reported in **Appendix B**. The fit departed from the simulated curves with 10-times tighter and weaker $K_{Mn(II)}$. The affinity of MntR for Mn(II), $K_{Mn(II)}$, was determined to be 1.3 (±0.4) × 10^{-5} M expressed as dissociation constant (mean (±s.d.), n = 4 independent experiments). Compared to the previously determined affinities of the other *Salmonella* sensors for their cognate metals (see **Table 5.2**), MntR affinity for Mn(II) is the weakest of the set. This is consistent with the position of Mn(II) at the low end of the Irving-Williams series.

Based on *in vitro* studies on *Bs*MntR, four Mn(II) ions per MntR dimer are required for allosteric activation of the sensor (McGuire et al, 2013). Therefore, the metal-affinity determined here as an apparent average affinity for the four sites represents the affinity for the complement of allosteric sites. It is however noted that a *Bs*MntR mutant able to bind Mn(II) only at site A of each subunit (**Figure 3.1**) partially retained the ability to regulate some promoters (Golynskiy et al, 2005).

3.4 Analysis of the DNA-binding properties of MntR

3.4.1 MntR regulon in *Salmonella* by bioinformatic analysis

The bioinformatics analysis of the MntR regulon was performed in collaboration with Deenah Osman. Putative genes belonging to the MntR regulon in *Salmonella* were identified using the open access and manually curated Regprecise database (Novichkov et al, 2013). An MntR binding site upstream of these genes was identified by comparison with the MntR-binding DNA sequence from *E. coli* (Patzer & Hantke, 2001). Additionally, a MntR-regulated gene encoding a small protein involved in Mn(II)-homeostasis recently identified in *E. coli*, *mntS*, was identified

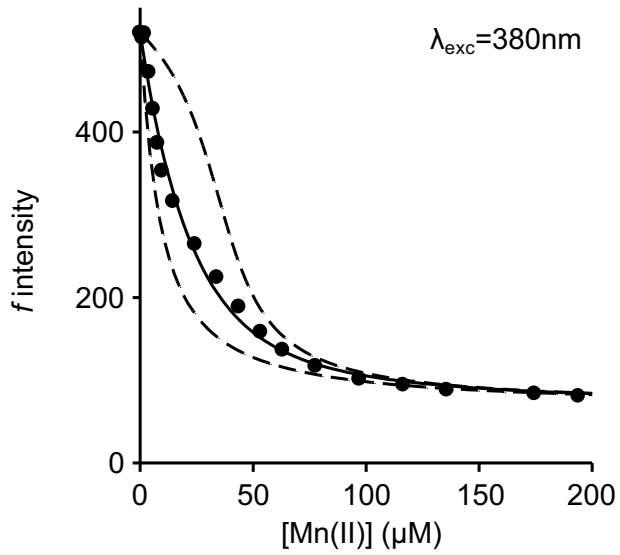

Figure 3.7. MntR competes with mag-fura-2 for Mn(II).
Representative (n = 4) mag-fura-2 (1.95 μM) fluorescence quenching when titrated with Mn(II) in the presence of MntR (18.7 μM). Fluorescence emission was monitored at 505 nm, T = 20 °C. The metal partitions between the probe and the protein in this assay. The solid line represents the fit to a model describing a single apparent Mn(II) affinity for the complement of allosteric effective sites (four metal-binding sites per MntR dimer). The fit departs from the simulated curves with a $K_{Mn(II)}$ for MntR ten times tighter or weaker (dashed lines). Figure and caption are adapted from (Osman et al, 2019).

also in *Salmonella* (Martin et al, 2015; Waters et al, 2011). An MntR-binding sequence was found in the promoter region of *Salmonella mntS*. The regulon of MntR in *Salmonella* comprises five targets: the *mntR* gene itself, predicted to be co-transcribed with *ybiR* encoding a putative anion transporter, *sitABCDE* and *mntH*, which encode two manganese uptake systems, *mntP*, which has been recently identified in *E. coli* as a Mn(II)-efflux pump, and *mntS* (Kehres et al, 2002b; Kehres et al, 2000; Waters et al, 2011). MntR is predicted to repress these genes in the presence of Mn(II), with the exception of *mntP* whose expression is enhanced in the presence of the metal. **Figure 3.8a** shows the multiple sequence alignment of the promoter regions of the target genes, with the MntR-binding sites highlighted. The sequences of the MntR binding sites in the promoters of the *Salmonella* genes were used to identify the consensus sequence (**Figure 3.8b**). The binding sequence in the promoter of *mntP* is further upstream of the starting codon of MntP (>250 bp) compared to the other targets (Waters et al, 2011). A similar dual role in regulation was observed in a genome-wide analysis of the regulon of the MntR homologue SloR from *S. mutans* (O'Rourke et al, 2010). The genes downregulated by SloR in the presence of Mn(II) have a SloR recognition element (SRE) within 50 bp from the translational start site. By contrast, the upregulated genes have a SRE 100 to 300 bp upstream of the ATG initiation codon. Also *B. subtilis* MntR has been reported to act both as a co-repressor and as an activator on different genes (Huang et al, 2017).

The regulation of these target genes is complex, as the MntR regulon overlaps with other regulatory networks. Iron-sensing Fur has a binding site in the promoter of *mntH*, *sitABC* and *mntP*, the oxidative stress regulator OxyR controls the expression of *mntH* and a Mn(II)-riboswitch is present upstream of *mntP* (Ikeda et al, 2005; Kehres et al, 2002a; Waters et al, 2011). This complicates the interpretation of gene expression experiments in *Salmonella* to study a MntR-specific response. The only genes whose expression is anticipated to be regulated exclusively by MntR are the divergently transcribed *mntR* gene itself and *mntS* (**Figure 3.9**). Therefore, *mntS* was chosen as a target to be employed for both *in vivo* and *in vitro* studies. There are two MntR binding sites in the promoter of *mntS*. The oligonucleotides for the *in vitro* studies were designed to include only one of the two binding sites (the closest to MntS open reading frame).

3.4.2 Analysis of MntR-DNA stoichiometry by size-exclusion chromatography

Deenah Osman confirmed that MntR regulates *mntS* in *Salmonella* with *in vivo* studies. The expression of *mntS* was repressed in *Salmonella* cells grown in the presence of a non-lethal concentration of Mn(II), compared to bacterial growth in media with no metal supplementation (Osman et al, 2019).

a

```
   mntH  CCATTGAAATGCACTTGATAATCATTATCAATAAACATAGCATGAAACATAGCAAAGGCTATGTTTTTGAG -7
 sitABCD TCGCAAATAAGAATTATTTTCATTTATCCATACCTTGTGCTATATAACATAGCAAAGGCTATATTCGATGA -30
   mntP  AAGATATAGCCTCAACTATGTTTTTCGAATTTTATTTCGAATCATAATATAGCTAAGGCTATATTTTCTAT -281
   mntR  CGTGAGGGATGTCTGCATTACATACAGATATAGCACAGGCTATGTTTTATAGCTATTGCTAAAACGTTAAT -52
   mntS  GAGTTGTCTGGGCACAAAAAATTAACGTTTTAGCAATAGCTATAAAACATAGCCTGTGCTATATCTGTATG -82
```

b

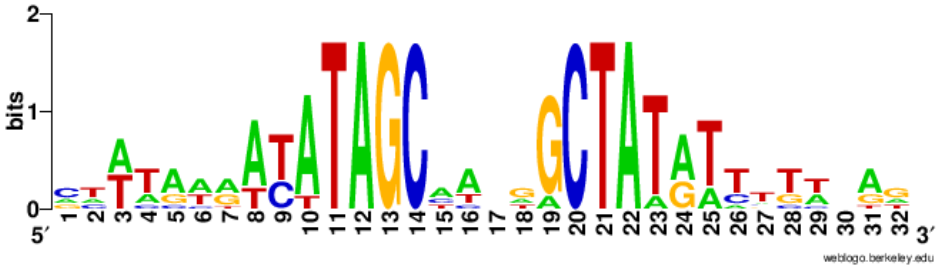

Figure 3.8. The MntR regulon in *Salmonella*.
a, Architecture of the promoter regions of the genes regulated by MntR in *Salmonella* based on homology with *E. coli*. The nucleotide-binding sites are highlighted in grey (the upstream regions of *mntP*, *mntR* and *mntS* genes contain two MntR binding sites). **b**, *Salmonella* MntR consensus sequence identified from the eight protein-binding sites from **a**.

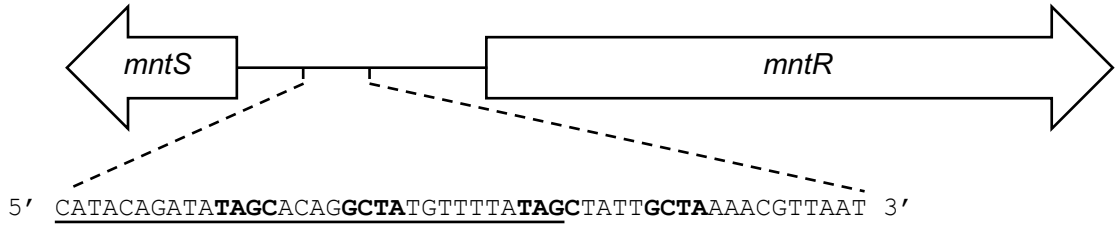

Figure 3.9. The *mntS* and *mntR* promoter.
Schematic to scale representation of the *mntR* and *mntS* promoter architecture. *mntS* is divergently transcribed from *mntR*. Recognised riboswitches or binding sites for other sensors are absent. The MntR nucleotide-binding sites are in bold and the reverse complement of the underlined sequence was used to design the oligonucleotides for the *in vitro* DNA-binding experiments.

In order to study the interaction of MntR and the *mntS* promoter *in vitro*, a preliminary study of the stoichiometry of protein-DNA interaction was performed using size-exclusion chromatography. The 32 bp oligonucleotide *mntS*Pro-un, containing one of the MntR recognition sequences in the *mntS* promoter (**Figure 3.9**), was designed as reported in **Figure 3.10a**. The oligonucleotide was annealed with its reverse complement by heating the mixture of the two strands and slowly cooling the reaction to room temperature. **Figure 3.10b** shows subsequent native PAGE confirming annealing.

It has been shown that one *Bs*MntR dimer binds to a 26 bp oligonucleotide containing its recognition sequence from the *mntH* promoter (Lieser et al, 2003). In order to study the stoichiometry of the interaction between *Salmonella* MntR and *mntS*Pro-un, increasing amounts of the protein were incubated with *mntS*Pro-un before resolving the mixture on a size-exclusion column (**Figure 3.11**). As MntR is a putative co-repressor (i.e. its affinity for DNA is tighter when the sensor is in its metalated form), the buffers used to prepare the protein-DNA samples and to perform the chromatography contained 200 μM Mn(II) to ensure DNA-binding activation. The elution of DNA was monitored by looking at the absorbance at 260 nm. As shown in **Figure 3.11a**, when *mntS*Pro-un was incubated with one equivalent of MntR monomer, the DNA eluted in two peaks: one consistent with free DNA and the other (at a lower elution volume) consistent with the formation of the MntR:*mntS*Pro-un complex. The free DNA peak disappeared at a DNA:MntR monomer ratio of 1:2 and the lower volume peak did not shift even when the DNA was incubated with higher concentrations of protein. Moreover, at a DNA:MntR ratio of 1:4, a slight increase in absorbance was observed at an elution volume greater than free *mntS*Pro-un (~14 ml). This is likely due to the elution of free Mn(II)-MntR, as shown from comparison with the chromatogram for Mn(II)-MntR alone (**Figure 3.11b**). These results suggest that the stoichiometry for the interaction of *mntS*Pro-un with MntR is 1:2, or one MntR dimer per DNA molecule.

To follow the elution of the protein in the chromatograms shown in **Figure 3.11a**, the eluate from the column was collected in fractions that were subsequently analysed for protein content by Bradford assay (**Figure 3.12**). At 1:1 DNA:protein ratio, MntR eluted in a single peak. The protein concentration in the peak increased at a 1:2 ratio and remained fairly unchanged when the DNA was incubated with larger amounts of MntR. By contrast, with a higher proportion of protein in the loaded sample, a second peak gradually appeared, at an elution volume consistent with free Mn(II)-MntR (white symbols as a reference). These results are consistent with the stoichiometry suggested from **Figure 3.11a**, as after one MntR dimer has bound to *mntS*Pro-un, free protein starts to accumulate. Is should be noted, however, that these assays employing size-exclusion chromatography might not reveal the formation of additional higher order weak DNA-protein complexes.

a

F 5′CTATAAAACATAGCCTGTGCTATATCTGTATG 3′

b

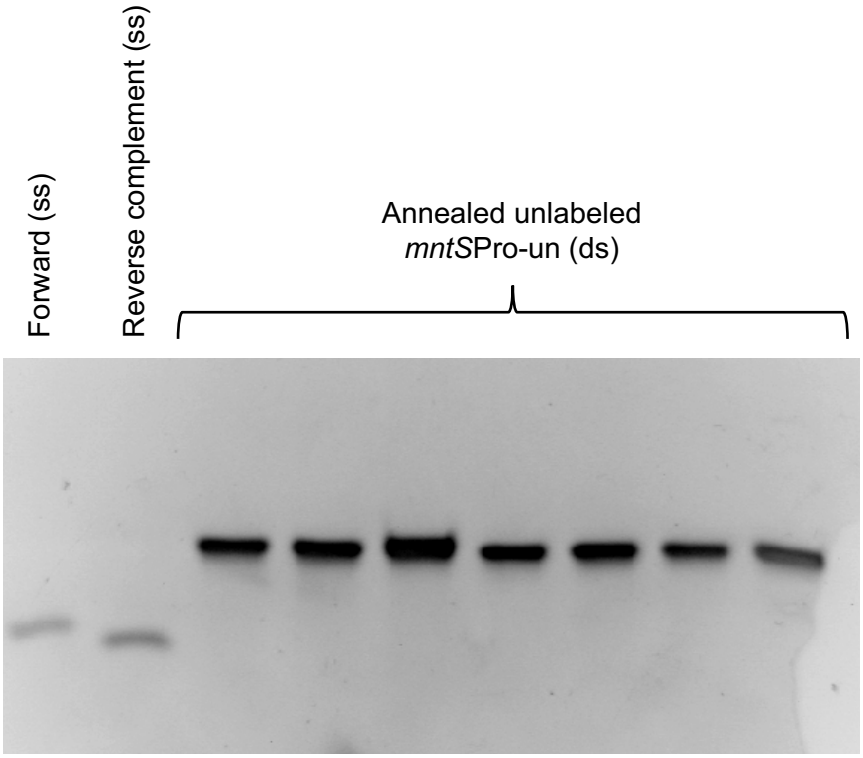

Figure 3.10. Production of the double-stranded oligonucleotide *mntS*Pro-un for size-exclusion experiments.
a, 32 bp oligonucleotide containing the identified MntR recognition site (underlined) and flanking nucleotides in the *mntS* promoter. The shown oligonucleotide was annealed with its reverse complement. **b**, Annealing was confirmed by native PAGE (12% w/v), staining the DNA with with ethidium bromide. The single-stranded (ss) oligonucleotides were run on the same gel as a control to show the different migration from the double-stranded (ds) unlabelled *mntS*Pro-un.

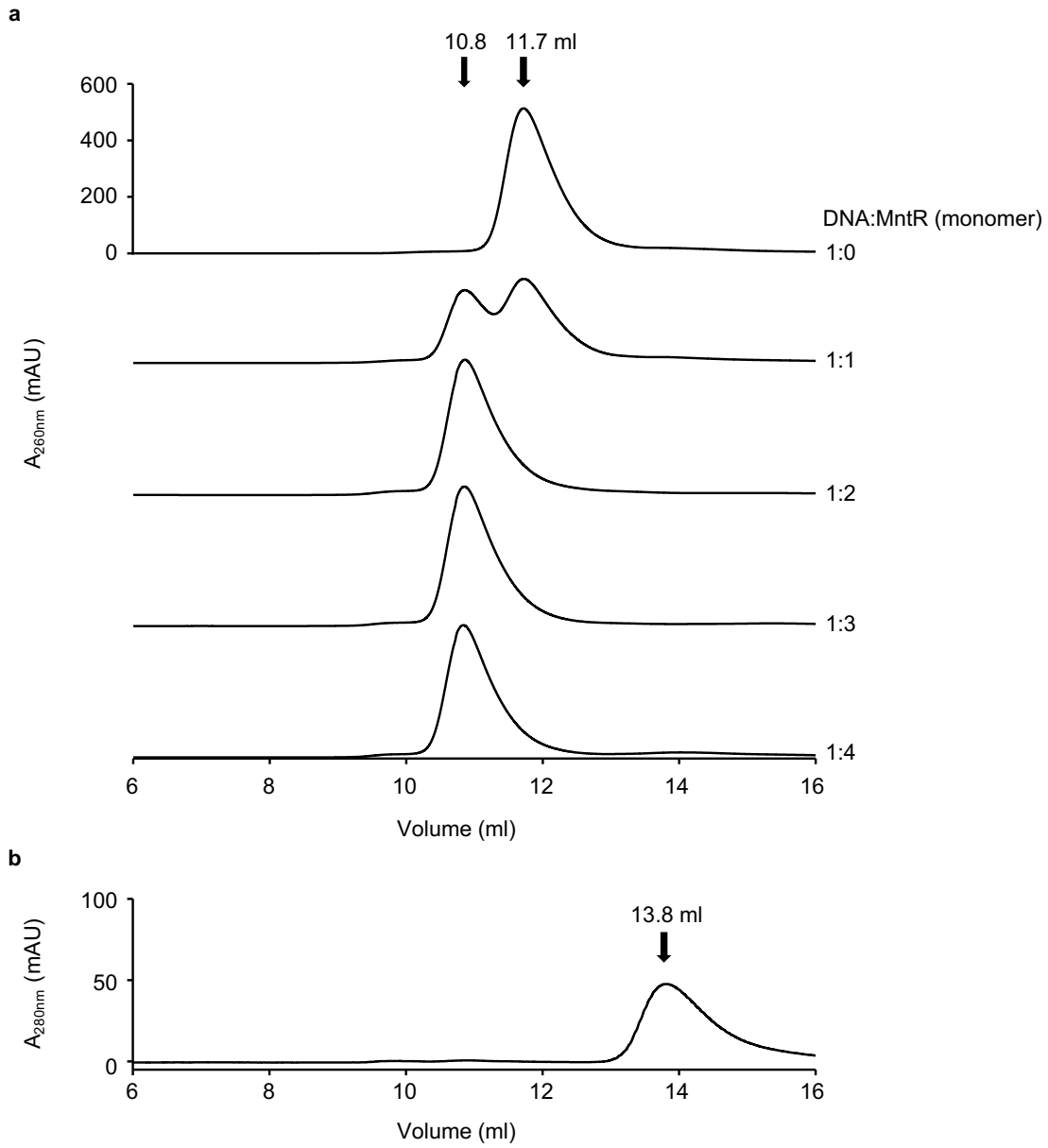

Figure 3.11. Analysis of MntR-DNA stoichiometry by size-exclusion chromatography. **a**, *mntS*Pro (10 μM) was pre-incubated with various concentrations of MntR (0, 10, 20, 30, 40 μM protein monomer) in the presence of 200 μM Mn(II) and the mixture resolved on a Superdex 75 10/300 GL column. The elution profile of the DNA was followed by measuring the absorbance at 260 nm. **b**, MntR (100 μM) was incubated with 200 μM Mn(II) and resolved with the same column. The elution profile was monitored via absorbance at 280 nm.

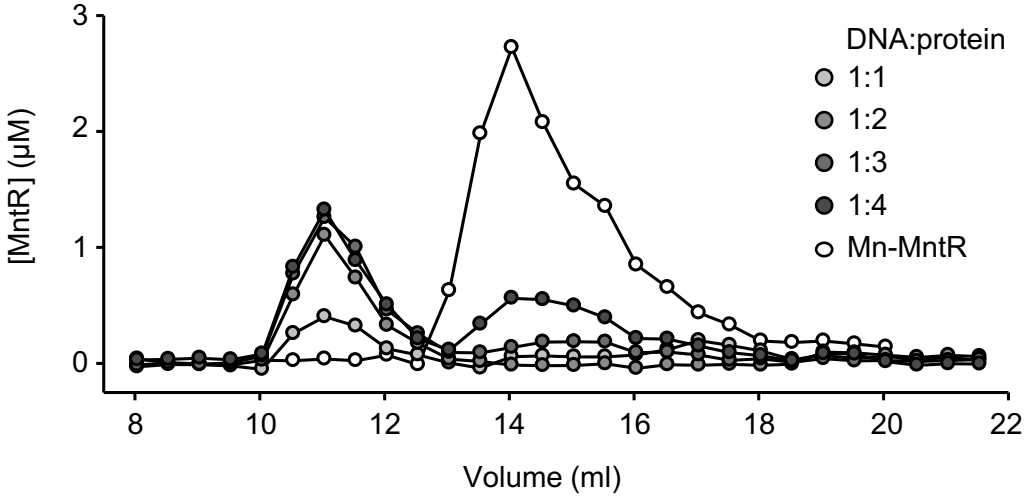

Figure 3.12. Determination of protein concentration following size-exclusion chromatography of Mn(II)-MntR-*mntS*Pro mixtures.
The protein concentration in the fractions (0.5 ml) collected from the size-exclusion experiments (Superdex 75 10/300 GL column) in **Figure 3.11a** (1:1, 1:3, 1:3. 1:4) and **Figure 3.11b** (Mn(II)-MntR) was determined by Bradford assay.

3.4.3 Fluorescence anisotropy principles

Fluorescence anisotropy is a powerful technique to investigate protein-ligand interactions. It has been employed to study the interaction of several metal sensors with DNA fragments containing their recognition sequence, with affinities spanning four to five orders of magnitude (Foster et al, 2014b; Harvie et al, 2006; Lieser et al, 2003; Osman et al, 2017; VanZile et al, 2002). This technique is based on the fact that when many fluorophores are excited with polarised light, also the emitted radiation is polarised (Lakowicz, 2006). The emitted radiation is depolarised by the rotational diffusion of the fluorophore between the absorption of the photon and its emission. The rate of rotational diffusion of a molecule depends on its shape and size. Therefore, the degree of depolarisation of the emitted radiation can be correlated to the size of the fluorophore. In fluorescence anisotropy experiments, following excitation of the fluorophore with vertically polarised light, the intensity of the emitted horizontally and vertically polarised radiation is measured. This allows the calculation of the (dimensionless) anisotropy (r_{obs}) as:

$$r_{obs} = \frac{I_{\parallel} - I_{\perp}}{I_{\parallel} + 2I_{\perp}}$$

where $I_{\parallel}$ and $I_{\perp}$ are the intensities of the emitted light polarised parallelly or perpendicularly, respectively, to the polarised excitation radiation. Typically, the incident light is vertically polarised and fluorescence emission is measured in the vertical (parallel) and horizontal (perpendicular) planes (Lakowicz, 2006).

To monitor sensor binding to DNA via fluorescence anisotropy, fluorescently labelled oligonucleotides are titrated with the sensory protein. The fluorescent tags typically employed have high absorption coefficients and good quantum yield, so that the DNA concentration in the assay can be adjusted down to 10^{-9} M, if needed, to measure tighter K_{DNA}. The free DNA fragments in solution show a low anisotropy (r_0). However, upon sensor-binding, the bigger size of the protein:DNA complex and slower rate of rotation determine an increase in fluorescence anisotropy. Sensor binding to DNA can be followed from change in fluorescence anisotropy ($\Delta r_{obs} = \Delta r_{obs} - r_0$) as a function of the concentration of protein added (Grossoehme & Giedroc, 2012). Fluorescence anisotropy assays can be used to determine the stoichiometry of protein:DNA binding if the concentration of DNA in the assay is sufficiently high to observe stoichiometric binding of the sensor. In the presence of sub-stoichiometric binding, the Δr_{obs} data can be fit to determine the K_{DNA}.

3.4.4 Determination of MntR-DNA stoichiometry by fluorescence anisotropy

3.4.4.1 Fluorescence anisotropy experiments with mntSPro

In order to confirm the stoichiometry of 1:2 DNA:MntR observed in **Figure 3.11**, the fluorescently labelled oligonucleotide *mntS*Pro was prepared (**Figure 3.13**). The DNA sequence

was the same as the nucleotide in **Figure 3.10** used in the size-exclusion chromatography experiment, with the fluorophore hexachlorofluorescein (HEX) bound to the 5′ end. A high concentration of *mntS*Pro (1 μM) was titrated with MntR in the presence of 200 μM Mn(II) (~ 10-fold the $K_{Mn(II)}$, see section 3.3.3.3) to fully activate sensor binding to DNA. The change in anisotropy was measured after each protein addition. As shown in **Figure 3.14**, Δr_{obs} increased linearly up to a point of inflection corresponding to binding of one MntR dimer per *mntS*Pro molecule. Instead of showing saturation of DNA binding as seen for other sensors (Osman et al, 2017; Osman et al, 2015; Osman et al, 2016), Δr_{obs} sharply increased after the initial point of inflection. The data suggest that the first event observed is binding of a MntR dimer to *mntS*Pro, as seen in the size-exclusion experiment (**Figure 3.11**). However, at higher protein:DNA ratios, weaker, higher order binding events occur between MntR and *mntS*Pro (and possibly between different protein:DNA complexes). The change in anisotropy associated with binding of one MntR dimer to *mntS*Pro was obtained from the linear regression analysis of the first portion of the titration: $\Delta r_{obs} \approx 1.3 \times 10^{-2}$. If the weaker binding events occur also in the presence of a lower concentration of DNA (10^{-8}–10^{-9} M), this might complicate the analysis of the data to determine K_{DNA}.

3.4.4.2 Fluorescence anisotropy experiments with mntSPro-short

The affinity of the sensors for DNA is affected by the length of the oligonucleotide used in the assay. In an effort to reduce the formation of the higher order complexes between MntR and DNA, the fluorescence anisotropy experiment was repeated with the shorter oligonucleotide (18 bp) *mntS*Pro-short (**Figure 3.15**). When 1 μM *mntS*Pro-short was titrated with Mn(II)-MntR, the fluorescence anisotropy increased almost linearly to a point of inflection corresponding to one MntR dimer (**Figure 3.16**). After the point of inflection, Δr_{obs} increased steeply as previously observed with the 32 bp oligonucleotide *mntS*Pro. This suggests that the higher order binding events are occurring also on a shorter DNA fragment.

a

F 5′[HEX]-CTATAAAACATAGCCTGTGCTATATCTGTATG 3′

b

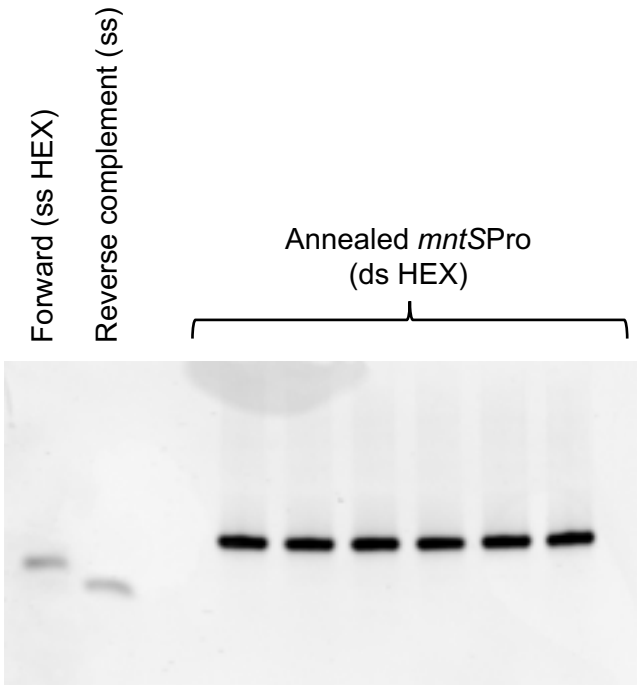

Figure 3.13. Production of the double-stranded oligonucleotide *mntS*Pro for fluorescence anisotropy experiments.
a, 32 bp oligonucleotide containing the identified MntR recognition site (underlined) and flanking nucleotides in the *mntS* promoter. The shown oligonucleotide (fluorescently labelled, 5′-HEX) was annealed with its unlabelled reverse complement. **b**, Annealing was confirmed by native PAGE (12% w/v), staining the DNA with with ethidium bromide. The single-stranded (ss) oligonucleotides were run on the same gel as a control to show the different migration from the double-stranded (ds) *mntS*Pro.

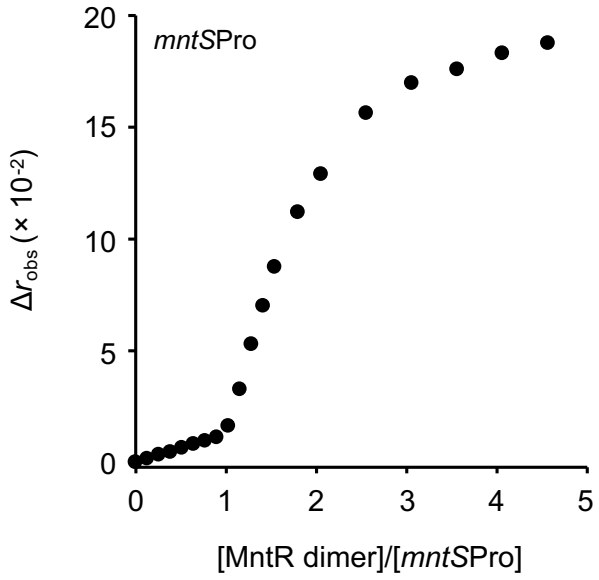

Figure 3.14. One MntR dimer binds to *mntS*Pro with tight affinity.
Representative (n = 2) fluorescence anisotropy change (Δr_{obs}) following titration of an elevated concentration of *mntS*Pro (1 μM) with Mn(II)-MntR. Δr_{obs} increases linearly to a point of inflection at one MntR dimer per *mntS*Pro, followed by a sharp increase indicative of weaker higher order binding events. Binding of the first dimer is associated with a Δr_{obs} of ~1.3×10^{-2} and this value was used to determine MntR DNA affinities (see **Figure 3.17**). Figure and caption are adapted from (Osman et al, 2019).

a

5′ [HEX]-ACATAGCCTGTGCTATAT 3′

b

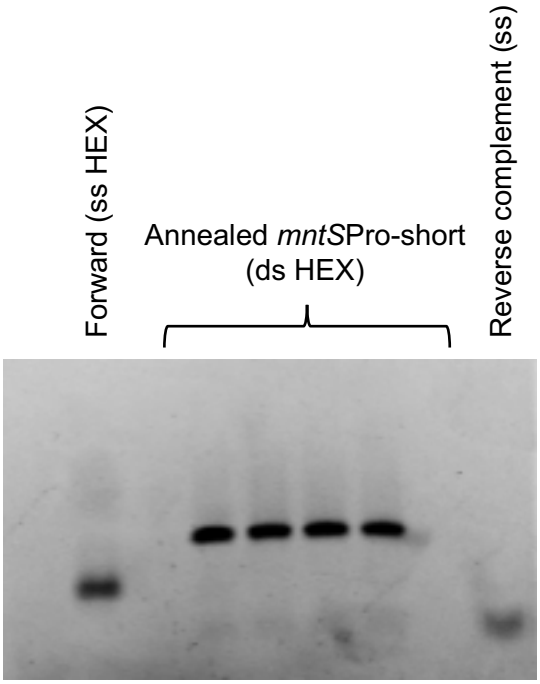

Figure 3.15. Production of the double stranded oligonucleotide *mntS*Pro-short for fluorescence anisotropy experiments.
a, *mntS*Pro-short is an oligonucleotide shorter (18 bp) than the one shown in **Figure 3.13**. It contains the identified MntR recognition site (underlined) and only three flanking nucleotides in the *mntS* promoter. The shown oligonucleotide (fluorescently labelled, 5′-HEX) was annealed with its unlabelled reverse complement. **b.** Annealing was confirmed by native PAGE (12% w/v), staining the DNA with with ethidium bromide. The single-stranded (ss) oligonucleotides were run on the same gel as a control to show the different migration from the double-stranded (ds) *mntS*Pro-short.

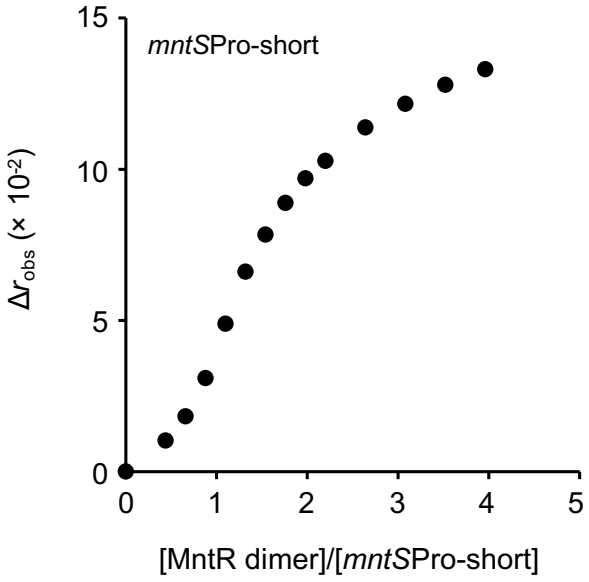

Figure 3.16. Higher order binding occurs also with a shorter (18 bp) oligonucleotide. Fluorescence anisotropy change (Δr_{obs}) following titration of *mntS*Pro-short (1 μM) with Mn(II)-MntR (n = 1). After a point of inflection at one MntR dimer per *mntS*Pro-short, the Δr_{obs} has a sharp increase suggesting that higher order binding events occur even on a shorter DNA fragment.

3.4.5 Determination of the DNA-binding affinity by fluorescence anisotropy

To determine the affinity of MntR for *mntS*Pro (**Figure 3.13**), the fluorescence anisotropy experiments were performed using a lower concentration of DNA to avoid stoichiometric binding of the sensor to its recognition sequence. *mntS*Pro at 10 nM concentration was titrated with MntR in the absence and presence of Mn(II) (**Figure 3.17**). In the presence of 200 μM, to fully saturate the sensor with metal, MntR bound to *mntS*Pro forming the higher order complexes previously observed in section 3.4.4 (**Figure 3.17a**). The change in fluorescence anisotropy detected during the titration greatly exceeded the Δr_{obs} value associated with one MntR dimer binding to mntSPro ($\Delta r_{obs} \approx 1.3 \times 10^{-2}$, **Figure 3.14**). In the absence of Mn(II) (EDTA was included in the experimental buffer to exclude the presence of any other contaminating metal), MntR had a weaker affinity for *mntS*Pro compared to its metalated form. However, the higher order binding events occurred also in the presence of apo-MntR (**Figure 3.17b**).

The tighter affinity for DNA in its metalated form confirms that MntR regulates the genes in its regulon by acting as a co-repressor. When the availability of Mn(II) in the cell increases, the sensor becomes metalated and binds to the promoter of its target genes, contributing to the repression of the Mn(II)-import systems MntH and SitABCD and the activation of the Mn(II)-efflux system MntP (**Figure 3.8** and section 3.4.1).

The stoichiometry experiment (**Figure 3.14**) clearly showed the formation of the first MntR dimer:DNA complex, but it was not possible to tease out what the species forming after the inflection point are (interaction between different MntR:DNA complexes might also be occurring in view of the steepness of the curve). Without knowing what species are forming during the titration and the stoichiometry of the MntR:DNA complexes, it is not possible to fit the data in **Figure 3.17** using Dynafit. It is, however, possible to obtain the K_{DNA} values for the first binding event (binding of a MntR dimer to *mntS*Pro) in the absence and presence of Mn(II). Under equilibrium conditions for the formation of a 1:1 complex, the concentration of ligand at which the ligand-binding molecule is 50% saturated corresponds to the numerical value of the dissociation constant describing the equilibrium reaction. Therefore, the concentration of MntR dimer at the point where the change in anisotropy reaches half of the Δr_{obs} associated with a sensor dimer biding to *mntS*Pro, will give an estimate of the dissociation constant for the first event. In order to do this, the data from **Figure 3.17** were fit to a second-degree polynomial regression. The MntR concentration at interception of the line of best fit with the half of the Δr_{obs} for one dimer binding to DNA gave the K_{DNA} for all the independent experiments in **Figure 3.17** (n = 3 for both the data in **a** and **b**). The average values, expressed as dissociation constants and as mean (±s.d.), are $K_{DNAapo} = 8.6 (\pm 1.7) \times 10^{-8}$ M and $K_{DNAMn(II)} = 5 \times 10^{-9}$ M.

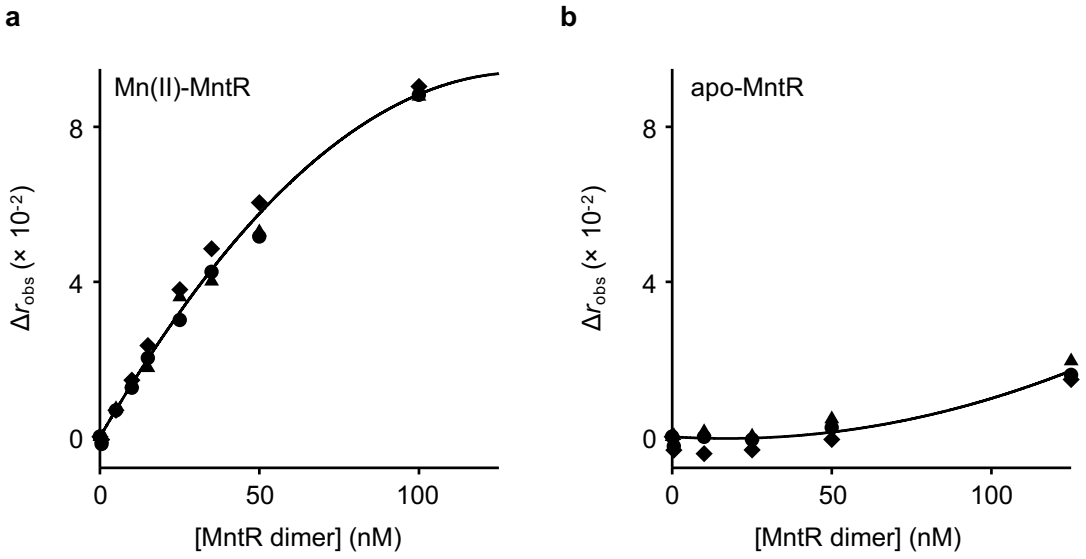

Figure 3.17. Determination of MntR affinities for *mntS*Pro.
Fluorescence anisotropy change (Δr_{obs}) following titration of *mntS*Pro (10 nM) with Mn(II)-MntR in 200 μM Mn(II) (**a**) and apo-MntR in 5 mM EDTA (**b**). Shapes represent individual experiments. The data were fit to a second-degree polynomial regression and limit values for the DNA affinities were determined at the intersection of the regression line and half of the change in fluorescence anisotropy value associated with a MntR dimer binding to *mntS*Pro (**Figure 3.14**). The solid line is a simulation with the average K_{DNA} obtained from the individual experiments (n = 3 for both **a** and **b**). Figure and caption are adapted from (Osman et al, 2019).

The value obtained for $K_{DNAMn(II)}$ is at the limit of the assay, as 10 nM mntSPro was used in the experiment (i.e. the affinity of metalated MntR for DNA might be tighter). Moreover, the change in fluorescence anisotropy in the first part of the titration is almost linear and $\Delta r_{obs} \approx 1.3 \times 10^{-2}$ was reached approximately at 10 nM MntR dimer (1:1 stoichiometric binding). In order to test the limit of the assay, *mntS*Pro titration with Mn(II)-MntR was repeated using a lower concentration of DNA (2 nM *mntS*Pro, **Figure 3.18**). The data could not be fit to any model describing MntR dimer binding to DNA using Dynafit. This could be due to the low concentration of DNA (and thus of fluorophore, decreasing of signal-to-noise ratio), or to the fact that at low concentration of protein it might be necessary to consider protein dimerization equilibria to fully describe the system. A dimerization constant of ~1.75×10^{-7} M (expressed as a dissociation constant) was determined for *Bs*MntR by ultracentrifugation, however this values is likely to be an upper limit due to the limit of detection of the instrument (Lieser et al, 2003). Nevertheless, the data in **Figure 3.18** show that the $\Delta r_{obs} = 1.3 \times 10^{-2}$ was reached at a concentration of MntR greater than 2 nM. This suggests that in this experiment the metalated protein is not binding stoichiometrically to DNA and, therefore, Mn(II)-MntR affinity for *mntS*Pro is weaker than 1×10^{-9} M. This is in accordance with the $K_{DNAMn(II)} = 5 \times 10^{-9}$ M obtained from **Figure 3.17**. Another approach to confirm the value obtained for $K_{DNAMn(II)}$ would be to repeat the DNA-binding experiments with a higher concentration of salt in the buffer, to diminish MntR affinity for DNA. If the dependence of K_{DNA} on [salt] for MntR can be determined, it will be possible to calculate the DNA affinity at 300 mM salt (240 mM KCl plus 60 mM NaCl, the same conditions used for the other *Salmonella* sensors) from the data collected at higher salt concentration. For example, a similar approach (albeit decreasing the salt concentration to increase protein affinity for DNA) was used in section 5.4 to measure the affinity of *Salmonella* Zur for non-specific DNA.

In Chapter 5, $K_{Mn(II)}$, $K_{DNAMn(II)}$ and K_{DNAapo} determined here for MntR will be used to model the response of the sensor as a function of Mn(II) availability in the cell. Binding of the first dimer to the promoter of the target genes will be assumed to be sufficient to affect gene expression. However, the formation of the higher order protein-DNA complexes observed in the fluorescence anisotropy experiments might be part of the mechanism of regulation by MntR. MtsR from *S. pyogenes* and ScaR from *S. gordonii*, other members from the DtxR family of metalloregulators, have been reported to undergo multimerization on DNA (Bates et al, 2005; Jakubovics et al, 2000). A recent paper showed that the interaction between FeoA domains (see section 3.1) of MtsR dimers participates in sensor multimerization on DNA (Do et al, 2019). Mutations of the FeoA domain to impair oligomerization caused loss of response to Mn(II), suggesting that the formation of MtsR multimers on DNA is crucial for the regulation of gene expression in *S. pyogenes*. *Salmonella* MntR lacks the FeoA domain (**Figure 3.1**). However, it is possible that inter-dimer interactions through another portion of the protein might modulate gene regulation.

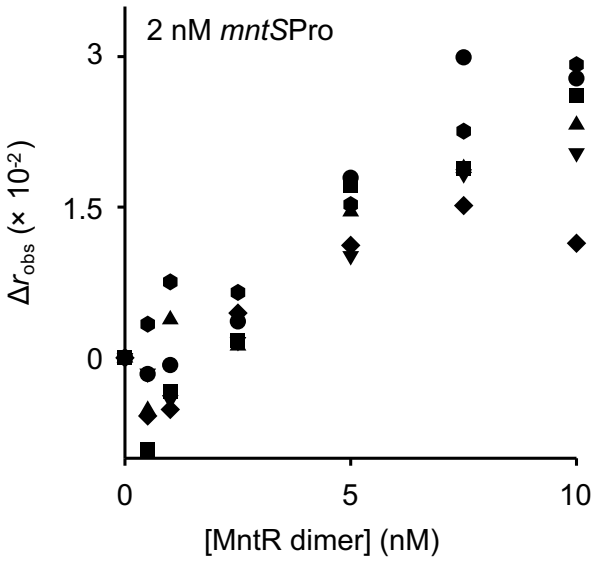

Figure 3.18. Titration of a low concentration of *mntS*Pro1 with MntR.
Fluorescence anisotropy change (Δr_{obs}) following titration of *mntS*Pro (2 nM) with Mn(II)-MntR in 200 μM Mn(II). Shapes represent individual experiments (n = 6). A Δr_{obs} equating the change in fluorescence anisotropy value associated with a MntR dimer binding to *mntS*Pro (Figure 3.14) is reached at a concentration of Mn(II)-MntR greater than 2nM, consistent with the K_{DNA} determined in **Figure 3.17**.

Chapter 4.

Characterisation of the iron sensor Fur from *Salmonella*

4.1 Bioinformatic analysis of Fur

The Fur family of metal sensors is a widespread family of proteins. The founding member of this 'superfamily' is the Fe(II)-sensing *E. coli* Fur, but other proteins belonging to other Fur subfamilies can act as sensors for other metals (Zur for Zn(II), Mur for Mn(II), and Nur for Ni(II)), cofactors (Irr for haem) and even oxidative stress (PerR) (section 1.5.3). Many Fur-like regulators from all the different subfamilies have been biochemically characterised *in vitro* (Butcher et al, 2012; Deng et al, 2015; Dian et al, 2011; Gao et al, 2008; Ma et al, 2012; Pecqueur et al, 2006; Perard et al, 2018; Pohl et al, 2003; Sheikh & Taylor, 2009; Wee et al, 1988). **Figure 4.1** shows a comparison of the amino acid sequence of Fur from *Salmonella* with the sequences of other characterised Fe(II)-sensing Fur-like proteins. *Salmonella* Fur shares 97.3% sequence similarity and 96.7% sequence identity with *E. coli* Fur (**Table 8.2**).

Many Fur proteins have been structurally characterised (asterisks in **Figure 4.1**). Most Fur-like proteins are dimers. The structure of the dimers comprises two domains: a DNA-binding N-terminal domain and a C-terminal dimerization domain (Dian et al, 2011; Pohl et al, 2003). Four Cys residues are well conserved across the family and are known to be involved in binding of a structural Zn(II) per subunit. The structures of Fur from *H. pylori*, *C. jejuni* and *F. tularensis* showed a Zn(II)-S_4 site, with the Zn(II) ion coordinated by two C-XX-C motifs as reported also for the oxidative stress sensor PerR (Lee & Helmann, 2006). By contrast, in *E. coli* Fur the Zn(II) ion is coordinated by two Cys residues and two (yet to be identified) N/O donor ligands (Althaus et al, 1999; Gonzalez de Peredo et al, 1999; Jacquamet et al, 1998). All the Cys residues are conserved in *Salmonella* but it is unknown whether this protein has a structural Zn(II) and, if it does, how many S-donor ligands are involved in metal coordination. In addition to the structural site, one to two Fe(II)-binding regulatory sites have been reported per protein subunit. Despite the different stoichiometries reported in the literature (see section 1.5.3 and section 4.3.1), the residues involved in metal-binding in both sites are well conserved across all of the Fe(II)-binding Fur proteins examined in **Figure 4.1**. No information about the metal-binding stoichiometry is available for *Salmonella* Fur. **Figure 8.3** in **Appendix A** reports the amino acid composition of Fur and the calculation of some theoretical properties of the protein based on its primary sequence.

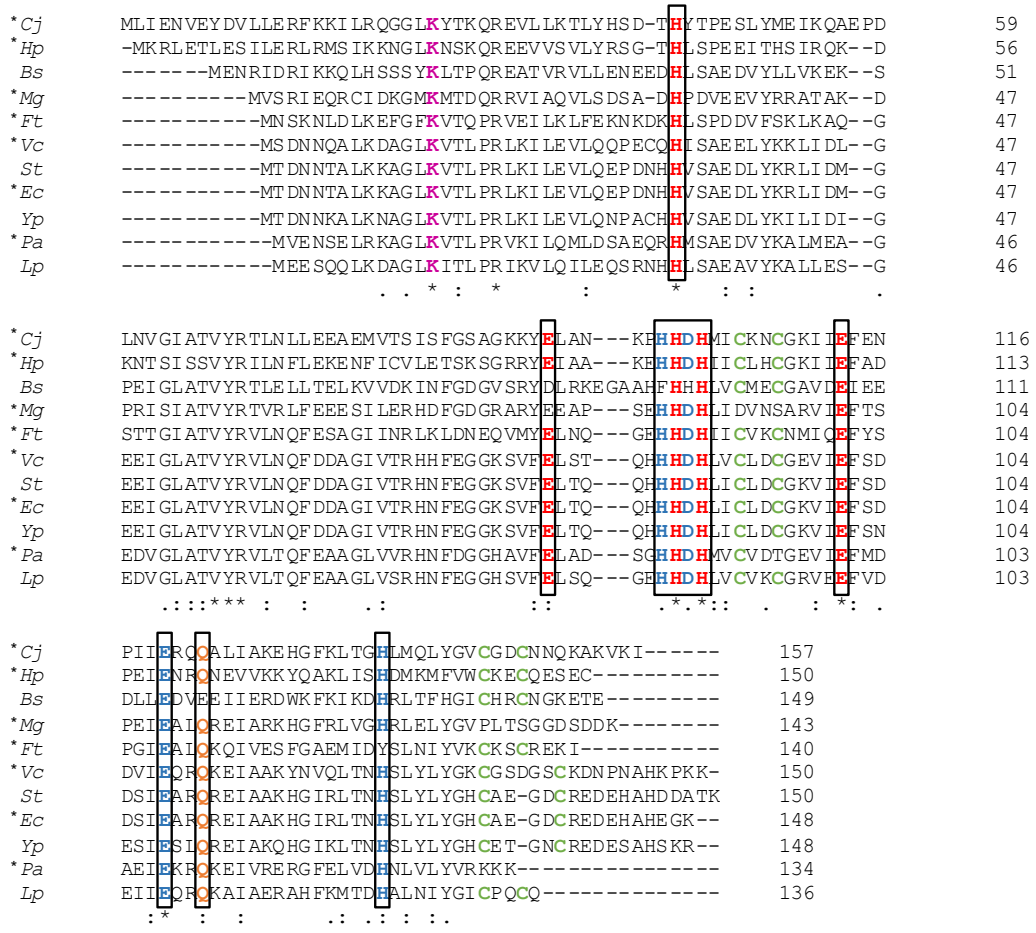

Figure 4.1. Multiple sequence alignment of characterised Fur proteins.
Alignment of multiple protein sequences of characterised Fur proteins from *C. jejuni* (*Cj*), *H. pylori* (*Hp*), *B. subtilis* (*Bs*), *M. gryphiswaldens* (*Mg*), *F. tularensis* (*Ft*), *V. cholerae* (*Vc*), *S. Typhimurium (St*), *E. coli* (*Ec*), *Y. pestis* (*Yp*), *P. aeruginosa* (*Pa*), *L. pneumophila* (*Lp*). The sensors marked with an asterisk have been structurally characterised. The highly conserved Cys residues are highlighted in green. In *Ec*Fur, Cys92 and Cys95 are involved in Zn(II)-binding in the structural site while in other Fur sensors all of the four Cys residues bind the Zn(II) ion. The residues involved in metal-binding in the regulatory sites are highlighted by the black boxes. Even though different metal-binding stoichiometries have been reported for the Fur homologues, the residues involved in metal binding are highly conserved (including in *S.* Typhimurium Fur). In Fur proteins reported to have two regulatory sites (e.g. *Hp*Fur and *Mg*Fur), metal at site 1 (red) is required for DNA-binding, while metal-binding at site 2 (blue) has been suggested to modulate DNA-affinity. In *Mg*Fur, the highly conserved Gln111 (orange) is indirectly involved in metal-binding via a water molecule. The conserved lysine (purple) is required for DNA-binding in *M. gryphiswaldens*, as it interacts with the negative electrostatic potential in the DNA minor grooves (Deng et al, 2015)). Similarity and identity scores of the amino acid sequence of *S.* Typhimurium Fur compared with the ones of the other Fur sensors are reported in **Table 8.1**.

4.2 Expression and purification of recombinant Fur

Salmonella Fur was expressed in *E. coli* as a recombinant protein. As previously described for MntR (section 3.2), Fur was expressed without any affinity tag and the purification protocol relied on its intrinsic properties (metal-binding, DNA-binding and size). The first step of the purification protocol involved loading the crude cell extract on a nickel affinity column, exploiting the Fur putative metal-binding sites identified by sequence alignment. Fur bound to the nickel column and eluted with a high concentration of imidazole (**Figure 4.2**). SDS-PAGE confirmed the presence of a highly abundant protein with a molecular weight consistent with Fur (theoretical molecular weight ~17.0 kDa as monomer) in the fractions collected. Fractions containing a high concentration of Fur had an orange to pink colour, suggesting that Ni(II) ions were released from the affinity column and bound to the Fur metal-binding site(s). Fur eluted in high concentration with 100 mM imidazole (fraction 2 in **Figure 4.2**). However, so did other contaminating proteins that could not be separated from Fur in the first purification attempts. Fur eluted in a relatively high concentration also in the subsequent fractions at 300 mM imidazole (fractions 3–8 in **Figure 4.2**) with higher purity. Therefore, the Fur fractions eluted in 300 mM imidazole were further purified as described below.

4.2.1 Metalation of the Zn(II) structural site

Previous attempts at purifying Fur showed that, unlike MntR and other sensors (Osman et al, 2015), this protein did not bind to a heparin affinity column if the pH of the buffer was higher than ~6.0. However, the acidic pH hindered binding of Zn(II) to the structural site (*vide infra*). The presence of an empty structural site (or a mixed population of Zn(II)-bound and Zn(II)-free Fur) can complicate the interpretation of the *in vitro* experiments: The two forms might have different affinities for metals and DNA. Therefore, a different column matrix needed to be used to concentrate Fur and allow the buffer to be exchanged in the final step of the purification, in order to prepare the sample for the *in vitro* experiments, while retaining Zn(II)-metalation. Fur can bind to a HiTrap Q HP anion exchange column. However, so does the negatively charged EDTA present in the purification buffers to prevent contamination of the protein with unwanted metals. To avoid contamination by both EDTA and metals in the final purified protein sample, Fur was incubated with EDTA after the nickel affinity column (**Figure 4.2**) and then loaded on a HiLoad 26/600 Superdex 75 size-exclusion chromatography column equilibrated in Chelex-treated buffer (**Figure 4.3**). By doing this, treatment with EDTA should remove any contaminating metal bound to Fur (the orange colour observed after the nickel affinity step gradually disappeared during EDTA-treatment) and the size-exclusion step with Chelex-treated buffer should separate the protein from EDTA without introducing contaminating metals. The final step of the purification would involve loading Fur on a HiTrap Q anion exchange column, buffer exchange the protein

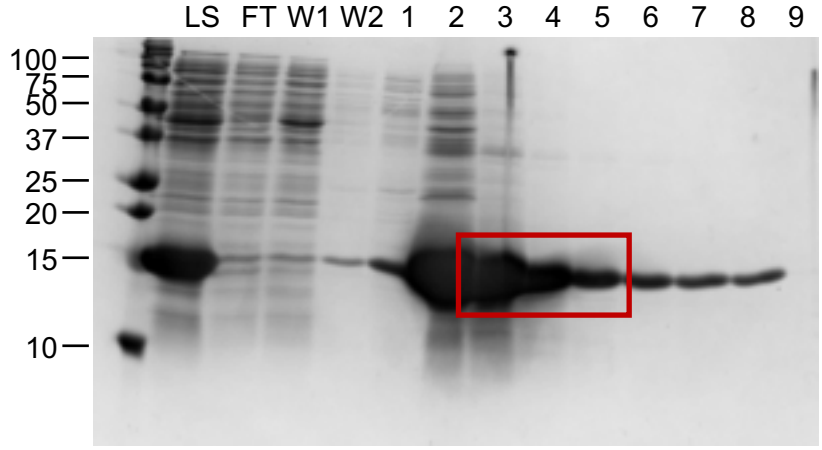

Figure 4.2. Purification of recombinant Fur from crude cell extracts.
SDS-PAGE of fractions eluted from a nickel affinity column. LS: loaded lysate of *E. coli* cells overexpressing Fur (1:5 dilution); FT: flowthrough with unbound species (1:5 dilution); W1: wash (5 column volumes) with buffer A; W2: wash (2 column volumes) with buffer A plus 10 mM imidazole; 1-9: collected fractions eluted with 10 mM (fraction 1, lag fraction 4.5 ml), 100 mM (fraction 2, 5 ml) and 300 mM (fractions 3–9, fraction 3 was 5.5 ml, other fractions 5 ml) imidazole. Fraction 2 routinely contained the highest concentration of Fur. However, fractions 3–5 (highlighted) contained fewer contaminating proteins and were therefore used for subsequent purification.

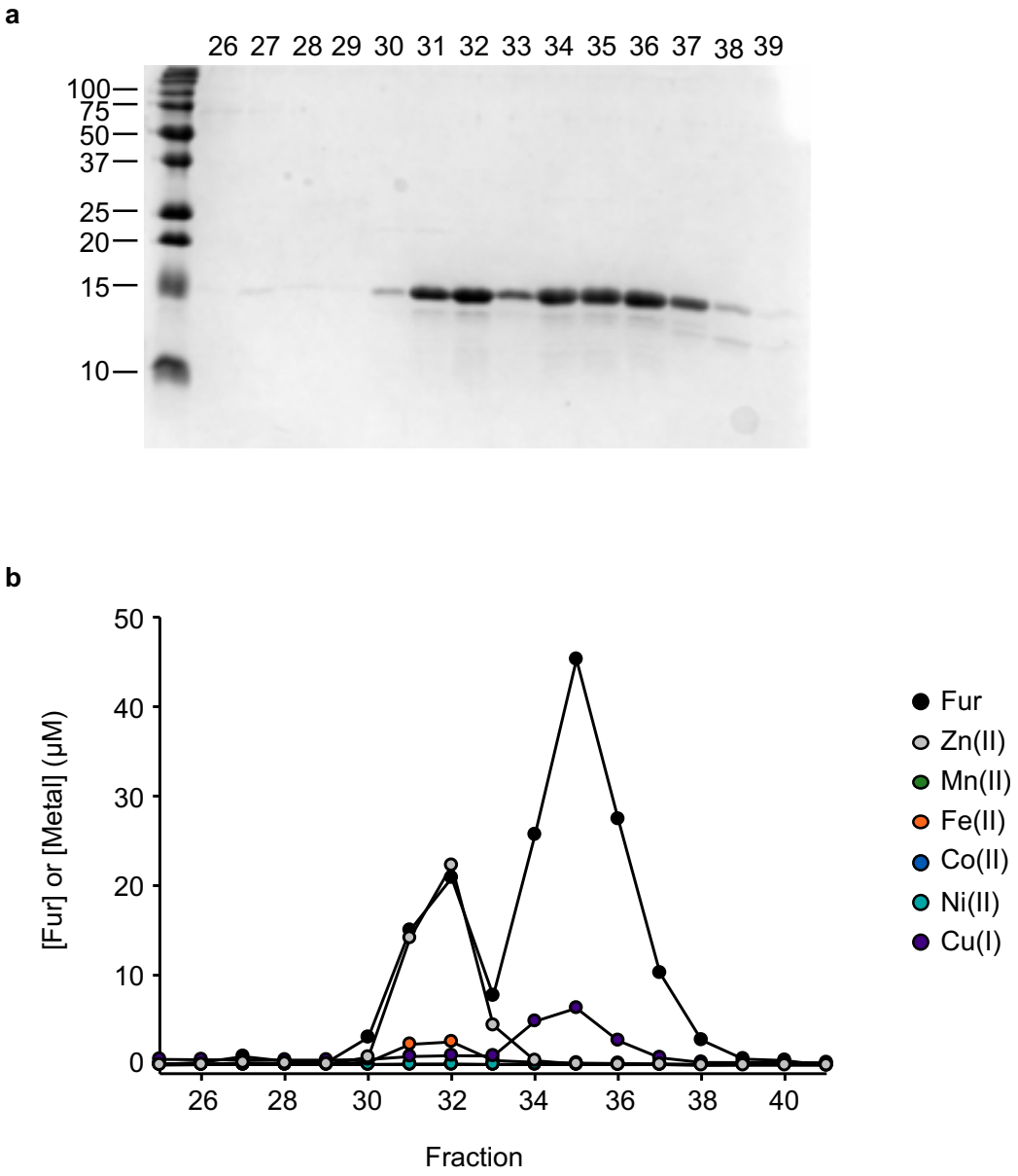

Figure 4.3. The absence of Zn(II) in the structural site affects the migration of Fur on a size-exclusion column.
a, SDS-PAGE of fractions (5ml) eluted from a HiLoad 26/600 Superdex 75 pg column loaded with 5 ml of fraction 3 from **Figure 4.2**. **b**, Metal content (grey symbols for Zn(II), green for Mn(II), orange for Fe(II), blue for Co(II), cyan for Ni(II) and purple for Cu(I)) and protein concentration (black symbols) in the fractions were determined by absorbance at 280 nm and ICP-MS respectively.

and elute it in the anaerobic glovebox. During the size-exclusion chromatography, EDTA-treated Fur eluted over a broad range of fractions, which appeared to comprise two distinct peaks (**Figure 4.3**). The concentration of Fur in the fractions was measured from the absorbance at 280 nm (the SDS-PAGE gel showed negligible contamination by other proteins) and the metal content was measured by ICP-MS (**Figure 4.3b**). The first peak contained Fur metalated with one equivalent of Zn(II), consistent with the presence of a filled Zn(II) structural site (Althaus et al, 1999) also in *Salmonella* Fur. The second peak contained Fur without any bound Zn(II) and ICP-MS showed a partial mis-metalation with copper. These results suggested that metalation of the structural site with Zn(II) affects the oligomeric state or the conformation of *Salmonella* Fur. A similar behaviour has been observed for *E. coli* Fur (D'Autreaux et al, 2007).

To maximise the recovery of Zn(II)-bound Fur from the purification protocol, the protein was incubated with Zn(II) prior to metal removal with EDTA. Fractions recovered from the nickel affinity column containing a high concentration of Fur (in 300 mM imidazole) were combined and concentrated on a HiTrap Q HP anion exchange column. Fur bound to the anionic exchange column and was eluted in a single step with a high concentration of NaCl (**Figure 4.4**). The sample eluted from the anionic exchange column was incubated with two equivalents of Zn(II) for one hour and then incubated with EDTA overnight to remove excess metal. The Zn(II)-EDTA-treated Fur sample was loaded on the HiLoad 26/600 Superdex 75 size-exclusion column (**Figure 4.5**). Fur eluted in three peaks. The first peak was observed at a lower retention volume than observed in the previous chromatogram (**Figure 4.3**), suggesting the formation of higher order oligomers. The second peak contained the highest concentration of Fur and was found at the same elution volume as Zn(II)-bound Fur in **Figure 4.3**. Finally, the third small peak corresponded to the elution volume of Fur without Zn(II) in the structural site in **Figure 4.3**. The analysis of protein concentration and metal content revealed that the first two peaks contained Fur co-migrating with one equivalent of Zn(II), while the third peak contained apo-Fur (**Figure 4.5b**).

To further examine the various species observed in the chromatograms in **Figure 4.3** and **Figure 4.5**, the HiLoad 26/600 Superdex 75 size-exclusion column was calibrated with molecular weight standards (**Figure 4.6**). The elution volume of the first Fur peak corresponded to an assembly of molecular weight of 73.1 kDa, mostly consistent with a Fur tetramer (theoretical monomer MW ≈ 17.0 kDa). The elution volumes of the second and third peak corresponded to 42.0 kDa and 30 kDa assemblies respectively.

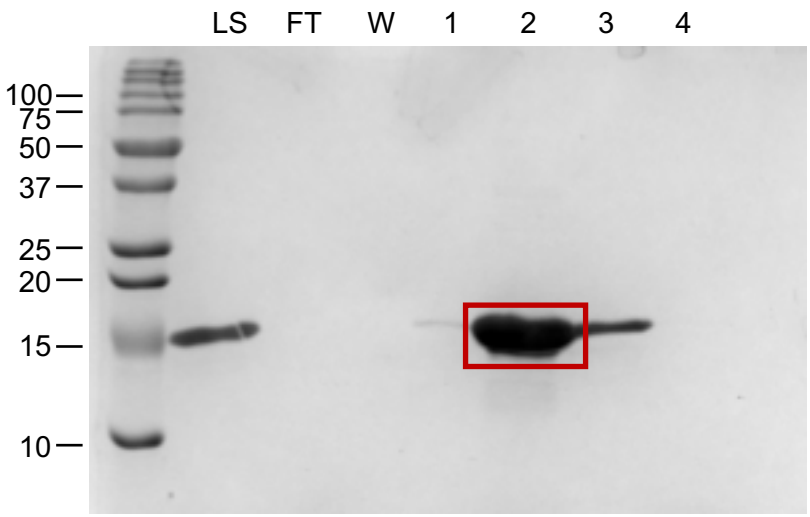

Figure 4.4. Concentration of purified Fur on a anionic exchange column
SDS-PAGE of fractions eluted from a HiTrap Q HP anion exchange chromatography column loaded with pooled fraction 3–5 from **Figure 4.2**. LS: loaded sample; FT: flowthrough with unbound species; W: wash (5 column volumes) with buffer B; 1–4: collected fractions eluted in buffer B with 100 mM (fraction 1, lag fraction 4.5 ml) or 1000 mM (fractions 2–4, fraction 2 was 5.5 ml, other fractions 5 ml) NaCl. The highlighted fraction was purification by size-exclusion chromatography.

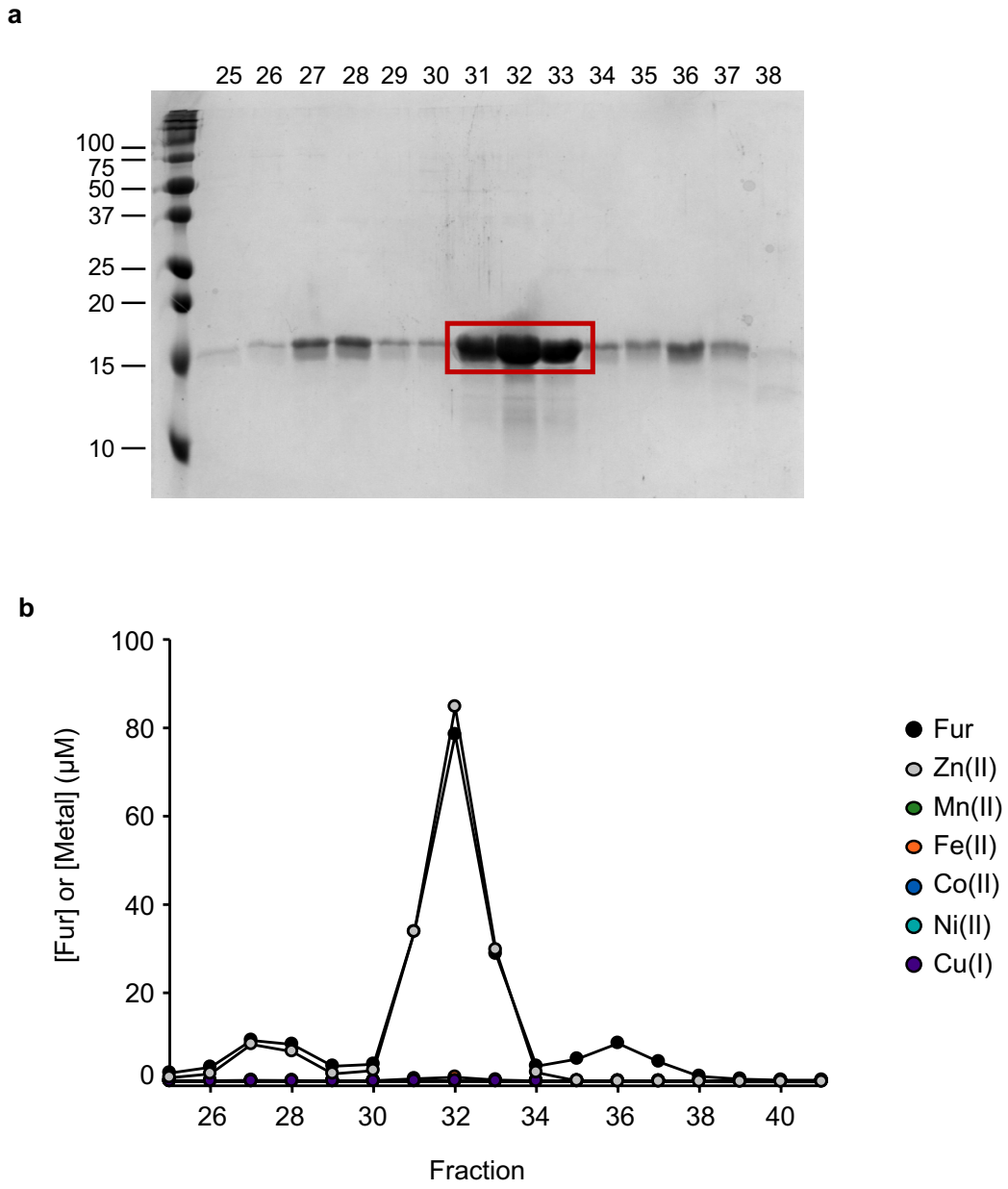

Figure 4.5. The structural site remains filled after pre-incubation of Fur with Zn(II) and then EDTA.
a, SDS-PAGE of fractions (5ml) eluted from a HiLoad 26/600 Superdex 75 pg column loaded with 5 ml of fraction 2 from **Figure 4.4** following incubation with 2 equivalents of Zn(II) per Fur monomer for 1 h and then with 7.5 mM EDTA overnight. **b**, Metal content (grey symbols for Zn(II), green for Mn(II), orange for Fe(II), blue for Co(II), cyan for Ni(II) and purple for Cu(I)) and protein concentration (black symbols) in the fractions were determined by absorbance at 280 nm and ICP-MS respectively.

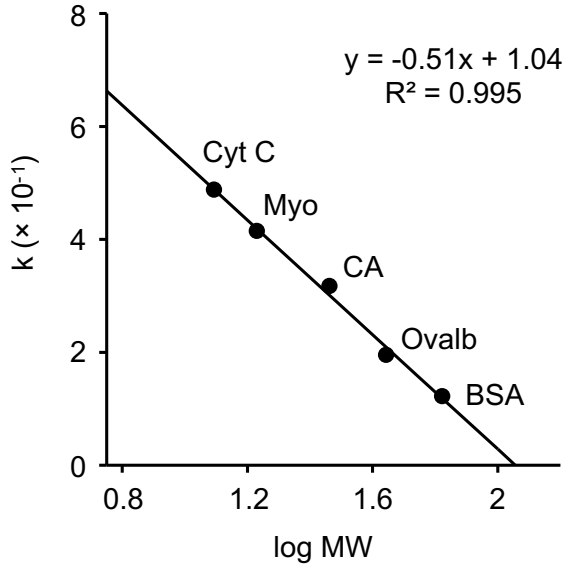

Figure 4.6. Calibration of the HiLoad 26/600 Superdex 75 pg size-exclusion column. A mixture (~0.7 mg of each component) of molecular weight standard was resolved by size-exclusion chromatography: bovine serum albumin (BSA), MW ≈ 66 kDa; albumin for chicken egg white (Ovalb), MW ≈ 44 kDa; carbonic anhydrase (CA), MW ≈ 29 kDa; myoglobin (Myo), MW ≈ 17 kDa; cytochrome c (Cyt C), MW ≈ 12.4 kDa. The experimental buffer contained 100 mM NaCl, 0.5 mM TCEP, 10 mM HEPES pH 7.0. The protein elution was monitored by absorbance at 280 nm and SDS-PAGE (**Figure 8.4**). k is the gel distribution coefficient: $k = (V_e - V_0)/(V_t - V_0)$ where V_e= elution volume, V_0 = void volume (115 ml, determined with Blue Dextran), V_t = total column volume (320 ml).

The 42.0 kDa complex was likely Fur in its dimeric form, while the latter might either be Fur in its monomeric form or a dimer with a less compact conformation. Studies on *E. coli* Fur showed that in solution the protein can be present as a monomer, dimer, tetramer and hexamer (Kuzmic, 1996). The equilibrium between the dimeric, tetrameric and hexameric forms is affected by the protein concentration, the salt concentration and the pH. By contrast, the monomeric and dimeric forms are not in equilibrium. In its monomeric form, *E. coli* Fur is an apo-protein. The dimerization can be triggered by adding Zn(II) (or another divalent cation) in the presence of reductants to maintain the two Cys residues in the structural site in the reduced form (D'Autreaux et al, 2007; Pecqueur et al, 2006).

4.2.2 Preparation of oxygen-free Fur with no metal contamination

The definitive purification protocol for Fur involved the incubation of protein with Zn(II) and EDTA after the nickel affinity column and the size-exclusion chromatography step in Chelex-treated buffer (as in **Figure 4.4** and **Figure 4.5**). The fractions collected after size-exclusion chromatography, containing dimeric Fur with a fully metalated Zn(II) structural site (identified by ICP-MS), were pooled and applied on a HiTrap Q HP anion exchange column. Purified Fur on the HiTrap Q column was moved to the anaerobic glovebox, buffer exchanged to a Chelex-treated, oxygen free buffer and eluted with a high concentration of KCl plus NaCl. Unless otherwise stated, all the *in vitro* experiments involving Fur were performed under anaerobic conditions. The concentration of residual metals in the protein samples was determined by ICP-MS. Purified Fur samples were routinely found to contain ~1 equivalent of Zn(II) and less than 5% contamination by other metals. **Figure 4.7a** shows the SDS-PAGE separation of purified Fur. The protein concentration was determined from the absorbance at 280 nm using the experimentally determined extinction coefficient $\varepsilon_{280\ nm}$ = 6,672 M^{-1} cm^{-1} (**Figure 4.7b**). The extinction coefficient was obtained from quantitative amino acid analysis (Alta Bioscience) performed on purified metal-free (with the exception of one equivalent of Zn(II)) Fur.

4.2.3 Determination of reactive thiol content

The concentration of reduced thiols in Fur samples was measured by reaction with Ellman's reagent. As shown in **Figure 4.8**, two thiols reacted within 40 min from the addition of Ellman's reagent. After 2 h from the start of the experiment (approximately at the point where the reaction of the third thiol was complete), the rate of the reaction slowed down significantly. Only after more than 20 h was the complete reaction of four thiols observed. *Salmonella* Fur has four cysteine residues (**Figure 4.1**, **Figure 8.3**). In *E. coli* Fur, Cys92 and Cys95 are involved in Zn(II) binding in the structural site (Gonzalez de Peredo et al, 1999; Jacquamet et al, 1998). The other two residues (Cys133 and Cys137) are located in the C-terminal domain and, even though they are not directly involved in metal-binding, they are in the reduced form.

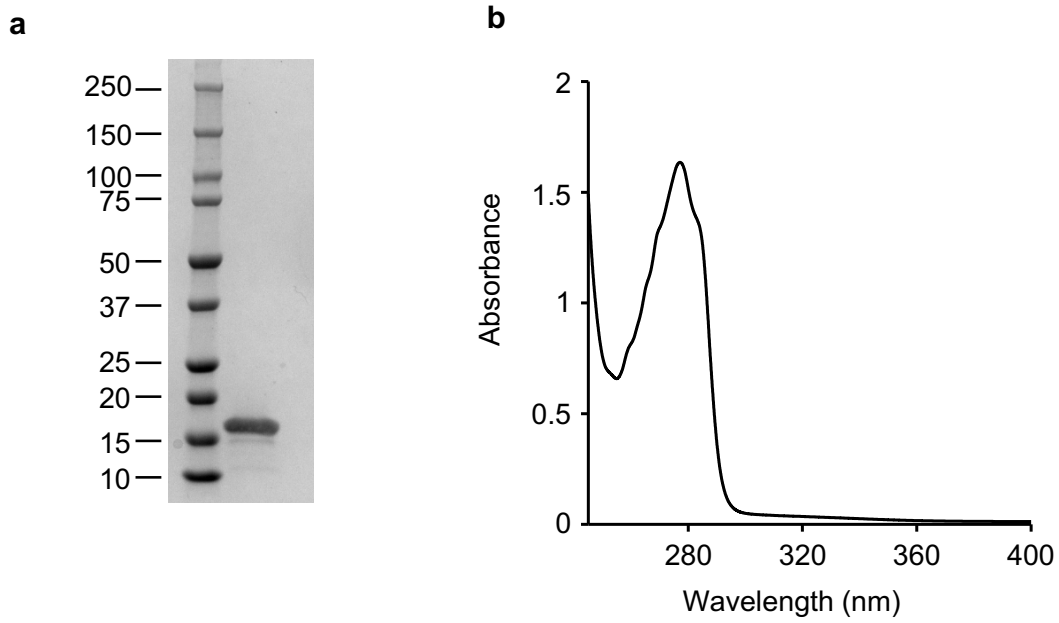

Figure 4.7. Analysis of purified Fur.
a, SDS-PAGE of purified Fur using a 4−20% w/v gradient gel with size marker indications. **b**, Spectrum of purified Fur; the protein was quantified using the experimentally determined extinction coefficient ε_{280nm} = 6,672 M^{-1} cm^{-1}.

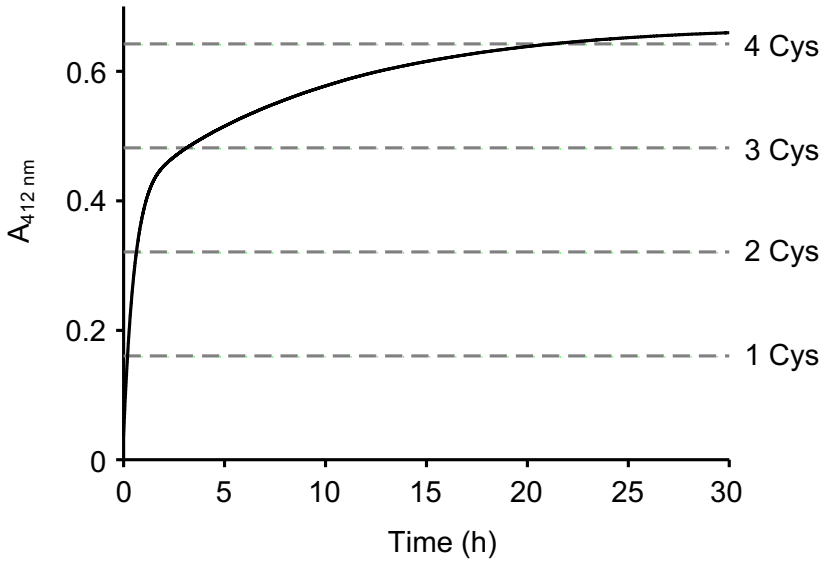

Figure 4.8. All the four cysteine residues of Fur are reactive to Ellman's reagent.
Fur (11.4 μM) was added to a solution of Ellman's reagent and the absorbance at 412 was monitored over time. The theoretical absorbance associated with 1 to 4 reactive cysteine residues is reported for comparison. Two thiols react swiftly while the other two slowly.

Thiol alkylation studies on *E. coli* Fur showed the presence of a pair of fast-reacting thiols and a pair of slow-reacting ones (Gonzalez de Peredo et al, 1999). Cys92 and Cys95 were identified as the slow reacting residues and it was proposed that Zn(II) was protecting the two thiols from alkylation. The Cys residues in *E. coli* Fur are conserved in *Salmonella* (section 4.1 and **Figure 4.1**). It is likely that the two slow reacting thiols observed in the Ellman's assay belong to the two Cys residues involved in Zn(II)-binding (Cys92 and Cys95 in the *Salmonella* numbering). The Ellman's reagent contains EDTA (~18 μM in the final reaction sample), but this is likely not sufficient to chelate the metal (section 4.3.2) and enhance reaction of the Zn(II)-bound Cys residues. A quick reaction might be observed in the presence of denaturing agents. The four thiols of Fur were routinely found to be >90% reduced.

4.3 Analysis of the metal-binding properties of Fur

4.3.1 Characterisation of homologous proteins

Despite being one of the first metal sensors to be discovered (Bagg & Neilands, 1987b), the characterisation of the metal-binding sites of Fur remained elusive for decades (section 1.5.3). Most of the data collected on metal-bound Fur proteins come from structural studies, therefore providing information only on the protein conformations that can be crystallized. Moreover, the instability of Fe(II) towards oxidation required the use of other redox-stable metals (typically manganese or zinc) as a surrogate for ferrous iron. Different metal ions have different coordination preferences and this might affect the results observed on Fur bound to non-cognate metals. Early studies on *E. coli* Fur revealed the presence of the Zn(II) structural site coordinated by Cys92 and Cys95 (section 4.1). In addition to the Zn(II) structural site, a regulatory site per subunit was reported in *E.coli* (Jacquamet et al, 1998; Mills & Marletta, 2005). Based on X-ray and Mössbauer spectroscopy data, in this site the metal ion is coordinated by five or six N/O-donor ligands (Adrait et al, 1999; Jacquamet et al, 1998; Katigbak & Zhang, 2012). However, the identity of the amino acid ligands was not defined. Most of the Fur proteins that were structurally or biochemically characterised revealed the presence of the Zn(II) structural site and either of one (*E. coli*, *C. jejuni*, *F. tularensis*) or two (*P. aeruginosa*, *V. cholerae*, *H. pylori, M. gryphiswaldens*, *B. subtilis*) additional metal-binding sites per subunit, all with N/O-donor ligands. Although various metal-binding stoichiometries were proposed, the residues involved in metal-binding are well conserved across the Fur proteins (**Figure 4.1**), even in those family members exhibiting only one putative Fe(II) site.

Fe(II)-affinities have been determined only for *E. coli* and *B. subtilis* Fur. *E. coli* Fur was reported to bind Fe(II) with an affinity of $K_{Fe(II)} = 1 \times 10^{-6}$ M (dissociation constant), determined in a competition assay with sodium citrate (Mills & Marletta, 2005). Positive cooperativity of metal-binding to the protein was observed. This was attributed to cooperative

binding of metal to the same site in the two different subunits (the determined metal stoichiometry was one Fe(II) plus one Zn(II) ion per monomer). Section 4.4 discusses cooperative metal-binding in *Salmonella* Fur. The Fe(II)-affinity of *B. subtilis* Fur was determined in an assay based on fluorescence anisotropy which, instead of directly detecting metal-binding to the sensor (or a competing probe), indirectly monitored binding of Fur to DNA after activation with metal (Ma et al, 2012). The affinity reported for *B. subtilis* Fur was $K_{Fe(II)} = 8.3 \times 10^{-7}$ M (dissociation constant). For *E. coli*, *B. subtilis* and *M. gryphiswaldens* Fur, the Mn(II)-affinity was also determined (Deng et al, 2015).

4.3.2 Kinetic trapping of Zn(II) in the structural site

From the purification protocol, Fur was obtained with one equivalent of Zn(II) per protein monomer (section 4.2.1). To test the effect of a strong chelator on the Zn(II)-binding site, the protein was incubated with a high concentration of EDTA before resolving the mixture on a Sephadex G25 matrix column (**Figure 4.9**) (the elution buffer did not contain EDTA). Fur concentration in the fractions collected was determined by Bradford assay and the Zn(II) content by ICP-MS. Even after incubation with the chelator, Fur co-migrated with one equivalent of Zn(II) on the size-exclusion column. This suggests that the metal in the structural site is kinetically trapped. Treatment with EDTA under denaturing conditions might be needed to chelate the Zn(II) ion.

4.3.3 Fe(II)-binding properties

4.3.3.1 Ferrous iron preparation

In order to study the Fe(II)-binding properties of Fur, a ~100 mM acidic solution of $(NH_4)_2Fe(SO_4)_2 \cdot 6H_2O$ (Mohr's salt) was prepared under strict anaerobic conditions. To determine the concentration of ferrous iron in the metal stock, the metal was titrated (after serial dilutions in oxygen-free water) into an excess (~tenfold) of ferrozine (**Figure 4.10**). Ferrozine is a chelant containing the bidentate ferroin group and forms a stable complex with ferrous iron with a stoichiometry of three ferrozine molecules per Fe(II) ion (Stookey, 2002). The formation of the complex is accompanied by an increase in absorbance at 562 nm in the UV-visible spectrum, with an extinction coefficient of $\varepsilon_{562\ nm} = 27{,}900\ M^{-1}\ cm^{-1}$ (**Figure 4.10a**). The concentration of Fe(II) in the stock was determined from the change in absorbance at 562 nm and this value was compared with the determination of iron content (ferrous + ferric iron) by ICP-MS (**Figure 4.10b**). The metal stock was used only if confirmed to be >90% Fe(II). For the *in vitro* Fe(II)-binding experiments, dilution from the concentrated ferrous iron stock (stored under anaerobic conditions) were prepared daily and tested by ferrozine assay to confirm that the metal was still in the reduced form.

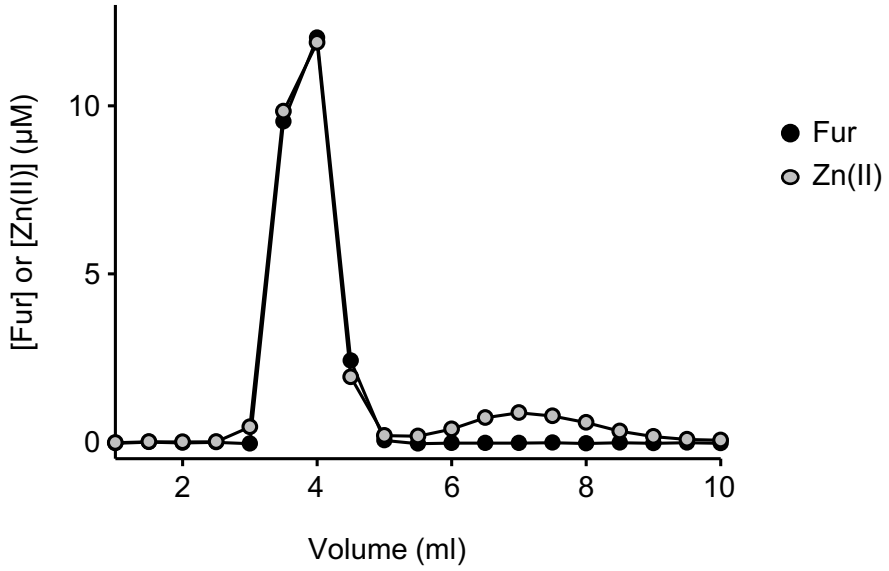

Figure 4.9. EDTA does not remove Zn(II) from Fur structural site.
Gel-filtration chromatography on Sephadex G25 of apo-Fur (20 μM) after incubation with 1 mM EDTA. Fractions (0.5 ml) were analysed for protein content (black symbols) by Bradford assay and for Zn(II) (grey symbols) by ICP-MS. Figure and caption are adapted from (Osman et al, 2019).

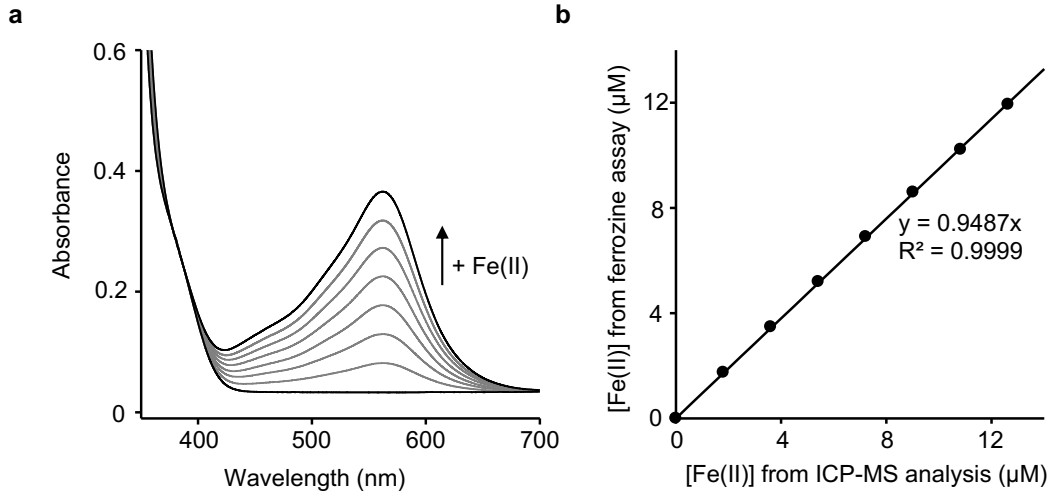

Figure 4.10. Determination of reduced Fe(II) in metal stocks by ferrozine assay.
a, Spectra of ferrozine (~tenfold excess) upon titration with Fe(II). The amount of Fe(II) can be determined from the absorbance at 562 nm (ε_{562nm} = 27,900 M^{-1} cm^{-1} for the ferrozine$_3$:Fe(II) complex). **b**, Comparison of iron concentration determined by ferrozine assay (Fe(II) only) and ICP-MS (Fe(II)+Fe(III)). All the metal stocks used were >90% reduced and the ferrozine assay was performed daily on freshly prepared Fe(II) dilutions from an acidic 100 mM Fe(II) stock.

4.3.3.2 Determination of Fe(II)-binding stoichiometry by size-exclusion chromatography

To determine the stoichiometry of Fe(II)-binding, as seen previously for MntR (section 3.3.2), Fur was incubated with Fe(II) and the mixture was resolved on a Sephadex G25 matrix column (**Figure 4.11**). The relatively weak Fe(II)-affinities determined for *E. coli* and *B. subtilis* Fur (section 4.3.1) suggest that Fur will lose any bound metal during the elution if the experimental buffer is not supplemented with extra Fe(II). Therefore, the buffer used to equilibrate the column and elute the protein contained 50 μM Fe(II) to retain metal co-migration with Fur. The fractions collected were analysed for Fe(II) and Zn(II) content by ICP-MS and for protein content by absorbance at 280 nm. Fur co-migrated with approximately one equivalent of Zn(II) and two equivalents of Fe(II) per monomer. This suggested a stoichiometry of four Fe(II) ions per dimer (as observed for Fur from *M. gryphiswaldens* and *H. pylori*) plus two Zn(II) ions per dimer in the structural sites.

4.3.3.3 Determination of Fe(II)-binding stoichiometry by direct titration of the sensor

Salmonella Fur has four Tyr residues which are conserved in *E. coli* Fur. Mills and Marletta have reported that when *E. coli* Fur is titrated with metals, the intrinsic fluorescence of the protein is quenched in a metal-dependent way (Mills & Marletta, 2005). *Salmonella* Fur was therefore titrated with Fe(II), monitoring the change in fluorescence emission intensity after every addition. As shown in **Figure 4.12a**, Fur intrinsic fluorescence was quenched upon Fe(II) addition. The binding isotherm (**Figure 4.12b**) showed that the fluorescence emission intensity decreased linearly to a point of inflection corresponding to two Fe(II) equivalents per Fur monomer. After the point of inflection, the fluorescence signal did not quench further. Together with the size-exclusion experiment in **Figure 4.11**, these results confirmed a stoichiometry of four Fe(II) ions per Fur dimer (two per monomer). The linear decrease in fluorescence intensity indicated that, under the conditions used in the experiment, Fe(II)-binding was so tight as to be stoichiometric, leaving no significant fraction of unbound metal. This suggested that Fur had a $K_{Fe(II)}$ in the sub-micromolar range. Therefore, in order to determine $K_{Fe(II)}$, the protein needs to compete with another molecule for Fe(II)-binding during titration. Protein fluorescence quenching can be used as a measure of protein saturation with metal during such an experiment.

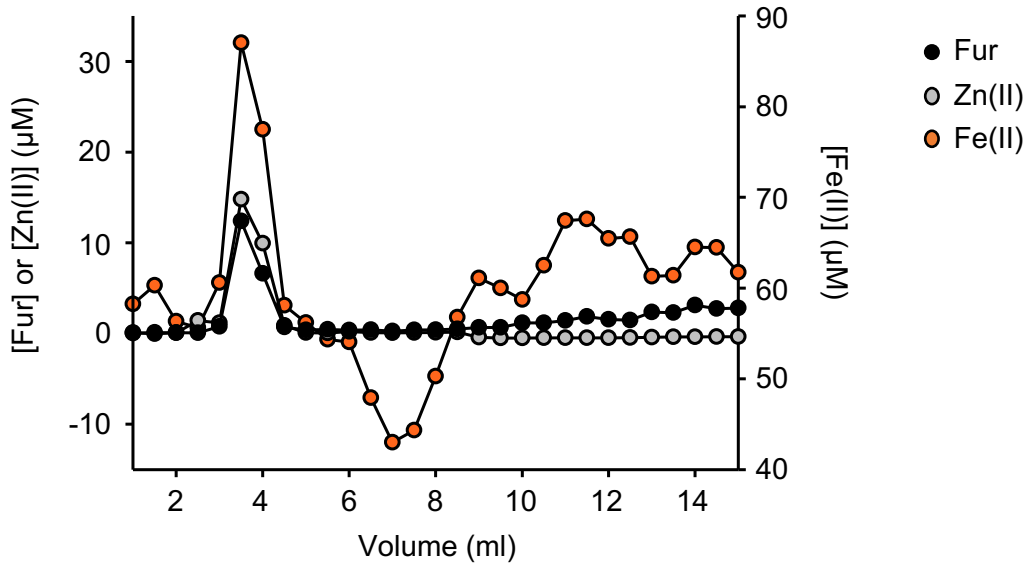

Figure 4.11. Fur co-migrates with one equivalent of Zn(II) and two equivalents of Fe(II) on a size-exclusion column.
Gel-filtration chromatography on Sephadex G25 of apo-Fur (20 µM) after incubation with 50 µM Fe(II). The elution buffer contained Fe(II) to retain the comigration of Fe(II) with Fur. Fractions (0.5 ml) were analysed for protein content by absorbance at 280 nm and for Zn(II) and Fe(II) by ICP-MS. Figure and caption are adapted from (Osman et al, 2019).

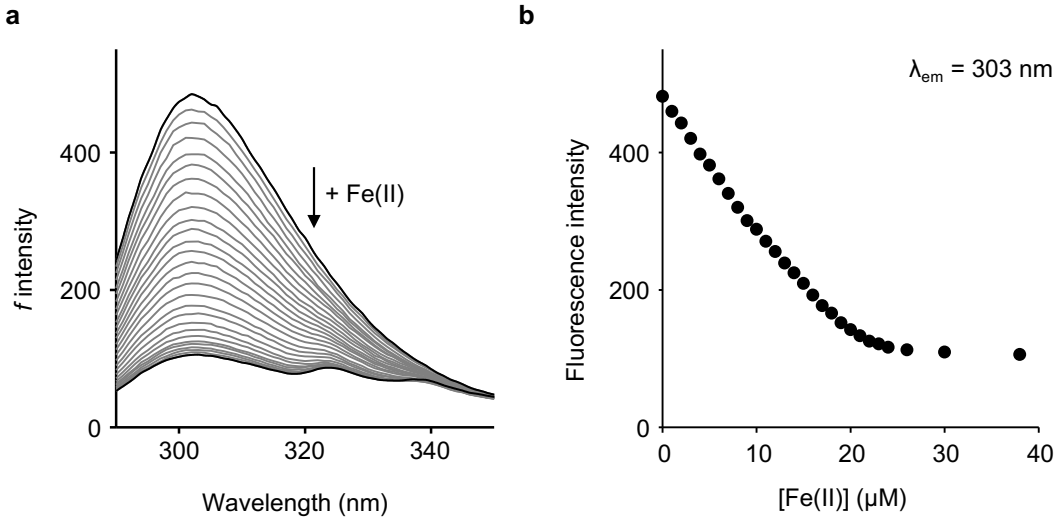

Figure 4.12. Fur florescence is quenched upon Fe(II) binding.
a, Representative (n = 3) quenching of Fur (10.3 μM) fluorescence emission when the protein is titrated with Fe(II). Excitation wavelength: 276 nm, T = 25 °C. **b**, Binding isotherm depicting the feature at 303 nm in **a**. The fluorescence intensity decreases linearly to a point of inflection at two Fe(II) equivalents per Fur monomer. Figure and caption are adapted from (Osman et al, 2019).

4.4 Determination of Fe(II)-binding affinity

In order to observe metal-partitioning to the sensor, Fur needs to compete with another molecule for Fe(II)-binding. As it is possible to follow metal-binding to Fur via the protein intrinsic fluorescence, the ideal candidate to compete with the sensor is a chelant with no fluorescence spectral features. The Fe(II)-affinity of several chelants is available in the literature (Xiao & Wedd, 2010). Nitrilotriacetic acid (NTA) has an affinity in a suitable range to be used to compete with Fur ($K_{Fe(II)} = 6.77 \times 10^{-7}$ M at pH 7.0, calculated from the literature value using Schwarzenbach's α coefficient (see section 2.7.5)). NTA is spectrally silent in the experiment monitoring Fur fluorescence.

Fur was titrated with Fe(II) in the presence of NTA. As shown in **Figure 4.13**, even though the concentration of protein in the assay was the same as in **Figure 4.12**, a higher concentration of Fe(II) was required to completely quench Fur fluorescence, as NTA was competing with the sensor for metal-binding. The shape of the binding isotherm indicated that metal-binding under these conditions was no longer stoichiometric. This sigmoidal shape of the curve also suggested positive cooperativity between metal-binding to different sites within the Fur dimer. In order to fit the data, several models were tested with Dynafit to describe Fe(II)-binding to Fur. The simpler models tested (for example describing metal-binding to the protein in a single event to obtain an apparent affinity for the complement of allosteric sites) all failed to describe the data, probably due to positive cooperativity between the metal-binding sites. The final model used to fit the data considered four sequential Fe(II)-binding events to four sites per Fur dimer. In this model, the metal-binding sites involved in the first two and in the last two Fe(II)-binding events had respectively the same individual (microscopic) $K_{Fe(II)}$ (named $K_{1Fe(II)}$ and $K_{3Fe(II)}$). The (macroscopic) $K_{Fe(II)}$ were therefore linked by statistical factors: $K_{2Fe(II)} = 4 \times K_{1Fe(II)}$ and $K_{4Fe(II)} = 4 \times K_{3Fe(II)}$ (as dissociation constants) (Wyman & Gill, 1990). NTA was modelled to bind Fe(II) with a 1:1 stoichiometry. The Dynafit script used to fit the data is reported in **Appendix B**. The individual affinities for the first two sites were determined to be $K_{1Fe(II)} = 2.6\ (\pm 0.3) \times 10^{-7}$ M, while the individual affinities of sites three and four were $K_{3Fe(II)} = 6.4\ (\pm 0.6) \times 10^{-8}$ M (all affinities expressed as dissociation constants and as mean (±s.d.), n = 4 independent experiments). The fit departed from the simulated curves with 10-fold tighter or weaker $K_{1Fe(II)}$ and $K_{2Fe(II)}$ (second pair of $K_{Fe(II)}$ fixed), and with 10-fold tighter or weaker $K_{3Fe(II)}$ and $K_{4Fe(II)}$ (first pair of $K_{Fe(II)}$ fixed).

To further validate the metal-affinities determined in **Figure 4.13**, the titration was repeated using half the amount of NTA (**Figure 4.14**). In the presence of a smaller concentration of competitor, quenching of Fur fluorescence occurred at a lower concentration of Fe(II). This is emphasized by the comparison of the binding isotherms (**Figure 4.14b**) obtained using the two different concentrations of NTA.

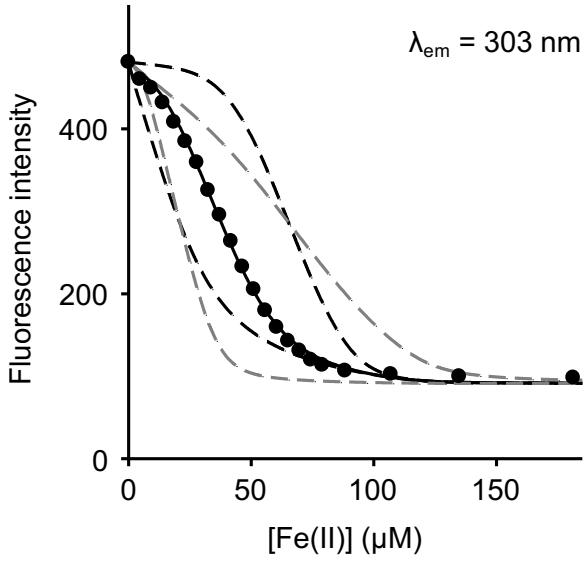

Figure 4.13. Determination of Fur affinity for Fe(II) via a metal-competition assay with NTA.
Representative (n = 4) Fur (10.2 μM) fluorescence quenching upon Fe(II) binding in the presence of NTA (100 μM). NTA is spectrally silent in this assay. Excitation wavelength: 276 nm, T = 25 °C. The solid line represents the fit to a model describing four sequential binding events per Fur dimer with positive cooperativity between two pairs of sites. The fit departs from the simulated curves with a $K_{Fe(II)}$ ten times tighter or weaker for each pair (while keeping the other one fixed). Dashed black line: simulation for the first pair; dashed grey line: simulation for the second pair. Figure and caption are adapted from (Osman et al, 2019).

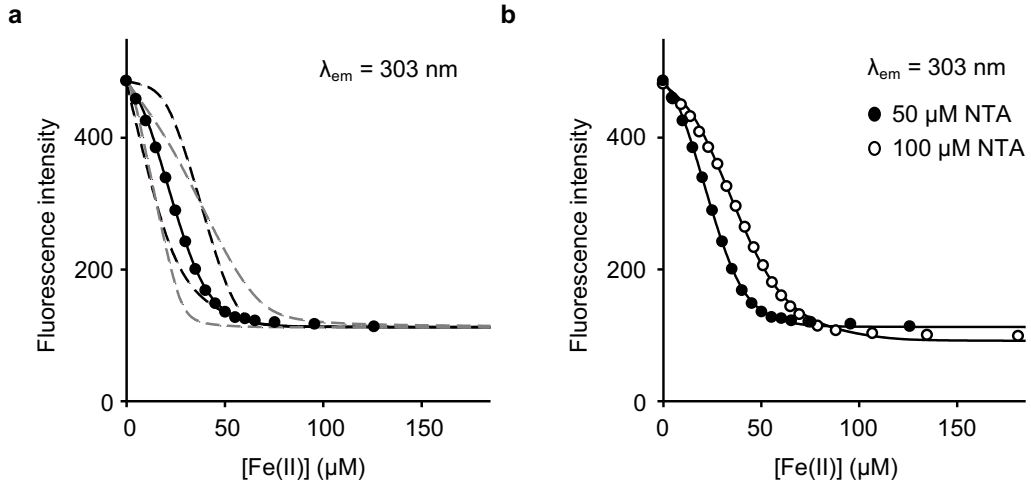

Figure 4.14. Fe(II)-binding competition using a different ratio Fur:NTA.
a, Fur (10.0 μM) fluorescence quenching upon Fe(II) binding in the presence of NTA (50 μM) (n = 1). Excitation wavelength: 276 nm, T = 25 °C. The solid line represents the fit to a model describing four sequential binding events per Fur dimer with positive cooperativity between the two pairs of sites. The fit departs from the simulated curves with $K_{Fe(II)}$ ten times tighter of weaker for each pair (keeping the other one fixed). Black dashed line: simulation for the first pair; grey dashed line: simulation for the second pair. **b**, Comparison of Fur (~10 μM) fluorescence quenching in the presence of two concentrations of NTA.

The data in **Figure 4.14** were fit to the same model described for **Figure 4.13**. The individual affinities obtained for the two couples of sites were $K_{1Fe(II)} = 2.3 \times 10^{-7}$ M and $K_{3Fe(II)} = 7.0 \times 10^{-8}$ M (n = 1). These are in good agreement with the value determined from **Figure 4.13** and presented above.

Reports on *H. pylori* and *M. gryphiswaldens* Fur suggested that metal-binding to site 1 is essential for allosteric activation of the sensor, while binding of metal to site 2 modulates the response by increasing the affinity for DNA (Deng et al, 2015; Dian et al, 2011). From the titration in **Figure 4.13** it is not possible to determine which site corresponds to the affinities determined. Assuming that the first two binding events observed in **Figure 4.13** occur at site 1 of each Fur subunit, the determined individual affinity for the first two events can be converted to a single averaged value describing filling of the complement of allosteric sites: $K_{Fe(II)} = 5.3\ (\pm 0.7) \times 10^{-7}$ M.

4.5 Analysis of the DNA-binding properties of Fur

4.5.1 Fur regulon in *Salmonella*

Fur has a critical role in the regulation of iron metabolism in bacteria. Moreover, recent studies have shown direct involvement of this sensor in the regulation of fundamental cell processes, such as DNA synthesis, biofilm production and energy metabolism (section 1.5.3). As a consequence, its regulon tends to be larger than those of the other metal sensors (**Table 5.2**). When it was discovered, Fur was initially described as an iron-dependent regulator repressing the expression of iron uptake genes under iron-replete conditions. An early model proposed Fur metalated by Fe(II) under Fe(II)-replete conditions, activation of sensor-binding via a conformational change, binding of Fur to the promoter region of the target genes and consequent repression of the iron uptake systems to avoid metal overload. However, more recent studies suggested that the mechanism of gene regulation by Fur might be more complex and might include also positive regulation of gene expression (section 1.5.3.1.2). When acting as an iron-dependent repressor, Fur binds to a 19 bp consensus sequence known as the 'Fur Box': GATAATnATTATCATTATC (De Lorenzo et al, 1987) and often the same promoter can contain multiple partially overlapping Fur box sequences (section 1.5.3.1.2).

Bioinformatics analysis of the Fur regulon was performed in collaboration with Deenah Osman. Putative genes belonging to the Fur regulon in *Salmonella* were identified using the Regprecise database. From the comparison with the *E. coli* Fur box (De Lorenzo et al, 1987), a Fur binding site upstream of these genes was identified. Alignment of the binding sites identified in *Salmonella* was used to identify the consensus sequence of Fur in this organism, which is identical to the *E. coli* one (**Figure 4.15**).

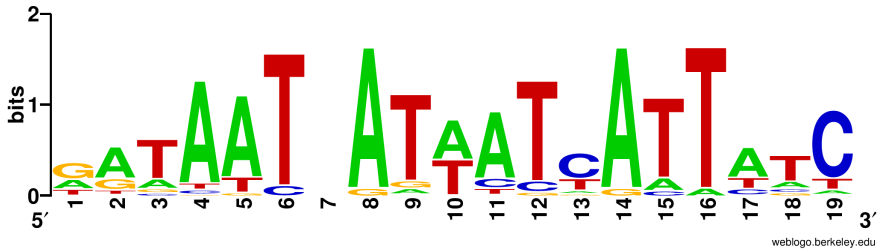

Figure 4.15. Fur nucleotide-binding sequence: The Fur Box.
Consensus sequence built with Weblogo based of the Fur nucleotide-binding sites identified in *Salmonella* using RegPrecise, based on homology with *E. coli*. The Fur Box in *Salmonella* is almost identical to the one from *E. coli*.

The Fur regulon overlaps with the regulatory networks of other transcriptional regulators. For example, section 3.4.1 described how most of the genes regulated by MntR have an identified Fur Box in the promoter region. However, *iroB* (iron regulated outer membrane protein) is regulated only by Fur in *Salmonella*. This genes belongs to the *iroBCDE* operon, which encodes proteins required for the conversion of the enterobactin siderophore into salmochelin, a stealth siderophore employed in iron-uptake (Bäumler et al, 1996; Muller et al, 2009). Expression of *iroBCDE* operon was reported to be down-regulated by iron in wild-type *Salmonella* cells, and its expression increased when *fur* was deleted (Taylor et al, 2009; Troxell et al, 2011). Deenah Osman confirmed that Fur regulates *iroB* also in the *Salmonella* strain used in this work by gene expression analysis (Osman et al, 2019). When *Salmonella* cells were grown in the presence of Fe(II) (the concentration of metal in the media was adjusted so that growth was not enhanced by more than 15% compared to standard M9 growth medium), the expression of *iroB* was repressed compared to growth in media with no metal supplementation. Therefore, *iroB* was chosen as a target to study the interaction between Fur and DNA in *in vitro* studies. There are three partially overlapping Fur binding sites in the promoter of *iroB* (**Figure 4.16**), with different degree of similarity with the canonical *Salmonella* Fur Box (**Figure 4.15**). The sequence underlined in **Figure 4.16** was used to design the oligonucleotide for the *in vitro* characterisation (section 4.5.2).

In Chapter 5, the change in fractional promoter occupancy by Fur as a function of the buffered concentration of iron will be calculated combining several experimentally determined parameters. One of the parameters required is the number of Fur target genes in *Salmonella*. Due to the complexity of this regulatory network, the simple bioinformatic analysis performed with the manually curated Regprecise database might not provide a complete picture of the Fur regulon in this organism. Recently, a genome-wide characterisation of Fur regulatory network was performed in *E. coli*, combining data from chromatin immunoprecipitation with lambda exonuclease digestion followed by high-throughput sequencing (ChIP-exo) for Fur and RNA polymerase (RNAP) and from strand-specific massively parallel complementary DNA sequencing (RNA-seq) (Seo et al, 2014). A total of 81 genes, grouped in 42 transcriptional units (i.e. 42 promoter regions) were found to be regulated by Fur. Among these, 37 transcriptional units were associated with sequences bound by Fur under iron-replete conditions but not iron-starvation. A number of 37 DNA targets was therefore used for *Salmonella* Fur in **Table 5.2**.

TTCACCGCTTAACGCTCTCATCTTTCCCGATTTTTACGCAAAAA

ATCATCACATGATCAAGTGTCATATTAGTTATTGCATTTTACAA

ATGATATTGGTAATTATTATCATTCTCATTAACGACTTGTTCGA

TTTATGACGTGGAGAGAGAGGATTTCTCATGCGTATTCTGTTTG

Figure 4.16. The *iroB* promoter.
Architecture of the promoter region of the Fur-regulated gene *iroB*. Three partially overlapping putative Fur binding sequences are present upstream of *iroB* (underlined, highlighted and bold sequences respectively). In red: *iroB* coding region with the start codon ATG. The underlined binding sequence was used to design the oligonucleotides for the *in vitro* DNA-binding experiments.

4.5.2 Analysis of Fur DNA-binding properties on *iro*BPro

4.5.2.1 Analysis of Fur-iroBPro stoichiometry by size-exclusion chromatography

In order to study the interaction of Fur and the *iroB* promoter *in vitro*, a preliminary study of the stoichiometry of protein-DNA interaction was performed using size-exclusion chromatography. The 37 bp oligonucleotide *iroBPro*-un, containing one of the Fur recognition sequences in the *iroB* promoter (**Figure 4.16**), was designed as reported in **Figure 4.17**. The oligonucleotide was annealed with its reverse complement by heating the mixture of the two strands and slowly cooling the reaction to room temperature. **Figure 4.17b** shows native PAGE confirming successful annealing. Increasing amounts of the protein were incubated with *iroB*Pro-un before resolving the mixture on a size-exclusion column (**Figure 4.18**). Fur was anticipated to bind to *iroB*Pro in its metal-bound form, requiring, therefore, to include Fe(II) in the buffer to activate the sensor to DNA-binding. However, as the experiment needed to be performed outside of the anaerobic glovebox to access the chromatographic system, the oxygen-sensitive metal could not be employed. Manganese was used instead as a surrogate and all the buffers employed contained 500 μM of Mn(II) to ensure DNA-binding activation. The elution of DNA was monitored from the absorbance at 260 nm (**Figure 4.18a**). When *iroB*Pro-un was incubated with one equivalent of Fur dimer, the DNA eluted in two peaks. One had the same elution volume as free DNA and the other (at a lower elution volume, 14.0 ml) was consistent with the formation of a Fur:*iroB*Pro-un complex. The free DNA peak disappeared at a DNA:Fur dimer ratio of 1:2, suggesting that the second peak observed was *iroB*Pro-un in complex with two Fur dimers. At higher protein:DNA ratios, the peak gradually shifted to a lower retention volume, indicating the formation of larger complexes. The experiment was stopped after incubation of *iroBPro*-un with 7 equivalents of Fur dimer; at this point, the DNA:Fur peak eluted at 12.9 ml. Interestingly, in the chromatography runs where a high concentration of protein was employed, a slight increase in absorbance was observed at an elution volume greater than free DNA (~15.4 ml). The comparison with the chromatogram of Mn(II)-Fur alone (**Figure 4.18b**) suggested that the small increase in absorbance might be due to the elution of free protein. These results suggested the formation of a tight complex between one *iroB*Pro-un molecule and two Fur dimers, plus the formation of weaker larger complexes at higher concentrations of protein.

a

F 5′ AAT<u>GATATTGGTAATTATTATCATTCTCATTAAC</u>GAC 3′

b

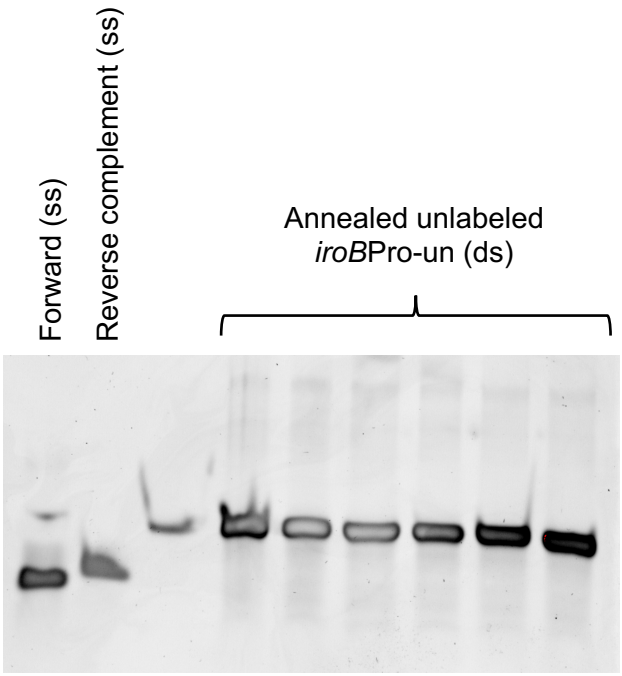

Figure 4.17. Production of the double stranded oligonucleotide *iroB*Pro-un for size-exclusion chromatography experiments.
a, 37 bp oligonucleotide containing the identified Fur recognition site (underlined) and flanking nucleotides in the *iroB* promoter. The shown oligonucleotide was annealed with its reverse complement. **b**, Annealing was confirmed by native PAGE (12% w/v), staining the DNA with with ethidium bromide. The single-stranded (ss) oligonucleotides were run on the same gel as a control to show the different migration from the double-stranded (ds) *iroB*Pro-un.

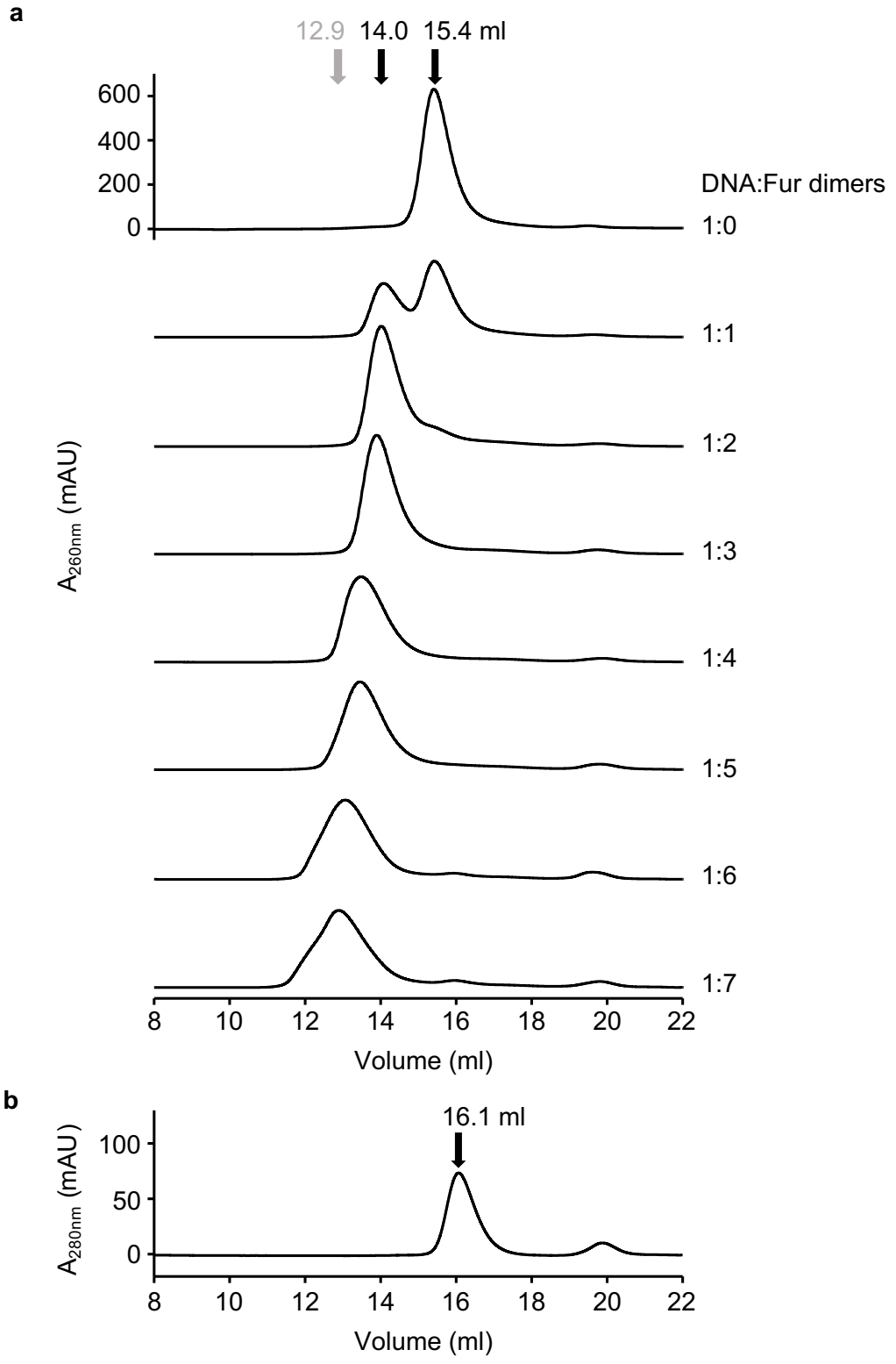

Figure 4.18. Determination of Fur-DNA stoichiometry by size-exclusion chromatography.
a, *iroB*Pro (10 μM) was pre-incubated with various concentrations of Fur (0–140 μM protein monomer) in the presence of 500 μM Mn(II) and the mixture resolved on a Superdex 200 10/300 GL column. The elution profile of the DNA was followed by measuring the absorbance at 260 nm. **b**, Fur (200 μM) was incubated with 500 μM Mn(II) and resolved on the same column. The elution profile was monitored via absorbance at 280 nm.

To better interpret the data in **Figure 4.18**, Fur elution was followed by measuring the protein content by Bradford assay in the fractions collected during the size-exclusion experiments (**Figure 4.19**). At 1:1 DNA:protein ratio, Fur eluted in a single peak corresponding to the same elution volume of the first DNA:protein peak observed in **Figure 4.18** (14.05 ml). The sensor concentration in the peak increased at 1:2 ratio. In the presence of larger amounts of Fur, the peak gradually shifted to a lower retention volume, reaching 13.05 ml at 1:7 DNA:protein ratio. After the 1:3 ratio, a shoulder appeared at 16.05 ml and then became a defined peak in the presence of a higher concentration of protein. This peak is consistent with the presence of free Mn(II)-Fur (white symbols as a reference). The results in **Figure 4.18** and **Figure 4.19** suggested that tight binding of two Fur dimers to *iroB*Pro-un was initially observed. As the DNA was incubated with increasing amounts of sensor, higher order complexes of protein:DNA started forming. They appeared to be weaker than the ternary *iroB*Pro-un:Fur complex and free Mn(II)-Fur started accumulating as well. However, it was not possible to define the stoichiometry of these higher-order complexes.

4.5.2.2 Analysis of Fur-iroBPro stoichiometry by fluorescence anisotropy

The Fur-*iroB*Pro stoichiometry was further investigated by fluorescence anisotropy (for a description of the technique see section 3.4.3). The fluorescently labelled version of the *iroB*Pro oligonucleotide was prepared with HEX fluorophore at the 5′ end (**Figure 4.20**). To mimic the conditions of the experiment in **Figure 4.18**, a high concentration of *iroB*Pro (1 μM) was titrated with Fur in the presence of 500 μM Mn(II). The change in anisotropy was measured after each addition of metalated sensor. The change in fluorescence anisotropy, Δr_{obs}, increased linearly up to a point of inflection corresponding to two Fur dimers bound per *iroB*Pro molecule (**Figure 4.21**). As observed previously for MntR (section 3.4.4), after the point of inflection the Δr_{obs} sharply increased instead of plateauing as a consequence of DNA saturation with protein. These data confirmed what was observed in the size-exclusion experiment (**Figure 4.18** and **Figure 4.19**): The first event observed is tight binding of two Fur dimers to *iroB*Pro while at higher protein:DNA ratios, weaker, higher order binding events occur between Fur and *iroB*Pro (and possibly between different protein:DNA complexes). The formed DNA:protein complexes have an unknown stoichiometry. Fur proteins have been reported to undergo oligomerization on DNA (Le Cam et al, 1994; Roncarati et al, 2016). In the case of *iroB*, this phenomenon might be enhanced by the presence of three overlapping Fur-binding sites (**Figure 4.16**) in the promoter region. In fact, the DNA sequence chosen to design *iroB*Pro contains also a proportion of the adjacent binding site (**Figure 4.16**) which might contribute to several Fur dimers binding to the oligonucleotide.

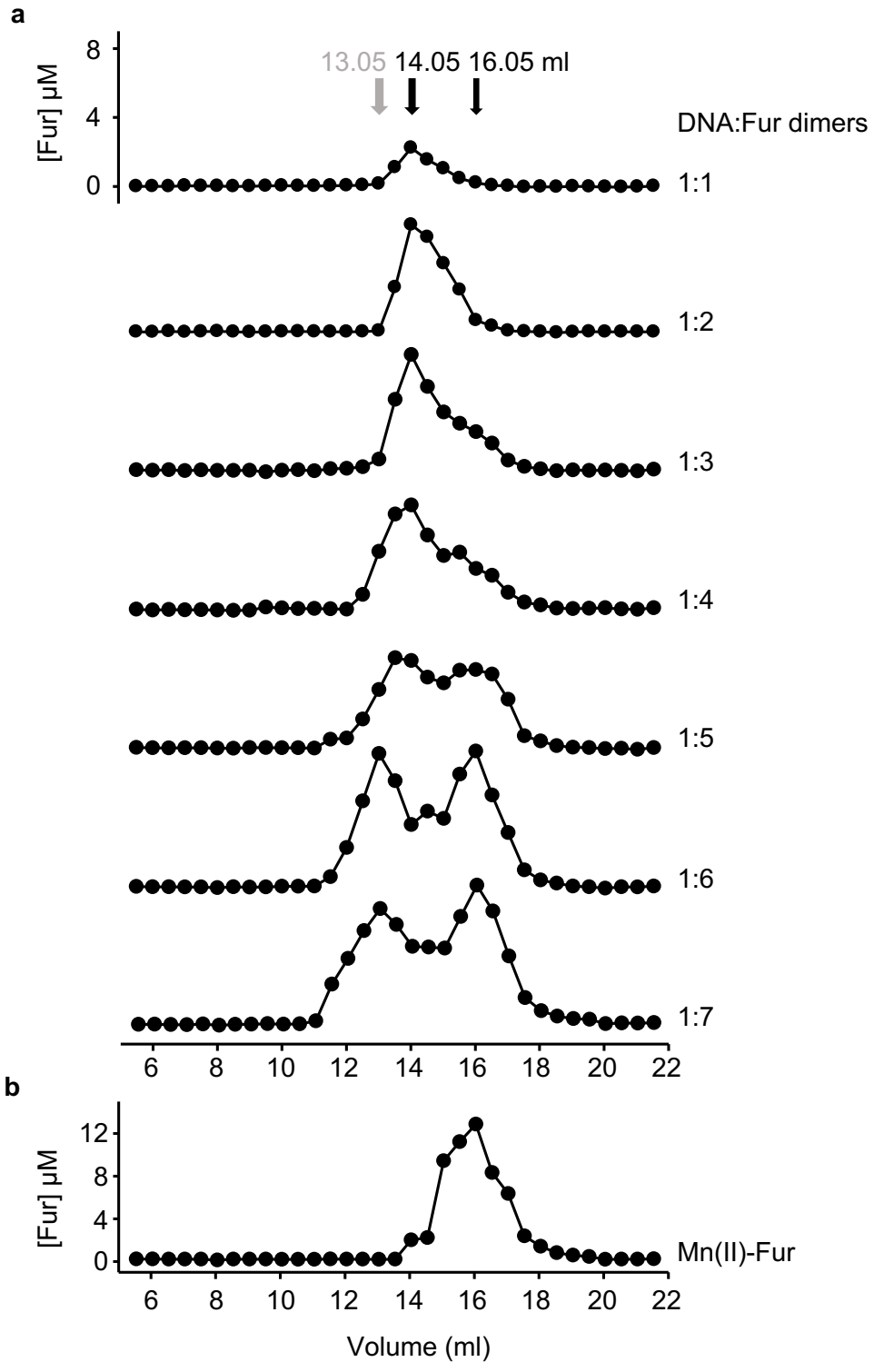

Figure 4.19. Determination of protein concentration following size-exclusion chromatography of Mn(II)-Fur-*iroB*Pro mixtures.
The protein concentration in the fractions (0.5 ml) collected from the size-exclusion chromatography (Superdex 200 10/300 GL column), shown in **Figure 4.18,** was determined by Bradford assay.

a

F 5′[HEX]-AATGATATTGGTAATTATTATCATTCTCATTAACGAC 3′

b

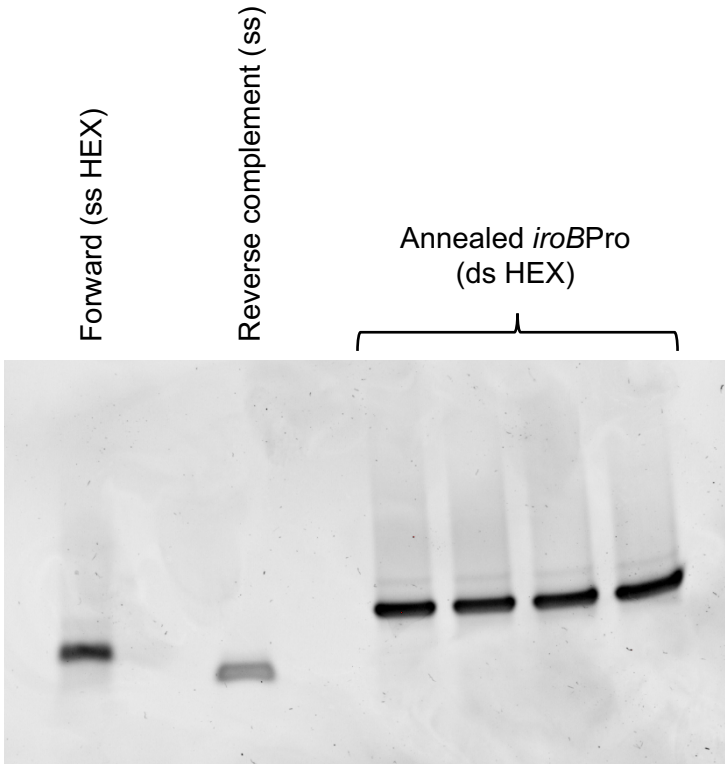

Figure 4.20. Production of the double stranded oligonucleotide *iroB*Pro for fluorescence anisotropy experiments.
a, 37 bp oligonucleotide containing the identified Fur recognition site (underlined) and flanking nucleotides in the *iroB* promoter. The shown oligonucleotide (fluorescently labelled, 5′-HEX) was annealed with its unlabelled reverse complement. **b**, Annealing was confirmed by native PAGE (12% w/v), staining the DNA with with ethidium bromide. The single-stranded (ss) oligonucleotides were run on the same gel as a control to show the different migration from the double-stranded (ds) *iroB*Pro.

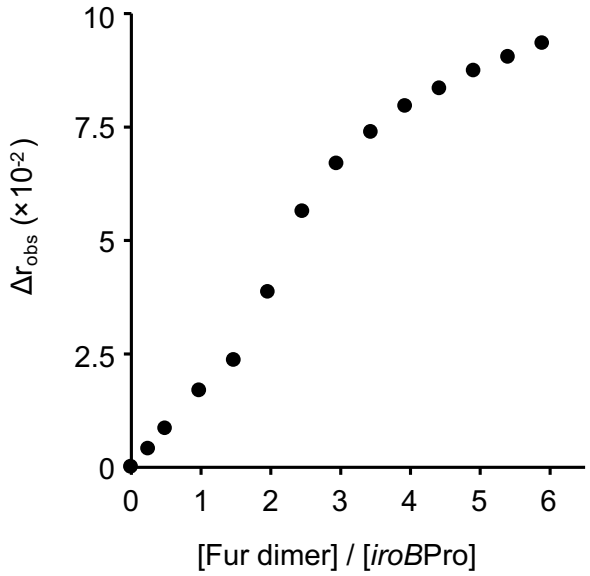

Figure 4.21. Higher order binding events are confirmed by fluorescence anisotropy. Fluorescence anisotropy change (Δr_{obs}) following titration of an elevated concentration of *iroB*Pro (1 μM) with Mn(II)-Fur. Δr_{obs} shows a point of inflection at two Fur dimers per *iroB*Pro, followed by a sharp increase indicative of weaker higher order binding events.

4.5.3 Analysis of Fur DNA-binding properties on *furbox*

In an attempt to reduce Fur oligomerization on DNA, fluorescence anisotropy experiments were performed in the presence of a shorter fluorescently labelled oligonucleotide (**Figure 4.22**). The 25 bp *furbox* oligonucleotide only contained the Fur DNA-recognition sequence plus three guanine bases at each end. Fluorescence anisotropy experiments using a similar oligonucleotide were performed on *E. coli* Fur (D'Autreaux et al, 2007). As all of these experiments could be performed under anaerobic conditions, Fe(II) was employed to study the metalated form of the sensor. Therefore, all the buffers for the experiments involving Fe(II)-Fur contained 5-50 μM Fe(II) (this concentration is sufficient to ensure full metalation of Fur, as it is ~ 10-fold greater than the $K_{Fe(II)}$, see section 4.4).

4.5.3.1 Determination of Fur-furbox stoichiometry by fluorescence anisotropy

To determine the stoichiometry of DNA-binding of Fur to *furbox*, a high concentration of oligonucleotide (1 μM) was titrated with Fe(II)-Fur in the presence of 50 μM of ferrous iron. As shown in **Figure 4.23**, the fluorescence anisotropy increased linearly to a point of inflection corresponding to two Fur dimers bound to DNA. After the point of inflection, only a slight increase in fluorescence anisotropy was observed, probably due to non-specific binding of Fur to DNA due to the high concentration of protein and DNA present in the assay. These results suggested a stoichiometry of two Fur dimers per *furbox* molecule. These results are consistent with the recently solved structure of *M. gryphiswaldens* Fur bound to the Fur Box from *P. aeruginosa* (Deng et al, 2015).

4.5.3.2 Determination of the DNA-binding affinity on furbox by fluorescence anisotropy

To determine the affinity of Fur for *furbox* (**Figure 4.22**), the fluorescence anisotropy experiments were performed in the presence of a low concentration of DNA. *furbox* (10 nM) was titrated with Fur in the absence and presence of Fe(II) (**Figure 4.24**). In the presence of Fe(II), binding of Fur to *furbox* was observed. In the absence of Fe(II) (EDTA was included in the buffers to exclude the presence of any other contaminating metal), Fur exhibited a weaker affinity for *furbox* compared to its metalated form. Binding to DNA could be observed only at high concentration (>1 μM) of apo-sensor. The tighter affinity for DNA of Fe(II)-Fur compared to its apo-form confirmed its role as a co-repressor on *iroB*. When Fe(II) availability in the cell increases, Fur is metalated and binds to the promoter of *iroBCDE*, repressing the expression of this operon. This contributes to a reduction in Fe(II)-uptake. However, as already mentioned (section 1.5.3), Fur can regulate its target genes via a variety of different mechanisms (including direct and indirect gene regulation).

a

F 5′[HEX]-GGG<u>GATAATGATAATCATTATC</u>GGG 3′

b

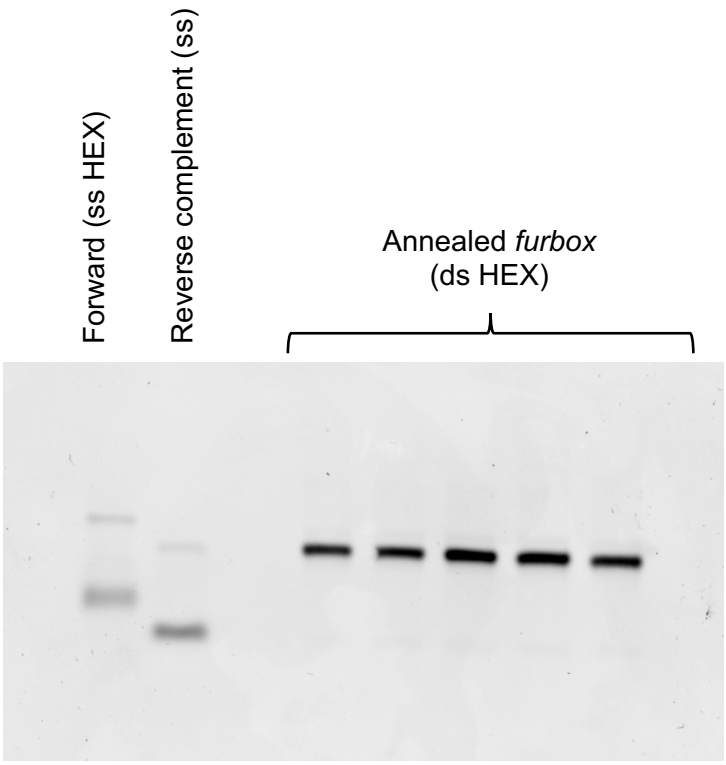

Figure 4.22. Production of the double stranded oligonucleotide *furbox* for fluorescence anisotropy experiments.
a, 25 bp oligonucleotide containing the identified Fur consensus sequence (underlined), with additional nucleotides at the extremes. The shown oligonucleotide (fluorescently labelled, 5′ HEX) was annealed with its unlabelled reverse complement. **b**, Annealing was confirmed by native PAGE (12% w/v), staining the DNA with with ethidium bromide. The single-stranded (ss) oligonucleotides were run on the same gel as a control to show the different migration from the double stranded (ds) *furbox*.

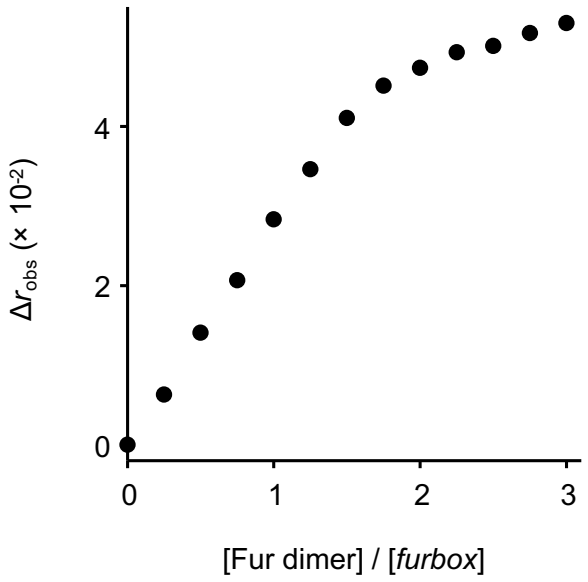

Figure 4.23. Two Fur dimers bind to *furbox* with tight affinity.
Representative (n = 3) fluorescence anisotropy change (Δr_{obs}) following titration of an elevated concentration of *furbox* (1 μM) with Fe(II)-Fur. Δr_{obs} increases linearly to a point of inflection at two Fur dimers per *furbox*. Figure and caption are adapted from (Osman et al, 2019).

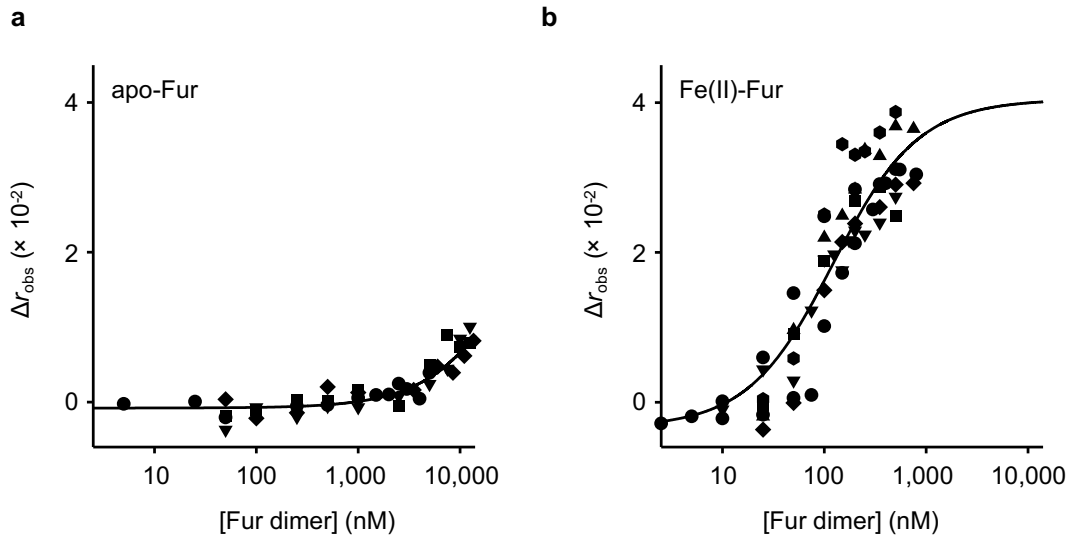

Figure 4.24. Determination of Fur affinities for *furbox*.
Fluorescence anisotropy change (Δr_{obs}) following titration of *furbox* (10 nM) with apo-Fur in 5 mM EDTA (**a**) and Fe(II)-Fur in 5-50 µM Fe(II) (**b**). Shapes represent different experiments. The data were fit to a model describing two Fur dimers binding sequentially to *furbox*. The solid line is a simulation with the average of K_{DNA} obtained from the individual experiments (n = 4 in **a**; n = 7 in **b**). Figure and caption are adapted from (Osman et al, 2019).

On the basis of the stoichiometry determined from the experiment in **Figure 4.23**, the data in **Figure 4.24** were fit to a model describing two Fur dimers binding sequentially to *furbox*. In this model, the two Fur-binding sites on *furbox* had the same individual affinity for the sensor. The two (macroscopic) constants obtained from the fit were therefore linked by statistical factors: $K_{2DNA} = 4 \times K_{1DNA}$. First, the individual Fe(II)-Fur experiments in **Figure 4.24a** were fit independently. The DNA-affinity of the metalated form of the sensors was determined for each dataset, as well as the change in anisotropy that, in these experiments, is associated with the formation of the complex of *furbox* with two Fur dimers (the 'response' in Dynafit). The average 'response' value was subsequently used as a fixed parameter to fit the apo-Fur datasets independently (**Figure 4.24b**). This was necessary as the weak affinity for DNA of apo-Fur did not allow the observation of *furbox* saturation with protein during the titration (a much higher concentration of protein would be needed). The absence of an end-point in the titration could complicate the fit of the data. The Dynafit script used to fit the data is reported in **Appendix B**. The obtained averaged DNA affinities for the first binding events, expressed as dissociation constants and as mean (±s.d.), were $K_{DNAapo} = 2.4\ (\pm 0.6) \times 10^{-5}$ M (n = 4) and $K_{DNAFe(II)} = 5.6\ (\pm 2.1) \times 10^{-8}$ M (n = 7). The solid lines in **Figure 4.24** are simulations calculated using the averaged K_{DNA} values.

Chapter 5.

Computing sensor responses as a function of cellular metal availability

5.1 Derivation of the thermodynamic model

5.1.1 Current thermodynamic models for metal sensing

5.1.1.1 Allosteric coupling

As described for the first time by Giedroc and collaborators (Giedroc & Arunkumar, 2007; Grossoehme & Giedroc, 2009; VanZile et al, 2002), the allosteric activation or inhibition of sensor-DNA interactions by metal-binding can be modelled with a thermodynamic cycle, where the metal- and DNA-binding equilibria are coupled (**Figure 5.1a**). Here, the sensor is represented in its four possible allosteric conformations (or 'end' states): the free sensor P, the two binary complexes $P{\cdot}M_2$ (in this case, two metals bind per protein assembly) and P·D and the ternary complex $P{\cdot}M_2{\cdot}D$. The model assumes that the sensor is an undissociable multimer active towards DNA-binding (for example a homodimer for MntR and Fur) and that metal-binding to the complement of allosteric site(s) occurs as a sole event with one thermodynamic constant. The allosteric coupling free energy between metal- and DNA-binding ($^{12}\Delta G_c$) for the sensor in **Figure 5.1** is defined as:

$$^{12}\Delta G_c = -RT \ln\left(\frac{^2K_1}{^0K_1}\right) = -RT \ln\left(\frac{^1K_M}{^0K_M}\right)$$

where R is the molar gas constant and T the temperature at which the experiments were performed. The first part of the equation contains the ratio of the DNA-affinity constants of the metalated ($P{\cdot}M_2$) and apo- (P) forms of the sensor, while the second contains the ratio of the metal-affinities of the DNA-bound (P·D) and DNA-free (P) sensor. The equality is a consequence of the system being a closed thermodynamic cycle and, as a result, it is necessary to determine only one of the two couples of thermodynamic constants to determine $^{12}\Delta G_c$ for a particular sensor. The sign of $^{12}\Delta G_c$ indicates whether binding of one of the two ligands inhibits or enhances binding of the second. If metal-binding enhances DNA-binding (for example in the case of a co-repressor) the favourable allosteric coupling free energy is $^{12}\Delta G_c < 0$. On the contrary, when metal-binding decreases DNA-affinity (for example in the case of a de-repressor) the allosteric coupling free energy is $^{12}\Delta G_c > 0$.

a

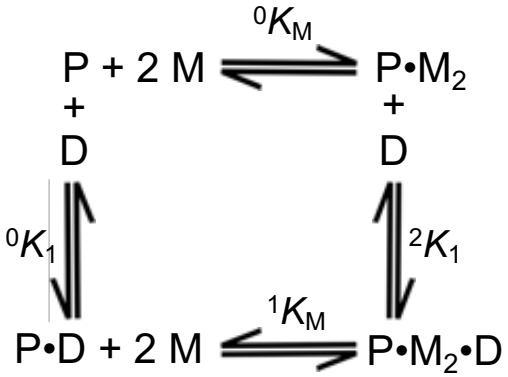

b

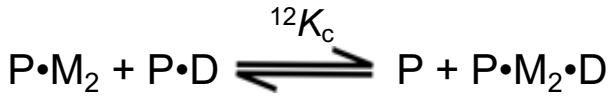

Figure 5.1. Allosteric coupling of metal- and DNA-binding.
a, Semi-schematic representation illustrating the coupled equilibria linking the four allosteric states of a sensor (P) binding to two allosteric ligands: the metal (M) and the DNA (D). **b**, Ligand exchange or 'dismutation' reaction dictating the degree of allosteric coupling between metal- and DNA-binding.

The coupling free energy $^{12}\Delta G_c$ can also be defined as the free energy associated with the 'dismutation' reaction in **Figure 5.1b**. With a favourable coupling free energy $^{12}\Delta G_c < 0$, the thermodynamic constant of the reaction is $^{12}K_c > 1$ and the equilibrium is shifted towards the right-hand side, with formation of the ternary complex ($P \cdot M_2 \cdot D$) over the two binary ones. With the coupling free energy $^{12}\Delta G_c > 0$, $^{12}K_c < 1$ and the equilibrium is shifted towards the binary complexes $P \cdot M_2$ and $P \cdot D$. Using the DNA-affinities measured for MntR and Fur (in Chapter 3 and Chapter 4 respectively), it is possible to calculate their allosteric coupling free energy. For MntR, K_{DNAapo} 8.6 (±1.7) × 10^{-8} M and $K_{DNAMn(II)} = 5 \times 10^{-9}$ M (mean ±s.d.). This gives ΔG_c = −1.7 (±0.1) kcal mol^{-1} (T = 298.15 K, 25° C). For Fur, K_{DNAapo} = 2.4 (±0.6) × 10^{-5} M and $K_{DNAFe(II)}$ = 5.6 (±2.1) × 10^{-8} M, giving ΔG_c = −3.6 (±0.2) kcal mol^{-1}. Both MntR and Fur, two co-repressors, have a negative ΔG_c. This reflects metal-binding enhancing DNA-binding, as $K_{DNAmetal}$ is tighter than K_{DNAapo}. The formation of the ternary complex protein:metal:DNA is favoured over the two binary complexes protein:metal and protein:DNA. The degree of allosteric activation is smaller for MntR, consistently with the $K_{DNAMn(II)}$ and K_{DNAapo} being only one order of magnitude apart.

5.1.1.2 Three-body equilibria

The system described by Giedroc is a typical example of a more general linear three-body (ternary complex) thermodynamic cycle, as shown in **Figure 5.2** (Douglass et al, 2013). In these systems of chemical equilibria, the species A and C can form binary and ternary complexes with B (acting as bridging species, **Figure 5.2a**), while they do not interact with each other. In the case of the metal sensors, B is the sensory protein while A and C can represent metal and DNA respectively. If binding of A or C affects binding of the other ligand, the thermodynamic constant associated with this second event is rescaled by the cooperativity factor α ($\alpha = 1$ indicates a non-cooperative system). In the presence of cooperativity, the system can be either positively ($\alpha > 1$) or negatively ($\alpha < 1$) cooperative, if binding of A to B favours or inhibits, respectively, binding of C to form the ternary complex. In terms of the allosteric coupling free energy described above, $\alpha > 1$ corresponds to $^{12}\Delta G_c < 0$ and $\alpha < 1$ to $^{12}\Delta G_c > 0$.

While more than a century ago Langmuir's studies on gas absorption (Langmuir, 1916) made a significant contribution to the mathematical characterisation of binary complexes equilibria, the mathematical characterisation of three-body equilibria has remained elusive for decades. To draw a complete mathematical characterisation of the system, the ideal goal would be to derive analytical solutions to calculate all the variables present in the system ([A], [B], [C], [AB], [BC] and [ABC]) as a function of the measurable parameters. These are the thermodynamic constants (K_A, K_B), the cooperativity factor (α) and the total concentrations of the species involved ($[A]_{tot}$, $[B]_{tot}$, $[C]_{tot}$).

a

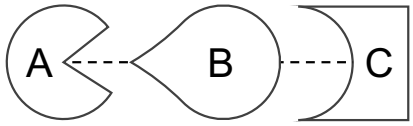

b

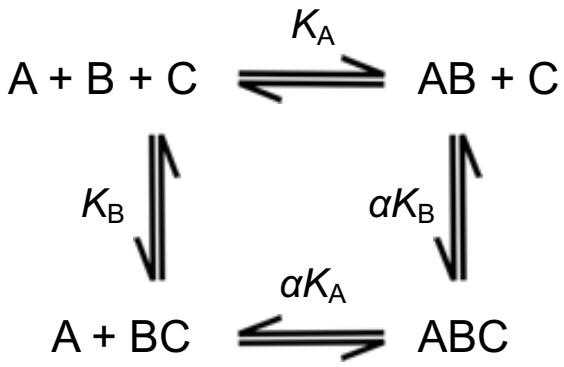

Figure 5.2. Three-body equilibria.
a, Schematic representation of a linear three-body (ternary complex) between A, B and C. B acts as a bridging species, while A and C do not interact directly. B can for binary complexes with both A and C. **b**, thermodynamic cycle representing the chemical equilibria involved in the formation of a ternary complex. In the presence of cooperativity, the binding constants are rescaled by the cooperative factor α.

However, Spiegel and collaborators have recently demonstrated that for three-body equilibria where cooperativity is present ($\alpha \neq 1$) an analytical solution cannot be derived (Douglass et al, 2013). A generally unsolvable quintic polynomial is in fact obtained when attempting to solve the simultaneous equations describing the system. Consequently, modelling three-body equilibria requires either making assumptions on the system (in order to simplify computation) or relying on numerical methods.

5.1.1.3 A model for sensor responses

The Robinson's group has used a variation of the three-body thermodynamic cycle to calculate the response of the metal sensors as a function of buffered concentration of metals (**Figure 5.3**) (Foster et al, 2017; Osman et al, 2017; Osman et al, 2019; Osman et al, 2015). Similarly to **Figure 5.1**, in this system the sensor is represented in the four allosteric conformations (P, PM, PD, (PM)D) linked by coupled metal- (K_1, K_2) and DNA-binding (K_3, K_4) equilibria. Also in this case, the model assumes that the sensor is in its multimeric state capable of binding DNA, and this state is undissociable (i.e. homo-oligomerization equilibria are not considered). The thermodynamic constant K_1 describes a single metal-binding affinity for the complement of allosterically effective sites (four sites per MntR dimer, two per Fur dimer, sections 3.3.3 and 4.4). In this model, in addition to the sensory protein (P), metal (M) and DNA (D), a hypothetical metal buffer system (B) is present, with additional chemical equilibria governed by K_5, K_6, K_7. These additional reactions represent metal exchange between the sensor and the metal buffer system that occur with an associative mechanism (with formation of the complexes PMB and (PMB)D), without involving the slow release of hydrated metal ions in the cytosol.

The occupancy of sensor with metal (based purely on the metal-affinity K_1) had commonly been used a surrogate measure of the sensitivity. To consider both the contributions of metal-affinity and allostery, the Robinson's group investigated the fractional occupancy of the target operator-promoters to define sensor sensitivity. The fraction of target DNA occupied by the cognate sensor at any given buffered metal concentration (θ_D) is defined as:

$$\theta_D = \frac{[PD] + [PMD]}{[D] + [PD] + [PMD]},$$

while the sub-fraction occupied uniquely by metalated sensor (θ_{DM}) is:

$$\theta_{DM} = \frac{[PMD]}{[D] + [PD] + [PMD]}.$$

θ_D is important for co-repressors and de-repressors, while θ_{DM} is the relevant parameter for the MerR-like activators because of their mode of action (section 1.5). From the change in θ_D and θ_{DM} for a sensor as a function of buffered concentration of its cognate metal, the sensor sensitivity can be determined.

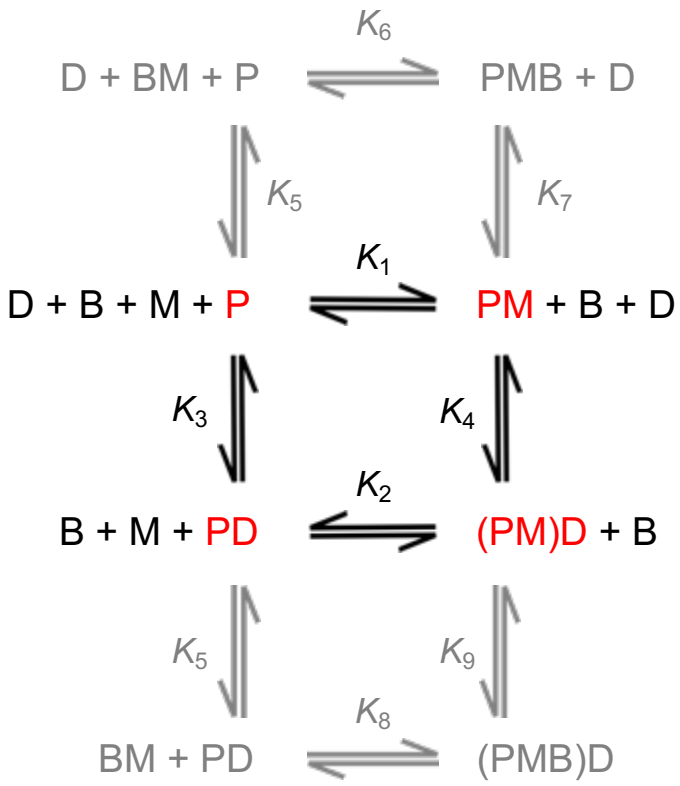

Figure 5.3. Thermodynamic coupling of metal-binding and DNA-binding to describe sensor response
Semi-schematic representation of a metal sensor in its four allosteric conformations: apo-protein (P), metal-protein (PM), apo-protein-DNA (PD) and metal-protein-DNA ((PM)D). The four states are linked by coupled thermodynamic equilibria (K_1 to K_4). Buffered metals exchange from and to the buffer occurs via association with the sensor molecule (K_5 to K_9). Figure and caption are adapted from (Osman et al, 2019).

Calculating θ_D and θ_{DM} for a sensor requires knowing three of the four thermodynamic constants (K_1, K_2, K_3, K_4) for the metal- and DNA-binding equilibria, the number of DNA targets (D_T) and the copy number of active sensors multimers per cell (P_T). As seen in section 5.1.1.2, metal sensors are an example of three-body cooperative equilibria and an analytical solution for the system cannot be obtained (Douglass et al, 2013). However, the intractable restrains of a three-body system were (inadvertently) bypassed by considering the metal to be buffered. A mathematical method to express θ_D and θ_{DM} as a function of the buffered metal concentration was developed. Building up on previous simpler models to calculate sensor responses (Foster et al, 2017; Osman et al, 2015), a numerical method based on the nonlinear least-squares regression analysis program DynaFit (Kuzmic, 1996) was derived by Deenah Osman and Andrew Foster (both from Durham University) (Osman et al, 2017).

To mathematically define the buffered metal concentration, the model makes use of a stratagem involving the hypothetical buffer B. The buffered metal concentration is governed by the affinity of the buffer for the metal (K_5) and this parameter is altered iteratively during the computation. By doing this, buffered metal concentration can span thirteen orders of magnitude in the calculations. The constants K_6 and K_7 are not involved in the mathematical calculations and simply describe the associative route of metal exchange. The concentration of buffering species is set 10-fold higher than the total concentration of metal in the system, which is in turn 1000-fold higher than the concentration of sensory protein in the cell. This ensures that metal-binding to the sensor does not alter the buffered metal concentration by depleting the buffer system of metal. This method was used to examine sensitivity and specificity of Co(II) and Zn(II) sensors from *Salmonella* (Osman et al, 2017) and will be applied in the next section to Fur.

5.1.2 Incorporation of change in protein abundance

For both MntR and Fur, three thermodynamic constants (K_1, K_3, K_4) and the number of DNA targets in *Salmonella* have been determined (Chapter 3 and Chapter 4). In order to calculate sensor responses using Dynafit (Osman et al, 2017), it is necessary to determine also the abundance of the two sensors in *Salmonella* cells. Deenah Osman, in collaboration with Junjun Chen and Thomas Huggins (Procter and Gamble), determined sensor abundances in *Salmonella* by quantitative multiple reaction monitoring mass spectrometry (MRM-MS) (**Table 5.1**) (Osman et al, 2017; Osman et al, 2019). Osman, Chen and Huggins analysed the lysates of *Salmonella* cells grown in M9 media (control condition, giving protein abundance P_0) and in M9 media supplemented with a non-lethal concentration of cognate metals (giving protein abundance P_1). The analysis revealed that the abundance of some sensors changes in response to a variation in metal concentration in the growth media.

Table 5.1. Metals change the abundance of some sensors to modify regulation.

Sensor	P_0 (multimers cell^{-1})	P_1 (multimers cell^{-1})
MntR	19 (±2)	20 (±5)
Fur	201 (±8)	547 (±120)
RcnR	22 (±2)	95 (±17)
NikR	68 (±4)	81 (±4)
CueR	24 (±11)	41 (±10)
ZntR	34 (±15)	29 (±4)
Zur	21 (±7)	36 (±3)

Abundances of each metal sensors in *Salmonella* lysate. Measurements were performed on cells grown in the absence (P_0) and in the presence (P_1) of non-lethal concentrations of the respective cognate metals. Data are reported as mean (±s.d.) of biologically independent samples. Data collected by Deenah Osman in collaboration with Junjun Chen and Thomas Huggins (Procter and Gamble). Table and caption adapted from (Osman et al, 2019).

In particular, the abundances of Fur and RcnR (the Co(II)/Ni(II)-sensing de-repressor, section 1.5.4) increased by about two- and four-fold, respectively, in response to an increase in concentration of their respective cognate metals. The change in sensor copy number as a function of buffered metal concentration adds a level of complexity to the mathematical modelling of the system, as protein abundance P_T is now one of the variables and not one of the fixed measurable parameters (as, for instance, the thermodynamic constants and the number of DNA targets). For each sensor, the two boundary states for protein abundance (P_0, at low metal concentration, and P_1, at high metal concentration) are known, but not how P_T transitions between these two 'end' states.

The computational method based on the Dynafit software (Osman et al, 2017) does not consider the change in protein abundance. Additionally, it is not possible to add such constraints to the model with the scripting language used by this software. However, the Dynafit script can be used to calculate sensor responses with constant P_0 and P_1, as shown in **Figure 5.4** for Fur. The light orange line (θ_D calculated using P_0) can describe well DNA occupancy by Fur only at low buffered [Fe(II)], while the dark orange trace (θ_D calculated with P_1) can describe well only the response at high [Fe(II)]. The comparison of the two responses revealed that the increase in Fur abundance in elevated iron determines an increase in DNA occupancy of about 15% (calculated from the difference between θ_D values calculated with P_0 and P_1 at high [Fe(II)]). If Fur exhibits a range of different affinities for its recognition sites within the large regulon, the change in protein abundance can contribute towards a graded response to metal, as the weaker DNA sites will be occupied by the sensors only when its abundance in the cell increases from P_0 towards P_1 in response to increased iron. A Fur graded response to iron was observed in *B. subtilis* (Pi & Helmann, 2017).

The values of fractional promoter occupancy (θ_D) reached at low and high [cognate metal], θ_{D0} and θ_{D1} respectively, represent the two boundary states for θ_D. For Fur (and more in general for the co-repressors), these are respectively the minimum and maximum values assumed by θ_D, while the opposite applies to de-repressors (for example, RcnR). P_T and θ_D are now two co-dependent variables: As the fractional DNA occupancy transitions from θ_{D0} to θ_{D1}, the autoregulatory sensor affects the transcription of its own gene, leading to the transition from P_0 to P_1. In order to understand how θ_D transitions from θ_{D0} to θ_{D1}, the fractional promoter occupancy was calculated with Dynafit using fixed protein abundances values at 10% increments between P_0 and P_1 (grey lines in **Figure 5.4**). Assuming a direct relationship between the change in θ_D and the change in P_T, data points where each 10% increment in DNA occupancy between θ_{D0} to θ_{D1} in reached in correspondence of the respective 10% increment in protein abundance between P_0 and P_1 were manually identified on the graph (black symbols).

a

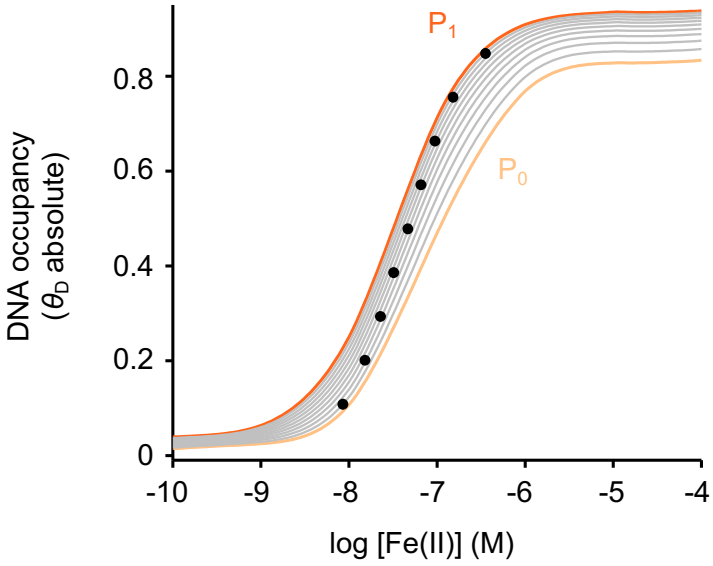

b

$$\frac{P_T - P_0}{P_1 - P_0} = \frac{\theta_D - \theta_{D0}}{\theta_{D1} - \theta_{D0}}$$

Figure 5.4. The relationship between change in protein abundance and change in DNA occupancy.
a, Fractional DNA occupancy (θ_D) calculated for Fur using the model presented in (Osman et al, 2017) and using constant protein abundances P_0 (light orange line), P_1 (dark orange line) and 10% increments between P_0 and P_1 (grey lines). Black symbols represent DNA occupancy where the total Fur abundance per cell at any given [Fe(II)] is linearly proportional to θ_D (**b**). The DNA occupancies θ_{D0} and θ_{D1} were calculated using P_0 and P_1 at low and high [Fe(II)] respectively. Figure and caption are adapted from (Osman et al, 2019).

These data points describe Fur-mediated response to Fe(II) taking into account the change in sensor abundance, something not achievable using solely the Dynafit script. Mathematically, the linear relationship between θ_D and the change in P_T can be expressed as:

$$\frac{P_T - P_0}{P_1 - P_0} = \frac{\theta_D - \theta_{D0}}{\theta_{D1} - \theta_{D0}}.$$

θ_{DM0} and θ_{DM1} represent, respectively, the lowest and highest values that θ_{DM} can assume (boundary states). The corresponding relationship between θ_{DM} and protein abundance for the MerR-like activators is:

$$\frac{P_T - P_0}{P_1 - P_0} = \frac{\theta_{DM} - \theta_{DM0}}{\theta_{DM1} - \theta_{DM0}}.$$

These equations, along with others describing mass balance and chemical equilibria relationships, were included in a set of simultaneous equations describing the system. Once solved, these simultaneous equations provided an analytical solution to calculate θ_D and θ_{DM} as a function of the buffered metal concentration including the change in protein abundance. Section 5.1.3 will describe some assumptions that simplify the computation, while section 5.2 will describe the mathematical solution of the simultaneous equations.

5.1.3 Metal buffer system and simplification of computation

As stated earlier, the model described by the thermodynamic cycle in **Figure 5.3** includes the hypothetical buffer system B. The sensory protein can exchange metal to and from the buffer via an associative mechanism, allowing the metal-exchange to be quick. In fact, for the tight-binding metal ions (for example Zn(II) and Cu(I)) the off-rates are so slow that equilibrium between the metal-bound and the metal-hydrated state cannot be reached in a viable lifetime (Foster et al, 2014a). Moreover, the associative mechanism allows the buffer to operate at a buffered concentration of metal that is less than one hydrated ion per cell (Foster et al, 2014a). For *Salmonella* and *E. coli* (cell volume = 1 fl), this equates to a concentration of about 10^{-10}–10^{-9} M, well above the sensitivities estimated for the Zur and CueR from *E. coli* (Changela et al, 2003; Outten & O'Halloran, 2001) and ZiaR from *Synechocystis* PCC 6803 (Foster et al, 2014b).

In the model for sensor response, the buffered metal is equally available to all the metal-binding sites of the sensor, without any kinetic bias arising from facilitated access to a particular site within the protein. Similarly to what was described previously for the Dynafit method (Osman et al, 2017), the concentration of buffering species is considered to be at least 10-fold in excess of the total concentration of metal, so that the buffer cannot be saturated with metal. The total metal concentration, also, greatly (1000-fold, at least) exceeds the concentration of sensor, so that metal-binding to the sensors has a negligible effect on the buffered concentration of metal. Conceptually, we can imagine that once a specific value for the buffered metal concentration is

set, metal flows from the exchangeable buffered pool to the sensors (or vice versa) until equilibrium is reached as dictated by the thermodynamic constants and the concentration of protein and DNA. The actual amount of exchanged metal is so small compared to the total metal present in the buffer, that the set buffered metal concentration remains unchanged. Mathematically, this means that the buffered metal concentration can be handled as an independent variable and that all of the other variables can be expressed as a function of it. This also means that it is not necessary to consider a mass balance equation for the metal, greatly simplifying the mathematical complexity of the system. It is therefore possible to analytically solve the simultaneous equations without obtaining high-order unsolvable equations as in the general three-body equilibria problem (Douglass et al, 2013).

5.2 Derivation of quadratic equations

5.2.1 Simultaneous equations

Given the system in **Figure 5.3**, we can write these relationships for the thermodynamic equilibrium constants of the metal- and DNA-binding equilibria:

$$K_1 = \frac{[PM]}{[P][M]}, \quad K_2 = \frac{[PMD]}{[PD][M]}, \quad K_3 = \frac{[PD]}{[P][D]}, \quad K_4 = \frac{[PMD]}{[PM][D]}.$$

As the system is a closed thermodynamic cycle, this relationship applies to the equilibrium constants, meaning that the experimental determination is required only for three of them:

$$K_3 = \frac{K_1}{K_2} K_4.$$

As described in the previous section, the buffered metal concentration $[M]$ can be treated as an independent variable and the other variables can be calculated as a function of it. It is thus necessary to write mass balance equations only for two of the species involved in the system, the target DNA ($[D_T]$) and sensor protein ($[P_T]$):

$$[D_T] = [D] + [PD] + [PMD] \qquad [P_T] = [P] + [PM] + [PD] + [PMD]$$

The numerical values for the concentration $[D_T]$ can be obtained converting the number of DNA targets per cell into moles per cell and then dividing by the cell volume. As described in section 5.1.1.3, the fractional DNA occupancy θ_D and its sub-fraction θ_{DM}, are defined at each buffered metal concentration as:

$$\theta_D = \frac{[PD] + [PMD]}{[D_T]} \qquad \theta_{DM} = \frac{[PMD]}{[D_T]}$$

While $[D_T]$ is a constant value and is independent of $[M]$, both θ_D (or θ_{DM}) and $[P_T]$ change as a function of $[M]$. Moreover, θ_D (or θ_{DM}) and $[P_T]$ are linearly co-dependent and their relationship is:

$$\frac{[P_T] - [P_0]}{[P_1] - [P_0]} = \frac{\theta_D - \theta_{D0}}{\theta_{D1} - \theta_{D0}} \qquad \frac{[P_T] - [P_0]}{[P_1] - [P_0]} = \frac{\theta_{DM} - \theta_{DM0}}{\theta_{DM1} - \theta_{DM0}}$$

The concentrations $[P_0]$ and $[P_1]$ can be obtained from the sensor abundances (expressed as multimers cell^{-1}) by converting them into moles cell^{-1} and then dividing by the cell volume. As described earlier, these equations form a system of simultaneous equations describing the equilibria in **Figure 5.3**:

$$\begin{cases} K_1 = \dfrac{[PM]}{[P][M]} \\ K_2 = \dfrac{[PMD]}{[PD][M]} \\ K_4 = \dfrac{[PMD]}{[PM][D]} \\ [D_T] = [D] + [PD] + [PMD] \\ [P_T] = [P] + [PM] + [PD] + [PMD] \\ \theta_D = \dfrac{[PD] + [PMD]}{[D] + [PD] + [PMD]} \qquad \theta_{DM} = \dfrac{[PMD]}{[D] + [PD] + [PMD]} \\ \dfrac{[P_T] - [P_0]}{[P_1] - [P_0]} = \dfrac{\theta_D - \theta_{D0}}{\theta_{D1} - \theta_{D0}} \qquad \dfrac{[P_T] - [P_0]}{[P_1] - [P_0]} = \dfrac{\theta_{DM} - \theta_{DM0}}{\theta_{DM1} - \theta_{DM0}} \end{cases}$$

The values for the parameters K_1, K_2, K_4, $[D_T]$, $[P_0]$, $[P_1]$ are known as they can be experimentally determined. In the first instance, values for θ_{D0} and θ_{D1} (or θ_{DM0} and θ_{DM1} in case the sensor under study is an activator from the MerR family) can be calculated using the Dynafit script (developed by Foster and Osman in (Osman et al, 2017), see section 5.1.1.3) if the other parameters are known; an alternative approach to calculate θ_{D0}, θ_{D1}, and θ_{DM0}, θ_{DM1} will be presented here. Once solved, the simultaneous equations will provide an analytical solution to express all of the variables (including θ_D and θ_{DM}) as a function of the buffered metal concentration $[M]$.

5.2.2 Solution of the simultaneous equations

To simplify the computation, the variables and the constant parameters are renamed as follows:

$$\begin{aligned} x &= [P], & v &= [PD], & a &= K_1, \\ y &= [M], & w &= [PMD], & b &= K_2, \\ z &= [D], & P_T &= [P_T], & c &= K_3, \\ D_T &= [D_T], & P_0 &= [P_0], & d &= K_4. \\ u &= [PM], & P_1 &= [P_1], \end{aligned}$$

The chemical equilibria and mass balance give these relationships between variables:

$$a = \frac{u}{xy}, \tag{1}$$

$$b = \frac{w}{vy}, \tag{2}$$

$$d = \frac{w}{zu}, \tag{3}$$

$$D_{\mathrm{T}} = z + v + w, \tag{4}$$

$$P_{\mathrm{T}} = x + u + v + w = x + u + D_{\mathrm{T}} - z. \tag{5}$$

By rearranging equations (1), (2) and (3), u and w can be expressed as:

$$u = axy, \qquad w = bvy = duz. \tag{6}$$

From (4), using the expression of w in (6), v can be determined:

$$D_{\mathrm{T}} = z + v + w = z + v + duz \;\Rightarrow\; v = D_{\mathrm{T}} - z - duz.$$

By substituting v into the right-hand side of (6), z can be expressed:

$$byv = by(D_{\mathrm{T}} - z - duz) = duz,$$

$$z = \frac{D_{\mathrm{T}} by}{du + by + bduy}. \tag{7}$$

5.2.2.1 Derivation of quadratic equation to determine θ_D

The linear relationship between the change in P_{T} and the change in θ_{D} can be rewritten as:

$$P_{\mathrm{T}} = \frac{\Delta P}{\Delta \theta_{\mathrm{D}}} \theta_{\mathrm{D}} + A_{\mathrm{D}}, \tag{8}$$

where

$$\Delta P = P_1 - P_0,$$

$$\Delta \theta_{\mathrm{D}} = \theta_{\mathrm{D}1} - \theta_{\mathrm{D}0},$$

$$A_{\mathrm{D}} = P_0 - \frac{\theta_{\mathrm{D}0} \Delta P}{\Delta \theta_{\mathrm{D}}}. \tag{9}$$

Using (4), the expression for θ_{D} can be rearranged as:

$$\theta_{\mathrm{D}} = \frac{v + w}{D_{\mathrm{T}}} = 1 - \frac{z}{D_{\mathrm{T}}}, \tag{10}$$

and substituted into equation (8), giving:

$$P_{\mathrm{T}} = \frac{\Delta P}{\Delta \theta_{\mathrm{D}}} \theta_{\mathrm{D}} + A_{\mathrm{D}},$$

$$x+u+D_{\mathrm{T}}-z=\frac{\Delta P}{\Delta\theta_{\mathrm{D}}}\left(1-\frac{z}{D_{\mathrm{T}}}\right)+A_{\mathrm{D}},$$

$$x+u-C_1z=C_2, \tag{11}$$

where the two constant parameters C_1 and C_2 have been defined as:

$$C_1=1-\frac{\Delta P}{\Delta\theta_{\mathrm{D}}\cdot D_{\mathrm{T}}}, \tag{12}$$

$$C_2=\frac{\Delta P}{\Delta\theta_{\mathrm{D}}}+A_{\mathrm{D}}-D_{\mathrm{T}}. \tag{13}$$

By substituting u and z into equation (11), an expression for x can be obtained:

$$x+axy-C_1\cdot\frac{D_{\mathrm{T}}by}{adxy+by+abdxy^2}=C_2,$$

$$x(1+ay)(adx+b+abdxy)-C_1D_{\mathrm{T}}b=C_2(adx+b+abdxy),$$

$$x^2(1+ay)(ad+abdy)+x[b(1+ay)-C_2(ad+abdy)]-C_1D_{\mathrm{T}}b-C_2b=0. \tag{14}$$

Equation (14) is a quadratic equation expressing the variable x (corresponding to the concentration of free apo-protein [P]) as a function of y (the buffered metal concentration [M]). In order to simplify the solution of the quadratic equation, the coefficients α, β and γ are introduced, so that (14) can be written as:

$$\alpha x^2+\beta x+\gamma=0,$$

$$\alpha=(1+ay)(ad+abdy),$$

$$\beta=b(1+ay)-C_2(ad+abdy),$$

$$\gamma=-b(C_1D_{\mathrm{T}}+C_2).$$

By substituting the known numerical values for the parameters a, b, d, C_1 and C_2, it is noted that for any given value of y, the coefficient α is always positive and γ is negative. It is known that the two solutions of a quadratic equation, x_1 and x_2, are linked by the relationship:

$$x_1x_2=\frac{\gamma}{\alpha}$$

In our case, $\frac{\gamma}{\alpha}<0$ indicates that the two solutions have opposite sign. As x represents a physical value (the concentration of free apo-protein [P]), the negative solution is meaningless. The positive solution can then be retained to give x as a function of y:

$$x=\frac{-\beta+\sqrt{\beta^2-4\alpha\gamma}}{2\alpha}. \tag{15}$$

Finally, equation (10) can be rearranged to express θ_D as a function of x:

$$\theta_D = 1 - \frac{z}{D_T}$$

$$\theta_D = 1 - \frac{by}{du + by + bduy}$$

$$\theta_D = 1 - \frac{b}{b + (ad + abdy)x}. \quad (16)$$

Equation (15) can be substituted into (16) to express the fractional DNA occupancy θ_D as a function of the buffered metal concentration (y). Equation (16), by substituting back the initial parameters for the thermodynamic constants and considering that A_D, C_1 and C_2 are expressed by equations (9), (12) and (13) respectively, can be rewritten as:

$$\theta_D = 1 - \frac{2K_2(1+K_1[M])}{K_2(1+K_1[M]) + C_2K_1K_4(1+K_2[M]) + \sqrt{K_2^2(1+K_1[M])^2 + K_1K_4(1+K_2[M])[C_2^2K_1K_4(1+K_2[M]) + K_2(4A_D - 2C_2)(1+K_1[M])]}}. \quad (17)$$

In order to obtain an easy-to-use tool that others could employ to calculate the fractional promoter occupancy, an electronic spreadsheet based on equations (15) and (16) was implemented to calculate θ_D given a range of buffered metal concentrations (**Figure 5.5**). The spreadsheet first calculates x using (15) and then uses the numerical values obtained to calculate θ_D from (16). The electronic spreadsheet, with instructions to enable the calculations, is available online in the Supplementary Information of the paper (Osman et al, 2019) as 'Supplementary Dataset'. By using equation (15) to substitute x in equations (1–6) it is possible to calculate how all of the other variables ([P], [PD], [PM], [PMD], [P_T], [D]) change as a function of the buffered metal concentration.

A simplified form of equation (17) can be written to calculate θ_D as a function of buffered [metal] when protein abundance P_T remains constants. In this case, $P_1 - P_0 = \Delta P = 0$, causing $A_D = P_0$, $C_1 = 1$ and $C_2 = P_0 - D_T$. The simplified equation can be used to calculate θ_{D0} and θ_{D1} with the electronic spreadsheet (using constant P_0 and P_1, respectively), without the need to use the Dynafit script to obtain the numerical values for the θ_D boundary states. Therefore, the calculations require to input numerical values solely for the parameters K_1, K_2, K_4, [D_T], P_0, P_1.

5.2.2.2 Derivation of quadratic equation to determine θ_{DM}

In the case of the MerR-like activators, the relationship between the change in P_T and the change in θ_{DM} can be rewritten as:

$$P_T = \frac{\Delta P}{\Delta \theta_{DM}} \theta_{DM} + A_{DM}, \quad (18)$$

where:

$$\Delta\theta_{DM} = \theta_{DM1} - \theta_{DM0},$$

$$A_{DM} = P_0 - \frac{\theta_{DM0}\Delta P}{\Delta\theta_{DM}}. \tag{19}$$

The expression for θ_{DM} can be substituted into equation (18) and by using the expression for P_T in (5) it is possible to write:

$$\theta_{DM} = \frac{w}{D_T}$$

$$x + u + D_T - z = B\frac{w}{D_T} + A_{DM}, \tag{20}$$

where the constant parameter B has been defined as:

$$B = \frac{\Delta P}{\Delta\theta_{DM}}. \tag{21}$$

The expressions for the variables u, w, z can be substituted into equation (20) using (6) and (7) to find x:

$$x + axy - \frac{bD_T}{adx + b + abdxy} - \frac{B \cdot abdxy}{adx + b + abdxy} = A_{DM} - D_T,$$

$$x^2(1+ay)(ad+abdy) + x[b(1+ay) - Babdy - (A_{DM} - D_T)(ad+abdy)] - bA_{DM} = 0. \tag{22}$$

Similarly to the previous case, the quadratic equation in (22) expresses x (corresponding to $[P]$) as a funcion of the buffered metal concentration y. To simplify the solution, the coefficients λ, μ and ν are introduced so that (22) can be written in the more familiar form:

$$\lambda x^2 + \mu x + \nu = 0,$$

where:

$$\lambda = (1+ay)(ad+abdy),$$
$$\mu = b(1+ay) - Babdy - (A_{DM} - D_T)(ad+abdy),$$
$$\nu = -bA_{DM}.$$

As seen previously for the derivation of the equations for θ_D, if numerical values for the parameters a, b, d, A_{DM} and B are substituted in the equations, it is noted that $\lambda > 0$ and $\nu < 0$ for any given value of y, meaning that the two solutions for the quadratic equations are one positive and one negative. Also in this case, the positive solution is retained:

$$x = \frac{-\mu + \sqrt{\mu^2 - 4\lambda\nu}}{2\lambda}. \tag{23}$$

The expression for θ_{DM} can be rearranged using (6) and (7) and expressed as a function of x:

$$\theta_{DM} = \frac{w}{D_T}$$

$$\theta_{DM} = \frac{duz}{D_T}$$

$$\theta_{DM} = \frac{abdxy}{b + (ad + abdy)x}. \quad (24)$$

By substituting equation (23) in (24), the fractional DNA occupancy θ_{DM} can be expressed as a function of the buffered metal concentration y. The final equation is more complex than the one presented for θ_D (equation (17)) and it is thus not reported here in its final form. However, equation (24) can easily be solved using an electronic spreadsheet, considering that x can be obtained from (23) for a range of buffered metal concentrations (y). Also in this case, the electronic spreadsheet with instructions to enable the calculations is available online in the Supplementary Information of the paper (Osman et al, 2019) as Supplementary Dataset (**Figure 5.5**). The calculation of θ_{DM} can be found in the 'activators' tab. By using equation (23) to substitute x in equations (1-6) it is possible to calculate how all of the other variables ([P], [PD], [PM], [PMD], [P_T], [D]) for the activators change as a function of the buffered metal concentration.

A simplified form of equation (24) can be written to calculate θ_{DM} as a function of buffered [metal] when protein abundance P_T remains constants. In this case, $\Delta P = P_1 - P_0 = 0$, determining $A_{DM} = P_0$ (19) and $B = 0$ (21). The simplified equation can be used to calculate θ_{DM0} and θ_{DM1} with the electronic spreadsheet (using constant P_0 and P_1 respectively), without the need to use the Dynafit script to obtain the numerical values for the θ_{DM} boundary states.

5.3 Application of mathematical model on experimental data

5.3.1 Responses of metal sensors from *Salmonella*

The equations derived in section 5.2 can be applied to the *Salmonella* sensors. The calculations in the electronic spreadsheet require to input $1/K_1$, $1/K_3$ and $1/K_4$ (the metal-affinity and the two DNA-affinities expressed as dissociation constants), P_0 and P_1 as sensor multimers per cell (if the abundance remains constant, the same value can be inserted twice), and the number of DNA targets. The user can also input the cell volume, so that [P_0], [P_1] and [D_T] can be calculated. A cell volume of 1 fl was used for *Salmonella*. The determination of the thermodynamic parameters for MntR and Fur was reported in Chapter 3 and 4 respectively, while the measure of protein abundance was reported in section 5.1.2. The parameters for all of the other sensors were determined by other members of the Robinson's group over the course of six years (Osman et al, 2017; Osman et al, 2019; Osman et al, 2015; Osman et al, 2016). The same experimental approach shown in Chapters 3 and 4 for MntR and Fur was applied to the other sensors.

Figure 5.5. An easy-to-use electronic spreadsheet allows the calculation of sensor responses. As described in section 5.2.2, a set of equations was derived to calculate sensor responses from the metal-affinities, DNA-affinities, sensor abundances and number of DNA target. The electronic spreadsheet file (here reported as a screenshot) is available in the supplementary information of (Osman et al, 2019).

Metal-affinities ($1/K_1$) were determined in competition assays between sensors and chelants having known affinity for the metal under study, while DNA-affinities were determined in the absence ($1/K_3$) and presence ($1/K_4$) of saturating amount of metals monitoring DNA-binding via fluorescence anisotropy. All the $1/K_1$, $1/K_3$ and $1/K_4$ values determined and the number of DNA targets for the seven *Salmonella* metal sensors are reported in **Table 5.2** (Osman et al, 2019).

Fractional DNA occupancies (θ_D for MntR, Fur, RcnR, NikR, Zur, and θ_{DM} for ZntR, CueR) were calculated as a function of buffered metal concentration from the values in **Table 5.1** and **Table 5.2** using the electronic spreadsheet (**Figure 5.5**) developed from the equations in section 5.2. The calculated absolute DNA occupancies are reported in **Figure 5.6a**. The absolute DNA occupancies were normalised from 0 to 1 independently for each sensor to facilitate inter-comparison of sensor responses (**Figure 5.6.b**). Remarkably, the sensitivities of the various sensors span twelve orders of magnitude, from the Cu(I)-sensor CueR (0.5 of normalised response at 1.2×10^{-18} M) to the Mn(II)-sensor MntR (0.5 of normalised response at 2.6×10^{-6} M). As mentioned in section 5.2.2, the equations developed allow the calculation not only of θ_D and θ_{DM}, but also of all the variables present in the system ([*P*], [*PD*], [*PM*], [*PMD*], [*D*], P_T) as a function of the buffered metal concentration. **Figure 5.7** shows the Fur variables calculated as a function of buffered Fe(II) concentration. The concentrations of [*P*], [*PD*] and [*D*] decrease in high [Fe(II)] as these species are replaced by [*PM*] and [*PMD*]. As described in section 5.1.2, when Fur starts responding to [Fe(II)], its abundance sharply increases from P_0 to P_1, as a result of Fur being autoregulatory. The peak observed for [*P*] and [*PD*] is likely caused by the newly produced Fur. However, the extent of this feature might be a function of the assumed linear relationship between P_T and θ_D.

Table 5.2. Metal-affinities, DNA-affinities, allosteric free energies and number of DNA targets for the sensors in *Salmonella*.

Sensor	Metal	K_{Metal} ($1/K_1$) (M)	K_{DNA} ($1/K_3$) (M)	K_{DNA} ($1/K_4$) (M)	ΔG_C (kcal mol^{-1})	No. DNA targets
MntR	Mn(II)	$1.3\ (\pm0.4) \times 10^{-5}$	$8.6\ (\pm1.7) \times 10^{-8}$	5×10^{-9}§§	-1.7 (±0.1)	4
Fur	Fe(II)	$5.3\ (\pm0.7) \times 10^{-7}$‡	$2.4\ (\pm0.6) \times 10^{-5}$	$5.6\ (\pm2.1) \times 10^{-8}$	-3.6 (±0.2)	37
RcnR	Co(II)	$5.1\ (\pm0.9) \times 10^{-10}$‡‡	$1.5\ (\pm0.8) \times 10^{-7}$‡‡	$1.5\ (\pm0.2) \times 10^{-5}$‡‡	+2.7 (±0.2)‡‡	1
NikR	Ni(II)	$2.5\ (\pm0.4) \times 10^{-12}$	$1.1\ (\pm0.1) \times 10^{-5}$	$9.5\ (\pm0.8) \times 10^{-9}$	-4.2 (±0.1)	2
CueR	Cu(I)	$3.3\ (\pm0.7) \times 10^{-19}$‡‡	$3.2\ (\pm1.2) \times 10^{-8}$§	$3.8\ (\pm1.8) \times 10^{-7}$§	+1.4 (±0.4)§	3
Zur	Zn(II)	$6.4\ (\pm0.4) \times 10^{-13}$‡‡	$2.7\ (\pm0.4) \times 10^{-5}$‡‡	$4.1\ (\pm1.0) \times 10^{-8}$‡‡	-3.9 (±0.2)‡‡	4
ZntR	Zn(II)	$3.2\ (\pm0.7) \times 10^{-12}$‡‡	$1.1\ (\pm0.4) \times 10^{-7}$	$7.8\ (\pm1.3) \times 10^{-7}$	+1.2 (±0.2)	1

All thermodynamic values are reported as mean (±s.d.) and are reported as dissociation constants. The metal-binding data were fit to models describing a single combined affinity for the complement of allosterically effective sites: four sites per MntR dimer and NikR tetramer, two per Fur and Zur dimer, two per RcnR tetramer, one per CueR and ZntR dimer. Except for the MntR and Fur data shown in this thesis, the other thermodynamic values were determined by members of the Robinson and Chivers groups over the course of five years: § from (Osman et al, 2019); ‡ from (Osman et al, 2015); ‡‡ from (Osman et al, 2016); §§ from (Osman et al, 2017). Table and caption adapted from (Osman et al, 2019).

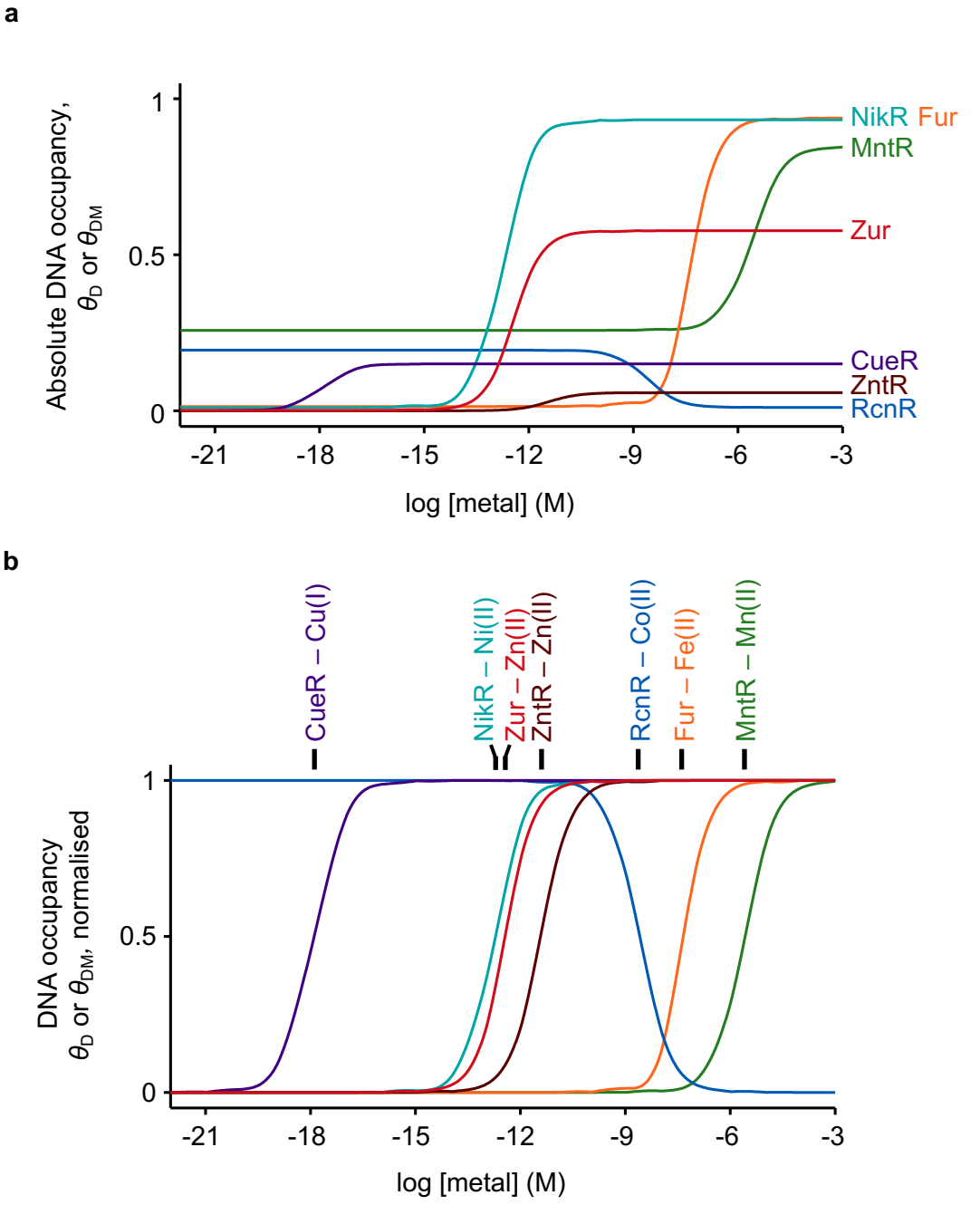

Figure 5.6. Calculation of sensor responses.
Absolute (**a**) and normalised (**b**) calculated DNA occupancy for all of the sensors in response to increasing buffered concentrations of cognate metals. The calculations combined metal affinities, DNA affinities, sensor abundances and number of DNA targets (**Table 5.1** and **Table 5.2**) using the equations in the electronic spreadsheet (**Figure 5.5**). Sensor responses are expressed as θ_D for MntR, Fur, RcnR, NikR, Zur, and θ_{DM} for ZntR and CueR. Figure and caption are adapted from (Osman et al, 2019).

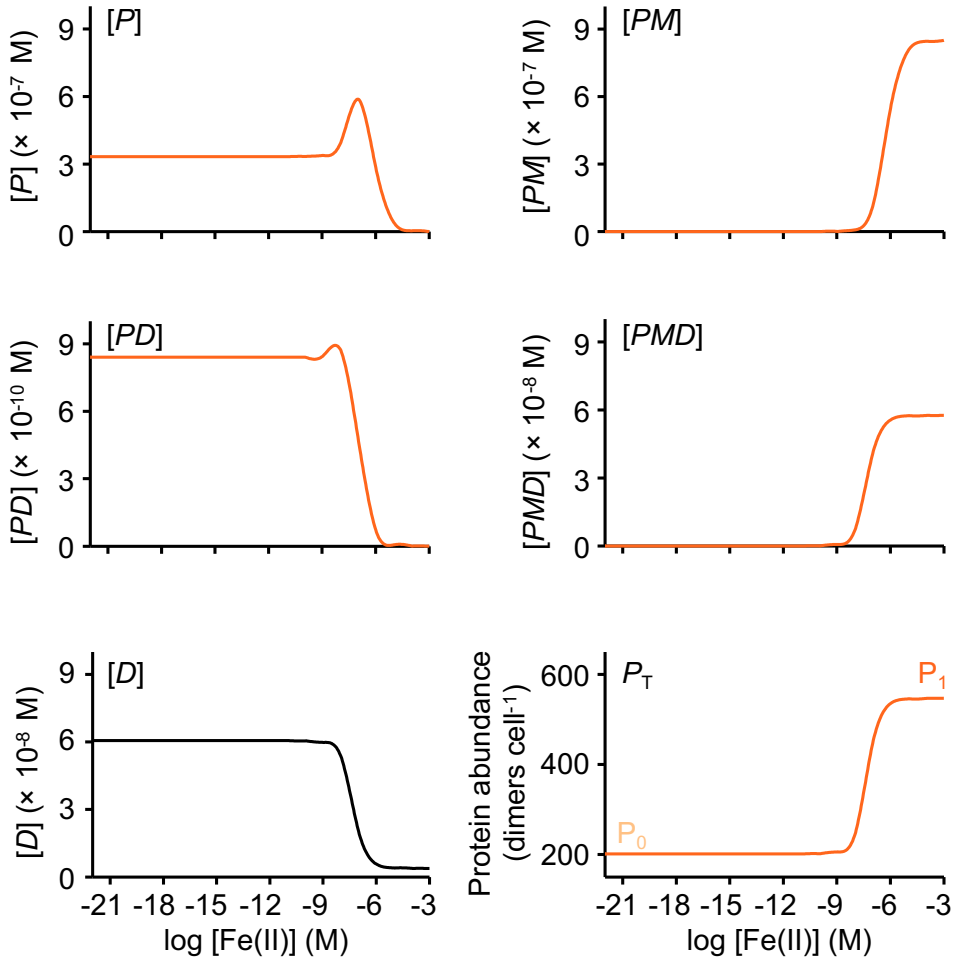

Figure 5.7. Concentration of the various Fur species as a function of buffered iron
The concentrations [*P*], [*PD*], [*PM*], [*PMD*], [*D*] and P_T (the latter expressed as number of multimers per cell) were calculated for Fur as a function of the buffered concentration of iron, using the equations developed.

5.3.2 Simulations to show different contributing factors to sensitivity

As mentioned in section 5.1.1.3, the metal-affinities of the sensors (K_1) were routinely used as a surrogate measure for sensitivity. The response of each sensor inferred from K_1 only was thus compared with the response based on θ_D and θ_{DM} that considered also DNA-binding. As shown in **Figure 5.8**, the response inferred solely from K_1 can closely approximate the calculated response of only two sensors: the Zn(II)-sensing co-repressor Zur and the Zn(II)-sensing activator ZntR. The responses of all the other sensors are shifted by about one order of magnitude (either higher or lower) compared to the sensitivity inferred from K_1. If compared to the difference in sensitivity of the various sensors (up to twelve orders of magnitude between CueR- and MntR-mediated responses), these differences of one or two orders of magnitude might seem small. However, as it will be discussed in section 6.3.3, these can make a significant difference in the prediction of protein metalation, highlighting the importance of including DNA-binding and changing protein abundance in the model to calculate sensor responses. In order to understand what modulates the sensitivity of the various sensors and determines a shift from K_1, a series of simulations was performed using the electronic spreadsheet (**Figure 5.5**). In these simulations, either one or more parameters for a sensor were altered, keeping the others constant.

As shown in **Table 5.1**, the abundance of the Co(II)/Ni(II) sensor RcnR increases by four-fold when *Salmonella* cells are exposed to Co(II). **Figure 5.9** shows the fractional DNA occupancy θ_D calculated for RcnR with constant protein abundance P_0 and P_1 (dashed light blue and grey lines, respectively) or with P_T changing linearly with θ_D (solid blue line). RcnR-mediated response with changing P_T is shifted to a higher buffered concentration of Co(II) compared to both the responses calculated with fixed P_0 and P_1. In this case, hysteresis modulates RcnR-mediated response. RcnR is a de-repressor and in its apo-form binds to its own promoter, repressing the expression of its own gene. As the buffered metal concentration increases, RcnR binds Co(II) and dissociates from DNA, allowing the transcription of *rcnR* to occur and leading to an increase in RcnR abundance. The newly synthesised RcnR, in turn, binds to DNA, suppressing the magnitude of de-repression caused by the metal increase. This causes an attenuation of RcnR-mediated response at low buffered Co(II) concentration. Fur-mediated response shows a similar behaviour, although with an opposite (and smaller) effect: The newly produced Fur contributes towards an increase in DNA occupancy, causing a sharp increase in θ_D when Fur starts responding. A Fur binding site is present in its own promoter. However, it is unknown how the interaction with DNA determines an increase in sensor abundance. Fur commonly acts as a co-repressor, but it is known to be involved in direct and indirect gene expression activation in several organisms (section 1.5.3.1) (Seo et al, 2014; Troxell & Hassan, 2013).

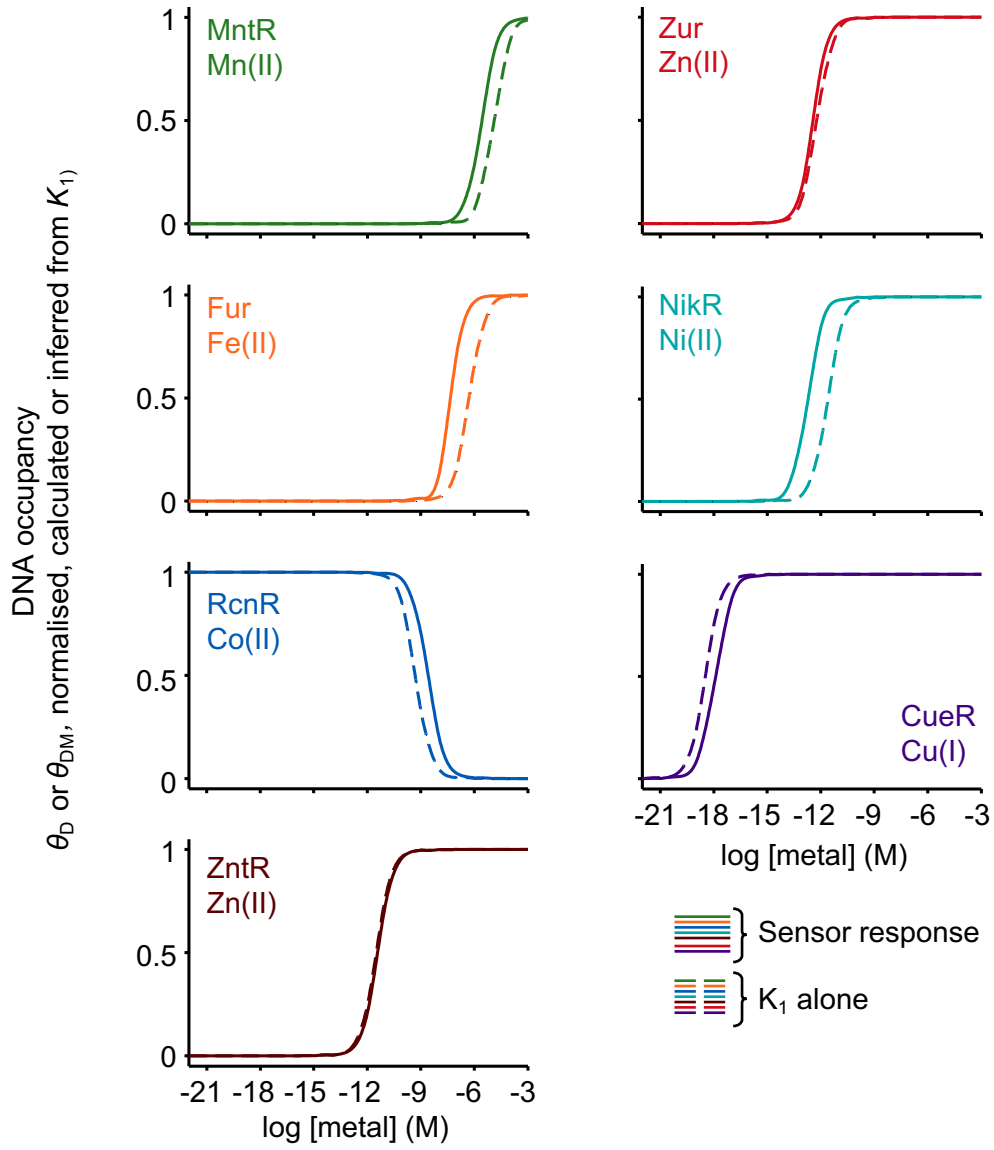

Figure 5.8. Metal affinities can closely approximate well the response of only two sensors. Sensor responses calculated using the thermodynamic model in **Figure 5.3** (solid lines) compared to responses inferred from metal affinity (K_1) only (dashed lines). Figure and caption are adapted from (Osman et al, 2019).

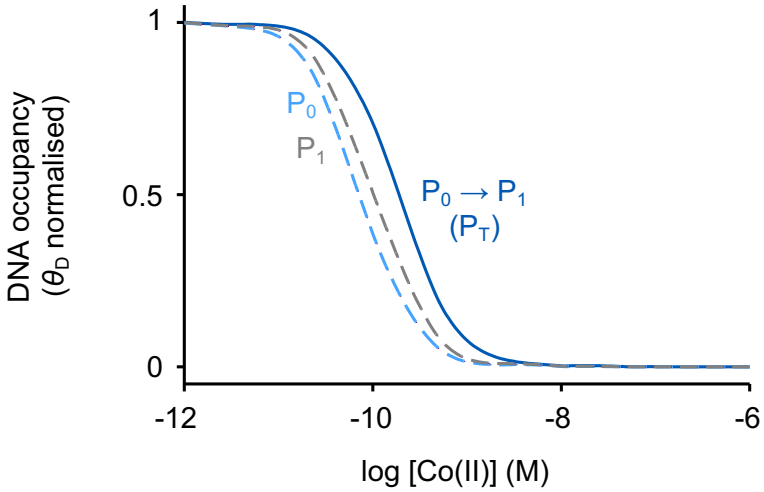

Figure 5.9. RcnR-mediated response is modulated by hysteresis.
Fractional DNA occupancy (θ_D, normalised) calculated for RcnR using P_T (solid blue line) or constant protein abundances P_0 (dashed light blue line) and P_1 (dashed grey line). θ_D was normalised independently for each curve. The change in protein abundance as a function of [Co(II)] is responsible for the delayed response at low [cognate metal] (hysteresis). Figure and caption are adapted from (Osman et al, 2019).

All the co-repressors except Zur show a shift in sensor response to a lower buffered metal concentration compared to K_1. **Figure 5.10a** compares the absolute fractional DNA occupancies for the co-repressors (solid lines): The sensors MntR, Fur and NikR exhibit a higher absolute DNA occupancy than Zur. For these sensors, DNA binding modulates sensitivity: the sensitivities are shifted towards the responses inferred from K_2, the metal-affinity of the DNA-bound form of the sensor (for Fur there is also a contribution from hysteresis as discussed earlier). For the co-repressors, the metal-affinity K_2 is tighter than K_1, as a result of the metal-bound form of the sensor having a tighter affinity for DNA. Zur-mediated response was simulated with 10-fold tighter K_3 and K_4 (dashed red line), so that the allosteric free energy (determined by the ratio $\frac{K_4}{K_3}$) remained unchanged. The tighter DNA affinity caused an increase in absolute DNA occupancy and a shift in sensitivity reflecting an enhanced contribution from K_2 (dashed red line in **Figure 5.10a**). This is even more evident from the comparison of the normalised Zur-mediated responses (**Figure 5.10b**).

5.3.3 Responses of metal sensors in other organisms

The equations developed in section 5.2 can be applied to any other metal sensor, if the parameters needed for the calculations (or their estimates) are available. In *B. subtilis* and *E. coli*, Zur has been reported to have a graded response to Zn(II) (Gilston et al, 2014; Ma et al, 2011; Shin & Helmann, 2016). The equations can be used to model the graded Zur-mediated response to Zn(II) in these two organisms.

In *B. subtilis* the graded response is modulated by negative cooperativity in Zn(II)-binding to the complement of allosteric sites: the second binding event is about twenty-fold weaker than the first one (Ma et al, 2011; Shin & Helmann, 2016). Some target genes can be repressed by Zn_3-Zur (Zur dimer with one allosteric site metalated, plus two Zn(II) structural sites), while others require Zn_4-Zur for regulation. Therefore, when Zur binds Zn(II) in the first site, the expression of some 'early' genes is repressed, while the other 'middle' and 'late' genes are regulated only when Zn(II) availability is sufficiently high to metalate the second (weaker) Zn(II)-site (Shin & Helmann, 2016). **Figure 5.11a** shows *B. subtilis* Zur-mediated response on *znuA* (a 'middle' gene) and *rpsNB* (an 'early' gene) compared to the *Salmonella* Zur on *znuA*. The calculations used published values for K_1, K_3, K_4 from *B. subtilis* (Ma et al, 2011; Shin & Helmann, 2016) and P_0, P_1 from *Salmonella* (**Table 5.1**). As DNA occupancy was calculated on a specific promoter, the number of target genes in the computation equated one. The gene *znuA* encodes the periplasmatic component of the ATP-dependent, high-affinity, zinc uptake system ZnuABC, both in *Samonella* and *B. subtilis* (Ammendola et al, 2007; Campoy et al, 2002; Patzer & Hantke, 1998). Notably, the set-point of *B. subtilis* Zur on *znuA* is extremely similar to the one of *Salmonella* Zur. The gene *rpsNB* encodes a ribosomal protein paralogue (S14*), required for *de novo* ribosome synthesis, that does not require Zn(II)

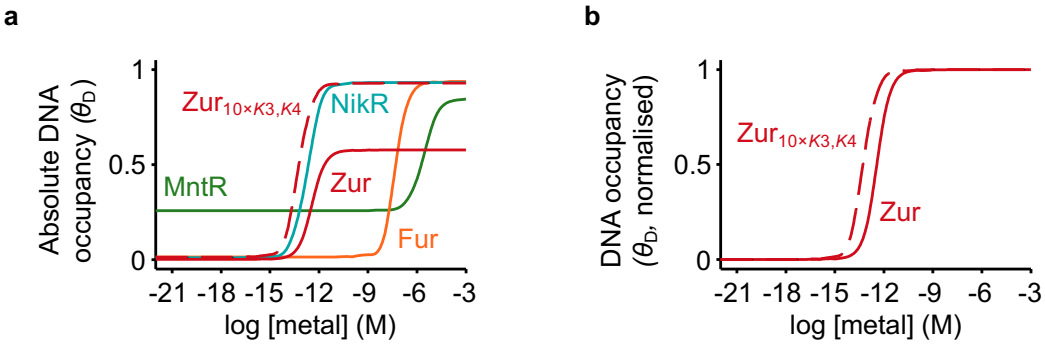

Figure 5.10. Simulations show the effect of DNA affinities on sensor responses.
a, Absolute values for DNA occupancy (θ_D) calculated for the co-repressors (solid lines). The red dashed line is a simulation of Zur-mediated response with 10-fold tighter DNA affinities K_3 and K_4 (the allosteric free energy ΔG_C remains constant). **b**, Zur-mediated responses as in **a**, normalised. The increased DNA affinity determines a shift from the response dictated by K_1. Figure and caption are adapted from (Osman et al, 2019).

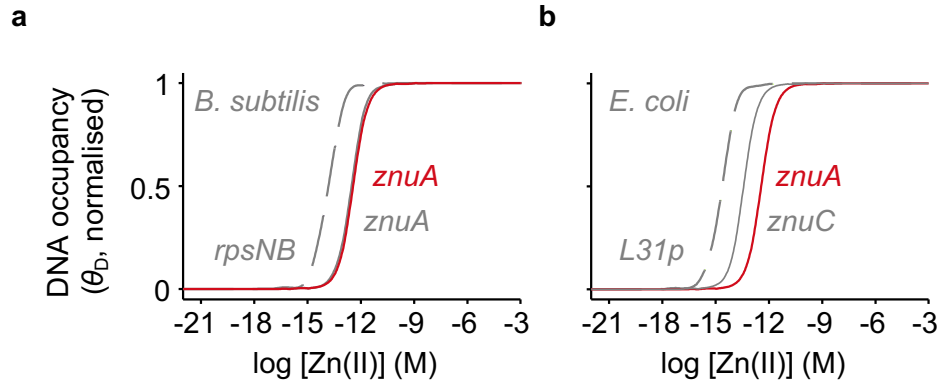

Figure 5.11. Graded response to Zn(II) in *B. subtilis* and *E. coli*.
a, Simulated response of *B. subtilis* Zur on *znuA* (solid grey line) and *rpsNB* (dashed grey line) promoters using published values for K_1, K_3, K_4 (P_0 and P_1 from *Salmonella*, **Table 5.1**) (Ma et al, 2011; Shin & Helmann, 2016) compared with *Salmonella* Zur-mediated response on *znuA* (solid red line). **b**, Simulated response of *E. coli* Zur on *znuC* (solid grey line) and *L31p* (dashed grey line) promoters using published values for K_4 (obtained from the square root of a β value, measured at pH 8.0 (Gilston et al, 2014)) and other parameters from *Salmonella* (**Table 5.1**, **Table 5.2**) compared with *Salmonella* Zur on *znuA* (solid red line). Figure and caption are adapted from (Osman et al, 2019).

for function. S14* is expressed in Zn(II)-deficient conditions as part of a Zn(II)-sparing mechanism (Natori et al, 2007). *B. subtilis* Zur set-point on *rpsNB* is approximately one order of magnitude lower than the one on *znuA*, consistently with *rpsNB* function in Zn(II)-sparing under Zn(II)-depletion.

The graded response in *E. coli* was attributed to a difference in DNA-affinities (K_4) for different target genes within the Zur regulon (Gilston et al, 2014). Two Zur dimers bind to the Zur-binding DNA sequence in a highly cooperative fashion. In the electrophoretic mobility shift assay (EMSA) used to determine DNA-binding affinities, the thermodynamic constants for the two individual binding events could not be determined. Therefore, β values for the formation of the ternary complex $(Zur)_2 \cdot DNA$ were reported (Gilston et al, 2014). The determined β values on different promoters span five orders of magnitude. To model the graded response, *E. coli* Zur DNA occupancy was calculated using the square root of the published β values as K_4 and K_1, K_3, P_0, P_1 from *Salmonella* (**Table 5.1**, **Table 5.2**). Because of the highly cooperative binding, $\sqrt{\beta}$ represents an upper limit for K_4, i.e. the actual thermodynamic constant for the first DNA-binding event to form the $(Zur) \cdot DNA$ complex is likely weaker than $\sqrt{\beta}$ (this would bring the sensitivity of *E. coli* Zur closer to *Salmonella*). Moreover, it should be noted that the EMSA assays were performed at pH 8.0 instead of at pH 7.0 as in the *Salmonella* studies, which can contribute to an increased sensor affinity for the negatively charged DNA. As seen in section 5.3.2, a tighter DNA affinity can increase co-repressors sensitivity. **Figure 5.11b** shows *E. coli* Zur-mediated response on *L31p* and *znuC* genes (dashed and solid grey lines, respectively) and *Salmonella* Zur on *znuA* (red line). The gene *znuC* encodes the ATPase component of the ZnuABC Zn(II)-importer (*znuA* and *znuC* are part of the same *znu* operon), while *L31p* encodes a ribosomal protein paralogue (Panina et al, 2003). Similarly to what was seen in *B. subtilis*, *E. coli* Zur is at least one order of magnitude more sensitive on the *L31p* promoter than on the *znuC* one.

The graded responses of Zur in the two organisms are modulated by two different factors: Variation in K_1 for *B. subtilis* and variation in K_4 for *E. coli*. However, in both cases this causes the expression of the ribosome-switching gene (a Zn(II)-sparing mechanism that can act as a 'fail-safe' to sustain protein synthesis when Zn(II) is depleted) to occur when Zn(II) is at least ten times less available than for expression of the ZnuABC importer.

5.4 Inclusion of non-specific DNA into the model

To test the robustness of the model, we considered how inclusion of competition from non-specific DNA (DNA not containing the sensor-specific recognition sequence) for sensor binding affects sensor response. This more complex system is exemplified in **Figure 5.12**.

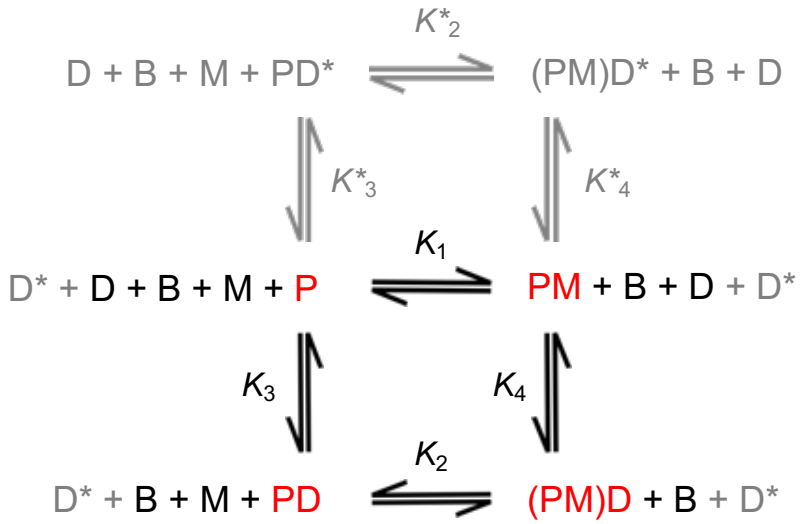

Figure 5.12. Thermodynamic model including competition from non-specific DNA. Semi-schematic representation of a metal sensor in its four allosteric conformations (as in **Figure 5.3**) including binding of the sensor to non-specific DNA (*D**, DNA affinities K_3*, K_4*). The equilibria showing metal-exchange from and to the buffer system are omitted for clarity. Figure and caption are adapted from (Osman et al, 2019).

D* represents the non-specific DNA, K_3* and K_4* the affinity of the apo- and metalated form of the sensor for D* and K_2* the metal-affinity of the sensor bound to non-specific DNA. Even though the equilibria showing metal-exchange to and from the metal buffer system were omitted in the scheme for clarity, metal-exchange between the sensor and the buffer still occurs via the quick associative mechanism.

Non-specific DNA affinities K_3* and K_4* are anticipated to be quite similar and their value to be close to the lower affinity for specific DNA (K_3 for co-repressors, K_4 for de-repressors and activator). This results in the residual allosteric coupling of metal to non-specific DNA binding being small. The residual allosteric coupling free energy is defined as:

$$\Delta G_c^* = -RT \ln\left(\frac{K_4^*}{K_3^*}\right)$$

Andrew Foster determined the affinity of Zur for a non-specific DNA target by performing fluorescence anisotropy experiments on the *nixA* promoter (*nixA* is one of the target genes of the Ni(II)-sensing co-repressor NikR). The experiments were performed in the absence and in the presence of a saturating amount of Zn(II) to determine K_3* and K_4* respectively (**Figure 5.13**). The affinities for non-specific DNA are expected to approximate K_3 and this value ($1/K_3 = 2.7 \times 10^{-5}$ M for Zur) is often close to the lower limit of the assay for co-repressors. For this reason, the experiments were performed at a lower concentration of salt (80 mM KCl, 20 mM NaCl) than the one used for the determination of the values in **Table 5.2**. DNA-affinities have a log-log dependence on salt concentration (Campanello et al, 2013; Record et al, 1991). If the concentration of salt in the assay is lowered, DNA affinities increase, in this case moving away from the limit of the assay and facilitating the experimental determination of K_3* and K_4*. The measured values for Zur were (mean ±s.d.) $1/K_3^* = 9.0\ (\pm 1.0) \times 10^{-6}$ M and $1/K_4^* = 7.6\ (\pm 0.7) \times 10^{-7}$ M. The log-log dependence of Zur DNA-binding on [salt] was determined by Andrew Foster by performing fluorescence anisotropy experiments on the *znuA* promoter in the presence of different concentrations of salt (data not shown in this thesis): $\log K_3 = -2.23 \log [\text{salt}] + 3.53$ and $\log K_4 = -2.33 \log [\text{salt}] + 6.23$ (Osman et al, 2019). This dependence was used to calculate the non-specific DNA affinities at 300 mM salt (240 mM KCl, 60 mM NaCl), giving $1/K_3^* = 1.2 \times 10^{-4}$ M and $1/K_4^* = 9.8 \times 10^{-6}$ M. The residual allosteric coupling free energy is $\Delta G^*_c = -1.5$ kcal mol^{-1}, smaller than the allosteric coupling free energy on specific DNA $\Delta G_c = -3.9$ kcal mol^{-1} (see **Table 5.2**).

The non-specific DNA affinities for the other sensors were estimated based upon the Zur data. The estimated K^*_3 and K^*_4 were set to flank K_3 for the co-repressors and K_4 for de-repressors and activators, so that K_3 (or K_4) represented the midpoint between K^*_3 and K^*_4 on a logarithmic scale. The same proportion between ΔG^*_c and ΔG_c found for Zur was maintained

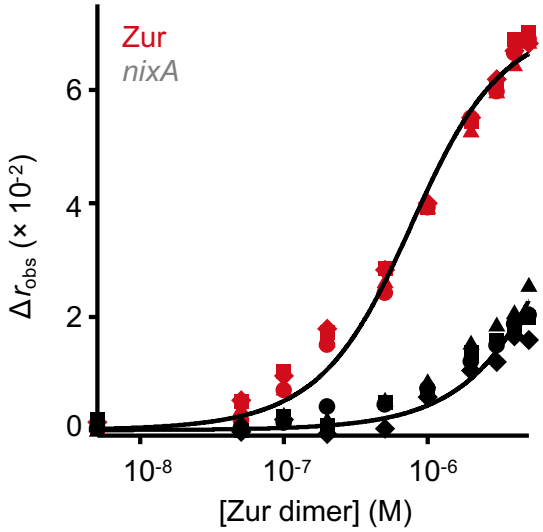

Figure 5.13. Determination of Zur affinity for non-specific DNA.
Fluorescence anisotropy change (Δr_{obs}) following titration of 10 nM *nikA*Pro (containing NikR binding site in the promoter region of the gene *nikA*) with Zn(II)-Zur (red symbols) and apo-Zur (black symbols). Shapes represent individual experiments (n = 4). The salt content of the experimental buffer was 80 mM KCl, 20 mM NaCl. Data collected by Andrew Foster. Figure and caption are adapted from (Osman et al, 2019).

for the other sensors. **Table 5.3** shows the value for $1/K^*_3$ and $1/K^*_4$ calculated for the other *Salmonella* sensors. Binding to non-specific DNA was also experimentally determined for Mn(II)-MntR by fluorescence anisotropy. The non-specific target (*mntS*Pro-swap) was obtained by randomising the MntR recognition sequence on the 32bp *mntS*Pro oligonucleotide (**Figure 3.13**), as shown in **Figure 5.14**. Interestingly, the higher-order binding observed on *mntS*Pro and *mntS*Pro-short (section 3.4.4) is retained on *mntS*Pro-swap. Therefore, the data were fit with the same method that was used for *mntS*Pro, giving $1/K^*_4 = 2.3\ (\pm 1.7) \times 10^{-8}$ M (mean ±s.d.). This value is comparable to the estimated $1/K^*_4 = 5.0 \times 10^{-8}$ M in **Table 5.3**.

The degree of competition of non-specific DNA versus specific DNA does not depend only on K_3^* and K_4^* versus K_3 and K_4, but also on the concentration of competing species (i.e. the concentration of available non-specific DNA). The total concentration of genomic DNA in *E. coli* is estimated to be approximately 10^{-2} M base pairs. However, a large proportion of the genomic DNA is occluded, for instance by the many DNA-binding proteins, leaving approximately 10^{-4} M bp (1%) available for competition with specific DNA (Stickle et al, 1994). The concentration of sensor binding sites on non-specific DNA ($[D_T^*]$) was obtained by dividing the available concentration non-specific DNA (10^{-4} M) bp by 33 bp, the average length of the DNA binding sequences used as specific targets in the fluorescence anisotropy experiments.

Even in this new complex system (**Figure 5.12**), the response of the sensors is obtained from the fraction of specific DNA bound to the sensory protein (section 5.2.1). The non-specific DNA is competing for sensor-binding, and it is anticipated that its effect will be to reduce the absolute occupancy of the sensor on specific DNA. With known numerical values for $[D_T^*]$, K_3^* and K_4^* (**Table 5.3**), plus the parameters in **Table 5.1** and **Table 5.2**, it is possible to calculate θ_D and θ_{DM}. The next section will describe the derivation of the equations to express θ_D and θ_{DM} as a function of the buffered metal concentration for the chemical equilibria in **Figure 5.12**. It is anticipated that the more complicated cycle will result in a more convoluted derivation and computation.

Table 5.3. Non-specific DNA affinities of the *Salmonella* sensors.

Sensor	$1/K_3$* (M)	$1/K_4$* (M)
MntR	1.5×10^{-7}	5.0×10^{-8}
Fur	7.7×10^{-5}	7.5×10^{-6}
NikR	4.3×10^{-5}	2.8×10^{-6}
RcnR	6.2×10^{-6}	3.6×10^{-5}
ZntR	5.4×10^{-7}	1.1×10^{-6}
CueR	2.4×10^{-7}	6.1×10^{-7}

Values for $1/K_3$* and $1/K_4$* for the *Salmonella* sensors estimated as flanking $1/K_3$ for co-repressor and $1/K_4$ for de-repressors and activators. The non-specific DNA affinities were calculated to give a smaller allosteric free energy on non-specific DNA (ΔG_C*) than the one on specific DNA. The estimated affinities maintained the same ratio of specific versus non-specific DNA allosteric free energy determined experimentally for Zur (data from Andrew Foster, **Figure 5.13**). Table and caption adapted from (Osman et al, 2019).

a

5′[HEX]-CTATAAAACAatgcCTGTcatgTATCTGTATG 3′

b

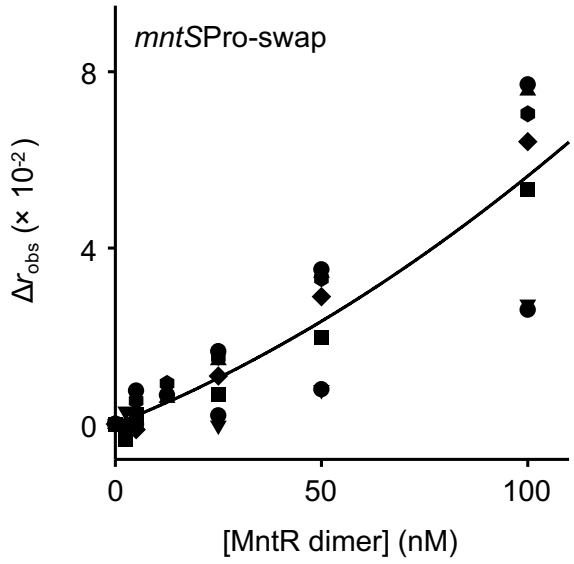

Figure 5.14. Determination of MntR affinity for non-specific DNA.
a, 32 bp oligonucleotide (*mntS*Pro-swap) containing a randomised MntR recognition site (underlined lower case, changed from the promoter sequence TAGC and GCTA as in **Figure 3.10**) and flanking nucleotides in the *mntS* promoter. The shown oligonucleotide (fluorescently labelled, 5′-HEX) was annealed with its unlabelled reverse complement. Annealing was confirmed by native PAGE (see **Figure 8.5**). **b**, Fluorescence anisotropy change (Δr_{obs}) following titration of *mntS*Pro-swap (10 nM) with Mn(II)-MntR in 200 μM Mn(II). Shapes represent individual experiments. The data were fit to the same model described in **Figure 3.17**. The solid line is a simulation with the average of K_{DNA} obtained from the individual experiments (n = 7). The mean (±s.d.) value for $1/K_4$* obtained from the fit is 2.3 (±1.7) × 10^{-8} M, comparable to the theoretical value estimated in **Table 5.3**. Figure and caption are adapted from (Osman et al, 2019).

5.4.1 Derivation of cubic equations to simulate the effect of non-specific DNA

To derive the equations to express the fractional DNA occupancy (θ_D or θ_{DM}) taking into account sensor binding to non-specific DNA, an approach similar to the one in section 5.2 was employed. For **Figure 5.12**, as seen in section 5.2.1, we can write these relationships between the constants K_1, K_2, K_3, K_4 and the concentrations at equilibrium of reactants and products. Three additional equations arise from the equilibria describing binding of the sensor to non-specific DNA (K_2*, K_3* and K_4*):

$$K_1 = \frac{[PM]}{[P][M]} \qquad K_2 = \frac{[PMD]}{[PD][M]} \qquad K_3 = \frac{[PD]}{[P][D]} \qquad K_4 = \frac{[PMD]}{[PM][D]}$$

$$K_2^* = \frac{[PMD^*]}{[PD^*][M]} \qquad K_3^* = \frac{[PD^*]}{[P][D^*]} \qquad K_4^* = \frac{[PMD^*]}{[PM][D^*]}$$

As the two thermodynamic cycles are closed, these relationships apply to the equilibrium constants, meaning that the experimental determination is required only for three constants for each cycle:

$$K_3 = \frac{K_1}{K_2} K_4$$

$$K_2^* = \frac{K_1^* K_4^*}{K_3^*}.$$

As described in section 5.1.3, the hypothetical metal buffer system in the model has an ideal behaviour, so that the buffered metal concentration $[M]$ can be treated as an independent variable. Therefore, the mass balance equations for the system are:

$$[D_T] = [D] + [PD] + [PMD]$$

$$[D_T^*] = [D^*] + [PD^*] + [PMD^*]$$

$$[P_T] = [P] + [PM] + [PD] + [PMD] + [PD^*] + [PMD^*].$$

Protein abundance $[P_T]$ and fractional DNA occupancy θ_D (θ_{DM} for the MerR-like activators) are linearly co-dependent as described in section 5.1.2. A system of simultaneous equations can thus be written also in this case, to mathematically describe the thermodynamic cycles in **Figure 5.12**:

$$
\begin{cases}
K_1 = \dfrac{[PM]}{[P][M]} \\
K_2 = \dfrac{[PMD]}{[PD][M]} \\
K_4 = \dfrac{[PMD]}{[PM][D]} \\
K_3^* = \dfrac{[PD^*]}{[P][D^*]} \\
K_4^* = \dfrac{[PMD^*]}{[PM][D^*]} \\
[D_\mathrm{T}] = [D] + [PD] + [PMD] \\
[D_\mathrm{T}^*] = [D^*] + [PD^*] + [PMD^*] \\
[P_\mathrm{T}] = [P] + [PM] + [PD] + [PMD] + [PD^*] + [PMD^*] \\
\theta_\mathrm{D} = \dfrac{[PD] + [PMD]}{[D_\mathrm{T}]} \qquad \theta_\mathrm{DM} = \dfrac{[PMD]}{[D_\mathrm{T}]} \\
\dfrac{[P_\mathrm{T}] - [P_0]}{[P_1] - [P_0]} = \dfrac{\theta_\mathrm{D} - \theta_\mathrm{D0}}{\theta_\mathrm{D1} - \theta_\mathrm{D0}} \qquad \dfrac{[P_\mathrm{T}] - [P_0]}{[P_1] - [P_0]} = \dfrac{\theta_\mathrm{DM} - \theta_\mathrm{DM0}}{\theta_\mathrm{DM1} - \theta_\mathrm{DM0}}
\end{cases}
$$

Once solved, the simultaneous equations will provide a solution to express all of the variables (including θ_D and θ_DM) as a function of the buffered metal concentration $[M]$, taking into account the presence of non-specific DNA. To simplify the computation, the variables and the constant parameters are renamed as in section 5.2.1, with these additional variables from the non-specific DNA-binding equilibria:

$$
\begin{aligned}
e &= K_3^*, & h &= [D^*] \\
f &= K_4^*, & i &= [PD^*] \\
g &= K_2^*, & j &= [PMD^*] \\
D_\mathrm{T}^* &= [D_\mathrm{T}^*].
\end{aligned}
$$

The chemical equilibria and mass balance give these relationships between variables:

$$e = \frac{i}{xh}, \tag{25}$$

$$f = \frac{j}{uh}, \tag{26}$$

$$D_\mathrm{T}^* = h + i + j, \tag{27}$$

$$P_\mathrm{T} = x + u + v + w + i + j = x + u + D_\mathrm{T} - z + D_\mathrm{T}^* - h. \tag{28}$$

Using (25) and (26), i and j can be expressed as:

$$i = exh, \qquad j = fuh \tag{29}$$

and h can then be derived from (27):

$$h = \frac{D_T^*}{1 + ex + fu}. \tag{30}$$

5.4.1.1 Derivation of cubic equation to determine θ_D

As seen in section 5.2.2.1, the relationship between the change in P_T and the change in θ_D can be rewritten as:

$$P_T = \frac{\Delta P}{\Delta \theta_D}\theta_D + A_D, \tag{31}$$

where ΔP, $\Delta\theta_D$ and A_D are defined in equation (9). Equation (31) can be rearranged using (10) and (28):

$$x + u + D_T - z + D_T^* - h = \frac{\Delta P}{\Delta \theta_D}\left(1 - \frac{z}{D_T}\right) + A_D,$$

$$x + u - C_1 z - h = C_2^*, \tag{32}$$

where C_1 and C_2* are defined as:

$$C_1 = 1 - \frac{\Delta P}{\Delta \theta_D \cdot D_T}, \tag{33}$$

$$C_2^* = \frac{\Delta P}{\Delta \theta_D} + A_D - D_T - D_T^*. \tag{34}$$

Finally, the variables u (6), z (7) and h (30) can be substitued into equation (32) to find x:

$$x + axy - C_1 \cdot \frac{D_T by}{adxy + by + abdxy^2} - \frac{D_T^*}{1 + ex + afxy} = C_2,$$

$$x^3(1+ay)(ad+abdy)(e+afy) + x^2\left\{(1+ay)(ad+abdy) + \left[b(1+ay) - C_2(ad+abdy)\right](e+afy)\right\} +$$
$$+ x\left[b(1+ay) - C_2(ad+abdy) - b(C_1D_T + C_2)(e+afy) - D_T^*(ad+abdy)\right] - b(C_1D_T + C_2 + D_T^*) \tag{35}$$

Equation (35) expresses x (the concentration of free apo-protein [P]) as a function of y (the buffered metal concentration [M]). In this case, the more complicated system led to a cubic equation instead of a quadratic one. The solution of a cubic equation requires handling complex analysis and, therefore, the analytical solution was not derived as beyond the scope of this work. However, the cubic equation can be easily solved numerically using an electronic spreadsheet or a computing environment. For this work, the cubic equation was solved for a range of buffered metal concentrations with an electronic spreasheet using Cardano's method (van der Waerden & Schulenberger, 1991). Depending on the parameters inserted (i.e. depending on the sensor), the user needs to act on the calculations present in the spreadsheet's

cells in a non-straightforward way, making it difficult to distribute the spreadsheet to others. Therefore, this eletronic spreadheet was included neither in the Supplementary Information of (Osman et al, 2019) nor in this thesis. In all the cases examined for the *Salmonella* sensors, the three roots of the cubic equation were all real numbers. One solution was positive and the remaining two negative. As x represents a physical value ([P]), the negative solutions are meaningless and solely the positive solution was retained.

Once x is known, θ_D can be calculated using equation (16), as already shown in section 5.2.2.1 for the simpler case without non-specific DNA. Similarly to what is described in section 5.2.2.1, a simplified form of equation (35) (setting $\Delta P = 0$) can be used to calculate numerical values of θ_{D0} and θ_{D1} using an electronic spreadsheet or a computing environment. From the solution of the cubic equation (35), all of the other variables can be calculated as a function of y (the buffered metal concentration [M]).

5.4.1.2 Derivation of cubic equation to determine θ_{DM}

As seen in section 5.2.2.2, the relationship between the change in P_T and the change in θ_{DM} can be rewritten as:

$$P_T = \frac{\Delta P}{\Delta \theta_{DM}} \theta_{DM} + A_{DM}, \tag{36}$$

where ΔP is defined in equation (9), while $\Delta\theta_{DM}$ and A_{DM} in (19). The expression for θ_{DM} can be substituted into equation (36) and by using the expression for w (6) and P_T (28) it is possible to write:

$$x + u + D_T - z + D_T^* - h = B\frac{w}{D_T} + A_{DM}, \tag{37}$$

where B is expressed by equation (21). The variables u (6), z (7) and h (30) can be substitued into (37) to find x:

$$x + axy + D_T - \frac{D_T by}{adxy + by + abdxy^2} + D_T^* - \frac{D_T^*}{1 + ex + afxy} = B\frac{abdxy^2}{adxy + by + abdxy^2} + A_{DM}$$

$$\begin{aligned} &x^3(1+ay)(ad+abdy)(e+afy) + x^2\Big\{(1+ay)(ad+abdy) + \big[b(1+ay) - Babdy - \\ &- (A_{DM} - D_T - D_T^*)(ad+abdy)\big](e+afy)\Big\} + x\Big[b(1+ay) - Babdy - (A_{DM} - D_T - \\ &- D_T^*)(ad+abdy) - b(A_{DM} - D_T^*)(e+afy) - D_T^*(ad+abdy)\Big] - bA_{DM} = 0 \end{aligned} \tag{38}$$

As seen in the previous case for the determination of θ_D, the cubic equation (38) can be numerically solved using an electronic spreadsheet or a computing environment. In all the cases examined for the *Salmonella* ZntR and CueR sensors, three real roots were obtained, one positive and two negative. The positive solution for x was retained to calculate θ_{DM} from equation (24). A simplified form ($\Delta P = 0$) of equation (38) can be used to calculate numerical

values of θ_{DM0} and θ_{DM1} using an electronic spreadsheet or a computing environment. From the solution of the cubic equation (38), all of the other variables for the MerR-like activators can be calculated as a function of y (the buffered metal concentration [M]).

5.4.2 The effect of non-specific DNA on the *Salmonella* sensors

Sensor responses were calculated including competition from non-specific DNA from the values in **Table 5.1**, **Table 5.2**, **Table 5.3**. As shown in **Figure 5.15**, including D* in the model (grey lines) had a negligible effect on sensor responses and thus on their sensitivities. As anticipated, the competition decreased the absolute DNA occupancy of the sensors (**Figure 5.15b**), albeit for most of the sensors this change was not large enough to determine a shift in sensitivity. MntR was the only sensor showing a (small) change in sensitivity, consistent with the Mn(II)-sensor having the tightest affinity for non-specific DNA ($1/K_4$*) of the *Salmonella* set (**Table 5.3**). The decrease in DNA-occupancy (**Figure 5.15b**) reduces the contribution of K_2 to MntR sensitivity, shifting sensor response towards the one inferred from K_1 only (section 5.3.2).

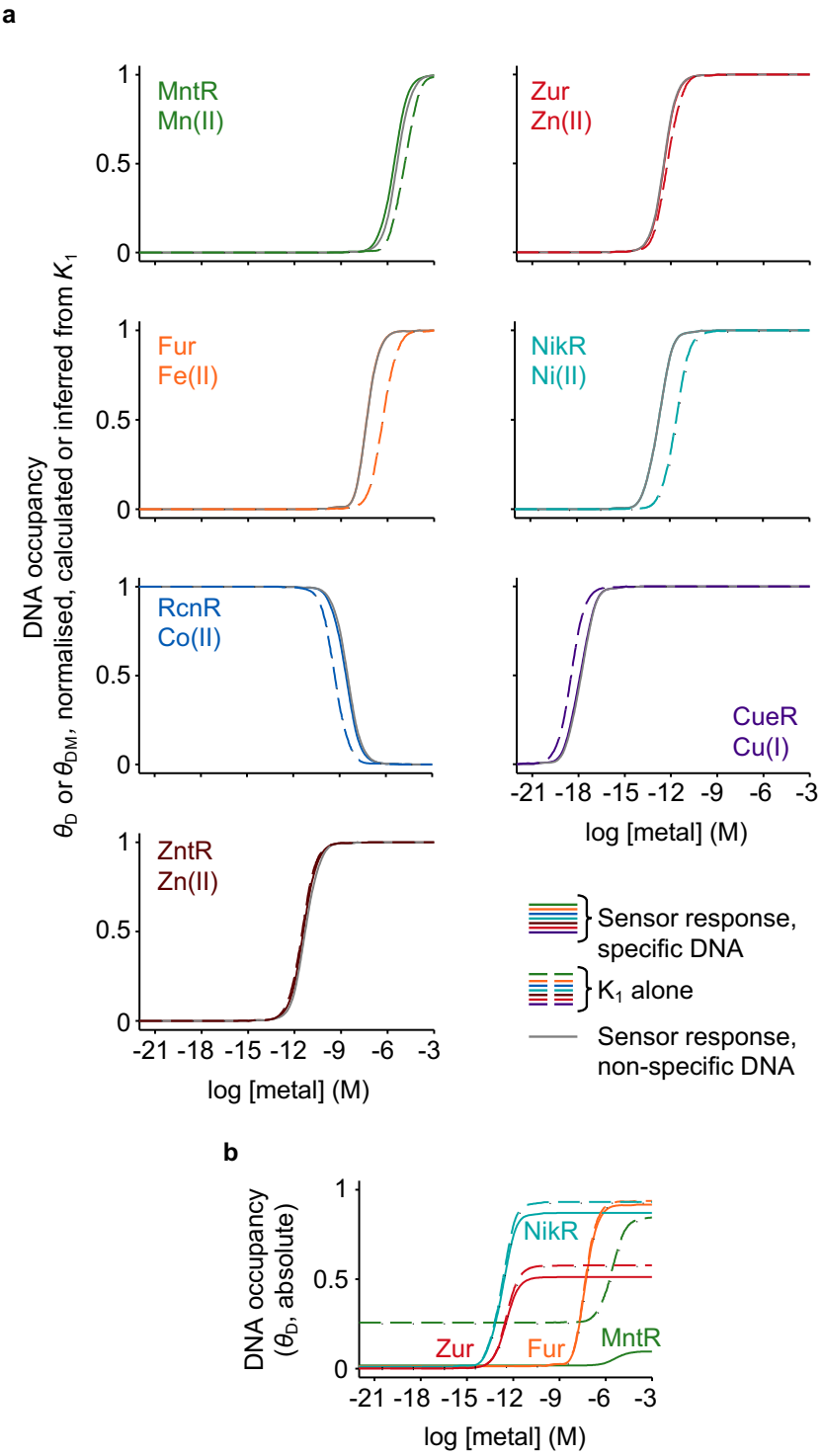

Figure 5.15 Consideration of non-specific DNA into the model has a negligible effect on sensitivity.
a, Comparison of sensor responses calculated to include binding to non-specific DNA (grey lines) with sensor responses inferred from K_1 (dashed coloured lines) and calculated without taking into account the non-specific DNA (solid coloured lines as in **Figure 5.6**). **b**, Absolute values for DNA occupancy (θ_D) calculated for the co-repressors with (dashed coloured lines) or without (solid coloured line) including competition from non-specific DNA. Figure and caption are adapted from (Osman et al, 2019)

Chapter 6.

Intracellular metal availabilities to predict metalation

6.1 Metal availabilities follow the Irving-Williams series

In Chapter 5, the response of the *Salmonella* sensors was calculated as a function of the buffered concentration of their cognate metals from the thermodynamic constants of metal- and DNA-binding, sensor abundances and number of DNA targets (**Figure 5.6**). As the sensors are tuned to the intracellular availabilities of their cognate metals (Foster et al, 2017) (section 1.5), metal availabilities in *Salmonella* were inferred from the buffered metal concentrations at which each sensor undergoes half of its response (θ_D or θ_{DM} = 0.5) (**Table 6.1**). The buffered concentration of Mg(II) was inferred from the affinity of the *B. subtilis* riboswitch (Dann et al, 2007). Two values for the Zn(II) buffered concentration are reported, as inferred from the responses of ZntR and Zur respectively. These buffered metal concentrations inform on the concentrations of hydrated metal ions present in the cytosol. However, these hydrated metals are not the relevant species to describe protein metalation and metal speciation *in vivo*. In fact, metal-exchange reactions can occur via association of the recipient molecule with the buffer-bound metal, without involving the (slow) release of the fully hydrated metal ions in the cytosol (equilibria governed by K_5, K_6, K_7 in **Figure 5.3**). Moreover, for most of the metals in **Table 6.1**, the concentration of hydrated species present in the cell is negligible. In fact, with the exception of Mn(II) and Fe(II), for all the other metals the concentration of hydrated species equates to less than one ion per cell. For *Salmonella* this corresponds approximately to a concentration from 10^{-8} to 10^{-9} M: Assuming a cell volume of 1 fl, one single ion per cell corresponds to 10^5 ions per litre; the molar concentration of free metal ions can be obtained by dividing the amount per litre by the Avogadro's number, obtaining ~1.7 10^{-9} M. These extremely low concentrations of hydrated species, however, do not need to imply negligible amounts of 'accessible' metal. The apparent concentrations of labile metals are often orders of magnitudes higher than the concentration of hydrated species, reflecting the fact that most of the labile metal is bound to the buffer pools. Section 6.2 will further discuss the difference between buffered metal concentration and the apparent concentration of accessible metal.

Although the buffered metal concentrations in **Table 6.1** do not directly describe a relevant species, they can indirectly provide information on the chemical state of the buffer-bound metal. They can inform on how stable the metal-buffer complex is or, conversely, on how tight the affinity of a molecule needs to be in order to acquire that particular metal from the cytosolic

Table 6.1. Buffered available metal concentrations and relative free energies for metalation in *Salmonella* cells.

Metal	Sensor	$[Metal]_{buffered}$ (M)	$\Delta G°$ (kJ mol^{-1})
Mg(II)	Riboswitch	2.7×10^{-3}‡	-14.7
Mn(II)	MntR	2.6×10^{-6}	-31.9
Fe(II)	Fur	4.8×10^{-8}	-41.8
Co(II)	RcnR	2.5×10^{-9}	-49.1
Zn(II)	ZntR	3.8×10^{-12}	-65.2
Zn(II)	Zur	3.7×10^{-13}	-71.0
Ni(II)	NikR	1.8×10^{-13}	-72.7
Cu(I)	CueR	1.2×10^{-18}	-102.3

The buffered available metal concentrations were determined from **Figure 5.6** when sensors undergo 0.5 of their response. The calculated standard free energy is associated with the formation of a metal complex in the *Salmonella* cytosol with 50% metalation. ‡Inferred from structural probing of the M box riboswitch (*B. subtilis*) upon Mg(II)-titration (Dann et al, 2007). Table and caption adapted from (Osman et al, 2019).

buffer. To describe metal availabilities, rather than using $[M]_{buffered}$ as an indirect measure of the buffered metal pool, it would be more useful to derive a way to directly describe the 'chemical potential' of the metal species bound to the buffer. Therefore, based on the buffered metal concentrations in **Table 6.1**, the standard free energies associated with the metalation reaction of a hypothetical protein that is 50% metalated when sensors undergo 0.5 of their responses were derived (**Table 6.1**, last column). When the protein is 50% metalated, the association constant for the formation of the protein-metal equilibrium equates to the inverse of the buffered concentration of metal ($K_A = \frac{1}{[M]}$). The standard free energy associated with the reaction were calculated using the equation:

$$\Delta G^{\circ} = -RT \ln K_A$$

The calculated standard free energy values were reported also in **Figure 6.1**, together with the free energies associated with the formation of metal complexes with 20% and 80% occupancy (θ_P) of the hypothetical protein. These data revealed the cellular logic for correct metalation: the metal availabilities to which the sensors are attuned follow the inverse of the Irving-Williams series:

WEAK TIGHT

Mg(II) < Mn(II) < Fe(II) < Co(II) < Ni(II) < Cu(II)* > Zn(II)

*Cu(I) also forms exceptionally tight complexes

That is, as moving along the series from Mg(II) to Cu(II) metal complexes become tighter and tighter, the cell sets metal availability lower and lower. By doing this, cells can allow the simultaneous metalation of different proteins with weak- and tight-binding metals, without the risk of mis-metalating all the binding sites with the more competitive metals. The knowledge that cells set the availability of metals as the inverse of metal-complex stability to achieve correct metalation is not a novelty, as it has been suggested by several experimental evidences over nearly two decades (Foster et al, 2017; Tottey et al, 2008; Waldron & Robinson, 2009; Williams & Da Silva, 2001). However, here this notion has been finally demonstrated from the determination of the metal availabilities the *Salmonella* sensors are attuned to.

The data in **Figure 6.1** provide a unique thermodynamic framework which can be used to predict the metalation of a molecule or a protein of interest. Currently, *Salmonella* is the only organism with determined intracellular metal availabilities based upon the derived sensitivities of its metal sensors (other estimates of metal availabilities where reported in section 1.4). This application will be further discussed in section 6.3.

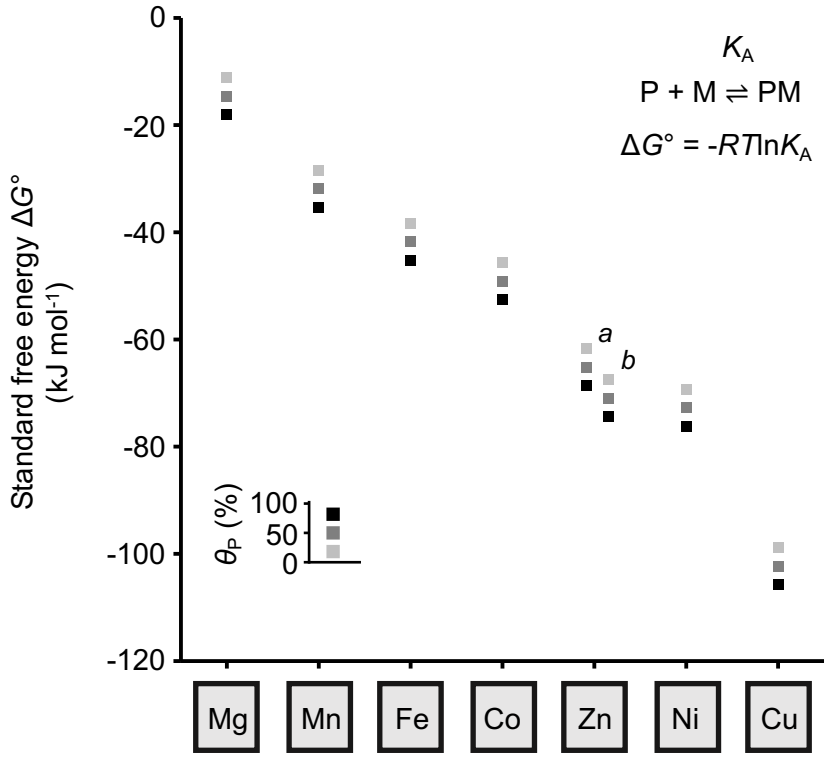

Figure 6.1. Standard free energy for formation of metal complexes in the *Salmonella* cytosol.
Metal availabilities are reported as standard free energies ($\Delta G°$) associated with the formation of a complex between metals and a hypothetical molecule (P in the inset) that in *Salmonella* cytosol is 20%, 50% or 80% metalated (θ_P) when the sensors undergo 0.5 of their response (**Figure 5.6**). The Zn(II) free energies are reported based on both ZntR (*a*) and Zur (*b*). Figure and caption are adapted from (Osman et al, 2019).

6.2 A model for a metal buffer system

As anticipated in section 6.1, the amount of labile metal ions (expressed as an apparent concentration herein) in a buffer system is orders of magnitudes higher than the buffered metal concentration. This can easily be illustrated with a mathematical model describing a metal buffer system. Using the same nomenclature for the equilibrium constants used in the thermodynamic scheme in **Figure 5.3**, the metal buffer system can be modelled as:

$$\mathrm{B} + \mathrm{M} \overset{K_5}{\rightleftharpoons} \mathrm{BM} \qquad K_5 = \frac{[BM]}{[B][M]} \tag{39}$$

where K_5 is the thermodynamic equilibrium for the formation of the complex between the buffering species and the metal ion. The mass balance for the metal and buffer are, respectively:

$$[M_\mathrm{T}] = [M] + [BM] \tag{40}$$

$$[B_\mathrm{T}] = [B] + [BM] \tag{41}$$

where $[B_\mathrm{T}]$ is the total concentration of buffering species, while $[M_\mathrm{T}]$ is the apparent concentration of labile metal in the system. Equations (40) and (41) can be used to express $[BM]$ and $[B]$ respectively:

$$[BM] = [M_\mathrm{T}] - [M] \tag{42}$$

$$[B] = [B_\mathrm{T}] - [BM] = [B_\mathrm{T}] - [M_\mathrm{T}] + [M] \tag{43}$$

The expression for $[BM]$ and $[B]$ can be substituted into equation (39):

$$K_5 = \frac{[M_\mathrm{T}] - [M]}{([B_\mathrm{T}] - [M_\mathrm{T}] + [M])\,[M]}. \tag{44}$$

Equation (44) can finally be rearranged to express $[M_\mathrm{T}]$ as a function of $[M]$, the buffered concentration of metal:

$$[M_\mathrm{T}] = \frac{K_5[M]^2 + (K_5[B_\mathrm{T}] + 1)[M]}{1 + K_5[M]}. \tag{45}$$

Experimental values determined for Zn(II) were employed to simulate the buffer system. In section 5.3.3, the graded response of Zur to Zn(II) was discussed. Equation (45) can not only be used to model a Zn(II) buffer system but also to further describe the graded response of the Zn(II)-sensors. To model the Zn(II) buffer, $[B_\mathrm{T}]$ was set so that the buffering species were able to bind half of the total Zn(II) present in Zn(II)-supplemented *Salmonella* cells (2.3×10^5 zinc atoms per cell, corresponding to apparent total Zn(II) concentration of 3.7×10^{-4} M, (Osman et al, 2019)). A Zn(II)-affinity value that was the average of the affinities of proteins with a site 50% occupied with Zn(II) when Zur and ZntR undergo 0.5 of their response was assigned

to K_5. The simulation of the buffers system, calculated using equation (45), was reported in **Figure 6.2**. This curve showed how the buffered metal concentration relates to the amount of labile Zn(II) in the buffer, during transitions from metal depletion to saturation. A metal buffer system behaves similarly to a more familiar pH buffer, with protons representing the metal and with K_a being the parameter corresponding to K_5. In the buffering region, the buffered concentration of metal remains close to the numerical value of K_5 (as dissociation constant) even with a large increase (or decrease) in amount of metal in the buffer. Once at elevated [M_T] the capacity of the buffer is fully saturated, even a small change in [M_T] can have a dramatic effect on the buffered concentration of metal, which increases sharply (almost horizontal part of the curve at high [M_T] in **Figure 6.2**).

The data points in **Figure 6.2** correspond to the buffered Zn(II) concentrations where the fractional DNA occupancy for *Salmonella* Zur and ZntR on the *znuA* and *zntA* promoters respectively, and for *B. subtilis* Zur on the *rpsNB* promoter is 0.5. Moving from Zn(II)-replete to Zn(II)-deplete conditions, first the expression of the Zn(II)-export system (the *zntA* gene product) is turned off as the saturation of the buffer starts decreasing. Then, the expression of the Zn(II)-import system is turned on (by de-repression of *znuA* by Zur) as the buffer is moving towards metal depletion. Finally, once the buffer in completely depleted, the 'fail-safe' Zn(II)-sparing systems are activated (*rpsNB*). This graph also shows how the small differences in buffered Zn(II) concentrations that trigger the sensors graded response (orders of magnitude smaller than the difference in sensitivity between the various sensors, **Figure 5.6**) become substantial when they are related to the saturation of a cytosolic metal buffer and hence the total amount of metals in a cell (Osman et al, 2019).

6.3 Prediction of protein metalation

The defined metal availabilities in the cytosol of *Salmonella* (**Figure 6.1**) allow the prediction of protein metalation *in vivo*. The preferred metal that CbiK, a protein involved in the biosynthesis of cobalamin (vitamin B_{12}, section 1.6) will bind in the *Salmonella* cytosol was determined as an exemplar. CbiK is a cobalt chelatase responsible for the cobalt insertion into sirohydrochlorin, a precursor of vitamin B_{12}. Andrew Foster determined the affinities of CbiK for a range of first-row transition metals and calculated the standard free energies associated with the metalation reaction (**Table 6.2**). CbiK was found to have a tight affinity for Cu(I) (dissociation constant ~10^{-14} M), almost six orders of magnitude tighter than its affinity for Co(II) (dissociation constant ~10^{-8} M). Alone, these data would suggest that this protein will preferentially bind Cu(I), as this metal could easily displace the cognate Co(II) ion. This raised the question on how CbiK can act as a cobalt chelatase in *Salmonella* and not as a copper chelatase.

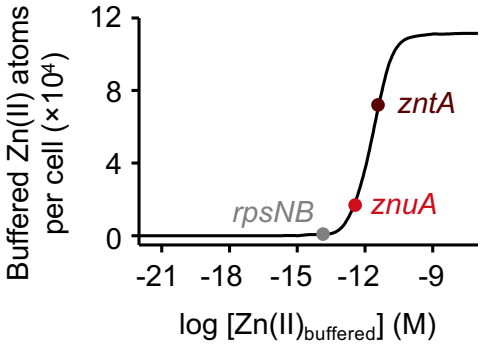

Figure 6.2. A model for a buffer system.
The simulation of a buffer system shows the relationship between the buffered Zn(II) concentration and the total Zn(II) ions associated with the buffer. Here, it is modelled that the buffer can bind up to half of the Zn(II) ions present in *Salmonella* cells under elevated metal (Osman et al, 2019). The symbols show where *Salmonella* ZntR and Zur, and *B. subtilis* Zur on the *rpsNB* promoter undergo 0.5 of their normalised responses. Figure and caption are adapted from (Osman et al, 2019).

Table 6.2. CbiK metal affinities and standard free energies.

Metal	K_{Metal} (M)	$\Delta G°$ (kJ mol^{-1})†
Mn(II)	$\geq 2.0 \times 10^{-5*}$	≥-26.8
Fe(II)	$4.7 (\pm 1.5) \times 10^{-6}$	-30.4
Co(II)	$1.4 (\pm 0.1) \times 10^{-8}$	-44.9
Zn(II)	$1.8 (\pm 0.2) \times 10^{-8}$	-44.2
Ni(II)	$5.4 (\pm 1.7) \times 10^{-9}$	-47.2
Cu(I)	$7.7 (\pm 1.3) \times 10^{-14}$	-74.9

*No binding detected. Estimate based on minimal migration of Mn(II) with CbiK by size-exclusion chromatography with 20 μM Mn(II) in buffer. Data collected by Andrew Foster. Table and caption are adapted from (Osman et al, 2019).

The answer to this question came from the comparison of the standard free energies for metalation determined for the *Salmonella* cytosol and the standard free energies associated with the metalation of CbiK (**Figure 6.3**). The standard free energy for the formation of Cu(I)-CbiK is not favourable enough for the chelatase to outcompete the buffer and to bind Cu(I). Formally, the standard free energy for the metalation of CbiK *in vivo* can be calculated from the difference between the standard free energy for the metalation of CbiK (**Table 6.2**) and the standard free energy for metalation of the buffer representing metal availability (**Table 6.1**). For Cu(I), this gives a largely positive standard free energy for the reaction, indicating that the flow of Cu(I) from the buffer to CbiK is a non-spontaneous process. On the other hand, the standard free energy associated with the formation of the complex between Co(II) and CbiK is close to the Co(II) availability (closed red symbol in **Figure 6.3**), meaning the CbiK can indeed bind this metal from the cytosolic buffered pool and transfer it to sirohydrochlorin. Therefore, even though its affinity for Cu(I) is tighter than for Co(II), CbiK cannot acquire Cu(I) *in vivo*, as its affinity for this metal does not match the intracellular availability. Conversely, CbiK has just sufficient affinity for Co(II) to acquire this metal in the cytosol. This is a clear example of how, by finely poising metal availabilities as the inverse of the Irving-Williams series, cells can achieve correct metalation of proteins even with the more weakly binding metals.

A similar analysis can be performed for any protein or molecule of interest located in the cytosol. If the affinities for the various metals are known, it should become possible to predict what metal (if any) it will bind, as done for CbiK. It might be predicted that the molecule will acquire the most competitive metal for which its standard free energy for metalation is most favourable relative to the metal buffer system (however, note considerations in section 7.3.1 related to **Figure 7.2**). For CbiK, this metal was Co(II) (**Figure 6.3**).

6.3.1 Quantitative prediction of protein metalation

From the data in **Figure 6.3** it is not only possible to acquire qualitative information on which metal a certain molecule will bind, but also quantitative information on the metalation state of that molecule. For a molecule involved in a ligand binding equilibrium (for example, a protein (P) binding a metal ion (M) with a thermodynamic association constant K_M), the fraction of the ligand-bound molecule can be calculated from the thermodynamic constant of complex formation and the concentration of available ligand (Langmuir equation):

$$\mathrm{P} + \mathrm{M} \rightleftharpoons^{K_M} \mathrm{PM} \qquad\qquad \theta_{\mathrm{PM}} = \frac{[PM]}{[P]+[PM]} = \frac{[M]K_M}{1+[M]K_M}$$

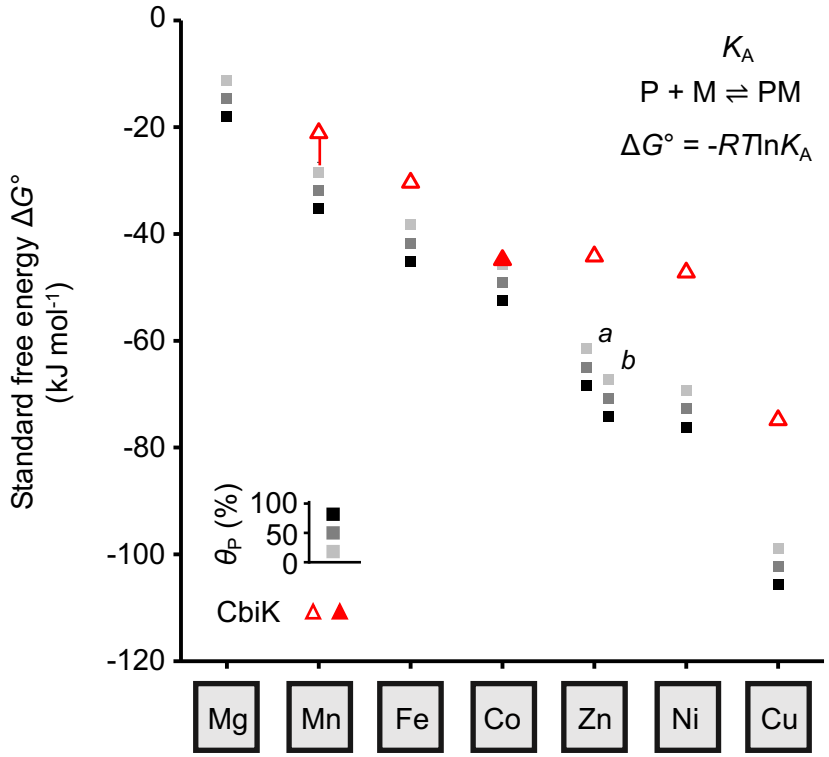

Figure 6.3. Enzyme metalation can be predicted in *Salmonella* based on metal availabilities.
Standard free energies for formation of CbiK-metal complexes (triangles) compared to standard free energies for protein-metal complex formation in the *Salmonella* cytosol which would give 20% (light grey squares), 50% (dark grey) or 80% (black) metalation (θ_P) (as in **Figure 6.1**). The Zn(II) free energies are reported based on both ZntR (*a*) and Zur (*b*). For Mn(II), the CbiK the standard free energy value represents a limiting affinity of 2.0×10^{-5} M (as dissociation constant) or weaker. Despite having a tighter affinity for Cu(I), the cobalt chelatase CbiK is predicted to bind Co(II) in *Salmonella*. The CbiK metal-affinities were determined by Andrew Foster. Figure and caption are adapted from (Osman et al, 2019).

However, a protein in the cytosol of a cell faces a different environment: The protein can potentially be involved in metal-binding equilibria with several metals (**Figure 6.4**). To determine the fraction of protein metalated with each metal, it is possible to write a different Langmuir equation for each thermodynamic equilibrium in **Figure 6.4**.

The fraction of all protein bound to metal ions can be calculated from the sum of the individual metalation fractions:

$$\theta_{\mathrm{PM_1}} = \frac{[M_1]K_{M_1}}{1+[M_1]K_{M_1}} \qquad \theta_{\mathrm{PM_2}} = \frac{[M_2]K_{M_2}}{1+[M_2]K_{M_2}}$$

$$\theta_{\mathrm{PM_3}} = \frac{[M_3]K_{M_3}}{1+[M_3]K_{M_3}} \qquad \theta_{\mathrm{PM}_n} = \frac{[M_n]K_{M_n}}{1+[M_n]K_{M_n}}$$

$$\theta_{\mathrm{PM}} = \sum_{i=1}^{n} \theta_{\mathrm{PM}_i}$$

However, depending on the relative affinities of the protein for the various metals and the availability of each metal ion, θ_{PM} could end up being greater than 1, which is meaningless for this parameter. This is due to the fact that the Langmuir equations written independently for each metal-binding equilibrium do not take into account that all the various metals are competing for the same metal-binding site within the protein. The fractional occupancy of the protein with a particular metal might in fact be smaller if the metal-binding site is already occupied by another metal.

6.3.2 Derivation of a modified equation to predict metalation *in vivo*

In order to reflect the conditions in **Figure 6.4**, modified Langmuir equations can be derived for each metal, taking into account their competition for the protein metal-binding site. For each metal-binding equilibrium (involving metals from M_1 to M_n) in **Figure 6.4**, it is possible to write the corresponding equilibrium constant equation:

$$\begin{aligned}
\mathrm{P} + \mathrm{M}_1 &\overset{K_{\mathrm{M}_1}}{\rightleftharpoons} \mathrm{PM}_1, & K_{\mathrm{M}_1} &= \frac{[PM_1]}{[P][M_1]},\\
\mathrm{P} + \mathrm{M}_2 &\overset{K_{\mathrm{M}_2}}{\rightleftharpoons} \mathrm{PM}_2, & K_{\mathrm{M}_2} &= \frac{[PM_2]}{[P][M_2]},\\
&\vdots & &\vdots\\
\mathrm{P} + \mathrm{M}_i &\overset{K_{\mathrm{M}_i}}{\rightleftharpoons} \mathrm{PM}_i, & K_{\mathrm{M}_i} &= \frac{[PM_i]}{[P][M_i]},\\
&\vdots & &\vdots\\
\mathrm{P} + \mathrm{M}_n &\overset{K_{\mathrm{M}_n}}{\rightleftharpoons} \mathrm{PM}_n, & K_{\mathrm{M}_n} &= \frac{[PM_n]}{[P][M_n]}.
\end{aligned}$$

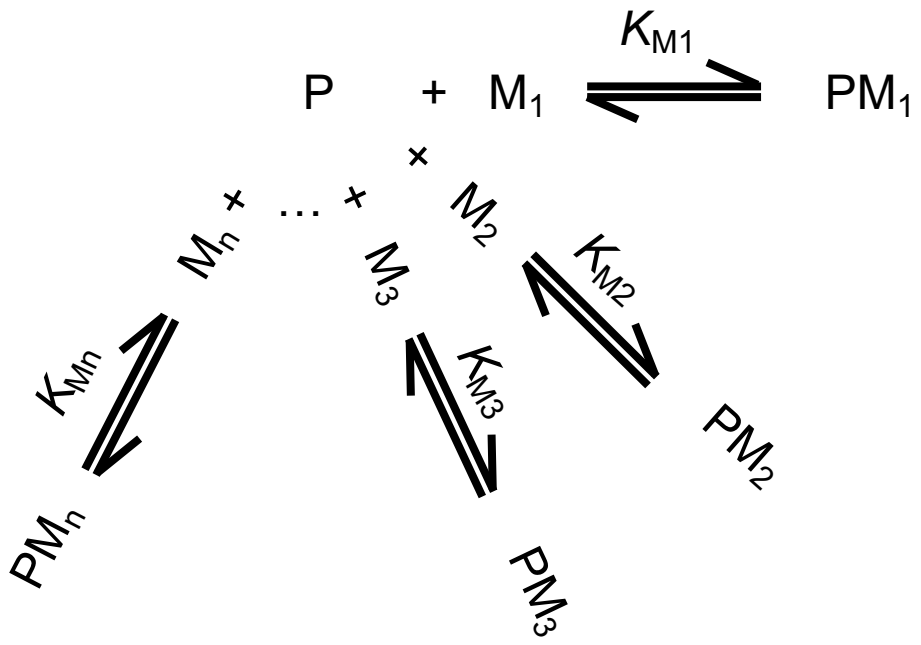

Figure 6.4. Different metal ions compete for the same metal-binding site *in vivo*
Semi-schematic representation of a protein involved in *n* simultaneous metal-binding equilibria with *n* different metals. The various metal ions all compete for the same metal-binding site within the protein.

The mass balance for the protein, considering all the complexes with the various metals from [PM_1] to [PM_n] is

$$[P_T] = [P] + [PM_1] + [PM_2] + \cdots + [PM_n] \tag{46}$$

As metal ions are buffered in the cytosol, as already described in section 5.1.3, it is possible to consider the buffered concentration of each metal ([M_1] to [M_n]) as an independent variable, without the need of including mass balance equations for these species. This simplification relies on the hypothesis that the protein concentration is orders of magnitude lower than the amount of metal present in the system, so that metal-binding to the protein does not affect the buffered concentration of metal (section 5.1.3).

The fraction of protein bound to a particular metal (e.g. M_i) is defined as:

$$\theta_{PM_i} = \frac{[PM_i]}{[P_T]} \tag{47}$$

and [P_T] can be substituted into (47) from equation (46):

$$\theta_{PM_i} = \frac{[PM_i]}{[P] + [PM_1] + [PM_2] + \cdots + [PM_n]} \tag{48}$$

Each equilibrium constant equation can be rearranged as:

$$[PM_i] = [P][M_i]K_{M_i} \tag{49}$$

and equation (49) can be substituted into (47) to give, after simplifying the [P] term,

$$\theta_{PM_i} = \frac{[M_i]K_{M_i}}{1 + [M_1]K_{M_1} + [M_2]K_{M_2} + \cdots + [M_n]K_{M_n}} \tag{50}$$

Equation (50) can be written in the general form:

$$\theta_{PM_i} = \frac{[M_i]K_{M_i}}{1 + \sum_{j=1}^{n} [M_j]K_{M_j}} \tag{51}$$

Equation (51) can be used to calculate the fractional occupancy of the protein with any of the n metals present in the system, provided all numerical values for [M_i] and K_{Mi} are known. The fraction of total metalated protein is given by the sum of the various θ_i and can never be greater than one as the metal competition for the same was included in the model. The fraction of apo-protein can be calculated from:

$$\theta_P = \frac{1}{1 + \sum_{j=1}^{n} [M_j]K_{M_j}} \tag{52}$$

Equation (51) was used with the CbiK data (using n = 6 different metals) to calculate the percentage of protein metalated with each metal ion. **Table 6.3** reports the protein metalation percentages calculated with or without the inclusion of metal-competition for the CbiK metal-binding site. As predicted from the data in **Figure 6.3**, CbiK is predominantly metalated by Co(II) using both models. In this particular case, considering metal-competition did not have a large effect on the metalation of CbiK. However, this might not be the case for a protein with the standard free energies for more than one metal indicating possible metalation under physiological conditions. An example will be given in Chapter 7. From the data in **Table 6.3**, it appeared that the only metal other than Co(II) that could metalate CbiK is Fe(II) (estimated occupancy 1.0% or 0.86% depending on the model used). Notably, CbiK was reported to partially complement for the lack of the iron chelatase CysG (a protein involved in the biosynthesis of sirohaem) in bacterial cells missing the *cysG* gene (Raux et al, 1997).

6.3.3 Protein metalation predicted from sensors K_1 values

In section 5.3.2, the differences in sensitivity between sensors responses inferred from the metal affinity K_1 alone or from the combination of all the other parameters were discussed. Based on the buffered metal concentrations inferred from K_1 alone (i.e. the buffered metal concentrations at which the sensors are 50% metalated with their cognate metals), the standard free energies for the metalation of the hypothetical protein with 20%, 50% and 80% occupancy were derived (**Figure 6.5**). These $\Delta G°$ values were compared with the standard free energy for metalation of CbiK, in order to predict the metalation of the chelatase at these metal availabilities. Interestingly, based on sensor responses inferred only from K_1 values, the metal availabilities would suggest that CbiK is not able to bind Co(II) but it would bind, instead, Fe(II). This highlights the importance of modelling the responses of the sensors taking into account not only their affinity for the cognate metals, but also the DNA-binding properties and the sensors abundances.

6.4 Metal availabilities for bespoke conditions

The standard free energies for metalation in **Table 6.1** were derived from the cellular metal availabilities at which the fractional DNA occupancy for each sensor in response to its cognate metal was 0.5. However, depending on the conditions (and hence metal content) the bacterium is exposed to, metal availabilities can vary, with consequent increase or decrease in DNA occupancy in response to the change in metal levels. Metal availability will therefore vary over a narrow range (as exemplified by the buffer model in **Figure 6.2**), but even though these changes are small compared to the differences in availability between different metals (**Figure 5.6** and **Figure 6.1**), they can have a substantial effect on the metalation state of a molecule in the cytosol.

Table 6.3. Occupancy of CbiK with metals in *Salmonella* cells.

Metal	$1/K_{metal}$ (M)	Metalation (%) *no competition*	Metalation (%) *with competition*
Mg(II)	n.d.	n.d.	n.d.
Mn(II)	2.0×10^{-5}	n.d.	n.d.
Fe(II)	$4.7 (\pm 1.5) \times 10^{-6}$	1.0	0.86
Co(II)	$1.4 (\pm 0.1) \times 10^{-8}$	15.4	15.02
Zn(II)	$1.8 (\pm 0.2) \times 10^{-8}$	0.01	0.01
Ni(II)	$5.4 (\pm 1.7) \times 10^{-9}$	0	0
Cu(I)	$7.7 (\pm 1.3) \times 10^{-14}$	0	0

The metalation percentages of CbiK were calculated with or without considering that the various metal ions are competing for the same metal-binding site in CbiK. The metal affinities of CbiK were determined by Andrew Foster. Table and caption adapted from (Osman et al, 2019). The metal availability of Zn(II) in these calculations was calculated from the average of the free energies inferred from ZntR- and Zur-mediated responses (**Table 6.1**).

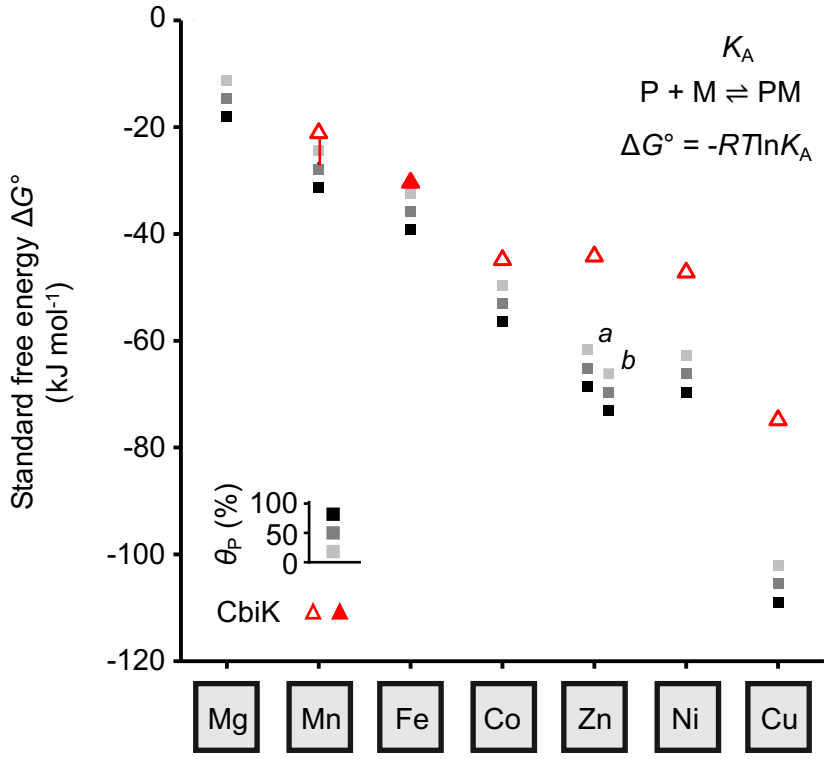

Figure 6.5. When metal availabilities were inferred from sensors K_1 values, CbiK ceased to bind Co(II).
Standard free energies for formation of CbiK-metal complexes (triangles) compared to the standard free energies for protein-metal complex formation in the *Salmonella* cytosol which would give 20% (light grey squares), 50% (dark grey) or 80% (black) metalation (θ_P), calculated using sensor responses inferred from K_1 alone (see **Figure 5.8**). The Zn(II) free energies are reported based on both ZntR (*a*) and Zur (*b*). In this case, CbiK is predicted to preferentially bind iron (filled symbol) over cobalt, in contrast with metal availabilities determined the complete thermodynamic cycle for sensor responses (as in **Figure 6.1**). Figure and caption are adapted from (Osman et al, 2019).

The percentage of metalation of CbiK, which was calculated when RcnR undergoes 0.5 of its response, might be different when *Salmonella* cells produce vitamin B_{12} under anaerobic conditions, causing a different metalation of CbiK with Co(II). Similarly, a particular metallochaperone might be expressed only under certain metal-replete or metal-deplete conditions (for example, if regulated by one of the sensors) and, in order to correctly predict which metal it will bind, it is necessary to know what the metal availabilities are under those conditions.

The response of the sensors (i.e. the variation in expression of the regulated genes) can be used as a readout of metal availability under different conditions. A simple experiment was performed to test whether the response of any of the *Salmonella* sensors was saturated when cells were grown in the commonly used metal-rich growth medium as LB. *Salmonella* cells were grown to mid-log phase and then exposed to 400 μM Mn(II), 2 μM Fe(II), 1 μM Co(II), 100 μM Ni(II), 50 μM Cu(II) or 100 μM Zn(II). Preliminary growth curve experiments were performed to identify the mid-log phase window under the growth conditions employed (**Figure 8.6**, **Appendix A**). The metal concentrations employed were twice the metal concentrations reported to inhibit growth of *Salmonella* cells in M9 medium by less than 15% (for iron, this was the metal concentration enhancing growth by less than 15%) (Osman et al, 2019). After 10 min of metal exposure, cells were harvested for RNA extraction. The expression of the target genes relative to a metal-untreated sample was measured by quantitative PCR (qPCR, **Figure 6.6**). In response to the increased metal concentrations, transcripts controlled by the activators ZntR and CueR and by the de-repressor RcnR increased in abundance. Conversely, the transcript abundance of *mntS*, regulated by the co-repressor MntR, decreased after cell exposure to Mn(II). The transcript abundance of *iroB* and *znuA* (regulated by Fur and Zur respectively) remained largely unchanged.

These results imply that, in cells grown in LB, Fur and Zur appear to have reached almost 100% of their responses (normalised fractional DNA occupancy close to 1). Therefore, even if cells are exposed to increasing amounts of Fe(II) and Zn(II), the fractional DNA occupancy cannot increase further. However, for Fur this might be due to the concentration of Fe(II) used in the experiment, which might be too low to elicit sensor response in this particular growth media. In order to have a clearer picture of the saturation of Fur response in LB media, the metal-exposure experiments should be repeated with higher concentrations of Fe(II). In contrast, the Zn(II) concentration used in the assay was enough to trigger the response of the other Zn(II) sensor ZntR, supporting the hypothesis that in LB Zur might be close to 100% of its response.

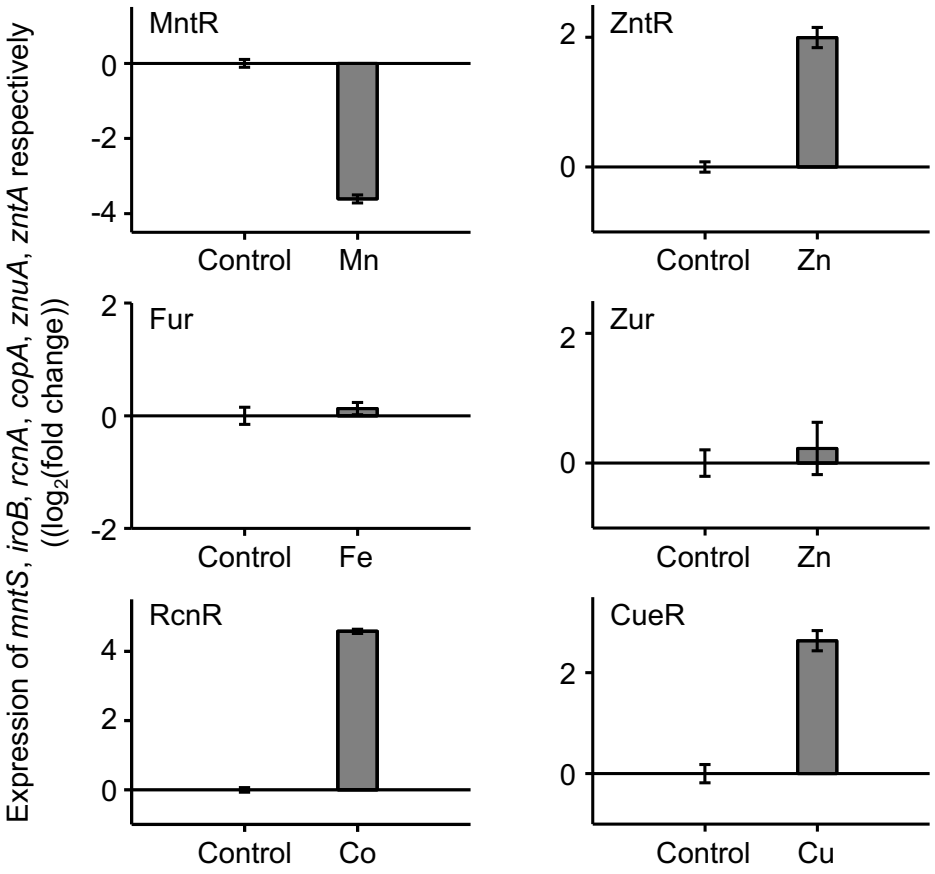

Figure 6.6. Sensors responses to supplementation of LB growth medium with elevated [metals].
qPCR analysis of *mntS* (regulated by MntR), *iroB* (regulated by Fur), *rcnA* (regulated by RcnR), *zntA* (regulated by ZntR), *znuA* (regulated by Zur) and *copA* (regulated by CueR) in cells grown in LB to mid-log phase ($OD_{600\ nm} \approx 0.3$) and exposed to metals for 10 minutes (400 µM $MnCl_2$, 2 µM $FeSO_4$, 1 µM $CoCl_2$, 100 µM $NiSO_4$, 50 µM $CuSO_4$, 100 µM $ZnSO_4$). Fur and Zur did not respond to the supplementation with metal. Data are mean ±s.d. of n = 3 technical replicates from one biological sample.

6.5 Calibration of Zur and ZntR responses

In order to better define Zn(II) availability in cells grown in LB, the responses of Zur and ZntR to Zn(II) were calibrated. The difference in sensitivity between the two sensors is approximately one order of magnitude (**Figure 6.7**). However, if they sense the same Zn(II) pool, their respective fractional DNA occupancy values under the same growth conditions should correspond to a similar metal availability. For example, if for Zur θ_D is about 0.80, under the same conditions and if the two proteins sense the same pool, θ_{DM} for ZntR should be 0.20−0.30. The response of the two sensors can be calibrated by measuring the change in transcript abundance of the two target genes *znuA* and *zntA* between two extreme conditions: a Zn(II)-deplete and a Zn(II)-replete one. These changes in gene expression correspond to the transition in fractional DNA occupancy from the low extreme of θ_D (or θ_{DM}) to the high one (for example, transition of θ_D/θ_{DM} from 0.01 to 0.99, or from 0.10 to 0.90). Once the maximum observable change in transcript abundance is known, the change in gene expression of *znuA* and *zntA*, relative to one of the two extreme conditions used for the calibration, can be measured for cells grown under any condition of interest. Using the calibration of the response, this specific experimentally determined change in transcript abundance can be correlated to a fractional DNA occupancy value for Zur and ZntR and, therefore, to the Zn(II) availability under those specific growth conditions.

In order to calibrate the response of the Zn(II) sensors, *Salmonella* cells were grown to mid-log phase and then treated for one hour with a chelant (to study the Zn(II)-deplete conditions) or with an elevated concentration of Zn(II) (to study the Zn(II)-replete conditions). The chelant employed was TPEN, a membrane-permeable chelator with high affinity for Zn(II) (Xiao & Wedd, 2010), which is commonly employed to sequester Zn(II) in *in vivo* experiments (Cho et al, 2007). In the metal-replete sample, *Salmonella* cells were treated with 1 mM Zn(II), tenfold higher than the metal concentration employed in **Figure 6.6**, to further push both θ_D for Zur and θ_{DM} for ZntR towards their higher limits. At the end of the 1-hour treatment, cells were harvested for RNA extraction. **Figure 6.8** reports the optical density of the *Salmonella* samples and the viability of the cells (measured as colony forming units per ml of culture) at the point of RNA extraction after the treatment with TPEN and Zn(II). Compared to the untreated sample (cells grown in standard LB, water was added instead of TPEN/Zn(II)), TPEN did not seem to drastically affect cells growth, while such a high concentration of Zn(II) started having toxic effects on the cells. The change in gene expression of *znuA* and *zntA* relative to the control sample was measured by qPCR (**Figure 6.9** for *znuA* and **Figure 6.10** for *zntA*).

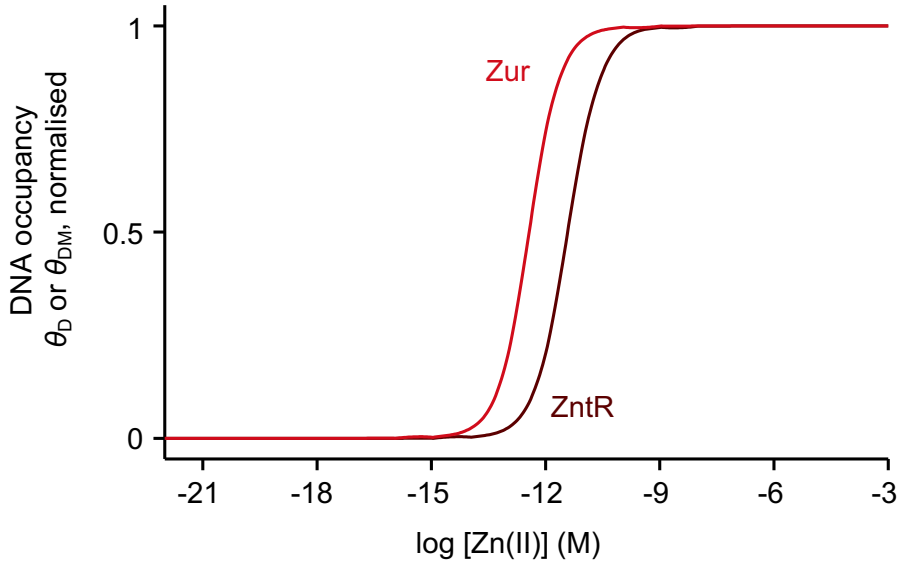

Figure 6.7. Zn(II) sensing in *Salmonella*.
Calculated responses for Zur and ZntR as in **Figure 5.6**. The two Zn(II) sensors have different set-points. One of the genes in the Zur regulon, *znuA*, encodes for a component of the ZnuABC Zn(II)-importer. ZntR regulates the transcription of *zntA*, a gene encoding for a Zn(II)-exporter.

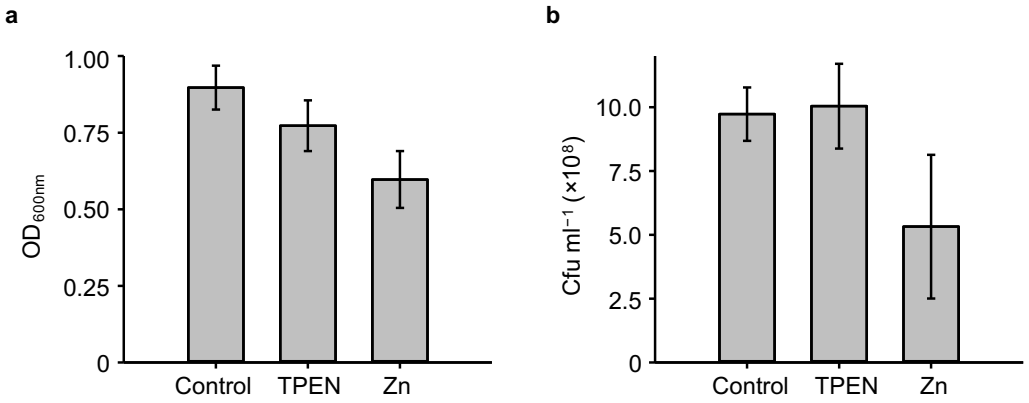

Figure 6.8. Cell growth after TPEN and Zn(II) exposure.
Cells were grown in LB media and exposed in mid-log phase ($OD_{600\,nm} \approx 0.3$) to 50 μM TPEN or 1 mM $ZnSO_4$ for 1 h before RNA extraction for qPCR data shown in **Figure 6.9** and **Figure 6.10**. Sterile water was added to the control sample. **a**, Optical density of cultures at the point of RNA extraction. **b**, Viability of cells (as colony forming unit ml^{-1}) following the 1 h shock. Data are mean ±s.d. of n = 3 biologically independent samples.

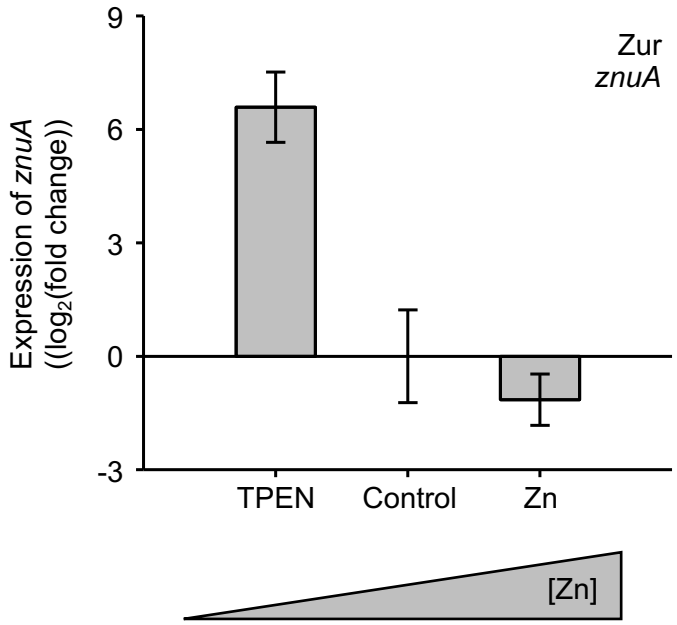

Figure 6.9. Calibration of Zur response to Zn(II).
qPCR of *znuA* from cells exposed to TPEN or Zn(II) as in **Figure 6.8** (Zur acts as a co-repressor). The TPEN- and the Zn(II)-treated sample represent respectively the minimum and maximum response (i.e. DNA occupancy) of Zur on the *znuA* promoter. Data are mean ±s.d. of n = 3 biologically independent samples.

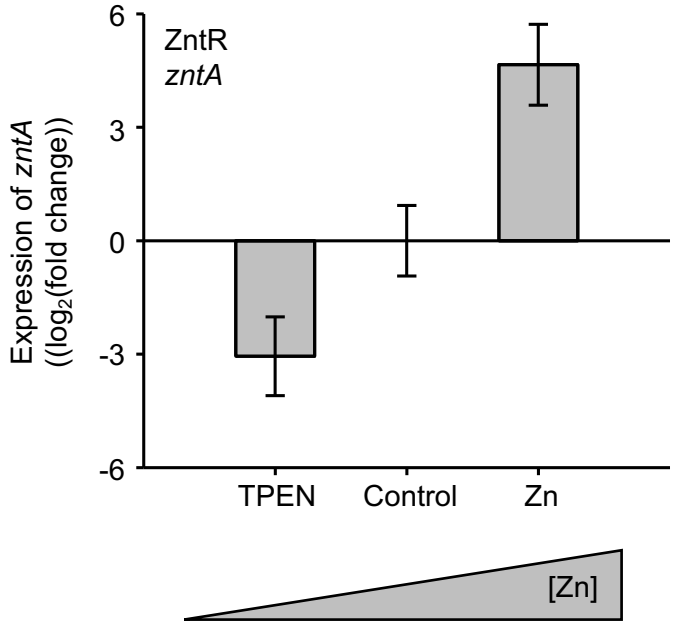

Figure 6.10. Calibration of ZntR response to Zn(II).
qPCR of *zntA* from cells exposed to TPEN or Zn(II) as in **Figure 6.10** (ZntR acts as an activator). The TPEN- and the Zn(II)-treated sample represent respectively the minimum and maximum response (i.e. DNA occupancy with metalated sensor) of ZntR on the *zntA* promoter. Data are mean ±s.d. of n = 3 biologically independent samples.

As anticipated from the mode of action of the two sensors, *znuA* was up-regulated in the TPEN-treated sample and down-regulated in the Zn(II)-treated sample (Zur acts as a co-repressor on this gene), while the opposite was observed for *zntA* (ZntR is an activator).

The transcript abundance data in **Figure 6.9** and **Figure 6.10** were expressed as fold change relative to the untreated sample in LB medium. The raw qPCR data were then re-analysed and expressed as fold change relative to the TPEN-treated sample, to better highlight how the various increases in the amount of Zn(II) in the medium (first by removing the chelant and then by supplementing the metal) affected gene expression (**Table 6.4**). Moving from the TPEN-treated sample to the Zn(II)-supplemented one, the expression of *znuA* decreased by approximately 200-fold while the expression of *zntA* increased by about 245-fold. These changes in gene expression were correlated to a change in fractional DNA occupancy from 0.01 to 0.90 for both Zur and ZntR (**Figure 6.11**). In the untreated sample (normal LB medium), a decrease in *znuA* expression of 78-fold compared to the TPEN sample was observed. Assuming a linear proportion between the change in transcript abundance and the change in fractional DNA occupancy, a θ_D value of 0.89 was calculated for Zur in LB medium (**Figure 6.11**). Similarly, in the LB sample *zntA* expression increased by 9-fold compared to the TPEN one (**Table 6.4**). This was calculated to correspond to a θ_{DM} of 0.13 for ZntR in LB (**Figure 6.11**).

Based on the fractional DNA occupancy values determined for Zur and ZntR in LB, metal availabilities were calculated and expressed as standard free energies. **Figure 6.12** reports the standard free energies determined from the point of mid-response of the sensors (**a**, as in **Figure 6.1**) compared with the standard free energy for Zn(II) in LB, determined from the calibration (**b**). In LB growth medium metal availabilities inferred from Zur and ZntR were 2.8×10^{-12} M and 5.7×10^{-13} M respectively, corresponding to standard free energies of −65.9 kJ mol^{-1} and −69.9 kJ mol^{-1} for the metalation of a hypothetical molecule with 50% metal-saturation. These values are relatively close and the mean is −67.9 kJ mol^{-1}, which is similar to that established from the mean of the mid-point of the two sensors.

There is scope for further optimisation of this calibration. For example, higher TPEN concentrations might be tested, as this chelant was proven to be quite well tolerated by *Salmonella* cells (**Figure 6.8**). While we assumed that in the TPEN samples the response of both of the sensors was 0.1, it is formally possible that the two sensors might indeed cease to respond to the Zn(II)-depletion at different metal availabilities. Similarly, different fractional DNA occupancy values could be employed for two limits of the calibration, for example 0.01 and 0.99 instead of 0.10 and 0.90. Nevertheless, this is the first attempt to calibrate the response of the Zn(II) sensors and a similar strategy could be employed for other sensors.

Table 6.4. Expression of *znuA* and *zntA* relative to a Zn(II)-depleted samples.

Gene	Condition	Fold change	Log_2(fold change)
znuA	TPEN	1.1 (±0.6)	0.0 (±0.9)
	LB	1.3 (±0.9) × 10^{-2}	-6.6 (±1.2)
	Zn(II)	5.0 (±2.3) × 10^{-3}	-7.7 (±0.7)
zntA	TPEN	1.2 (±0.8)	0.0 (±1.0)
	LB	9.4 (±5.3)	3.1 (±0.9)
	Zn(II)	244.5 (±140.0)	7.7 (±1.1)

Change in *znuA* and *zntA* transcript abundance in the same *Salmonella* samples used to generate the data in **Figure 6.9** and **Figure 6.10**, but calculated using the TPEN-treated sample instead of the untreated one as the reference condition. Data are reported as mean ±s.d. of n = 3 biologically independent samples.

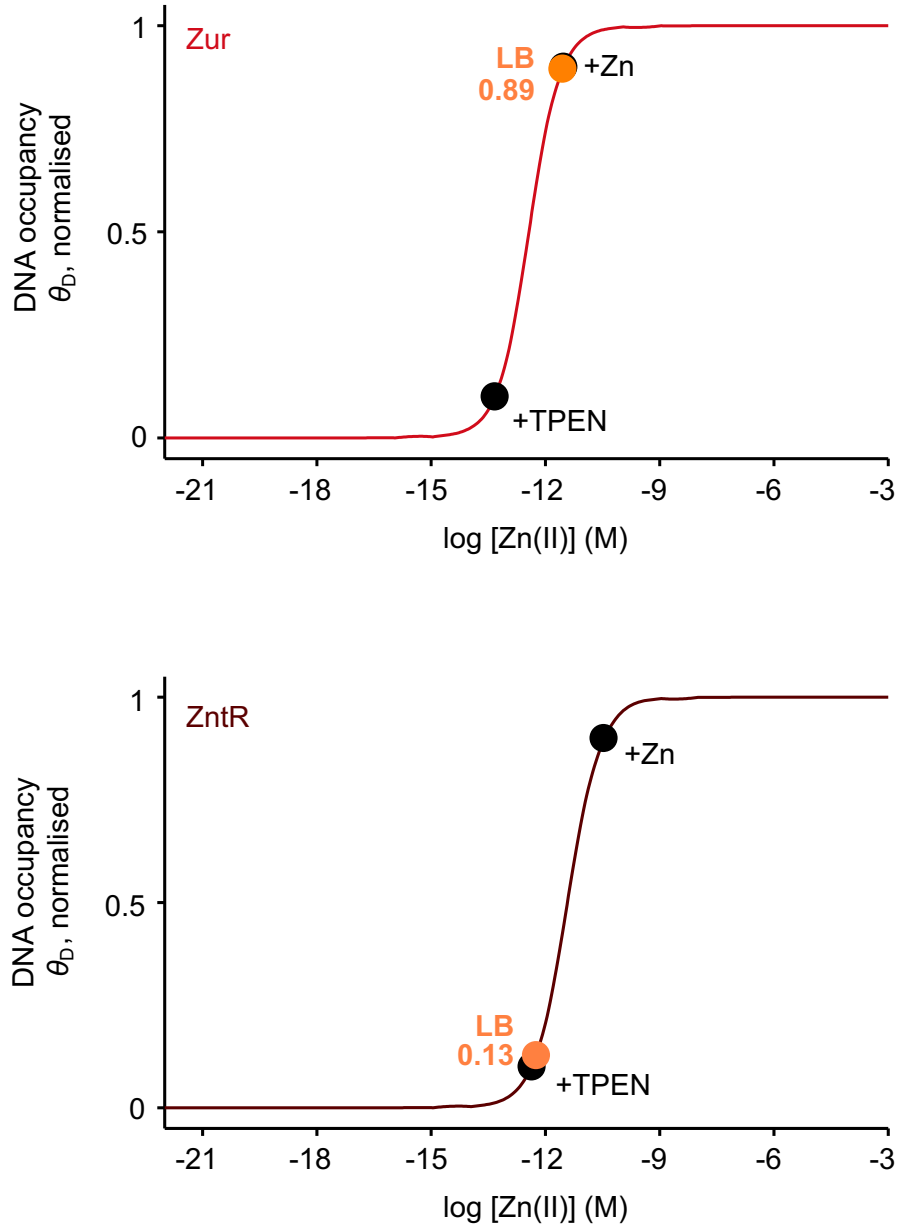

Figure 6.11. Zur and ZntR set points in LB media.
Calculated responses for Zur and ZntR as a function of buffered [Zn(II)] as in **Figure 6.7**. The black symbols represent the limit responses for the two sensors in LB media supplemented with 50 µM TPEN or 1 mM $ZnSO_4$ (0.1 and 0.9 response respectively). The degree of response for the two sensors in standard LB media (orange symbols) was calculated based on the calibration of sensor responses (qPCR data in **Figure 6.9** and **Figure 6.10**).

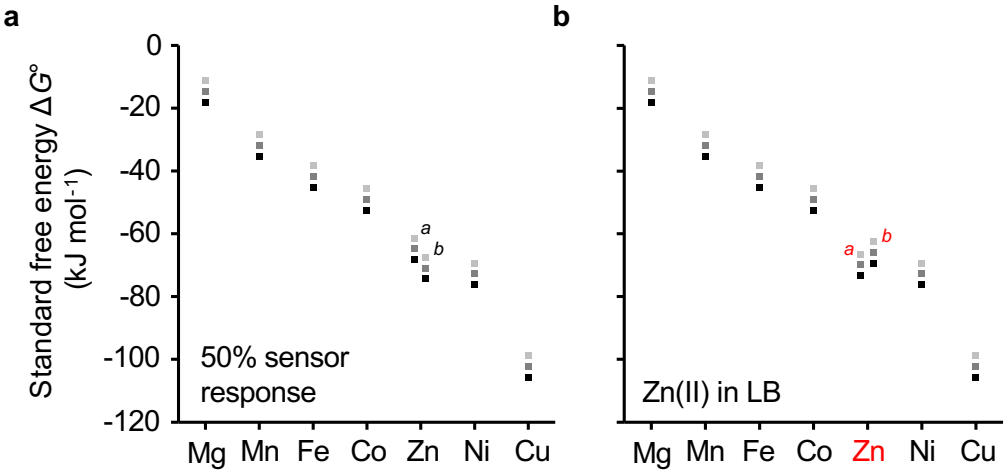

Figure 6.12. Refined Zn(II) availabilities in LB media.
Standard free energies ($\Delta G°$) associated with the formation of metal complexes in *Salmonella* cytosol (as in **Figure 6.1**). **a**, Standard free energies when sensors undergo 0.5 of their responses. **b**, Standard free energies for Zn(II) based on Zur and ZntR response in LB media (**Figure 6.11**), while the other sensors undergo 0.5 of their responses as in **a**.

So far, *Salmonella* is the only organisms in which the cytosolic metal availabilities have been determined from the sensitivities of its metal sensors (**Figure 6.1**), providing a reference framework to predict metalation. This implies that *Salmonella* can be considered a model organism to study *in vivo* metal-protein speciation. For example, this knowledge could be used to optimise metalloenzymes production in heterologous organisms, to study metal acquisition or release by antimicrobial ionophores, or even to calibrate metal-sensing probes for the determination of *in vivo* metal availabilities in other cells (Chapter 7).

Chapter 7.

Discussion and future work

7.1 *In vitro* characterisation of MntR and Fur

During the course of this work, the manganese sensor MntR and the iron sensor Fur from *Salmonella* were biochemically characterised to determine their sensitivities. In particular, the sensors were assayed to determine their metal-binding and DNA-binding properties. Both MntR and Fur had previously been characterised *in vivo* in *Salmonella*, confirming their response to manganese and iron respectively, and (partially) characterising their regulon (Ikeda et al, 2005; Kehres et al, 2002a; Troxell et al, 2011; Tsolis et al, 1995). However, the two proteins had never been characterised *in vitro* before.

MntR was shown to bind two equivalents of Mn(II) per protein monomer (four per dimer, the putative functional assembly) (**Figure 3.4**). Via competition with the fluorescent probe mag-fura-2 (the affinity of mag-fura-2 was determined during this study), MntR affinity for Mn(II) was determined to be $K_{Mn(II)}$ = 1.3 (±0.4) × 10^{-5} M for the complement of allosteric sites (section 3.3.3). Both the metal-binding stoichiometry and affinity were consistent with the data available in the literature on *B. subtilis* MntR, the best characterised sensor from the DtxR family (section 1.5.2). The MntR DNA recognition sequence was identified by bioinformatic analysis of the promoter of the genes in its regulon (**Figure 3.8** and **Figure 3.9**). The sensor was confirmed to bind its recognition sequence in the promoter of the *mntS* gene *in vitro*, with an affinity dependent on the metalation state of the protein (Mn(II)-dependent repression of *mntS* had been confirmed *in vivo* (Osman et al, 2019)) (sections 3.4.2–3.4.5). MntR bound to the promoter of *mntS* with a tighter affinity in the presence of Mn(II) compared to its apo-form, consistent with this sensor acting as a co-repressor on this promoter (**Figure 3.17**). Fluorescence anisotropy experiments revealed the formation of MntR-DNA multimeric species with undefined stoichiometry (**Figure 3.14** and **Figure 3.16**). Via fluorescence anisotropy and size-exclusion chromatography experiments, it was possible to observe the first binding event: a MntR dimer binding to the promoter of *mntS* with tight affinity (**Figure 3.11**, **Figure 3.14** and **Figure 3.16**). The thermodynamic constants for this first event were determined to be K_{DNAapo} = 8.6 (±1.7) × 10^{-8} M and $K_{DNAMn(II)}$ = 5 × 10^{-9} M respectively for the apo- and Mn(II)-bound form of the sensor (**Figure 3.17**).

Fur was confirmed to have a Zn(II) structural site per subunit, as other members of the Fur family (section 4.2.1, plus **Figure 4.9** and **Figure 4.11**). Based on the similarity with *E. coli* Fur and the slow reactivity of two thiols of the four present in the protein (**Figure 4.8**), is was hypothesised that Zn(II) is bound by Cys92 and Cys95. Several metal-binding stoichiometries

were reported in the literature for Fur family members. In this study, a stoichiometry of two Fe(II) ions (plus one structural Zn(II)) per protein monomer was suggested, based on the co-migration of the protein with metal on a size-exclusion column and the direct titration of the protein with Fe(II) (**Figure 4.11** and **Figure 4.12**). A similar stoichiometry for the Fe(II) sites was reported also for *P. aeruginosa*, *V. cholerae*, *H. pylori*, *M. gryphiswaldens*, *B. subtilis*. Interestingly, despite sharing 96.7% sequence identity (and the conserved metal-binding residues) with *Salmonella* Fur, *E. coli* Fur was reported to bind only one equivalent of metal per monomer in addition to the structural Zn(II) (Adrait et al, 1999; Jacquamet et al, 1998; Mills & Marletta, 2005). The affinity of Fur for Fe(II) was determined in competition with NTA to be $K_{Fe(II)}$ = 5.3 (±0.7) × 10^{-7} M for the complement of allosteric sites (**Figure 4.13**). Compared to other sensors, Fur has a larger regulon. The DNA sequence recognised by Fur (the *Salmonella* Fur Box, **Figure 4.15**) was identified in the promoter of *iroB* (**Figure 4.16**). The interaction of Fur with the *iroB* promoter was studied *in vitro* via size-exclusion chromatography and fluorescence anisotropy (section 4.5.2). This revealed a first event with two Fur dimers binding to the promoter with high affinity, with subsequent formation of undefined higher order complexes. Fluorescence anisotropy experiments using a shorter DNA sequence containing only the Fur box showed binding of two Fur dimers per DNA fragment (**Figure 4.23**), with an affinity for the first binding event of K_{DNAapo} = 2.4 (±0.6) × 10^{-5} M and $K_{DNAFe(II)}$ = 5.6 (±2.1) × 10^{-8} M for the apo- and Fe(II)-bound forms of the sensor respectively (**Figure 4.24**). The tighter affinity for DNA in the presence of metal confirmed the mode of action of Fur as a co-repressor on the *iroB* promoter.

Multimerization of the sensor on DNA was observed for both MntR and Fur (sections 3.4.4 and 4.5.2). However, this appeared to occur with a different mechanism for the two sensors. In this study, Fur was found to multimerize on a DNA fragment containing one of the Fur binding sites on the *iroB* promoter and flanking nucleotides (section 4.5.2). Three partially overlapping Fur boxes were identified in the *iroB* promoter and, therefore, the oligonucleotide used for the *in vitro* studies also contained part of adjacent Fur boxes (**Figure 4.16**). This promoter architecture formed by several Fur boxes (albeit with different degree of similarity with the canonical one) is common in the Fur regulon (De Lorenzo et al, 1988; Delany et al, 2005; Escolar et al, 1997). Fur homologues from several organisms have been reported to multimerize on these adjacent binding sites, and it has been hypothesised that this could confer a graded response to Fe(II) (Escolar et al, 2000; Frechon & Le Cam, 1994; Le Cam et al, 1994; Roncarati et al, 2016). When the experiments were performed with a nucleotide containing only the *Salmonella* Fur box, binding of only two dimers was observed, without the formation of additional weaker higher order species (**Figure 4.21**). Fur from *M. gryphiswaldens* is the only Fe(II)-sensing Fur protein that has been crystalized in a DNA-bound form, using a *M.*

gryphiswaldens promoter and the *P. aeruginosa* Fur box. The structure shows two Fur dimers bound on opposite sides of the *P. aeruginosa* Fur box; the two dimers interact, and this additional protein-protein interaction could confer cooperativity to the DNA-binding when Fur is binding to adjacent binding sites.

MntR was observed to form multimers on the promoter of *mntS* (**Figure 3.14**). Other DtxR proteins have been reported to undergo multimerization on DNA, for example *S. pyogenes* MtsR and *S. gordonii* ScaR. Even in the case of MntR, the oligonucleotide sequence from the *mntS* promoter used in the *in vitro* experiments contained a small proportion of an adjacent MntR binding site. However, the higher order protein-DNA complexes were not abolished in this case with the use of a shortened DNA fragment (**Figure 3.16**). This could suggest a different mechanism of protein-protein interaction in the multimerization on DNA of these two sensors. However, additional biochemical studies, possibly supported by structural studies, are needed to dissect these mechanisms. Nevertheless, the thermodynamic model used to simulate the response of MntR and Fur to metals assumed binding of one sensor dimer to the target genes promoter to be sufficient to hinder binding of the RNA polymerase and gene transcription. However, it could be possible that the multimerization of Fur and MntR on some promoters could result in the sensors acting as a rheostat to mediate minor variations in transcription (Delany et al, 2002). Notably, additional modelling will be needed to include the multimerization of the sensors on DNA in the calculations of the metal-sensitivity of MntR and/or Fur.

7.2 Calculation of sensor responses from experimentally determined parameters.

MntR and Fur responses to Mn(II) and Fe(II) were calculated from the combination of the metal- and DNA-binding thermodynamic constants, the number of DNA targets that each of the two sensors has in *Salmonella* (**Table 5.2**), and sensor abundance in the absence and presence of metals (**Table 5.1**, data collected by Osman, Chen and Huggins). Sensor responses expressed as fractional promoter occupancy were calculated using a thermodynamic model where metal-binding and DNA-binding are coupled (**Figure 5.3**). The protein abundances data revealed that some sensors (including Fur) respond to metals themselves so that the sensor copy number per cell changes as a function of metal availability (section 5.1.2). To include this component in the model, the change in sensor abundance was related to the change in fractional DNA occupancy (**Figure 5.4**) and equations were derived (section 5.2). In order to provide a tool which could be easily used by others, an electronic spreadsheet was implemented to calculate the fractional DNA occupancy as a function of the buffered concentration of metal (**Figure 5.5**); this electronic spreadsheet is available online as part of

the supplementary information of (Osman et al, 2019). The responses of MntR and Fur were calculated using the electronic spreadsheet, revealing that their sensitivities are tuned to respond at a buffered concentration of 2.6×10^{-6} M Mn(II) (for MntR) and 4.8×10^{-8} M Fe(II) (for Fur). These calculations were performed also for the other sensors in *Salmonella*, giving a complete picture of the set points for the entire set of sensors (**Figure 5.6**).

The developed mathematical model can be used to better understand how different factors contribute towards the determination of sensors sensitivity. For example, as discussed in section 5.3.2, the sensitivities of two sensors (Zur and ZntR) could be well approximated from their affinity for Zn(II) (K_1) (**Figure 5.8**). The response of other sensors shifted from the one inferred from K_1 because of the change in protein abundance and hysteresis (e.g. RcnR and Fur, **Figure 5.9**), or because of a greater contribution from K_2 (the metal-affinity of the DNA-bound form of the sensor, e.g. in the case of MntR, **Figure 5.10**). The calculations are also a useful tool to re-interpret findings from the literature, as the multiple parameters describing sensor responses can now be quantitatively combined (**Figure 5.11**).

Early publications on metal sensors described the interplay of affinity, allostery, access and abundance in determining metal specificity (Waldron et al, 2009). We now know that sensor specificity derives from the cognate sensor being the more sensitive in the set towards its cognate metal, while the availability of the other metals is controlled to avoid sensor mis-metalation and mal-responses (Osman et al, 2017). A series of studies in *Synechocystis* PCC 6803 exemplified the contribution of relative affinity, relative allostery and relative access to the selective metal detection by a sensor (Foster et al, 2012; Foster et al, 2014b; Patterson et al, 2013). The Ni(II)-responsive de-repressor InrS was found to have an affinity for Zn(II), a non-cognate metal, comparable with the Zn(II)-affinity of the two Zn(II)-sensors (the de-repressor ZiaR and the co-repressor Zur). However, *in vivo* studies showed how ZiaR but not InrS responded to prolonged Zn(II) exposure (Foster et al, 2014b). So how could the lack of response of InrS to Zn(II) be explained? DNA-binding studies revealed that although Zn(II) was able to elicit the allosteric response of InrS, it was a more effective de-repressor on the cognate sensor ZiaR. In fact, the allosteric coupling free energy (ΔG_c, 5.1.1) for Zn(II) was greater for the Zn(II)-sensor than for the Ni(II)-sensor. This implied that at some equivalent occupancy of the sensors with metal, a greater proportion of ZiaR than InrS would be off-DNA, de-repressing the target genes. This could potentially mean, however, that Zn(II), even though not fully inducing InrS allosteric response, could inhibit the response to Ni(II) by occupying the sensory metal-binding site.

These results suggested that the relative ΔG_c (allostery) was dictating why ZiaR was responding to Zn(II) *in vivo* and InrS was not. This conclusion can be now re-examined using the thermodynamic model for sensor response. The responses of InrS and ZiaR to Zn(II) were

calculated from the published values for $1/K_1$, $1/K_3$ and $1/K_4$ (**Figure 7.1**). As predicted from the similar $1/K_1$ values, the two sensors should respond at the same Zn(II) availability if the responses are inferred solely from the Zn(II)-affinity (**Figure 7.1a,** dashed lines). Nevertheless, when DNA-binding was included in the model, the sensitivity of the two de-repressors was shifted to a higher Zn(II) availability, consistent with a major contribution from K_2. ZiaR was more sensitive to Zn(II) than InrS, confirming how in this case DNA-binding has a major contribution in determining sensor sensitivity and hence specificity. However, as previously shown for Zur in **Figure 5.10**, the shift from the response inferred from K_1 is not due to the coupling free energy per se, but rather to the actual values of K_3 and K_4 (the DNA-affinities of the apo- and metalated form of the sensor respectively). The DNA-affinities of apo- and Zn(II)-InrS are both tighter than the respective parameters for ZiaR, causing the absolute DNA occupancy to be greater (**Figure 7.1b**). This determines a larger contribution from K_2 in the case of InrS than for ZiaR, shifting the response towards a greater Zn(II) availability by a larger extent. **Figure 7.1c** shows how the two sensors are metalated at similar Zn(II) availability. However, due to the high affinity of InrS for DNA, this does not immediately translate in de-repression of the promoter. It should be noted, however, that rigorous determination of the number of DNA targets of ZiaR and InrS in *Synechocystis* and the sensor abundances is needed to fully describe the responses of the two sensors (estimate values were used for the simulations in **Figure 7.1**).

7.3 A thermodynamic framework to predict metalation

From sensor responses (**Figure 5.6**), the metal availabilities to which each sensor is attuned were derived (**Table 6.1**). The mathematical modelling derived in Chapter 5 and, partially, in Chapter 6 all used the buffered concentration of the various cognate metals as the independent variable to derive all of the other parameters. In particular, sensor responses were calculated as fractional DNA occupancies (θ_D and θ_{DM}) as a function of the buffered metal concentration and hence metal availabilities derived from sensor sensitivities were expressed, in the first instance, as buffered [M]. Therefore, the term 'buffered metal concentration' has been widely used throughout this thesis as a synonym of 'metal availability'. However, as already discussed in section 6.1, despite being a useful tool to mathematically describe the system, the buffered metal concentration is not a helpful parameter to describe metal speciation in the cell. It informs on the concentration of hydrated species which are i) irrelevant as metal-exchange reactions between proteins and the cytosolic metal buffer pools occur via an associative mechanism and ii) present at negligible concentrations in the cell (often, less than one hydrated metal ion per cell).

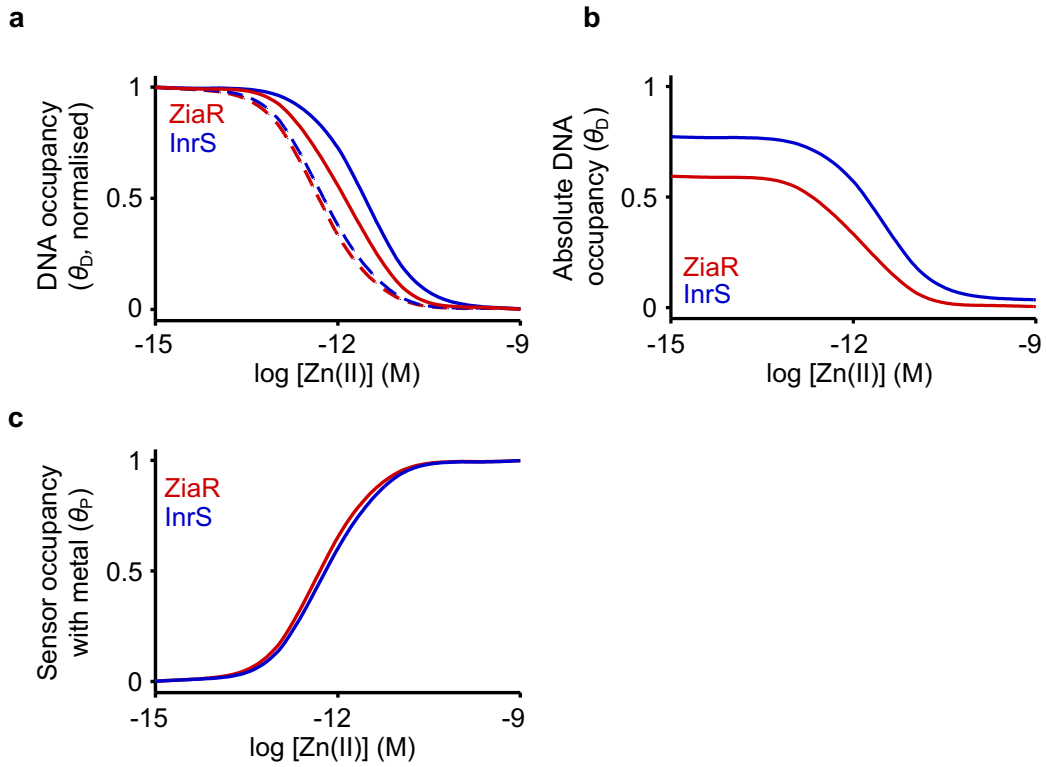

Figure 7.1. Response of *Synechocystis* ZiaR and InrS to Zn(II).
Simulated responses of ZiaR (Zn(II)-sensor, red) and InrS (Ni(II)-sensor, blue) to Zn(II) in *Synechocystis* using published values for K_1, K_3, K_4 (Foster et al, 2014b). The number of DNA targets for each sensor was set to one and the protein abundance, in the absence of any experimental evidence, was set to twenty copies per cell in both the metal deplete and replete conditions ($P_0 = P_1$). **a**, Normalised responses calculated with the complete thermodynamic model (solid line) or inferred solely from K_1 (dashed line). **b**, Absolute DNA occupancy obtained using the complete thermodynamic model. **c**, Occupancy of the proteins with metal ($\theta_P = \frac{[PM]+[PMD]}{[P_T]}$).

As exemplified in **Figure 6.2**, even though the buffered metal concentration can be extremely low, this can correspond to a large amount of readily exchangeable metal bound in the polydisperse buffer pool. The buffered metal concentration can, however, indirectly inform on the chemical state of the metal bound to the buffer and to its tendency to be exchanged or not from/to the buffer pool.

Therefore, a more appropriate term to describe metal availability in a quantitative way would be to refer to the 'chemical potential' of the buffer-bound metal, instead of the buffered concentration of metal. For this reason, the metal availabilities to which the sensors are attuned were expressed as the standard free energies for metalation (**Figure 6.1**).

From these data, protein metalation *in vivo* becomes predictable. This was exemplified here by CbiK, the cobalt chelatase for vitamin B_{12}. CbiK is predicted to correctly acquire Co(II) *in vivo* rather than more tightly binding metals because only its affinity for Co(II) matches Co(II) availability in *Salmonella*, while the availabilities of the most competitive metals are not set high enough to metalate this protein (**Figure 6.3**). This provides a cellular logic for metalation: metal availabilities are set as the inverse of the Irving-Williams series (Irving & Williams, 1948), so that only proteins with a sufficiently tight affinity can bind the most competitive metal. Cells can, therefore, simultaneously metalate proteins requiring weakly binding uncompetitive metals (e.g. manganese proteins) at the same time as proteins requiring the tightly binding metals (e.g. cuproproteins) (Osman et al, 2019). A protein will acquire only metals for which its metalation reaction *in vivo* (therefore considering the competition with the buffer) is favourable. A similar consideration can be made for the metal sensors themselves. As for the majority of proteins, *in vitro* each sensor will preferentially bind divalent cations with an order of affinities following the Irving-Williams series. However, sensitivities of metal sensors do not match the intracellular availabilities of the non-cognate metals. Therefore, metals need to be buffered over a really narrow range in order to avoid mis-metalation of sensors (and in general, of all metalloproteins), mal-responses and disruption of metal-sensing mechanisms (Foster et al, 2017; Osman et al, 2017; Scott, 2018).

As already discussed in Chapter 6, the knowledge that cellular metal availability is set as the inverse of the Irving-Williams has been proposed from various experimental evidences from many years (Foster et al, 2017; Tottey et al, 2008; Waldron & Robinson, 2009; Williams & Da Silva, 2001). However, the metal availabilities for the first row of transition metals (plus Mg(II)) required by living organisms have been defined for the first time from the sensitivities of the metal sensors, demonstrating this notion (Osman et al, 2019). In the Irving-Williams series, Zn(II) appeared to form less stable complexes than Cu(II), however there is some uncertainty in where to place this metal in respect to Co(II) and Ni(II). In *Salmonella*, the availability of Zn(II) is similar to that for Ni(II) (**Figure 6.1**).

7.3.1 Prediction of the metalation state

The data in **Figure 6.1** not only allow the prediction of what metal a particular molecule will acquire/release in the cytosol, but also the quantitative prediction of the metalation state of that molecule (sections 6.3.1 and 6.3.2). CbiK was again used as an example, calculating its metalation percentage with and without considering that the various metals present in the cytosol can compete for the same metal-binding site in the protein (**Table 6.3**). For CbiK, adopting one or the other model did not make a significant difference in the calculated percentages, as only Co(II) (and by a lesser degree Fe(II)) can metalate the protein to a relatively low estimated fractional occupancy. The situation is different if the molecule under study appears to be able to acquire two different metals from the buffer to higher fractional occupancies. **Figure 7.2** shows the free energies for metalation of a hypothetical molecule in the *Salmonella* cytosol with sufficiently tight affinities both for Co(II) and Zn(II) to bind these metals *in vivo*. Notably, when the metalation percentages are calculated without competition (**Table 7.1**), the molecule is predicted to be almost equally metalated with Co(II) and Zn(II) (however, the total metalation is predicted to be almost 205%, which is meaningless). Which metal will this molecule preferentially bind if the two metals are allowed to compete for the same site? Its affinity for Zn(II) is tighter than its affinity for Co(II) and this could probably suggest preferential binding of Zn(II), as this metal could outcompete Co(II). However, as shown in **Table 7.1**, the percentage metalations are higher for Co(II) (94.5%) than for Zn(II) (5.1%). This can be explained by looking at the thermodynamic scheme in **Figure 7.3**. The spontaneity of the two metalation reactions *in vivo* depends not only on the affinities of the molecule for the two metals ($K_{\text{molecule, Co(II)}}$ and $K_{\text{molecule, Zn(II)}}$), but also on the affinities of the buffer ($K_{\text{buffer, Co(II)}}$ and $K_{\text{buffer, Zn(II)}}$). In terms of the free energies for the metalation reaction, this corresponds to:

$$\Delta G^{\circ}_{\text{molecule},\,in\,vivo} = \Delta G^{\circ}_{\text{molecule}} - \Delta G^{\circ}_{\text{buffer}}$$

In this case, this 'ΔΔG°' is more favourable for Co(II), as exemplified also by the arrows in **Figure 7.2**.

7.4 Future work

7.4.1 An easy-to-use metalation calculator tool

It should be noted how in **Table 7.1** not considering that Zn(II) and Co(II) are competing for the same binding site can lead to a meaningless metalation percentage higher than 100% and how incorrect conclusions (for example almost 95% metalation with Zn(II), instead of 5%) could be drawn. Similar calculations, considering the competition between metals, can be performed for any molecule or protein of interest with known affinity for the first-row transition metals (or a subset) to predict its metalation state *in vivo*. Currently, this service is

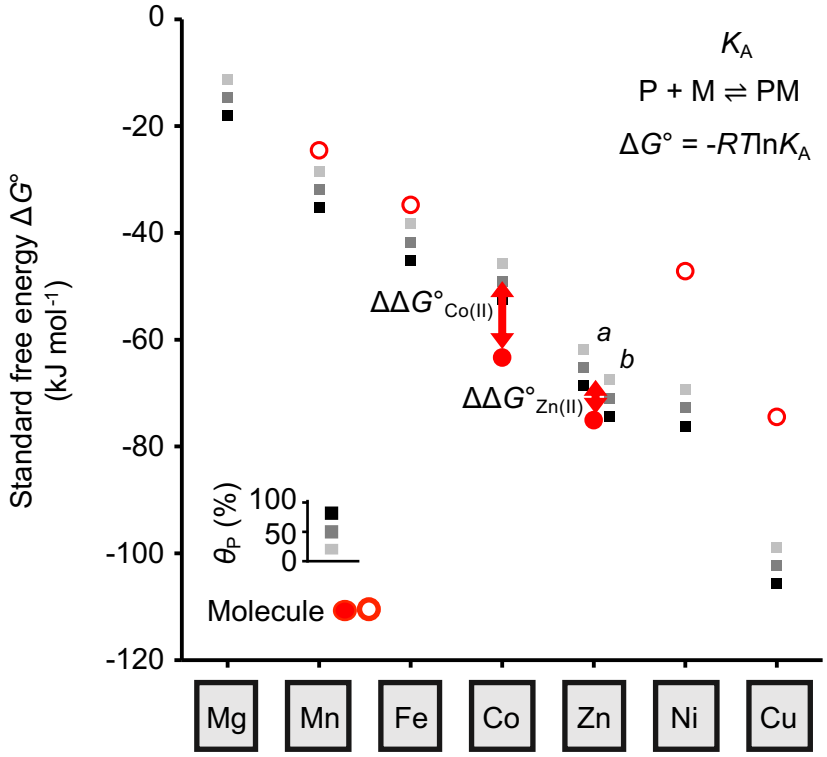

Figure 7.2. Metalation in vivo depends on the actual difference in standard free energy. Standard free energies for formation of complexes between metals and a hypothetical molecule (circles) compared to standard free energies for protein-metal complex formation in the *Salmonella* cytosol which would give 20% (light grey squares), 50% (dark grey) or 80% (black) metalation (θ_P) (as in **Figure 6.1**). The Zn(II) free energies are reported based on both ZntR (*a*) and Zur (*b*). The hypothetical molecule has a tight affinity for both Co(II) and Zn(II). Despite having a tighter affinity for Zn(II), this molecule is predicted to preferentially bind Co(II) due to the more favourable $\Delta\Delta G°$ (the Zn(II) $\Delta\Delta G°$ was calculated from the mid-point of the standard free energies for formation of protein complexes with 50% metalation inferred from Zur and ZntR responses).

Table 7.1. Metal affinities and calculated metalation percentages for the molecule shown in Figure 7.2.

Metal	$1/K_{metal}$ (M)	Metalation (%) *no competition*	Metalation (%) *with competition*
Mg(II)	n.d.	0.0	0.0
Mn(II)	5.0×10^{-5}	4.9	0.0
Fe(II)	8.0×10^{-7}	5.7	0.0
Co(II)	8.0×10^{-12}	99.7	94.5
Zn(II)	7.0×10^{-14}	94.4	5.1
Ni(II)	5.4×10^{-9}	0.0	0.0
Cu(I)	8.4×10^{-14}	0.0	0.0
Total metalation		204.7	99.7

In the absence of competition, the hypothetical molecule is predicted to be metalated with both Zn(II) and Co(II), yet reaching total metalation greater than 100%. When competition between the two metals is included in the model, the molecule is predicted to preferentially acquire Co(II) over Zn(II). The metal availability of Zn(II) in these calculations was calculated from the average of the free energies inferred from ZntR- and Zur-mediated responses (**Table 6.1**).

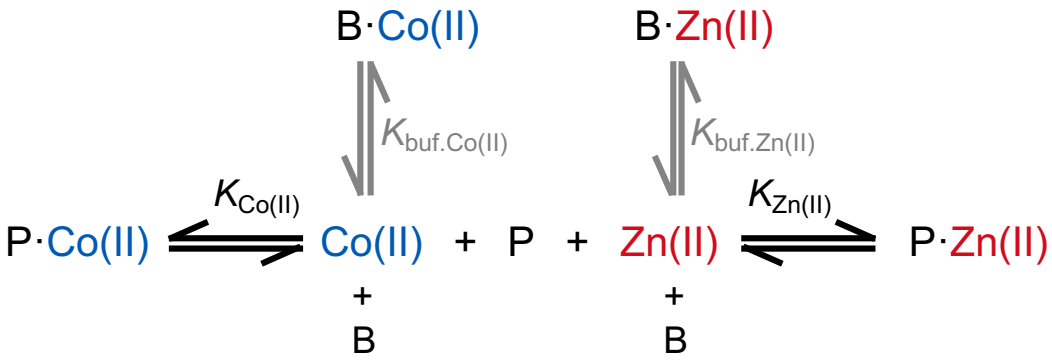

Figure 7.3. Competition from two buffered metals for the same site within a molecule. Semi-schematic representation of the metalation reaction of a hypothetical molecule with buffered Co(II) and Zn(II), which compete for the same metal-binding site. Metal-exchange occurs via an associative mechanism between the buffer system and the apo-molecule (equilibria with K_5, K_6, K_7 in **Figure 5.3**). However, these equilibria were omitted for clarity; The scheme shows the dissociative mechanism (the thermodynamic considerations are the same for both the kinetic mechanisms of ligand exchange). The more favourable reaction depends on the relative affinity of the buffer and the protein for the metal (**Figure 7.2**).

available on request from the website of the 'E3B: Elements of Bioremediation, Biomanufacturing & Bioenergy: Metals in Biology' BBSRC Network in Industrial Biotechnology and Bioenergy (https://sites.durham.ac.uk/mib-nibb/2019/07/10/metalation-calculator-predict-metal-occupancies-in-vivo/). However, a goal would be to develop a tool that everyone could easily use in the form of a website or an application. The metal availabilities currently employed in the calculator correspond to the sensors undergoing 0.5 of their responses. However, as already discussed in section 6.4, sensor responses might shift (either upwards or downwards) from the midpoint depending on the growth conditions of *Salmonella* (*vide infra*). Therefore, the calculator should ideally allow the user to choose the fractional DNA occupancy for each sensor to reflect the particular conditions of interest. A general scheme of how the calculator would work is reported in **Figure 7.4**. Once users have provided the experimental values of metal affinities for their molecule of interest, they would be offered a slider for the selection of possible values for θ_D/θ_{DM} for each sensor. In the supplementary information of (Osman et al, 2019) we have already provided a computational method (in fact, a MATLAB script) for computing [*M*] from numerical input values of θ_D and θ_{DM} (effectively, inverting the equations derived in section 5.2 and used in the electronic spreadsheet, **Figure 5.5**). The metalation percentages (considering competition between the various metal ions) can then be easily calculated from [*M*] (for example, with the use of an electronic spreadsheet). However, the web-based application would offer the whole computation without the need of using different programs in sequence. Current web technology easily allows linkage of the application to a server-side script (for example written in Python-NumPy) computing the relevant values, which may be then displayed in several graphical ways in the output section.

7.4.2 Calibration of sensor responses

As already discussed in section 6.4, determining the fractional DNA occupancies under specific growth conditions is pivotal to obtain a more accurate estimate of the metalation percentages of a molecule or protein of interest. This might be necessary for a protein with critical role under specific growth conditions: For instance, Co(II) availability might be different when *Salmonella* produces vitamin B_{12} under anaerobic conditions (Jeter et al, 1984). This could also apply to a protein that is expressed under specific metal availability conditions (for instance, a metallochaperone or a metallothionein which is expressed only in metal-deplete or replete conditions). Determining metal availability under specific growth conditions requires the calibration of the responses of the sensors, so that fractional DNA occupancy values can be inferred under any other growth condition. In Chapter 6, a first attempt to calibrate the response of the Zn(II)-sensors Zur and ZntR was reported (section 6.5). *Salmonella* cells were treated with the chelant TPEN or with a high concentration of Zn(II) to

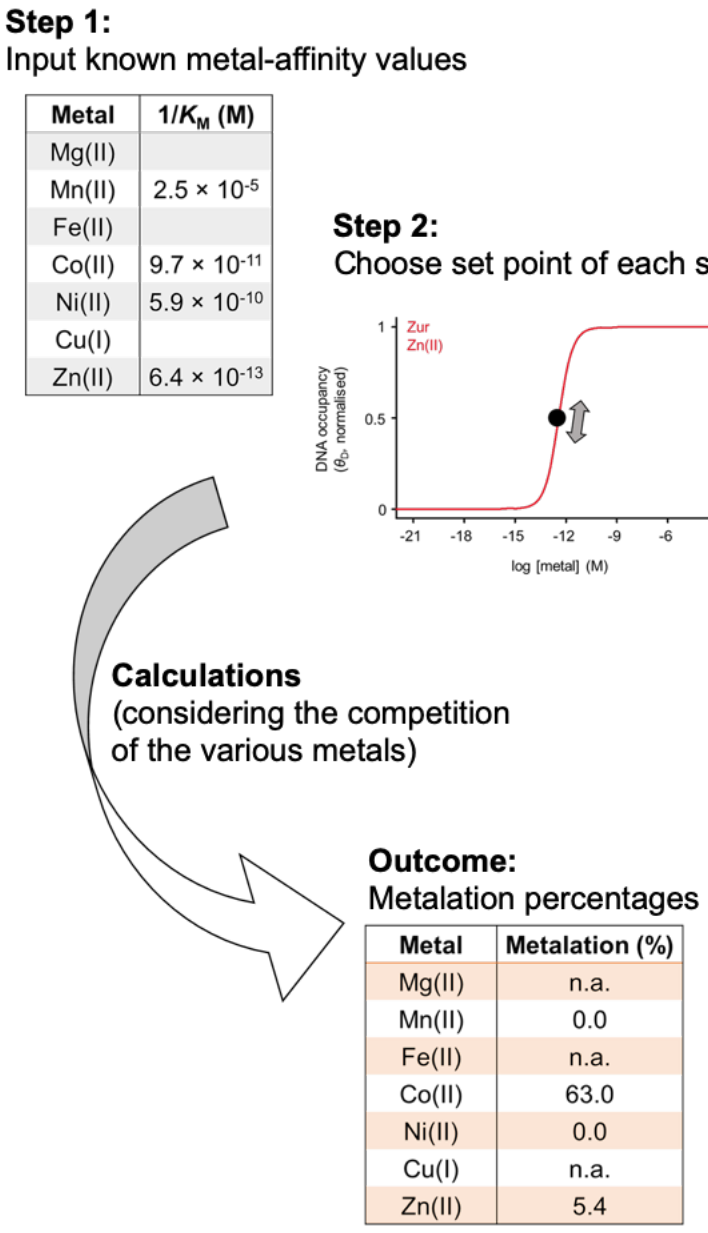

Figure 7.4. An easy-to-use metalation calculator application.
Schematic representation of the operation of the web-based metalation calculator tool. After inputting the know metal-affinities, the user will be able to choose the fractional DNA occupancy. This will allow, for example, to take into account the change in metal availabilities (if known) under different *Salmonella* growth conditions. Currently, the calculations can already be performed, but they require the sequential use of different pieces of software and codes. These will therefore be implemented in a single software.

measure the maximum change in DNA occupancy from Zn(II)-deplete to Zn(II)-replete conditions. The change in DNA occupancy was inferred from a linear correlation with the change in transcript abundance for two target genes (*znuA* for Zur and *zntA* for ZntR) measured by qPCR (**Figure 6.9** and **Figure 6.10**). On the basis of the calibration, Zn(II)-availability in LB medium was determined, showing how the Zur-mediated response is almost saturated when cells are grown, as in this case, in a rich medium. On the contrary, ZntR appeared to be at the lower end of its response curve (**Figure 6.11**).

Although the sensor response calibration protocol could be further optimised, a similar strategy could easily be employed to calibrate the response of the other *Salmonella* sensors. DNA occupancies for specific growth conditions could then be used in conjunction with the metalation calculator (section 7.4.1). For example, the calibration of RcnR could inform on the metalation state of CbiK under anaerobic conditions. Cells would therefore be grown to mid-log phase and subsequently exposed to high concentration of metals or chelants. Transcript abundance analysis via qPCR on harvested cells could infer on the DNA occupancy for the various sensors. Nevertheless, other techniques could be used to directly monitor the promoter occupancy by the sensor, instead of relying of an indirect measure via gene expression analysis. For example, in their recent study on Fur graded response in *B. subtilis* Helmann and Pi have used Chip-seq analysis to show how the de-repression of Fur-regulated genes was correlated to diminished Fur-occupancy as a function of Fe(II)-depletion (Pi & Helmann, 2017).

7.4.3 Translation to other organisms and compartments

The possible future directions discussed in sections 7.4.1 and 7.4.2 all refer to *Salmonella*. In fact, this is the only organism where the sensitivities of the complete set of metal sensors have been determined to define intracellular metal availabilities. However, there is a need to predict *in vivo* metalation also in other organisms or even in different cellular compartments. This is contingent on knowing what the intracellular metal availabilities are. For bacteria, one possibility would be to repeat the work done on the set of sensors from *Salmonella*. This would include identifying the metal sensors present in the genome, purifying them and characterising sensor abundance, number of DNA targets, metal-binding and DNA-binding properties. Sensor responses could then be calculated using the thermodynamic modelling derived in Chapter 5 (**Figure 5.5**). However, this process requires investing large amounts of time and resources as it might involve characterising nearly ten different proteins (the characterisation of the seven *Salmonella* sensors required about five to six years of work, and several different people contributed to the data presented in **Table 5.2**). A possible way to partially bypass the biochemical characterisation of the sensors would be to predict some properties (for example metal- and DNA-binding affinities) *in silico*. That is, based on the protein structure (including

the structure of the putative metal- and DNA- binding sites) and based on the similarities with already characterised homologous sensors, it would be possible to calculate the thermodynamic properties via quantum mechanics and molecular mechanics methodologies. Several early studies in this direction have already been presented in the literature (Jain & Jayaram, 2007; Liao et al, 2019; Schymkowitz et al, 2005; Sharma et al, 2018). *In silico* prediction of the metal-binding affinities proved to be particularly challenging, nevertheless it is possible that in the next decade new and improved methodologies will be developed.

A different strategy would be to use *Salmonella* as a model organism to calibrate metal probes. Over almost thirty years, fluorescent probe have been developed to visualise different metal ions in cells (Carter et al, 2014; Cotruvo et al, 2015; McRae et al, 2009). In addition to the specific photophysical properties (for example, suitable excitation and emission wavelength for *in vivo* use, brightness and photostability), probes need to be specific for a particular metal ion (Hare et al, 2015). This is not trivial, as the order of stability of probe-metal complexes will follow the Irving-William series. The spectral properties of a probe might be tailored to report on specific metal complexes, for example by monitoring features such as the fluorescence lifetime that might discern metals even if multiple elements can bind the probe. Moreover, in order to investigate the labile cellular metal pools *in vivo*, the probes need to be designed so that *in vivo* they do not deplete the metal buffer system or perturb cellular metal homeostasis. One strategy is to maximise signal intensity, so that only a few reporter molecules are needed per cell, in order to minimise their effect on metal levels. In this sense, lanthanide-based metal probes offer some attractive features, due to the particular spectral properties of the f-block metal complexes (Hanaoka et al, 2004; Heffern et al, 2014; Reany et al, 2000). Probes designed with specific hydrophobicity properties can be cell-permeable or even be designed to target specific cellular compartments. However, there is controversy on whether these developed probes are sufficiently specific and/or sensitive towards intracellular metal ions. If the intracellular metal availabilities of *Salmonella* cells grown under specific conditions are known (section 7.4.2), the probes can be monitored under the same conditions to validate and calibrate their responses to metal availabilities. The calibrated probes could then be used to measure metal availabilities in prokaryotic and eukaryotic cells and cellular compartments under different growth conditions.

7.4.4 Understanding metal speciation for biotechnology, nutritional immunity and mis-metalation

With almost half of all enzymes requiring a metal ion to function (Waldron et al, 2009), understanding what drives correct metal speciation in cells is a crucial question for bio-inorganic chemists and chemical biologists. As proteins tend to bind divalent cations following the Irving-Williams series, they are potentially subjected to mis-metalation with

'*wrong*' tightly binding metals. About 70% of metalloproteins are predicted to acquire their metal from the labile metal buffer pool (Foster et al, 2014a) (section 1.3). Moreover, the most parsimonious model is that delivery proteins are also metalated from this pool. Therefore, their metalation with the correct metal relies (to a significant degree) on their metal affinities being tuned to the intracellular availability of the cognate metal. Mis-metalation is avoided by buffering the non-cognate-metal availabilities below the standard free energy for metalation of the metalloprotein with those metals. The remaining 30% of metalloproteins is estimated to acquire their metal ions or pre-formed metal cofactors from delivery pathways. However, even these metalloproteins are potentially subject to mis-metalation if metal selectivity at the start of these pathways is lost.

7.4.4.1 Biotechnology

Determining intracellular metal availability and thus being able to predict metal speciation and protein metalation *in vivo* is not only crucial for biological chemistry, but also for biotechnology, for understanding metal-related diseases and for the use of metals and metal-related compounds as antimicrobial agents. For example, one of the possible applications of the results in **Figure 6.1** is the optimisation of heterologous expression of metalloproteins for biotechnology applications. Some metalloenzymes can catalyse some of the most fundamental energy converting processes, for example N_2-fixation (e.g. nitrogenase), H_2O-oxidation (e.g. photosystem II), or H_2-formation (e.g. hydrogenase) (Ragsdale, 2006). Moreover, metalloenzymes can be employed in manufacturing of speciality or bulk chemicals such as bioethanol or therapeutic compounds. The same reactions performed with heterogeneous or homogeneous purely inorganic catalysis often require high temperature and pressure or cannot reach the same activity. It is therefore not surprising that there is a growing interest in large-scale applications based on these enzymes. However, their use in biocatalysis is contingent on the possibility of large-scale production of active enzymes or of the activity occurring in a heterologous host to drive a bio-conversion (in a fermentation, for instance). This might not be obvious if the metalloenzyme is heterologously expressed in a host organism with different intracellular availabilities than the native one, or if the host is lacking the metal-delivery pathways eventually required for enzyme maturation.

In order to maximise the correct metalation of heterologously expressed metalloproteins, the metal-binding site of the proteins can be altered so that the metal-affinity is tuned to the cellular metal availability in the host organism. At the same time, the site can be altered in order to avoid tight affinity for non-cognate metals and prevent mis-metalation. A similar optimisation can be done for the metallochaperones responsible for inserting the correct metal into the metal-delivery pathways. Other possible strategies include tuning the growth media to optimise the percentage of saturation of the different metal buffers to optimise correct

metalation, or even altering homeostasis of metals (for instance, by mutating the metal sensors or the metal-import/-efflux systems). Therefore, a key starting point for the development of efficient strategies for the heterologous production of metalloproteins is knowing the intracellular metal availabilities in the host organism under the specific conditions that will be used for protein expression. Another example of the use and optimisation of metalloprotein biochemistry for biotechnology and synthetic biology application is the industrial production of vitamin B_{12} discussed in section 1.6.

7.4.4.2 Metal-related diseases

There is emerging evidence that metal accumulation and aberrant metalation of proteins is a common trait in neurological disorders and other chronic diseases (Barnham & Bush, 2008; Brown et al, 1997; Bush, 2003; Huang et al, 1999; Lovell et al, 1998; McCarthy & Kosman, 2015). Understanding metal availability in eukaryotic cells and subcellular compartments (plus what might determine an alteration in metal levels) is pivotal to better understand the role of mis-metalation in these degenerative processes. Moreover, if the affinities of the various proteins for metals are known or can be determined, it would be possible to predict which of the component of the system is predominantly subjected to mis-metalation by the highly competitive or abundant metal ions. Finding a strategy to translate the notion acquired on *Salmonella* to different systems and cell types is therefore crucial.

7.4.4.3 Metals as antimicrobials

The essential nature of correct protein metalation *in vivo* suggests that this parameter can potentially be targeted for antimicrobial strategies. For centuries metals or metal-related compounds have been used empirically as antimicrobial agents. Examples are the Cu(II)-containing Bordeaux mixture used in viticulture, metal compounds used to treat infections (e.g. arsenic and mercury to treat syphilis), or even the use of surgical tools made of silver to reduce the risk of wound infection (Lemire et al, 2013; Turner, 2017). More recently, metal surfaces or coating have been used in healthcare settings (Grass et al, 2011) and metal-related compounds such as chelators (e.g. EDTA) and ionophores (e.g. Zinc pyrithione) have been used in fast-moving consumer goods as preservatives or antimicrobial agents (Gill & Holley, 2000; Reeder et al, 2011). However, the exploitation of metals as a countermeasure against pathogenic infection has a much longer history. Nature evolved immune systems strategies that alter the availability of metal ions to invading bacteria in order to kill the pathogens.

The process of sequestering metal ions as a defence against infection is termed ‘nutritional immunity’ (Hood & Skaar, 2012; Kehl-Fie & Skaar, 2010). During host invasion, the pathogen exploits several strategies to ‘steal’ essential metals from the host. For example, the microorganism can release siderophores (chelating agents with an exceptionally high affinity for Fe(III)) as iron scavengers (Wandersman & Delepelaire, 2004). As a response, the host

limits iron availability at the site of infection, for example by producing the siderophore-binding protein siderocalin (also called lipocalin-2), to prevent iron acquisition by the pathogen (Flo et al, 2004; Goetz et al, 2002). Some organisms can release "stealth siderophores" (for example the *Salmonella* salmochelin) which can evade siderocalin (Skaar, 2010). A similar strategy aimed at reducing access to metal is exploited by the neutrophil-released protein calprotectin. Calprotectin is a calcium-binding protein. In the presence of Ca(II) (as in the extracellular environment), human calprotectin forms heterotetramers with a high affinity for metals, which can then be chelated to prevent acquisition by the pathogen (Zygiel & Nolan, 2018). While initial studies suggested that this protein was targeting preferentially Mn(II) and Zn(II) (Corbin et al, 2008; Kehl-Fie & Skaar, 2010), more recent reports from the Nolan group have shown that calprotectin can sequester also Fe(II) and Ni(II) (Nakashige et al, 2015; Nakashige et al, 2017). In fact, the metal-affinities of the promiscuous binding site in calprotectin follow the Irving-Williams series. The model proposed is that the metal calprotectin will preferentially target depends on the metal availability at the site of infection (Zygiel & Nolan, 2018). This is a clear example where knowing metal availabilities is pivotal to understanding protein metalation.

Host metal-based defence to pathogenic invasion is not limited to metal sequestration. There is increasing evidence that the toxic effects of mis-metalation and Fenton chemistry are exploited by exposing the invading microorganism to elevated concentrations of metal (Botella et al, 2012; Imlay, 2014). For example, excess copper is known to damage iron-sulphur clusters (Macomber & Imlay, 2009). Macrophages engulf pathogens and starve them of essential nutrients by pumping out of the compartment iron via the natural resistance associated macrophage protein 1 (NRAMP1) (Appelberg, 2006; Nevo & Nelson, 2006; Supek et al, 1996). At the same time, other transporters (for example the P-type ATPase ATP7A) pump in the phagosomal lumen a high dose of copper and zinc (Botella et al, 2011; White et al, 2009) to kill the pathogen with a concerted action of nutrient depletion and the toxic effects of excess metals. Disruption of the metal-detoxification systems (for example the copper exporters) was shown to enhance killing of bacteria (Osman et al, 2010; White et al, 2009; Wolschendorf et al, 2011).

Metal homeostasis appears to be an "Achilles heel" for microorganisms. Therefore, it is not surprising that, with the global rise of antibiotic resistance, disrupting the metal trafficking pathways of unwanted microorganisms is an attractive strategy for the development of novel antimicrobial agents (Reardon, 2015). Most of the metal-related antimicrobials currently employed were discovered empirically (Lemire et al, 2013). However, a thorough description of metal availabilities and of the processes responsible for their regulation *in vivo* could guide the rational design of novel compounds or combinations of available treatments to subvert

more effectively metal homeostasis. For example, if the $\Delta G°$ for metalation inside a pathogen cell was known, it would become possible to design new antimicrobial agents tailored to sequester a particular metal *in vivo*, or even to release a toxic metal (Osman et al, 2019).

Chapter 8. Appendix

8.1 Appendix A

Additional Tables and Figures

Table 8.1. Sequence identity and similarity of *S.* Typhimurium MntR with DtxR-family members.

***S.* Typhimurium MntR**	**Identity (%)**	**Similarity (%)**
B. subtilis MntR	22.7	37.0
E. coli MntR	89.8	93.0
C. diphtheriae DtxR	12.0	21.6
M. tuberculosis IdeR	13.6	23.1
S. epidermidis SirR	15.4	26.8
S. pyogenes MtsR	15.1	25.8
S. mutans SloR	14.8	25.6
S. gordonii ScaR	14.5	25.0
S. pneumoniae PsaR	16.9	26.5
M. tuberculosis MntR	15.6	25.7
T. pallidum TroR	17.5	32.0

Comparison of the amino acid sequences of *S.* Typhimurium MntR with other characterised members of the DtxR family of metalloregulators. The amino acid sequences used in the comparison are reported in **Figure 3.1**. Percentages of identity and similarity were calculated using the EMBOSS Needle web-based tool.

User-provided sequence:

```
        10         20         30         40         50         60
MGRRAGTPTT KKVTQLVNVE EHVEGFRQVR EAHRRELIDD YVELISDLII EVGEARQVDM

        70         80         90        100        110        120
AARLGVSQPT VAKMLKRLAS LGFIQMIPWR GVFLTPEGEK LAQESRERHQ IVENFLLVLG

       130        140        150
VSPEIARRDA EGMEHHVSQE TLDAFLAFTQ QHGTSAE
```

Number of amino acids: 157

Molecular weight: 17727.22

Theoretical pI: 5.70

Amino acid composition:

Ala (A)	13	8.3%
Arg (R)	14	8.9%
Asn (N)	2	1.3%
Asp (D)	6	3.8%
Cys (C)	0	0.0%
Gln (Q)	10	6.4%
Glu (E)	18	11.5%
Gly (G)	11	7.0%
His (H)	6	3.8%
Ile (I)	8	5.1%
Leu (L)	15	9.6%
Lys (K)	5	3.2%
Met (M)	5	3.2%
Phe (F)	6	3.8%
Pro (P)	5	3.2%
Ser (S)	7	4.5%
Thr (T)	9	5.7%
Trp (W)	1	0.6%
Tyr (Y)	1	0.6%
Val (V)	15	9.6%
Pyl (O)	0	0.0%
Sec (U)	0	0.0%
(B)	0	0.0%
(Z)	0	0.0%
(X)	0	0.0%

Total number of negatively charged residues (Asp + Glu): 24
Total number of positively charged residues (Arg + Lys): 19

Atomic composition:

Carbon	C	777
Hydrogen	H	1257
Nitrogen	N	229
Oxygen	O	235
Sulfur	S	5

Formula: $C_{777}H_{1257}N_{229}O_{235}S_5$
Total number of atoms: 2503

Extinction coefficients:
Extinction coefficients are in units of M^{-1} cm^{-1}, at 280 nm measured in water.

Ext. coefficient 6990
Abs 0.1% (=1 g/l) 0.394

Estimated half-life:

The N-terminal of the sequence considered is M (Met).

The estimated half-life is: 30 hours (mammalian reticulocytes, in vitro).
>20 hours (yeast, in vivo).
>10 hours (Escherichia coli, in vivo).

Instability index:
The instability index (II) is computed to be 38.24
This classifies the protein as stable.

Aliphatic index: 93.12

Grand average of hydropathicity (GRAVY): -0.309

Figure 8.1. Calculation of MntR properties based on the amino acid sequence.
Amino acid composition of MntR and calculation of some theoretical properties of the protein based on its primary sequence using the ProtParam ExPASy web-based too.

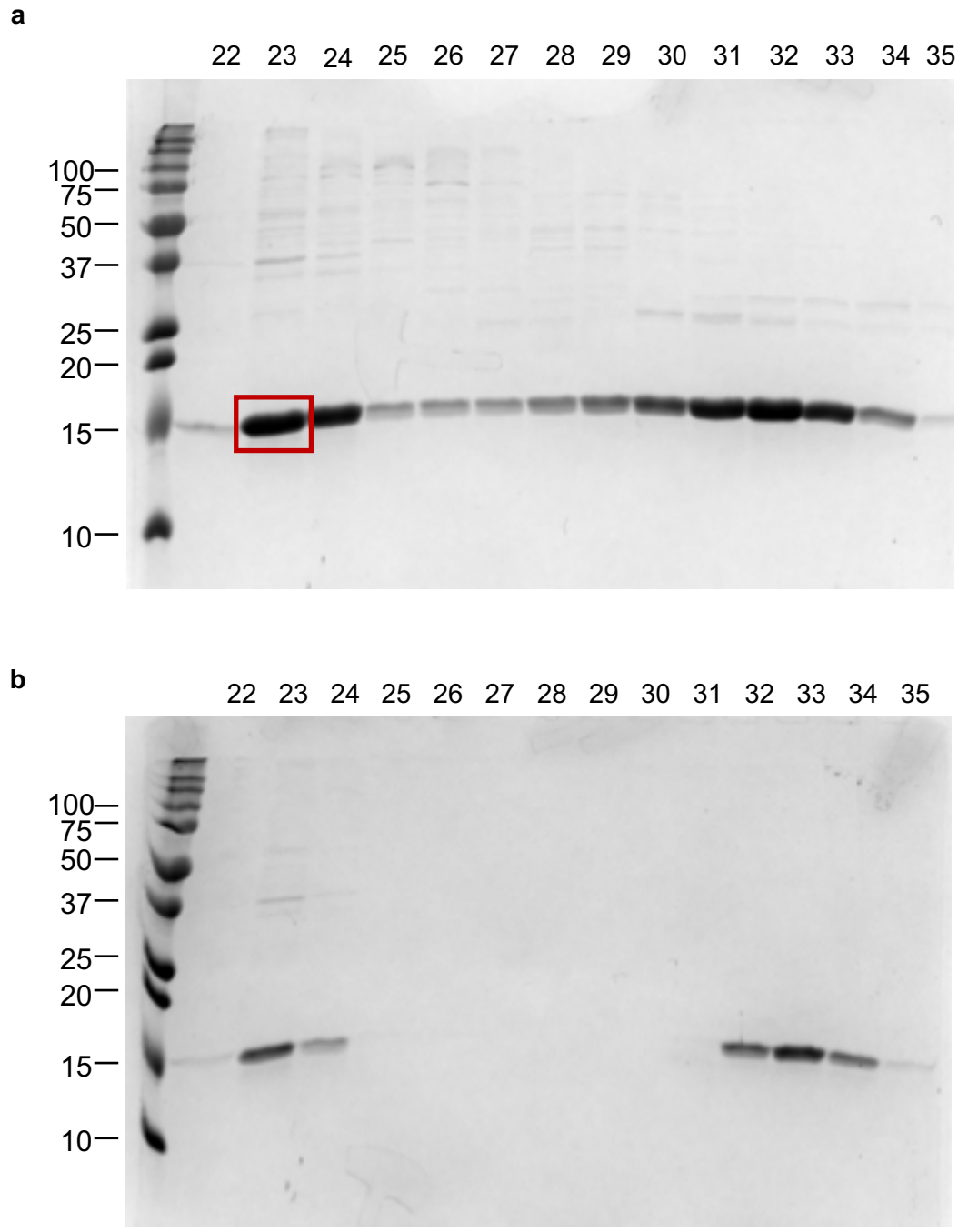

Figure 8.2. The formation of MntR oligomeric species observe in the size-exclusion chromatography step of the purification protocol is reversible.
a, SDS-PAGE of fractions (5 ml) 22-35 eluted from a HiLoad 26/600 Superdex 75 pg column loaded with 5 ml of fraction 2 from the nickel affinity column step of the MntR purification protocol (**Figure 3.2a**) (this gel is the copy of the one presented in **Figure 3.2b**). **b**, SDS-PAGE of fractions (5 ml) 22-35 eluted from a HiLoad 26/600 Superdex 75 pg column loaded with 5 ml of fraction 23 (highlighted in red) from **a**.

Table 8.2. Sequence identity and similarity of *Salmonella* Fur with other Fur proteins.

***S.* Typhimurium Fur**	**Identity (%)**	**Similarity (%)**
C. jejuni Fur	35.3%	50.3%
H. pylori Fur	29.5%	48.8%
B. subtilis Fur	31.2%	49.7%
M. gryphiswaldens Fur	34.6%	49.1%
F. tularensis Fur	38.0%	57.3%
V. cholerae Fur	74.8%	88.7%
E. coli Fur	96.7%	97.3%
Y. pestis Fur	84.7%	89.3%
P. aeruginosa Fur	50.0%	67.3%
L. pneumophila Fur	50.7%	72.0%

Comparison of the amino acid sequences of *Salmonella* Fur with other characterised Fe(II)-sensing members of the Fur family of metalloregulators. The amino acid sequences used in the comparison are reported in **Figure 4.1**. Percentages of identity and similarity were calculated using the EMBOSS Needle web-based tool.

User-provided sequence:

```
        10         20         30         40         50         60
MTDNNTALKK AGLKVTLPRL KILEVLQEPD NHHVSAEDLY KRLIDMGEEI GLATVYRVLN

        70         80         90        100        110        120
QFDDAGIVTR HNFEGGKSVF ELTQQHHHDH LICLDCGKVI EFSDDSIEAR QREIAAKHGI

       130        140        150
RLTNHSLYLY GHCAEGDCRE DEHAHDDATK
```

Number of amino acids: 150

Molecular weight: 17011.04

Theoretical pI: 5.56

Amino acid composition:

Ala (A)	11	7.3%
Arg (R)	8	5.3%
Asn (N)	6	4.0%
Asp (D)	14	9.3%
Cys (C)	4	2.7%
Gln (Q)	5	3.3%
Glu (E)	13	8.7%
Gly (G)	10	6.7%
His (H)	12	8.0%
Ile (I)	9	6.0%
Leu (L)	16	10.7%
Lys (K)	9	6.0%
Met (M)	2	1.3%
Phe (F)	4	2.7%
Pro (P)	2	1.3%
Ser (S)	5	3.3%
Thr (T)	8	5.3%
Trp (W)	0	0.0%
Tyr (Y)	4	2.7%
Val (V)	8	5.3%
Pyl (O)	0	0.0%
Sec (U)	0	0.0%
(B)	0	0.0%
(Z)	0	0.0%
(X)	0	0.0%

Total number of negatively charged residues (Asp + Glu): 27
Total number of positively charged residues (Arg + Lys): 17

Atomic composition:

Carbon	C	738
Hydrogen	H	1164
Nitrogen	N	218

Total number of atoms: 2359

Extinction coefficients:

This protein does not contain any Trp residues. Experience shows that this could result in more than 10% error in the computed extinction coefficient.

Extinction coefficients are in units of M^{-1} cm^{-1}, at 280 nm measured in water.

Ext. coefficient 6210
Abs 0.1% (=1 g/l) 0.365, assuming all pairs of Cys residues form cystines

Ext. coefficient 5960
Abs 0.1% (=1 g/l) 0.350, assuming all Cys residues are reduced

Estimated half-life:

The N-terminal of the sequence considered is M (Met).

The estimated half-life is: 30 hours (mammalian reticulocytes, in vitro).
>20 hours (yeast, in vivo).
>10 hours (Escherichia coli, in vivo).

Instability index:

The instability index (II) is computed to be 25.14
This classifies the protein as stable.

Aliphatic index: 87.80

Grand average of hydropathicity (GRAVY): -0.565

Figure 8.3. Calculation of Fur properties based on the amino acid sequence.
Amino acid composition of Fur and calculation of some theoretical properties of the protein based on its primary sequence using the ProtParam ExPASy web-based too.

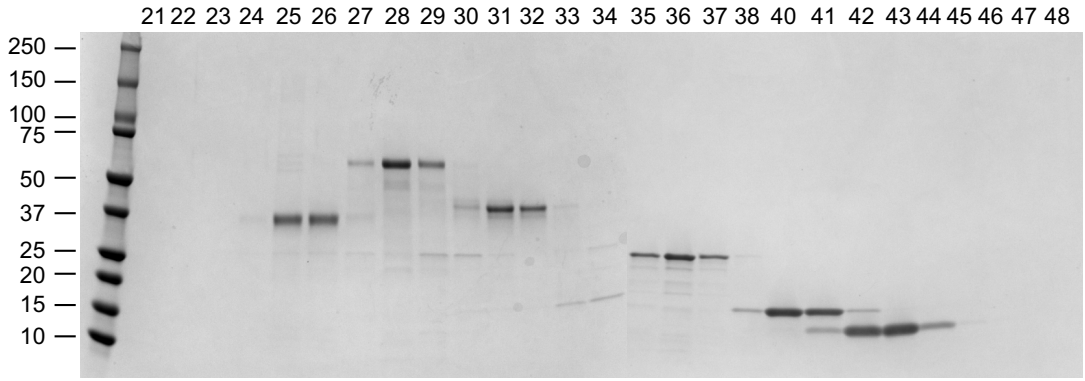

Figure 8.4 Calibration of the size-exclusion column.
SDS-PAGE of fractions from the calibration of the HiLoad 26/600 Superdex 75 pg column as in **Figure 4.6**. The protein shown are (in order of elution): alcohol dehydrogenase, MW ≈ 150 kDa (monomer MW ≈ 37K kDa, not included in the calibration curve); bovine serum albumin, MW ≈ 66 kDa; albumin for chicken egg white, MW ≈ 44 kDa; carbonic anhydrase, MW ≈ 29 kDa; myoglobin, MW ≈ 17 kDa; cytochrome c, MW ≈ 12.4 kDa. This figure is the combination of two gels (fractions 21–34 from gel 1 and 35–48 from gel 2).

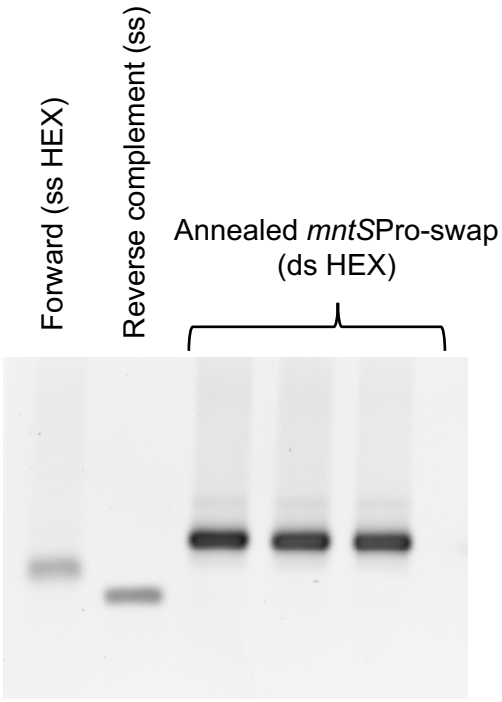

Figure 8.5. Native PAGE shows annealing of *mntS*Pro-swap used in Figure 5.14.
The single-stranded (ss) oligonucleotides were run on the same gel as a control to show the different migration from the double-stranded (ds) *mntS*Pro-swap. This oligonucleotide was used to determine the affinity of Mn(II)-MntR for non-specific DNA (**Figure 5.14)**

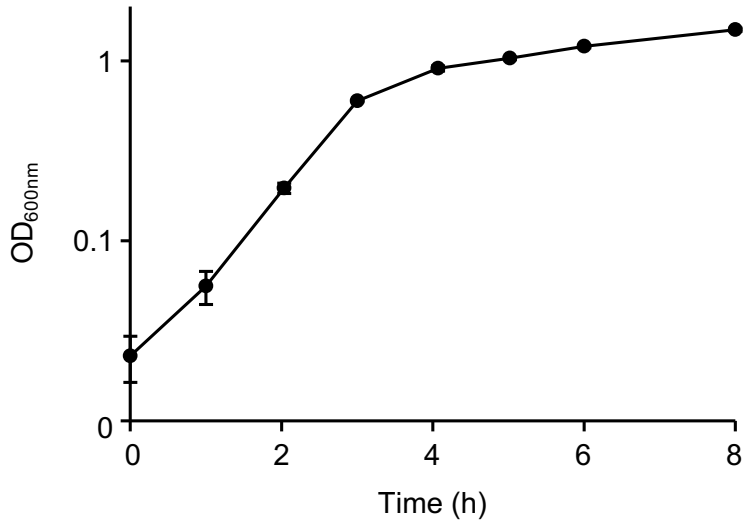

Figure 8.6. Growth curve of *Salmonella* in LB media
Data are mean ±s.d. of n = 3 biologically independent samples.

8.2 Appendix B

Dynafit (Kuzmic, 1996) scripts are adapted from (Osman et al., 2019)

Dynafit script to describe Mn(II)-binding to mag-fura-2 (Figure 3.6)

```
;M = Mn(II) ;C = Mf2

[task]
data = equilibria
task = fit

 [mechanism]
M + C <==> MC     :    Keq1   dissociation

[concentrations] uM
C = 2.05

[constants] uM
Keq1 = 6.1 ?

[responses]
MC = -266.265 ?

[equil]
variable M
offset = auto
set data2

[output]
directory C:/Dynafit/Outputs/Mag-Fura-2

[set:data2]
0           570.0813395
0.9697      511.7236125
1.9394      462.2620137
2.9091      421.3598531
3.8788      380.7863871
5.8182      325.2818502
7.7576      286.0484212
9.697       255.3408127
11.6364     230.1388194
15.5152     187.8307749
19.394      163.665151
29.091      124.1987229
38.788      100.7105001
48.485      87.3497874
67.879      70.63889567
87.273      61.5095644
106.667     55.10087077

[end]
```

Dynafit script to describe competition between mag-fura-2 and MntR for Mn(II) (Figure 3.7)

```
;M = manganese ; P = MntR Mn(II)-binding sites ; C = Mf2

[task]
data = equilibria
task = fit

[mechanism]
M + P <==> MP     :    Keq1   dissociation

M + C <==> MC     :    Keq2   dissociation


[concentrations]; uM
P = 37.4
C = 1.95

[constants]; uM
Keq1 = 10 ?
Keq2 = 6.1

[responses]
MC = -258.345 ?

[data]
variable M
offset = auto
set rep4

[output]
directory C:/Dynafit/Outputs/MntR

[set:rep4]
0           519.4812622
0.9697      513.2932129
1.9394      516.8894653
3.8788      471.8691508
5.8182      427.3053284
7.7576      386.2322082
9.697       352.65979
14.5455     315.9202779
24.2425     263.9388936
33.9395     223.8132223
43.6365     188.4968109
53.3335     157.9350128
63.0305     136.264684
77.576      116.7513428
96.97       101.0371119
116.364     93.93473435
135.758     87.80405426
174.546     83.55475617
193.94      80.37692261
```

Dynafit script to describe competition between NTA and Fur for Fe(II) (Figure 4.13 and Figure 4.14)

```
; F = Fur dimer ; M = Fe(II) ; C = Competitor (NTA)

[task]
task = fit
data = equilibria

[mechanism]
F + M        <==> F.M       :    Keq1   dissociation
F.M + M      <==> F.M.M     :    Keq2   dissociation
F.M.M + M    <==> F.M.M.M   :    Keq3   dissociation
F.M.M.M + M  <==> F.M.M.M.M :    Keq4   dissociation
C + M        <==> C.M       :    Keq5   dissociation

[constants]       ; uM
Keq1 = 0.246 ?
Keq2 = 4 * Keq1
Keq3 = 0.0724 ?
Keq4 = 4 * Keq3
Keq5 = 0.677

[concentrations]  ; uM
F     = 5.1
C     = 100

[responses]
F.M       =  0.25 * F.M.M.M.M
F.M.M     =  0.5 * F.M.M.M.M
F.M.M.M   =  0.75 * F.M.M.M.M
F.M.M.M.M = -72.73 ?

[data]
variable M
offset = auto
set data3

[output]
directory C:/Dynafit/Outputs/Fur

[set:data3]
0           480.6075983
4.652275986 459.5693109
9.304551971 449.2654658
13.95682796 431.4021174
18.60910394 407.9524698
23.26137993 384.2603083
27.91365591 358.9725046
32.5659319  325.2715693
37.21820789 295.1062861
41.87048387 263.5514256
46.52275986 232.3932428
51.17503584 204.9247777
55.82731183 179.4963719
60.47958781 159.1370681
65.1318638  142.6368494
69.78413978 130.6390162
74.43641577 119.6840372
```

```
79.08869176 113.2864974
88.39324373 106.4002772
107.0023477 101.9975011
134.9160036 99.62870886
181.4387634 97.98776849

[end]
```

Dynafit script to describe Fur binding to *furbox* (Figure 4.24)

All datasets for Fe(II)-Fur were globally fit (allowing Keq1 to vary) to determine a response value. The response was then fixed to fit individual datasets for Fe(II)-Fur, or apo-Fur, and determine Keq1.

```
[components] ; P = Fur dimer  ; D = furbox

[task]
task = fit
data = equilibria

[mechanism]
D + P   <==> D.P        :    Keq1   dissociation
D.P + P <==> D.P.P      :    Keq2   dissociation

[constants] ; nM
Keq1 = 56.1 ?
Keq2 = 4 * Keq1

[concentrations] ; nM
D = 10

[responses]
D.P = 0.5 * D.P.P
D.P.P = 0.00438589

[data]
variable    P
offset      = 0?
set data1
plot logarithmic

[set:data1]
0     0
2.5   -0.00285
5     -0.0019
10    0.0001
25    0.00595
50    0.01455
100   0.0248
200   0.0284
350   0.0291
500   0.0311

[output]
directory   C:/Dynafit/Outputs/Fur/FA

[end]
```

References

Achard, M. E., Tree, J. J., Holden, J. A., Simpfendorfer, K. R., Wijburg, O. L., Strugnell, R. A., Schembri, M. A., Sweet, M. J., Jennings, M. P. & McEwan, A. G. (2010) The multi-copper-ion oxidase CueO of *Salmonella enterica* serovar Typhimurium is required for systemic virulence. *Infect Immun*, 78(5), 2312-9.

Adrait, A., Jacquamet, L., Le Pape, L., Gonzalez de Peredo, A., Aberdam, D., Hazemann, J. L., Latour, J. M. & Michaud-Soret, I. (1999) Spectroscopic and saturation magnetization properties of the manganese- and cobalt-substituted Fur (ferric uptake regulation) protein from *Escherichia coli*. *Biochemistry*, 38(19), 6248-60.

Althaus, E. W., Outten, C. E., Olson, K. E., Cao, H. & O'Halloran, T. V. (1999) The ferric uptake regulation (Fur) repressor is a zinc metalloprotein. *Biochemistry*, 38(20), 6559-69.

Ammendola, S., Pasquali, P., Pistoia, C., Petrucci, P., Petrarca, P., Rotilio, G. & Battistoni, A. (2007) High-affinity Zn^{2+} uptake system ZnuABC is required for bacterial zinc homeostasis in intracellular environments and contributes to the virulence of *Salmonella enterica*. *Infect Immun*, 75(12), 5867-76.

Andreini, C., Bertini, I., Cavallaro, G., Holliday, G. L. & Thornton, J. M. (2008) Metal ions in biological catalysis: from enzyme databases to general principles. *J Biol Inorg Chem*, 13(8), 1205-18.

Ansari, A. Z., Bradner, J. E. & O'Halloran, T. V. (1995) DNA-bend modulation in a repressor-to-activator switching mechanism. *Nature*, 374(6520), 371-5.

Ansari, A. Z., Chael, M. L. & O'Halloran, T. V. (1992) Allosteric underwinding of DNA is a critical step in positive control of transcription by Hg-MerR. *Nature*, 355(6355), 87-9.

Appelberg, R. (2006) Macrophage nutriprive antimicrobial mechanisms. *J Leukoc Biol*, 79(6), 1117-28.

Bagg, A. & Neilands, J. B. (1987a) Ferric uptake regulation protein acts as a repressor, employing iron (II) as a cofactor to bind the operator of an iron transport operon in *Escherichia coli*. *Biochemistry*, 26(17), 5471-7.

Bagg, A. & Neilands, J. B. (1987b) Molecular mechanism of regulation of siderophore-mediated iron assimilation. *Microbiol Rev*, 51(4), 509-518.

Baichoo, N. & Helmann, J. D. (2002) Recognition of DNA by Fur: a reinterpretation of the Fur box consensus sequence. *J Bacteriol*, 184(21), 5826-32.

Baichoo, N., Wang, T., Ye, R. & Helmann, J. D. (2002) Global analysis of the *Bacillus subtilis* Fur regulon and the iron starvation stimulon. *Mol Microbiol*, 45(6), 1613-29.

Banci, L., Bertini, I., Cantini, F., Felli, I. C., Gonnelli, L., Hadjiliadis, N., Pierattelli, R., Rosato, A. & Voulgaris, P. (2006) The Atx1-Ccc2 complex is a metal-mediated protein-protein interaction. *Nat Chem Biol*, 2(7), 367-8.

Barnham, K. J. & Bush, A. I. (2008) Metals in Alzheimer's and Parkinson's diseases. *Curr Opin Chem Biol*, 12(2), 222-8.

Barynin, V. V., Whittaker, M. M., Antonyuk, S. V., Lamzin, V. S., Harrison, P. M., Artymiuk, P. J. & Whittaker, J. W. (2001) Crystal structure of manganese catalase from *Lactobacillus plantarum*. *Structure*, 9(8), 725-38.

Bates, C. S., Toukoki, C., Neely, M. N. & Eichenbaum, Z. (2005) Characterization of MtsR, a new metal regulator in group A streptococcus, involved in iron acquisition and virulence. *Infect Immun*, 73(9), 5743-53.

Becker, K. W. & Skaar, E. P. (2014) Metal limitation and toxicity at the interface between host and pathogen. *FEMS Microbiol Rev*, 38(6), 1235-49.

Bertini, I., Gray, H. B., Lippard, S. J. & Valentine, J. S. (1994) *Bioinorganic Chemistry*. Mill Valley, CA: University Science Books.

Bjarnason, J., Southward, C. M. & Surette, M. G. (2003) Genomic profiling of iron-responsive genes in *Salmonella enterica* serovar typhimurium by high-throughput screening of a random promoter library. *J Bacteriol*, 185(16), 4973-4982.

Bloom, S. L. & Zamble, D. B. (2004) Metal-selective DNA-binding response of *Escherichia coli* NikR. *Biochemistry*, 43(31), 10029-38.

Botella, H., Peyron, P., Levillain, F., Poincloux, R., Poquet, Y., Brandli, I., Wang, C., Tailleux, L., Tilleul, S., Charriere, G. M., Waddell, S. J., Foti, M., Lugo-Villarino, G., Gao, Q., Maridonneau-Parini, I., Butcher, P. D., Castagnoli, P. R., Gicquel, B., de Chastellier, C. & Neyrolles, O. (2011) Mycobacterial p(1)-type ATPases mediate resistance to zinc poisoning in human macrophages. *Cell Host Microbe*, 10(3), 248-59.

Botella, H., Stadthagen, G., Lugo-Villarino, G., de Chastellier, C. & Neyrolles, O. (2012) Metallobiology of host-pathogen interactions: an intoxicating new insight. *Trends Microbiol*, 20(3), 106-12.

Boyd, J., Oza, M. N. & Murphy, J. R. (1990) Molecular cloning and DNA sequence analysis of a diphtheria *tox* iron-dependent regulatory element (*dtxR*) from *Corynebacterium diphtheriae*. *Proc Natl Acad Sci U S A*, 87(15), 5968-72.

Boyer, E., Bergevin, I., Malo, D., Gros, P. & Cellier, M. F. (2002) Acquisition of Mn(II) in addition to Fe(II) is required for full virulence of *Salmonella enterica* serovar Typhimurium. *Infect Immun*, 70(11), 6032-42.

Brown, D. R., Qin, K., Herms, J. W., Madlung, A., Manson, J., Strome, R., Fraser, P. E., Kruck, T., von Bohlen, A., Schulz-Schaeffer, W., Giese, A., Westaway, D. & Kretzschmar, H. (1997) The cellular prion protein binds copper *in vivo*. *Nature*, 390(6661), 684-7.

Brown, N. L., Stoyanov, J. V., Kidd, S. P. & Hobman, J. L. (2003) The MerR family of transcriptional regulators. *FEMS Microbiology Reviews*, 27(2-3), 145-163.

Burke, B. E. & Pfister, R. M. (1986) Cadmium transport by a Cd^{2+}-sensitive and a Cd^{2+}-resistant strain of *Bacillus subtilis*. *Can J Microbiol*, 32(7), 539-42.

Bush, A. I. (2003) The metallobiology of Alzheimer's disease. *Trends Neurosci*, 26(4), 207-214.

Butcher, J., Sarvan, S., Brunzelle, J. S., Couture, J. F. & Stintzi, A. (2012) Structure and regulon of *Campylobacter jejuni* ferric uptake regulator Fur define apo-Fur regulation. *Proc Natl Acad Sci U S A*, 109(25), 10047-52.

Bäumler, A. J., Tsolis, R. M., van der Velden, A. W. M., Stojiljkovic, I., Anic, S. & Heffron, F. (1996) Identification of a new iron regulated locus of *Salmonella* typhi. *Gene*, 183(1-2), 207-213.

Campanello, G. C., Ma, Z., Grossoehme, N. E., Guerra, A. J., Ward, B. P., Dimarchi, R. D., Ye, Y., Dann, C. E., 3rd & Giedroc, D. P. (2013) Allosteric inhibition of a zinc-sensing transcriptional repressor: Insights into the arsenic repressor (ArsR) family. *J Mol Biol*, 425(7), 1143-57.

Campoy, S., Jara, M., Busquets, N., Perez De Rozas, A. M., Badiola, I. & Barbe, J. (2002) Role of the high-affinity zinc uptake *znuABC* system in *Salmonella enterica* serovar typhimurium virulence. *Infect Immun*, 70(8), 4721-5.

Capdevila, D. A., Edmonds, K. A. & Giedroc, D. P. (2017) Metallochaperones and metalloregulation in bacteria. *Essays Biochem*, 61(2), 177-200.

Carpenter, B. M., Gilbreath, J. J., Pich, O. Q., McKelvey, A. M., Maynard, E. L., Li, Z. Z. & Merrell, D. S. (2013) Identification and characterization of novel *Helicobacter pylori* apo-Fur-regulated target genes. *J Bacteriol*, 195(24), 5526-39.

Carpenter, B. M., Whitmire, J. M. & Merrell, D. S. (2009) This is not your mother's repressor: the complex role of Fur in pathogenesis. *Infect Immun*, 77(7), 2590-601.

Carter, K. P., Young, A. M. & Palmer, A. E. (2014) Fluorescent sensors for measuring metal ions in living systems. *Chem Rev*, 114(8), 4564-601.

Changela, A., Chen, K., Xue, Y., Holschen, J., Outten, C. E., O'Halloran, T. V. & Mondragon, A. (2003) Molecular basis of metal-ion selectivity and zeptomolar sensitivity by CueR. *Science*, 301(5638), 1383-7.

Checa, S. K., Espariz, M., Audero, M. E., Botta, P. E., Spinelli, S. V. & Soncini, F. C. (2007) Bacterial sensing of and resistance to gold salts. *Mol Microbiol*, 63(5), 1307-18.

Chivers, P. T. & Sauer, R. T. (1999) NikR is a ribbon-helix-helix DNA-binding protein. *Protein Sci*, 8(11), 2494-500.

Chivers, P. T. & Sauer, R. T. (2000) Regulation of high affinity nickel uptake in bacteria. Ni^{2+}-Dependent interaction of NikR with wild-type and mutant operator sites. *J Biol Chem*, 275(26), 19735-41.

Chivers, P. T. & Sauer, R. T. (2002) NikR Repressor: high-affinity nickel binding to the C-terminal domain regulates binding to operator DNA. *Chem Biol*, 9(10), 1141-1148.

Cho, Y.-E., Lomeda, R.-A. R., Ryu, S.-H., Lee, J.-H., Beattie, J. H. & Kwun, I.-S. (2007) Cellular Zn depletion by metal ion chelators (TPEN, DTPA and chelex resin) and its application to osteoblastic MC3T3-E1 cells. *Nutr Res Pract*, 1(1), 29-35.

Chou, C. J., Wisedchaisri, G., Monfeli, R. R., Oram, D. M., Holmes, R. K., Hol, W. G. & Beeson, C. (2004) Functional studies of the *Mycobacterium tuberculosis* iron-dependent regulator. *J Biol Chem*, 279(51), 53554-61.

Cobine, P. A., Ojeda, L. D., Rigby, K. M. & Winge, D. R. (2004) Yeast contain a non-proteinaceous pool of copper in the mitochondrial matrix. *J Biol Chem*, 279(14), 14447-55.

Coburn, B., Grassl, G. A. & Finlay, B. B. (2007) *Salmonella*, the host and disease: a brief review. *Immunol Cell Biol*, 85(2), 112-8.

Cong, X., Yuan, Z., Wang, Z., Wei, B., Xu, S. & Wang, J. (2018) Crystal structures of manganese-dependent transcriptional repressor MntR (Rv2788) from *Mycobacterium tuberculosis* in apo and manganese bound forms. *Biochem Biophys Res Commun*, 501(2), 423-427.

Corbin, B. D., Seeley, E. H., Raab, A., Feldmann, J., Miller, M. R., Torres, V. J., Anderson, K. L., Dattilo, B. M., Dunman, P. M., Gerads, R., Caprioli, R. M., Nacken, W., Chazin, W. J. & Skaar, E. P. (2008) Metal chelation and inhibition of bacterial growth in tissue abscesses. *Science*, 319(5865), 962-5.

Cotruvo, J. A., Jr., Aron, A. T., Ramos-Torres, K. M. & Chang, C. J. (2015) Synthetic fluorescent probes for studying copper in biological systems. *Chem Soc Rev*, 44(13), 4400-14.

Crowley, D. E., Wang, Y. C., Reid, C. P. P. & Szaniszlo, P. J. (1991) Mechanisms of iron acquisition from siderophores by microorganisms and plants. *Plant Soil*, 130, 179-198

Crump, J. A., Sjolund-Karlsson, M., Gordon, M. A. & Parry, C. M. (2015) Epidemiology, clinical presentation, laboratory diagnosis, antimicrobial resistance, and antimicrobial management of invasive *Salmonella* infections. *Clin Microbiol Rev*, 28(4), 901-37.

D'Aquino, J. A., Tetenbaum-Novatt, J., White, A., Berkovitch, F. & Ringe, D. (2005) Mechanism of metal ion activation of the diphtheria toxin repressor DtxR. *Proc Natl Acad Sci U S A*, 102(51), 18408-13.

D'Autreaux, B., Pecqueur, L., Gonzalez de Peredo, A., Diederix, R. E., Caux-Thang, C., Tabet, L., Bersch, B., Forest, E. & Michaud-Soret, I. (2007) Reversible redox- and zinc-dependent dimerization of the *Escherichia coli* Fur protein. *Biochemistry*, 46(5), 1329-42.

Dann, C. E., 3rd, Wakeman, C. A., Sieling, C. L., Baker, S. C., Irnov, I. & Winkler, W. C. (2007) Structure and mechanism of a metal-sensing regulatory RNA. *Cell*, 130(5), 878-92.

De Lorenzo, V., Giovannini, F., Herrero, M. & Neilands, J. B. (1988) Metal ion regulation of gene expression. *J Mol Biol*, 203(4), 875-884.

De Lorenzo, V., Wee, S., Herrero, M. & Neilands, J. B. (1987) Operator sequences of the aerobactin operon of plasmid ColV-K30 binding the ferric uptake regulation (*fur*) repressor. *J Bacteriol*, 169(6), 2624-30.

De Pina, K., Desjardin, V., Mandrand-Berthelot, M.-A., Giordano, G. & Wu, L.-F. (1999) Isolation and characterization of the *nikR* gene encoding a nickel-responsive regulator in *Escherichia coli*. *J Bacteriol*, 181(2), 670.

Delany, I., Ieva, R., Soragni, A., Hilleringmann, M., Rappuoli, R. & Scarlato, V. (2005) *In vitro* analysis of protein-operator interactions of the NikR and Fur metal-responsive regulators of coregulated genes in *Helicobacter pylori*. *J Bacteriol*, 187(22), 7703-15.

Delany, I., Rappuoli, R. & Scarlato, V. (2004) Fur functions as an activator and as a repressor of putative virulence genes in *Neisseria meningitidis*. *Mol Microbiol*, 52(4), 1081-90.

Delany, I., Spohn, G., Pacheco, A. B., Ieva, R., Alaimo, C., Rappuoli, R. & Scarlato, V. (2002) Autoregulation of *Helicobacter pylori* Fur revealed by functional analysis of the iron-binding site. *Mol Microbiol*, 46(4), 1107-22.

Deng, Z., Wang, Q., Liu, Z., Zhang, M., Machado, A. C., Chiu, T. P., Feng, C., Zhang, Q., Yu, L., Qi, L., Zheng, J., Wang, X., Huo, X., Qi, X., Li, X., Wu, W., Rohs, R., Li, Y. & Chen, Z. (2015) Mechanistic insights into metal ion activation and operator recognition by the ferric uptake regulator. *Nat Commun*, 6, 7642.

DeWitt, M. A., Kliegman, J. I., Helmann, J. D., Brennan, R. G., Farrens, D. L. & Glasfeld, A. (2007) The conformations of the manganese transport regulator of *Bacillus subtilis* in its metal-free state. *J Mol Biol*, 365(5), 1257-65.

Dian, C., Vitale, S., Leonard, G. A., Bahlawane, C., Fauquant, C., Leduc, D., Muller, C., de Reuse, H., Michaud-Soret, I. & Terradot, L. (2011) The structure of the *Helicobacter pylori* ferric uptake regulator Fur reveals three functional metal binding sites. *Mol Microbiol*, 79(5), 1260-75.

Do, H., Makthal, N., Chandrangsu, P., Olsen, R. J., Helmann, J. D., Musser, J. M. & Kumaraswami, M. (2019) Metal sensing and regulation of adaptive responses to manganese limitation by MtsR is critical for group A streptococcus virulence. *Nucleic Acids Res*, 47(14), 7476-7493.

Dodani, S. C., Domaille, D. W., Nam, C. I., Miller, E. W., Finney, L. A., Vogt, S. & Chang, C. J. (2011) Calcium-dependent copper redistributions in neuronal cells revealed by a fluorescent copper sensor and X-ray fluorescence microscopy. *Proc Natl Acad Sci U S A*, 108(15), 5980-5.

Douglass, E. F., Jr., Miller, C. J., Sparer, G., Shapiro, H. & Spiegel, D. A. (2013) A comprehensive mathematical model for three-body binding equilibria. *J Am Chem Soc*, 135(16), 6092-9.

Dudev, T. & Lim, C. (2008) Metal binding affinity and selectivity in metalloproteins: insights from computational studies. *Annu Rev Biophys*, 37, 97-116.

Dudev, T. & Lim, C. (2014) Competition among metal ions for protein binding sites: determinants of metal ion selectivity in proteins. *Chem Rev*, 114(1), 538-56.

Dupont, C. L., Butcher, A., Valas, R. E., Bourne, P. E. & Caetano-Anolles, G. (2010) History of biological metal utilization inferred through phylogenomic analysis of protein structures. *Proc Natl Acad Sci U S A*, 107(23), 10567-72.

Dupont, C. L., Yang, S., Palenik, B. & Bourne, P. E. (2006) Modern proteomes contain putative imprints of ancient shifts in trace metal geochemistry. *Proc Natl Acad Sci U S A*, 103(47), 17822-7.

Dwarakanath, S., Chaplin, A. K., Hough, M. A., Rigali, S., Vijgenboom, E. & Worrall, J. A. (2012) Response to copper stress in *Streptomyces lividans* extends beyond genes under direct control of a copper-sensitive operon repressor protein (CsoR). *J Biol Chem*, 287(21), 17833-47.

El-Gebali, S., Mistry, J., Bateman, A., Eddy, S. R., Luciani, A., Potter, S. C., Qureshi, M., Richardson, L. J., Salazar, G. A., Smart, A., Sonnhammer, E. L. L., Hirsh, L., Paladin, L., Piovesan, D., Tosatto, S. C. E. & Finn, R. D. (2019) The Pfam protein families database in 2019. *Nucleic Acids Res*, 47(D1), D427-D432.

Ellermeier, J. R. & Slauch, J. M. (2008) Fur regulates expression of the *Salmonella* pathogenicity island 1 type III secretion system through HilD. *J Bacteriol*, 190(2), 476-86.

Ellman, G. L. (1959) Tissue sulfhydryl groups. *Archives of Biochemistry*, 82(1), 70-77.

Ernst, J. F., Bennett, R. L. & Rothfield, L. I. (1978) Constitutive expression of the iron-enterochelin and ferrichrome uptake systems in a mutant strain of *Salmonella* Typhimurium. *J Bacteriol*, 135(3), 928-934.

Eschenmoser, A. & Wintner, C. E. (1977) Natural product synthesis and vitamin B_{12}. *Science*, 196(4297), 1410-20.

Escolar, L., de Lorenzo, V. & Perez-Martin, J. (1997) Metalloregulation *in vitro* of the aerobactin promoter of *Escherichia coli* by the Fur (ferric uptake regulation) protein. *Mol Microbiol*, 26(4), 799-808.

Escolar, L., Perez-Martin, J. & de Lorenzo, V. (1998) Binding of the Fur (ferric uptake regulator) repressor of *Escherichia coli* to arrays of the GATAAT sequence. *J Mol Biol*, 283(3), 537-47.

Escolar, L., Perez-Martin, J. & de Lorenzo, V. (2000) Evidence of an unusually long operator for the Fur repressor in the aerobactin promoter of *Escherichia coli*. *J Biol Chem*, 275(32), 24709-14.

Escolar, L., Pérez-Martín, J. & de Lorenzo, V. (1999) Opening the iron box: Transcriptional metalloregulation by the Fur protein. *J Bacteriol*, 181(20), 6223.

Fields, P. I., Swanson, R. V., Haidaris, C. G. & Heffron, F. (1986) Mutants of *Salmonella* Typhimurium that cannot survive within the macrophage are avirulent. *Proc Natl Acad Sci U S A*, 83(14), 5189-93.

Fillat, M. F. (2014) The FUR (ferric uptake regulator) superfamily: diversity and versatility of key transcriptional regulators. *Arch Biochem Biophys*, 546, 41-52.

Finney, L. A. & O'Halloran, T. V. (2003) Transition metal speciation in the cell: insights from the chemistry of metal ion receptors. *Science*, 300(5621), 931-6.

Flo, T. H., Smith, K. D., Sato, S., Rodriguez, D. J., Holmes, M. A., Strong, R. K., Akira, S. & Aderem, A. (2004) Lipocalin 2 mediates an innate immune response to bacterial infection by sequestrating iron. *Nature*, 432(7019), 917-21.

Foster, A. W., Osman, D. & Robinson, N. J. (2014a) Metal preferences and metallation. *J Biol Chem*, 289(41), 28095-103.

Foster, A. W., Patterson, C. J., Pernil, R., Hess, C. R. & Robinson, N. J. (2012) Cytosolic Ni(II) sensor in cyanobacterium: Nickel detection follows nickel affinity across four families of metal sensors. *J Biol Chem*, 287(15), 12142-51.

Foster, A. W., Pernil, R., Patterson, C. J. & Robinson, N. J. (2014b) Metal specificity of cyanobacterial nickel-responsive repressor InrS: Cells maintain zinc and copper below the detection threshold for InrS. *Mol Microbiol*, 92(4), 797-812.

Foster, A. W., Pernil, R., Patterson, C. J., Scott, A. J. P., Palsson, L. O., Pal, R., Cummins, I., Chivers, P. T., Pohl, E. & Robinson, N. J. (2017) A tight tunable range for Ni(II) sensing and buffering in cells. *Nat Chem Biol*, 13(4), 409-414.

Frechon, D. & Le Cam, E. (1994) Fur (ferric uptake regulation) protein interaction with target DNA: Comparison of gel retardation, footprinting and electron microscopy analyses. *Biochem Biophys Res Commun*, 201(1), 346-55.

Fuangthong, M. & Helmann, J. D. (2003) Recognition of DNA by three ferric uptake regulator (Fur) homologs in *Bacillus subtilis*. *J Bacteriol*, 185(21), 6348-57.

Furukawa, Y., Torres, A. S. & O'Halloran, T. V. (2004) Oxygen-induced maturation of SOD1: a key role for disulfide formation by the copper chaperone CCS. *EMBO J*, 23(14), 2872-2881.

Gaballa, A. & Helmann, J. D. (1998) Identification of a zinc-specific metalloregulatory protein, Zur, controlling zinc transport operons in *Bacillus subtilis*. *J Bacteriol*, 180(22), 5815-5821.

Gao, H., Zhou, D., Li, Y., Guo, Z., Han, Y., Song, Y., Zhai, J., Du, Z., Wang, X., Lu, J. & Yang, R. (2008) The iron-responsive Fur regulon in *Yersinia pestis*. *J Bacteriol*, 190(8), 3063-75.

Giedroc, D. P. & Arunkumar, A. I. (2007) Metal sensor proteins: Nature's metalloregulated allosteric switches. *Dalton Trans,* (29), 3107-20.

Gill, A. O. & Holley, R. A. (2000) Inhibition of bacterial growth on ham and bologna by lysozyme, nisin and EDTA. *Food Res Int*, 33(2), 83-90.

Gilston, B. A., Wang, S., Marcus, M. D., Canalizo-Hernandez, M. A., Swindell, E. P., Xue, Y., Mondragon, A. & O'Halloran, T. V. (2014) Structural and mechanistic basis of zinc regulation across the *E. coli* Zur regulon. *PLoS Biol*, 12(11), e1001987.

Glasfeld, A., Guedon, E., Helmann, J. D. & Brennan, R. G. (2003) Structure of the manganese-bound manganese transport regulator of *Bacillus subtilis*. *Nat Struct Biol*, 10(8), 652-7.

Goetz, D. H., Holmes, M. A., Borregaard, N., Bluhm, M. E., Raymond, K. N. & Strong, R. K. (2002) The neutrophil lipocalin NGAL is a bacteriostatic agent that interferes with siderophore-mediated iron acquisition. *Mol Cell*, 10(5), 1033-1043.

Golynskiy, M. V., Davis, T. C., Helmann, J. D. & Cohen, S. M. (2005) Metal-induced structural organization and stabilization of the metalloregulatory protein MntR. *Biochemistry*, 44(9), 3380-9.

Golynskiy, M. V., Gunderson, W. A., Hendrich, M. P. & Cohen, S. M. (2006) Metal binding studies and EPR spectroscopy of the manganese transport regulator MntR. *Biochemistry*, 45(51), 15359-72.

Gonzalez de Peredo, A., Saint-Pierre, C., Adrait, A., Jacquamet, L., Latour, J. M., Michaud-Soret, I. & Forest, E. (1999) Identification of the two zinc-bound cysteines in the ferric uptake regulation protein from *Escherichia coli*: Chemical modification and mass spectrometry analysis. *Biochemistry*, 38(26), 8582-9.

Grass, G., Rensing, C. & Solioz, M. (2011) Metallic copper as an antimicrobial surface. *Appl Environ Microbiol*, 77(5), 1541-7.

Griggs, D. W. & Konisky, J. (1989) Mechanism for iron-regulated transcription of the *Escherichia coli cir* gene: Metal-dependent binding of fur protein to the promoters. *J Bacteriol*, 171(2), 1048-54.

Grossoehme, N. E. & Giedroc, D. P. (2009) Energetics of allosteric negative coupling in the zinc sensor *S. aureus* CzrA. *J Am Chem Soc*, 131(49), 17860-70.

Grossoehme, N. E. & Giedroc, D. P. (2012) Illuminating allostery in metal sensing transcriptional regulators. *Methods Mol Biol*, 875, 165-92.

Grubbs, R. D. (2002) Intracellular magnesium and magnesium buffering. *Biometals*, 15(3), 251-9.

Grunden, A. M., Ray, R. M., Rosentel, J. K., Healy, F. G. & Shanmugam, K. T. (1996) Repression of the *Escherichia coli modABCD* (molybdate transport) operon by ModE. *J Bacteriol*, 178(3), 735-44.

Guedon, E. & Helmann, J. D. (2003) Origins of metal ion selectivity in the DtxR/MntR family of metalloregulators. *Mol Microbiol*, 48(2), 495-506.

Guedon, E., Moore, C. M., Que, Q., Wang, T., Ye, R. W. & Helmann, J. D. (2003) The global transcriptional response of *Bacillus subtilis* to manganese involves the MntR, Fur, TnrA and sigmaB regulons. *Mol Microbiol*, 49(6), 1477-91.

Haas, C. E., Rodionov, D. A., Kropat, J., Malasarn, D., Merchant, S. S. & de Crécy-Lagard, V. (2009) A subset of the diverse COG0523 family of putative metal chaperones is linked to zinc homeostasis in all kingdoms of life. *BMC Genomics*, 10(1), 470.

Haas, K. L. & Franz, K. J. (2009) Application of metal coordination chemistry to explore and manipulate cell biology. *Chem Rev*, 109(10), 4921-60.

Hall, D. R., Gourley, D. G., Leonard, G. A., Duke, E. M., Anderson, L. A., Boxer, D. H. & Hunter, W. N. (1999) The high-resolution crystal structure of the molybdate-dependent transcriptional regulator (ModE) from *Escherichia coli*: A novel combination of domain folds. *EMBO J*, 18(6), 1435-46.

Hall, H. K. & Foster, J. W. (1996) The role of Fur in the acid tolerance response of *Salmonella* Typhimurium is physiologically and genetically separable from its role in iron acquisition. *J Bacteriol*, 178(19), 5683-91.

Hanaoka, K., Kikuchi, K., Kojima, H., Urano, Y. & Nagano, T. (2004) Development of a zinc ion-selective luminescent lanthanide chemosensor for biological applications. *J Am Chem Soc*, 126(39), 12470-6.

Hantke, K. (1981) Regulation of ferric iron transport in *Escherichia coli* K12: Isolation of a constitutive mutant. *Mol Gen Genet*, 182(2), 288-92.

Hantke, K. (2001) Iron and metal regulation in bacteria. *Curr Opin Microbiol*, 4(2), 172-177.

Hare, D. J., New, E. J., de Jonge, M. D. & McColl, G. (2015) Imaging metals in biology: Balancing sensitivity, selectivity and spatial resolution. *Chem Soc Rev*, 44(17), 5941-5958.

Harvie, D. R., Andreini, C., Cavallaro, G., Meng, W., Connolly, B. A., Yoshida, K., Fujita, Y., Harwood, C. R., Radford, D. S., Tottey, S., Cavet, J. S. & Robinson, N. J. (2006) Predicting metals sensed by ArsR-SmtB repressors: Allosteric interference by a non-effector metal. *Mol Microbiol*, 59(4), 1341-56.

Heffern, M. C., Matosziuk, L. M. & Meade, T. J. (2014) Lanthanide probes for bioresponsive imaging. *Chem Rev*, 114(8), 4496-539.

Hider, R. C. & Kong, X. L. (2011) Glutathione: A key component of the cytoplasmic labile iron pool. *Biometals*, 24(6), 1179-87.

Hill, P. J., Cockayne, A., Landers, P., Morrissey, J. A., Sims, C. M. & Williams, P. (1998) SirR, a novel iron-dependent repressor in *Staphylococcus epidermidis*. *Infect Immun*, 66(9), 4123.

Hood, M. I. & Skaar, E. P. (2012) Nutritional immunity: Transition metals at the pathogen-host interface. *Nat Rev Microbiol*, 10(8), 525-37.

Huang, C. P., Fofana, M., Chan, J., Chang, C. J. & Howell, S. B. (2014) Copper transporter 2 regulates intracellular copper and sensitivity to cisplatin. *Metallomics*, 6(3), 654-61.

Huang, X., Cuajungco, M. P., Atwood, C. S., Hartshorn, M. A., Tyndall, J. D., Hanson, G. R., Stokes, K. C., Leopold, M., Multhaup, G., Goldstein, L. E., Scarpa, R. C., Saunders, A. J., Lim, J., Moir, R. D., Glabe, C., Bowden, E. F., Masters, C. L., Fairlie, D. P., Tanzi, R. E. & Bush, A. I. (1999) Cu(II) potentiation of Alzheimer abeta neurotoxicity. Correlation with cell-free hydrogen peroxide production and metal reduction. *J Biol Chem*, 274(52), 37111-6.

Huang, X., Shin, J. H., Pinochet-Barros, A., Su, T. T. & Helmann, J. D. (2017) *Bacillus subtilis* MntR coordinates the transcriptional regulation of manganese uptake and efflux systems. *Mol Microbiol*, 103(2), 253-268.

Hunt, M. D., Pettis, G. S. & McIntosh, M. A. (1994) Promoter and operator determinants for Fur-mediated iron regulation in the bidirectional *fepA-fes* control region of the *Escherichia coli* enterobactin gene system. *J Bacteriol*, 176(13), 3944-55.

Ikeda, J. S., Janakiraman, A., Kehres, D. G., Maguire, M. E. & Slauch, J. M. (2005) Transcriptional regulation of *sitABCD* of *Salmonella enterica* serovar Typhimurium by MntR and Fur. *J Bacteriol*, 187(3), 912-22.

Imlay, J. A. (2014) The mismetallation of enzymes during oxidative stress. *J Biol Chem*, 289(41), 28121-8.

Irving, H. & Williams, R. J. P. (1948) Order of Stability of Metal Complexes. *Nature*, 162(4123), 746-747.

Iwig, J. S., Leitch, S., Herbst, R. W., Maroney, M. J. & Chivers, P. T. (2008) Ni(II) and Co(II) sensing by *Escherichia coli* RcnR. *J Am Chem Soc*, 130(24), 7592-606.

Iwig, J. S., Rowe, J. L. & Chivers, P. T. (2006) Nickel homeostasis in *Escherichia coli* - the *rcnR-rcnA* efflux pathway and its linkage to NikR function. *Mol Microbiol*, 62(1), 252-62.

Jacquamet, L., Aberdam, D., Adrait, A., Hazemann, J. L., Latour, J. M. & Michaud-Soret, I. (1998) X-ray absorption spectroscopy of a new zinc site in the Fur protein from *Escherichia coli*. *Biochemistry*, 37(8), 2564-71.

Jain, T. & Jayaram, B. (2007) Computational protocol for predicting the binding affinities of zinc containing metalloprotein-ligand complexes. *Proteins*, 67(4), 1167-78.

Jakubovics, N. S., Smith, A. W. & Jenkinson, H. F. (2000) Expression of the virulence-related Sca (Mn^{2+}) permease in *Streptococcus gordonii* is regulated by a diphtheria toxin metallorepressor-like protein ScaR. *Mol Microbiol*, 38(1), 140-53.

Jeter, R. M., Olivera, B. M. & Roth, J. R. (1984) *Salmonella* Typhimurium synthesizes cobalamin (vitamin B_{12}) *de novo* under anaerobic growth conditions. *J Bacteriol*, 159(1), 206.

Kanyo, Z. F., Scolnick, L. R., Ash, D. E. & Christianson, D. W. (1996) Structure of a unique binuclear manganese cluster in arginase. *Nature*, 383(6600), 554-7.

Katigbak, J. & Zhang, Y. (2012) Iron binding site in a global regulator in bacteria - ferric uptake regulator (Fur) protein: structure, Mossbauer properties, and functional implication. *J Phys Chem Lett*, 2012(3), 3503-3508.

Kehl-Fie, T. E. & Skaar, E. P. (2010) Nutritional immunity beyond iron: A role for manganese and zinc. *Curr Opin Chem Biol*, 14(2), 218-24.

Kehres, D. G., Janakiraman, A., Slauch, J. M. & Maguire, M. E. (2002a) Regulation of *Salmonella enterica* serovar Typhimurium *mntH* transcription by H_2O_2, Fe^{2+}, and Mn^{2+}. *J Bacteriol*, 184(12), 3151-8.

Kehres, D. G., Janakiraman, A., Slauch, J. M. & Maguire, M. E. (2002b) SitABCD is the alkaline Mn^{2+} transporter of *Salmonella enterica* serovar Typhimurium. *J Bacteriol*, 184(12), 3159-66.

Kehres, D. G., Zaharik, M. L., Finlay, B. B. & Maguire, M. E. (2000) The NRAMP proteins of *Salmonella* Typhimurium and *Escherichia coli* are selective manganese transporters involved in the response to reactive oxygen. *Mol Microbiol*, 36(5), 1085-100.

Kliegman, J. I., Griner, S. L., Helmann, J. D., Brennan, R. G. & Glasfeld, A. (2006) Structural basis for the metal-selective activation of the manganese transport regulator of *Bacillus subtilis*. *Biochemistry*, 45(11), 3493-505.

Kochanczyk, T., Drozd, A. & Krezel, A. (2015) Relationship between the architecture of zinc coordination and zinc binding affinity in proteins - insights into zinc regulation. *Metallomics*, 7(2), 244-57.

Krezel, A. & Maret, W. (2006) Zinc-buffering capacity of a eukaryotic cell at physiological pZn. *J Biol Inorg Chem*, 11(8), 1049-62.

Kuzmic, P. (1996) Program DYNAFIT for the analysis of enzyme kinetic data: application to HIV proteinase. *Anal Biochem*, 237(2), 260-73.

Lakowicz, J. R. (2006) *Principles of Fluorescence Spectroscopy*. Springer Science & Business Media

Langmuir, I. (1916) The constitution and fundamental properties of solids and liquids. Part I. Solids. *J Am Chem Soc,* 38(11), 2221-2295.

Lau, C. K., Ishida, H., Liu, Z. & Vogel, H. J. (2013) Solution structure of *Escherichia coli* FeoA and its potential role in bacterial ferrous iron transport. *J Bacteriol*, 195(1), 46-55.

Lavrrar, J. L., Christoffersen, C. A. & McIntosh, M. A. (2002) Fur–DNA interactions at the bidirectional *fepdgc-ents* promoter region in *Escherichia coli*. *J Mol Biol*, 322(5), 983-995.

Le Cam, E., Frechon, D., Barray, M., Fourcade, A. & Delain, E. (1994) Observation of binding and polymerization of Fur repressor onto operator-containing DNA with electron and atomic force microscopes. *Proc Natl Acad Sci U S A*, 91(25), 11816-20.

Lee, J. W. & Helmann, J. D. (2006) The PerR transcription factor senses H_2O_2 by metal-catalysed histidine oxidation. *Nature*, 440(7082), 363-7.

Lee, J. W. & Helmann, J. D. (2007) Functional specialization within the Fur family of metalloregulators. *Biometals*, 20(3-4), 485-99.

Lemire, J. A., Harrison, J. J. & Turner, R. J. (2013) Antimicrobial activity of metals: Mechanisms, molecular targets and applications. *Nat Rev Microbiol*, 11(6), 371-84.

Lewin, A. C., Doughty, P. A., Flegg, L., Moore, G. R. & Spiro, S. (2002) The ferric uptake regulator of *Pseudomonas aeruginosa* has no essential cysteine residues and does not contain a structural zinc ion. *Microbiology*, 148(Pt 8), 2449-56.

Li, Y. (2014) Production of vitamin B_{12} in recombinant *Escherichia coli*: an important step for heterologous production of structurally complex small molecules. *Biotechnol J*, 9(12), 1478-9.

Liao, Q., Luking, M., Kruger, D. M., Deindl, S., Elf, J., Kasson, P. M. & Lynn Kamerlin, S. C. (2019) Long time-scale atomistic simulations of the structure and dynamics of transcription factor-DNA recognition. *J Phys Chem B*, 123(17), 3576-3590.

Lieser, S. A., Davis, T. C., Helmann, J. D. & Cohen, S. M. (2003) DNA-binding and oligomerization studies of the manganese(II) metalloregulatory protein MntR from *Bacillus subtilis*. *Biochemistry*, 42(43), 12634-42.

Lisher, J. P., Higgins, K. A., Maroney, M. J. & Giedroc, D. P. (2013) Physical characterization of the manganese-sensing pneumococcal surface antigen repressor from *Streptococcus pneumoniae*. *Biochemistry*, 52(43), 7689-701.

Litwin, C. M. & Calderwood, S. B. (1994) Analysis of the complexity of gene regulation by Fur in *Vibrio cholerae*. *J Bacteriol*, 176(1), 240-8.

Liu, T., Ramesh, A., Ma, Z., Ward, S. K., Zhang, L., George, G. N., Talaat, A. M., Sacchettini, J. C. & Giedroc, D. P. (2007) CsoR is a novel *Mycobacterium tuberculosis* copper-sensing transcriptional regulator. *Nat Chem Biol*, 3(1), 60-8.

Livak, K. J. & Schmittgen, T. D. (2001) Analysis of relative gene expression data using real-time quantitative PCR and the 2(-Delta Delta C(T)) Method. *Methods*, 25(4), 402-8.

Long, F., Su, C.-C., Lei, H.-T., Bolla, J. R., Do, S. V. & Yu, E. W. (2012) Structure and mechanism of the tripartite CusCBA heavy-metal efflux complex. *Philos Trans R Soc B*, 367(1592), 1047-1058.

Lovell, M. A., Robertson, J. D., Teesdale, W. J., Campbell, J. L. & Markesbery, W. R. (1998) Copper, iron and zinc in Alzheimer's disease senile plaques. *J Neurol Sci,* 158(1), 47-52.

Ma, Z., Chandrangsu, P., Helmann, T. C., Romsang, A., Gaballa, A. & Helmann, J. D. (2014) Bacillithiol is a major buffer of the labile zinc pool in *Bacillus subtilis*. *Mol Microbiol*, 94(4), 756-70.

Ma, Z., Faulkner, M. J. & Helmann, J. D. (2012) Origins of specificity and cross-talk in metal ion sensing by *Bacillus subtilis* Fur. *Mol Microbiol*, 86(5), 1144-55.

Ma, Z., Gabriel, S. E. & Helmann, J. D. (2011) Sequential binding and sensing of Zn(II) by *Bacillus subtilis* Zur. *Nucleic Acids Res*, 39(21), 9130-8.

Ma, Z., Jacobsen, F. E. & Giedroc, D. P. (2009) Coordination chemistry of bacterial metal transport and sensing. *Chem Rev*, 109(10), 4644-81.

Macomber, L. & Imlay, J. A. (2009) The iron-sulfur clusters of dehydratases are primary intracellular targets of copper toxicity. *Proc Natl Acad Sci U S A*, 106(20), 8344-9.

Majowicz, S. E., Musto, J., Scallan, E., Angulo, F. J., Kirk, M., O'Brien, S. J., Jones, T. F., Fazil, A., Hoekstra, R. M. & International Collaboration on Enteric Disease 'Burden of Illness, S. (2010) The global burden of nontyphoidal *Salmonella* gastroenteritis. *Clin Infect Dis*, 50(6), 882-9.

Martens, J. H., Barg, H., Warren, M. J. & Jahn, D. (2002) Microbial production of vitamin B_{12}. *Appl Microbiol Biotechnol*, 58(3), 275-85.

Martin, J. E., Waters, L. S., Storz, G. & Imlay, J. A. (2015) The *Escherichia coli* small protein MntS and exporter MntP optimize the intracellular concentration of manganese. *PLoS Genet*, 11(3), e1004977.

Masse, E. & Arguin, M. (2005) Ironing out the problem: new mechanisms of iron homeostasis. *Trends Biochem Sci*, 30(8), 462-8.

Masse, E. & Gottesman, S. (2002) A small RNA regulates the expression of genes involved in iron metabolism in *Escherichia coli*. *Proc Natl Acad Sci U S A*, 99(7), 4620-5.

Massé, E., Majdalani, N. & Gottesman, S. (2003) Regulatory roles for small RNAs in bacteria. *Curr Opin Microbiol*, 6(2), 120-124.

McCarthy, R. C. & Kosman, D. J. (2015) Iron transport across the blood-brain barrier: Development, neurovascular regulation and cerebral amyloid angiopathy. *Cell Mol Life Sci*, 72(4), 709-27.

McGuire, A. M., Cuthbert, B. J., Ma, Z., Grauer-Gray, K. D., Brunjes Brophy, M., Spear, K. A., Soonsanga, S., Kliegman, J. I., Griner, S. L., Helmann, J. D. & Glasfeld, A. (2013) Roles of the A and C sites in the manganese-specific activation of MntR. *Biochemistry*, 52(4), 701-13.

McRae, R., Bagchi, P., Sumalekshmy, S. & Fahrni, C. J. (2009) *In situ* imaging of metals in cells and tissues. *Chem Rev*, 109(10), 4780-827.

Meakins, S., Fisher, I. S., Berghold, C., Gerner-Smidt, P., Tschape, H., Cormican, M., Luzzi, I., Schneider, F., Wannett, W., Coia, J., Echeita, A., Threlfall, E. J. & Enter-net, p. (2008) Antimicrobial drug resistance in human nontyphoidal *Salmonella* isolates in Europe 2000-2004: a report from the Enter-net International Surveillance Network. *Microb Drug Resist*, 14(1), 31-5.

Mikhaylina, A., Ksibe, A. Z., Scanlan, D. J. & Blindauer, C. A. (2018) Bacterial zinc uptake regulator proteins and their regulons. *Biochem Soc Trans*, 46(4), 983-1001.

Mills, S. A. & Marletta, M. A. (2005) Metal binding characteristics and role of iron oxidation in the ferric uptake regulator from *Escherichia coli*. *Biochemistry*, 44(41), 13553-9.

Molbak, K., Baggesen, D. L., Aarestrup, F. M., Ebbesen, J. M., Engberg, J., Frydendahl, K., Gerner-Smidt, P., Petersen, A. M. & Wegener, H. C. (1999) An outbreak of multidrug-resistant, quinolone-resistant *Salmonella enterica* serotype Typhimurium DT104. *N Engl J Med*, 341(19), 1420-5.

Muller, S. I., Valdebenito, M. & Hantke, K. (2009) Salmochelin, the long-overlooked catecholate siderophore of *Salmonella*. *Biometals*, 22(4), 691-5.

Nader, S., Perard, J., Carpentier, P., Arnaud, L., Crouzy, S. & Michaud-Soret, I. (2019) New insights into the tetrameric family of the Fur metalloregulators. *Biometals*, 32(3), 501-519.

Nakashige, T. G., Zhang, B., Krebs, C. & Nolan, E. M. (2015) Human calprotectin is an iron-sequestering host-defense protein. *Nat Chem Biol*, 11(10), 765-71.

Nakashige, T. G., Zygiel, E. M., Drennan, C. L. & Nolan, E. M. (2017) Nickel sequestration by the host-defense protein human calprotectin. *J Am Chem Soc*, 139(26), 8828-8836.

Nandal, A., Huggins, C. C., Woodhall, M. R., McHugh, J., Rodriguez-Quinones, F., Quail, M. A., Guest, J. R. & Andrews, S. C. (2010) Induction of the ferritin gene (*ftnA*) of *Escherichia coli* by Fe^{2+}-Fur is mediated by reversal of H-NS silencing and is RyhB independent. *Mol Microbiol*, 75(3), 637-57.

Natori, Y., Nanamiya, H., Akanuma, G., Kosono, S., Kudo, T., Ochi, K. & Kawamura, F. (2007) A fail-safe system for the ribosome under zinc-limiting conditions in *Bacillus subtilis*. *Mol Microbiol*, 63(1), 294-307.

Nevo, Y. & Nelson, N. (2006) The NRAMP family of metal-ion transporters. *Biochim Biophys Acta*, 1763(7), 609-20.

Novichkov, P. S., Kazakov, A. E., Ravcheev, D. A., Leyn, S. A., Kovaleva, G. Y., Sutormin, R. A., Kazanov, M. D., Riehl, W., Arkin, A. P., Dubchak, I. & Rodionov, D. A. (2013) RegPrecise 3.0--a resource for genome-scale exploration of transcriptional regulation in bacteria. *BMC Genomics*, 14, 745.

O'Halloran, T. & Walsh, C. (1987) Metalloregulatory DNA-binding protein encoded by the *merR* gene: Isolation and characterization. *Science*, 235(4785), 211-4.

O'Halloran, T. V., Frantz, B., Shin, M. K., Ralston, D. M. & Wright, J. G. (1989) The MerR heavy metal receptor mediates positive activation in a topologically novel transcription complex. *Cell*, 56(1), 119-129.

O'Rourke, K. P., Shaw, J. D., Pesesky, M. W., Cook, B. T., Roberts, S. M., Bond, J. P. & Spatafora, G. A. (2010) Genome-wide characterization of the SloR metalloregulome in *Streptococcus mutans*. *J Bacteriol*, 192(5), 1433-43.

Osman, D. & Cavet, J. S. (2010) Bacterial metal-sensing proteins exemplified by ArsR-SmtB family repressors. *Nat Prod Rep*, 27(5), 668-80.

Osman, D. & Cavet, J. S. (2011) Metal sensing in *Salmonella*: implications for pathogenesis. *Adv Microb Physiol*, 58, 175-232.

Osman, D., Foster, A. W., Chen, J., Svedaite, K., Steed, J. W., Lurie-Luke, E., Huggins, T. G. & Robinson, N. J. (2017) Fine control of metal concentrations is necessary for cells to discern zinc from cobalt. *Nat Commun*, 8(1), 1884.

Osman, D., Martini, M. A., Foster, A. W., Chen, J., Scott, A. J. P., Morton, R. J., Steed, J. W., Lurie-Luke, E., Huggins, T. G., Lawrence, A. D., Deery, E., Warren, M. J., Chivers, P. T. & Robinson, N. J. (2019) Bacterial sensors define intracellular free energies for correct enzyme metalation. *Nat Chem Biol*, 15(3), 241-249.

Osman, D., Piergentili, C., Chen, J., Chakrabarti, B., Foster, A. W., Lurie-Luke, E., Huggins, T. G. & Robinson, N. J. (2015) Generating a metal-responsive transcriptional regulator to test what confers metal sensing in cells. *J Biol Chem*, 290(32), 19806-22.

Osman, D., Piergentili, C., Chen, J., Sayer, L. N., Uson, I., Huggins, T. G., Robinson, N. J. & Pohl, E. (2016) The effectors and sensory sites of formaldehyde-responsive regulator FrmR and metal-sensing variant. *J Biol Chem*, 291(37), 19502-16.

Osman, D., Waldron, K. J., Denton, H., Taylor, C. M., Grant, A. J., Mastroeni, P., Robinson, N. J. & Cavet, J. S. (2010) Copper homeostasis in *Salmonella* is atypical and copper-CueP is a major periplasmic metal complex. *J Biol Chem*, 285(33), 25259-68.

Outten, C. E. & O'Halloran, T. V. (2001) Femtomolar sensitivity of metalloregulatory proteins controlling zinc homeostasis. *Science*, 292(5526), 2488-92.

Outten, C. E., Tobin, D. A., Penner-Hahn, J. E. & O'Halloran, T. V. (2001) Characterization of the metal receptor sites in *Escherichia coli* Zur, an ultrasensitive zinc(II) metalloregulatory protein. *Biochemistry*, 40(35), 10417-23.

Pandey, R., Russo, R., Ghanny, S., Huang, X., Helmann, J. & Rodriguez, G. M. (2015) MntR(Rv2788): A transcriptional regulator that controls manganese homeostasis in *Mycobacterium tuberculosis*. *Mol Microbiol*, 98(6), 1168-83.

Panina, E. M., Mironov, A. A. & Gelfand, M. S. (2003) Comparative genomics of bacterial zinc regulons: enhanced ion transport, pathogenesis, and rearrangement of ribosomal proteins. *Proc Natl Acad Sci U S A*, 100(17), 9912-7.

Patterson, C. J., Pernil, R., Dainty, S. J., Chakrabarti, B., Henry, C. E., Money, V. A., Foster, A. W. & Robinson, N. J. (2013) Co(ll)-detection does not follow $K_{Co(II)}$ gradient: Channelling in Co(ll)-sensing. *Metallomics*, 5(4), 352-62.

Patzer, S. I. & Hantke, K. (1998) The ZnuABC high-affinity zinc uptake system and its regulator Zur in *Escherichia coli*. *Mol Microbiol*, 28(6), 1199-210.

Patzer, S. I. & Hantke, K. (2001) Dual repression by Fe^{2+}-Fur and Mn^{2+}-MntR of the *mntH* gene, encoding an NRAMP-like Mn^{2+} transporter in *Escherichia coli*. *J Bacteriol*, 183(16), 4806-13.

Pecqueur, L., D'Autreaux, B., Dupuy, J., Nicolet, Y., Jacquamet, L., Brutscher, B., Michaud-Soret, I. & Bersch, B. (2006) Structural changes of *Escherichia coli* ferric uptake regulator during metal-dependent dimerization and activation explored by NMR and X-ray crystallography. *J Biol Chem*, 281(30), 21286-95.

Perard, J., Coves, J., Castellan, M., Solard, C., Savard, M., Miras, R., Galop, S., Signor, L., Crouzy, S., Michaud-Soret, I. & de Rosny, E. (2016) Quaternary structure of Fur proteins, a new subfamily of tetrameric proteins. *Biochemistry*, 55(10), 1503-15.

Perard, J., Nader, S., Levert, M., Arnaud, L., Carpentier, P., Siebert, C., Blanquet, F., Cavazza, C., Renesto, P., Schneider, D., Maurin, M., Coves, J., Crouzy, S. & Michaud-Soret, I. (2018) Structural and functional studies of the metalloregulator Fur identify a promoter-binding mechanism and its role in *Francisella tularensis* virulence. *Commun Biol*, 1, 93.

Philips, S. J., Canalizo-Hernandez, M., Yildirim, I., Schatz, G. C., Mondragon, A. & O'Halloran, T. V. (2015) Allosteric transcriptional regulation via changes in the overall topology of the core promoter. *Science*, 349(6250), 877-81.

Pi, H. & Helmann, J. D. (2017) Sequential induction of Fur-regulated genes in response to iron limitation in *Bacillus subtilis*. *Proc Natl Acad Sci U S A*, 114(48), 12785-12790.

Pohl, E., Haller, J. C., Mijovilovich, A., Meyer-Klaucke, W., Garman, E. & Vasil, M. L. (2003) Architecture of a protein central to iron homeostasis: Crystal structure and spectroscopic analysis of the ferric uptake regulator. *Mol Microbiol*, 47(4), 903-15.

Pohl, E., Holmes, R. K. & Hol, W. G. (1999) Crystal structure of a cobalt-activated diphtheria toxin repressor-DNA complex reveals a metal-binding SH3-like domain. *J Mol Biol*, 292(3), 653-67.

Pomposiello, P. J. & Demple, B. (2000) Identification of SoxS-regulated genes in *Salmonella enterica* serovar typhimurium. *J Bacteriol*, 182(1), 23-9.

Posey, J. E., Hardham, J. M., Norris, S. J. & Gherardini, F. C. (1999) Characterization of a manganese-dependent regulatory protein, TroR, from *Treponema pallidum*. *Proc Natl Acad Sci U S A*, 96(19), 10887-92.

Que, Q. & Helmann, J. D. (2000) Manganese homeostasis in *Bacillus subtilis* is regulated by MntR, a bifunctional regulator related to the diphtheria toxin repressor family of proteins. *Mol Microbiol*, 35(6), 1454-68.

Rae, T. D., Schmidt, P. J., Pufahl, R. A., Culotta, V. C. & O'Halloran, T. V. (1999) Undetectable intracellular free copper: the requirement of a copper chaperone for superoxide dismutase. *Science*, 284(5415), 805-8.

Ragsdale, S. W. (2006) Metals and their scaffolds to promote difficult enzymatic reactions. *Chem Rev*, 106(8), 3317-37.

Raju, B., Murphy, E., Levy, L. A., Hall, R. D. & London, R. E. (1989) A fluorescent indicator for measuring cytosolic free magnesium. *Am J Physiol*, 256(3 Pt 1), C540-8.

Raux, E., Lanois, A., Levillayer, F., Warren, M. J., Brody, E., Rambach, A. & Thermes, C. (1996) *Salmonella* Typhimurium cobalamin (vitamin B_{12}) biosynthetic genes: functional studies in *S.* Typhimurium and *Escherichia coli*. *J Bacteriol*, 178(3), 753-67.

Raux, E., Thermes, C., Heathcote, P., Rambach, A. & Warren, M. J. (1997) A role for *Salmonella* Typhimurium *cbiK* in cobalamin (vitamin B_{12}) and siroheme biosynthesis. *J Bacteriol*, 179(10), 3202-12.

Reany, O., Gunnlaugsson, T. & Parker, D. (2000) A model system using modulation of lanthanide luminescence to signal Zn^{2+} in competitive aqueous media. *Perkin Trans, 2*(9), 1819-1831.

Reardon, S. (2015) Bacterial arms race revs up. *Nature*, 521(7553), 402-3.

Record, M. T., Ha, J.-H. & Fisher, M. A. (1991) Analysis of equilibrium and kinetic measurements to determine thermodynamic origins of stability and specificity and mechanism of formation of site-specific complexes between proteins and helical DNA, *Methods Enzymol*, 291-343.

Reeder, N. L., Kaplan, J., Xu, J., Youngquist, R. S., Wallace, J., Hu, P., Juhlin, K. D., Schwartz, J. R., Grant, R. A., Fieno, A., Nemeth, S., Reichling, T., Tiesman, J. P., Mills, T., Steinke, M., Wang, S. L. & Saunders, C. W. (2011) Zinc pyrithione inhibits yeast growth

through copper influx and inactivation of iron-sulfur proteins. *Antimicrob Agents Chemother*, 55(12), 5753-60.

Reyes-Caballero, H., Campanello, G. C. & Giedroc, D. P. (2011) Metalloregulatory proteins: Metal selectivity and allosteric switching. *Biophys Chem*, 156(2-3), 103-14.

Riddles, P. W., Blakeley, R. L. & Zerner, B. (1983) [8] Reassessment of Ellman's reagent, *Methods Enzymol*, 49-60.

Robinson, N. J. & Winge, D. R. (2010) Copper metallochaperones. *Annu Rev Biochem*, 79, 537-62.

Rodrigues, A. V., Kandegedara, A., Rotondo, J. A., Dancis, A. & Stemmler, T. L. (2015) Iron loading site on the Fe-S cluster assembly scaffold protein is distinct from the active site. *Biometals*, 28(3), 567-76.

Rohs, R., West, S. M., Sosinsky, A., Liu, P., Mann, R. S. & Honig, B. (2009) The role of DNA shape in protein-DNA recognition. *Nature*, 461(7268), 1248-53.

Rolerson, E., Swick, A., Newlon, L., Palmer, C., Pan, Y., Keeshan, B. & Spatafora, G. (2006) The SloR/Dlg metalloregulator modulates *Streptococcus mutans* virulence gene expression. *J Bacteriol*, 188(14), 5033-44.

Romao, C. V., Ladakis, D., Lobo, S. A., Carrondo, M. A., Brindley, A. A., Deery, E., Matias, P. M., Pickersgill, R. W., Saraiva, L. M. & Warren, M. J. (2011) Evolution in a family of chelatases facilitated by the introduction of active site asymmetry and protein oligomerization. *Proc Natl Acad Sci U S A*, 108(1), 97-102.

Roncarati, D., Pelliciari, S., Doniselli, N., Maggi, S., Vannini, A., Valzania, L., Mazzei, L., Zambelli, B., Rivetti, C. & Danielli, A. (2016) Metal-responsive promoter DNA compaction by the ferric uptake regulator. *Nat Commun*, 7, 12593.

Rowe, B., Ward, L. R. & Threlfall, E. J. (1997) Multidrug-resistant *Salmonella* Typhi: A worldwide epidemic. *Clin Infect Dis*, 24 Suppl 1, S106-9.

Ruijter, J. M., Ramakers, C., Hoogaars, W. M., Karlen, Y., Bakker, O., van den Hoff, M. J. & Moorman, A. F. (2009) Amplification efficiency: Linking baseline and bias in the analysis of quantitative PCR data. *Nucleic Acids Res*, 37(6), e45.

Sambrook, J. & Russell, D. W. (2001) *Molecular Cloning: A Laboratory Manual,* Cold Spring Harbor Laboratory Press.

Sanchez-Vargas, F. M., Abu-El-Haija, M. A. & Gomez-Duarte, O. G. (2011) *Salmonella* infections: An update on epidemiology, management, and prevention. *Travel Med Infect Dis*, 9(6), 263-77.

Sarvan, S., Butcher, J., Stintzi, A. & Couture, J. F. (2018) Variation on a theme: Investigating the structural repertoires used by ferric uptake regulators to control gene expression. *Biometals*, 31(5), 681-704.

Schaffer, S., Hantke, K. & Braun, V. (1985) Nucleotide sequence of the iron regulatory gene fur. *Mol Gen Genet*, 200(1), 110-3.

Schiering, N., Tao, X., Zeng, H., Murphy, J. R., Petsko, G. A. & Ringe, D. (1995) Structures of the apo- and the metal ion-activated forms of the diphtheria *tox* repressor from *Corynebacterium diphtheriae*. *Proc Natl Acad Sci U S A*, 92(21), 9843-50.

Schmitt, M. P. & Holmes, R. K. (1991) Iron-dependent regulation of diphtheria toxin and siderophore expression by the cloned *Corynebacterium diphtheriae* repressor gene *dtxR* in *C. diphtheriae* C7 strains. *Infect Immun*, 59(6), 1899.

Schmitt, M. P. & Holmes, R. K. (1994) Cloning, sequence, and footprint analysis of two promoter/operators from *Corynebacterium diphtheriae* that are regulated by the diphtheria toxin repressor (DtxR) and iron. *J Bacteriol*, 176(4), 1141-9.

Schreiter, E. R., Sintchak, M. D., Guo, Y., Chivers, P. T., Sauer, R. T. & Drennan, C. L. (2003) Crystal structure of the nickel-responsive transcription factor NikR. *Nat Struct Biol*, 10(10), 794-9.

Schreiter, E. R., Wang, S. C., Zamble, D. B. & Drennan, C. L. (2006) NikR-operator complex structure and the mechanism of repressor activation by metal ions. *Proc Natl Acad Sci U S A*, 103(37), 13676-81.

Schubert, H. L., Raux, E., Wilson, K. S. & Warren, M. J. (1999) Common chelatase design in the branched tetrapyrrole pathways of heme and anaerobic cobalamin synthesis. *Biochemistry*, 38(33), 10660-9.

Schwarzenbach, G. & Flaschka, H. A. (1969) *Complexometric titrations*. London, Methuen.

Schymkowitz, J. W., Rousseau, F., Martins, I. C., Ferkinghoff-Borg, J., Stricher, F. & Serrano, L. (2005) Prediction of water and metal binding sites and their affinities by using the Fold-X force field. *Proc Natl Acad Sci U S A*, 102(29), 10147-52.

Scott, A. J. P. (2018) *Determinants of metal-specific transcriptional responses in bacteria*. Doctoral Dissertation, Durham University.

Seo, S. W., Kim, D., Latif, H., O'Brien, E. J., Szubin, R. & Palsson, B. O. (2014) Deciphering Fur transcriptional regulatory network highlights its complex role beyond iron metabolism in *Escherichia coli*. *Nat Commun*, 5, 4910.

Sharma, A., Sharma, D. & Verma, S. K. (2018) *In silico* study of iron, zinc and copper binding proteins of *Pseudomonas syringae* pv. *lapsa*: Emphasis on secreted metalloproteins. *Front Microbiol*, 9, 1838.

Sheikh, M. A. & Taylor, G. L. (2009) Crystal structure of the *Vibrio cholerae* ferric uptake regulator (Fur) reveals insights into metal co-ordination. *Mol Microbiol*, 72(5), 1208-20.

Shin, J. H. & Helmann, J. D. (2016) Molecular logic of the Zur-regulated zinc deprivation response in *Bacillus subtilis*. *Nat Commun*, 7, 12612.

Skaar, E. P. (2010) The battle for iron between bacterial pathogens and their vertebrate hosts. *PLoS Pathog*, 6(8), e1000949.

Spatafora, G., Corbett, J., Cornacchione, L., Daly, W., Galan, D., Wysota, M., Tivnan, P., Collins, J., Nye, D., Levitz, T., Breyer, W. A. & Glasfeld, A. (2015) Interactions of the metalloregulatory protein SloR from *Streptococcus mutans* with its metal ion effectors and dna binding site. *J Bacteriol*, 197(22), 3601-15.

Spiering, M. M., Ringe, D., Murphy, J. R. & Marletta, M. A. (2003) Metal stoichiometry and functional studies of the diphtheria toxin repressor. *Proc Natl Acad Sci U S A*, 100(7), 3808-13.

Stabler, S. P. (2013) Clinical practice. Vitamin B_{12} deficiency. *N Engl J Med*, 368(2), 149-60.

Stabler, S. P. & Allen, R. H. (2004) Vitamin B_{12} deficiency as a worldwide problem. *Annu Rev Nutr*, 24, 299-326.

Stickle, D. F., Vossen, K. M., Riley, D. A. & Fried, M. G. (1994) Free DNA concentration in *E. coli* estimated by an analysis of competition for DNA binding proteins. *J Theor Biol*, 168(1), 1-12.

Stoll, K. E., Draper, W. E., Kliegman, J. I., Golynskiy, M. V., Brew-Appiah, R. A., Phillips, R. K., Brown, H. K., Breyer, W. A., Jakubovics, N. S., Jenkinson, H. F., Brennan, R. G., Cohen, S. M. & Glasfeld, A. (2009) Characterization and structure of the manganese-responsive transcriptional regulator ScaR. *Biochemistry*, 48(43), 10308-20.

Stookey, L. L. (2002) Ferrozine - A new spectrophotometric reagent for iron. *Anal Chem*, 42(7), 779-781.

Supek, F., Supekova, L., Nelson, H. & Nelson, N. (1996) A yeast manganese transporter related to the macrophage protein involved in conferring resistance to mycobacteria. *Proc Natl Acad Sci U S A*, 93(10), 5105-10.

Tanaka, T., Shinkai, A., Bessho, Y., Kumarevel, T. & Yokoyama, S. (2009) Crystal structure of the manganese transport regulatory protein from *Escherichia coli*. *Proteins*, 77(3), 741-6.

Tao, X., Schiering, N., Zeng, H. Y., Ringe, D. & Murphy, J. R. (1994) Iron, DtxR, and the regulation of diphtheria toxin expression. *Mol Microbiol*, 14(2), 191-7.

Tao, X., Zeng, H. Y. & Murphy, J. R. (1995) Transition metal ion activation of DNA binding by the diphtheria *tox* repressor requires the formation of stable homodimers. *Proc Natl Acad Sci U S A*, 92(15), 6803-7.

Taylor, C. M., Osman, D. & Cavet, J. S. (2009) Differential expression from two iron-responsive promoters in *Salmonella enterica* serovar Typhimurium reveals the presence of iron in macrophage-phagosomes. *Microb Pathog*, 46(2), 114-8.

Teixido, L., Cortes, P., Bigas, A., Alvarez, G., Barbe, J. & Campoy, S. (2010) Control by Fur of the nitrate respiration regulators NarP and NarL in *Salmonella enterica*. *Int Microbiol*, 13(1), 33-9.

Threlfall, E. J. (2000) Epidemic *Salmonella* Typhimurium DT 104 - A truly international multiresistant clone. *J Antimicrob Chemother*, 46(1), 7-10.

Tottey, S., Waldron, K. J., Firbank, S. J., Reale, B., Bessant, C., Sato, K., Cheek, T. R., Gray, J., Banfield, M. J., Dennison, C. & Robinson, N. J. (2008) Protein-folding location can regulate manganese-binding versus copper- or zinc-binding. *Nature*, 455(7216), 1138-42.

Troxell, B., Fink, R. C., Porwollik, S., McClelland, M. & Hassan, H. M. (2011) The Fur regulon in anaerobically grown *Salmonella enterica* sv. Typhimurium: Identification of new Fur targets. *BMC Microbiol*, 11, 236.

Troxell, B. & Hassan, H. M. (2013) Transcriptional regulation by Ferric Uptake Regulator (Fur) in pathogenic bacteria. *Front Cell Infect Microbiol*, 3, 59.

Tsolis, R. M., Baumler, A. J., Stojiljkovic, I. & Heffron, F. (1995) Fur regulon of *Salmonella* Typhimurium: Identification of new iron-regulated genes. *J Bacteriol*, 177(16), 4628-37.

Turner, R. J. (2017) Metal-based antimicrobial strategies. *Microb Biotechnol*, 10(5), 1062-1065.

van der Waerden, B. L. & Schulenberger, J. R. (1991) *Algebra.* Springer-Verlag New York.

VanZile, M. L., Chen, X. & Giedroc, D. P. (2002) Allosteric negative regulation of *smt* O/P binding of the zinc sensor, SmtB, by metal ions: a coupled equilibrium analysis. *Biochemistry*, 41(31), 9776-86.

Waldron, K. J. & Robinson, N. J. (2009) How do bacterial cells ensure that metalloproteins get the correct metal? *Nat Rev Microbiol*, 7(1), 25-35.

Waldron, K. J., Rutherford, J. C., Ford, D. & Robinson, N. J. (2009) Metalloproteins and metal sensing. *Nature*, 460(7257), 823-30.

Wandersman, C. & Delepelaire, P. (2004) Bacterial iron sources: From siderophores to hemophores. *Annu Rev Microbiol*, 58, 611-47.

Wang, D., Hurst, T. K., Thompson, R. B. & Fierke, C. A. (2011) Genetically encoded ratiometric biosensors to measure intracellular exchangeable zinc in *Escherichia coli*. *J Biomed Opt*, 16(8), 087011.

Warren, M. J., Raux, E., Schubert, H. L. & Escalante-Semerena, J. C. (2002) The biosynthesis of adenosylcobalamin (vitamin B_{12}). *Natural Product Reports*, 19(4), 390-412.

Waters, L. S., Sandoval, M. & Storz, G. (2011) The *Escherichia coli* MntR miniregulon includes genes encoding a small protein and an efflux pump required for manganese homeostasis. *J Bacteriol*, 193(21), 5887-97.

Wee, S., Neilands, J. B., Bittner, M. L., Hemming, B. C., Haymore, B. L. & Seetharam, R. (1988) Expression, isolation and properties of Fur (ferric uptake regulation) protein of *Escherichia coli* K12. *Biology of Metals*, 1(1), 62-68.

Wegner, S. V., Sun, F., Hernandez, N. & He, C. (2011) The tightly regulated copper window in yeast. *Chem Commun (Camb)*, 47(9), 2571-3.

White, A., Ding, X., vanderSpek, J. C., Murphy, J. R. & Ringe, D. (1998) Structure of the metal-ion-activated diphtheria toxin repressor/*tox* operator complex. *Nature*, 394(6692), 502-6.

White, C., Lee, J., Kambe, T., Fritsche, K. & Petris, M. J. (2009) A role for the ATP7A copper-transporting ATPase in macrophage bactericidal activity. *J Biol Chem*, 284(49), 33949-56.

Wilce, M. C., Bond, C. S., Dixon, N. E., Freeman, H. C., Guss, J. M., Lilley, P. E. & Wilce, J. A. (1998) Structure and mechanism of a proline-specific aminopeptidase from *Escherichia coli*. *Proc Natl Acad Sci U S A*, 95(7), 3472-7.

Williams, R. J. P. (1982) Free manganese(II) and iron(II) cations can act as intracellular cell controls. *FEBS Letters*, 140(1), 3-10.

Williams, R. J. P. & Da Silva, J. J. R. (2001) *The Biological Chemistry of the Elements: The Inorganic Chemistry of Life.* OUP Oxford.

Wolschendorf, F., Ackart, D., Shrestha, T. B., Hascall-Dove, L., Nolan, S., Lamichhane, G., Wang, Y., Bossmann, S. H., Basaraba, R. J. & Niederweis, M. (2011) Copper resistance is essential for virulence of *Mycobacterium tuberculosis*. *Proc Natl Acad Sci U S A*, 108(4), 1621-6.

Wyman, J. & Gill, S. J. (1990) *Binding and linkage : functional chemistry of biological macromolecules*. Mill Valley, CA: University Science Books.

Wösten, M. M. S. M., Kox, L. F. F., Chamnongpol, S., Soncini, F. C. & Groisman, E. A. (2000) A signal transduction system that responds to extracellular iron. *Cell*, 103(1), 113-125.

Xiao, Z. & Wedd, A. G. (2010) The challenges of determining metal-protein affinities. *Nat Prod Rep*, 27(5), 768-89.

Xu, C., Shi, W. & Rosen, B. P. (1996) The chromosomal *arsR* gene of *Escherichia coli* encodes a trans-acting metalloregulatory protein. *J Biol Chem*, 271(5), 2427-32.

Zygiel, E. M. & Nolan, E. M. (2018) Transition metal sequestration by the host-defense protein calprotectin. *Annu Rev Biochem*, 87, 621-643.